Hydrogen Production from Rich Combustion Inside Porous Media

Haakon Pedersen-Mjaanes

Trinity Hall

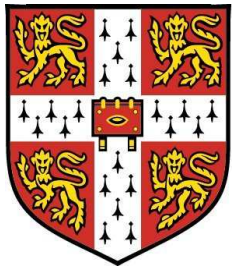

A dissertation submitted for the degree of

Doctor of Philosophy

Department of Engineering

University of Cambridge

2006

Declaration

The work described herein was undertaken in the Engineering Department within the Hopkinson Laboratory at the University of Cambridge between October 2002 and December 2005. This thesis is my own original work except where specifically indicated.

This dissertation contains approximately 45 000 words and 122 figures.

I would like to dedicate this thesis to my parents and friends.

Acknowledgements

Firstly, I would like to express my thanks to my supervisor, Dr. Epaminondas Mastorakos. I am extremely grateful for his support, invaluable guidance and for his efforts in obtaining funding for the research and my stay in Cambridge. I would also like to thank my advisor, Dr. Simone Hochgreb, for her valuable advice during reviews and especially getting me thinking about the Fast TCD.

I am also in debt to the gentlemen of the workshop who were able to transform my drawings into physical constructs. I would like to thank John, Michael, Peter, Robert, Roy and Trevor for their assistance in fabricating the apparatus.

The project was funded through the Chevening Scholarship Foundation, Bombardier, the Cambridge Engineering Department, the Common Wealth Society and Trinity Hall to whom I am grateful.

I am indebted to my colleagues from the Hopkinson Laboratory, namely Andres, Andy, Ben, Chang-Wook, Christos, Claire, Giorgio, Ik Soo, Kamal, Martha, Rama, Ronan, Samer, Seong-Woo, Simon, Teresa and Tom. Their help proved invaluable on many an occasion and the numerous tea breaks and discussions ensured that I kept my sanity and enjoyed my time in the Hopkinson Laboratory.

Finally, my sincere thanks go to my family who offered their unconditional support.

Abstract

Hydrogen is seen as a logical extension of the continuing decarbonization of our energy sector. To maximize hydrogen production, operating above the upper flammability limit is essential for most fuels. Extending the flammability range can be achieved by recirculation of heat and product, use of catalysts or injection of radicals from plasma jets. The simplest method is using some kind of heat exchanger to extract heat from after the combustion zone and use it to preheat the incoming reactants. A relatively new technique is to combust the gas mixture inside the voids formed by a porous medium, taking advantage of the materials' higher heat transfer properties to pre-heat the reactants. This thesis explores the possibility of using stationary rich combustion inside inert porous media to produce synthesis gas.

It is shown that stable combustion of methane, methanol, ethanol, kerosene, biodiesel, octane and petrol at fuel concentrations in excess of the rich flammability limit is possible. Large amounts of hydrogen and carbon monoxide as well as smaller concentrations of C_2 hydrocarbons are measured, with methane and methanol having the highest conversion efficiencies. Generally, these results agree with thermodynamic equilibrium calculations, however, as the equivalence ratio is increased and reaction kinetics slow, the results increasingly deviate from equilibrium.

In addition to commercial measurement instruments, a Fast Thermal Conductivity Detector was designed and fabricated to monitor on a continuous basis the hydrogen yield during transients and start-up. Hydrogen production initially follows changes in demand closely, but there is a time delay before a new equilibrium is reached and the hydrogen yield stabilizes. The ability to handle various liquid and gaseous fuels combined with high conversion efficiencies, quick start-up times, compact and simple design makes this technology suitable to be used as a reformer for both the transport and stationary power sector.

Contents

List of Figures

List of Tables

Nomenclature

A	cross sectional area (m^2)
ATR	autothermal reforming
CEA	Chemical Equilibrium with Applications
D	diameter (m)
ΔH	enthalpy of formation (kJ/mol)
d_m	characteristic pore size (m)
$EPSRC$	Engineering and Physical Sciences Research Council
F	shape factor
FTS	Fischer-Tropsch Synthesis
h	heat transfer coefficient ($W/m^2 \cdot K$)
$IAEA$	International Atomic Energy Agency
$I.C.$	internal combustion
$I.D.$	internal diameter (mm)
k	thermal conductivity ($W/m \cdot K$)
L	length (m)
LHV	lower heating value
LPM	litres per minute
MFC	mass flow controllers
MW	molecular weight ($kg/kmol$)
$\overline{MW}$	average molecular weight ($kg/kmol$)
Nu	Nusselt number
P	pressure (kPa)
Pe	Péclet number
PEM	proton exchange membrane
PM	porous media
POX	partial oxidation
PPC	pores per centimetre
ppm	parts per million
Pr	Prandtl number
PSA	pressure swing absorbtion
q	heat-transfer rate (W)

Re	Reynolds number
R	radius (m)
S_L	laminar flame speed (cm/s)
SR	steam reforming
T	temperatures (K)
TC	thermcouple
LPM	litres per minute
UFL	upper flammability limit
V	velocity (m/s)
W	watt
X	mole fraction $(kmol/kmol)$
Y	mass fraction (kg/kg)

Greek Symbols

α	thermal diffusivity of gas mixture (m^2/s)
Δ	difference
ϵ	emmissivity
η	efficiency (%)
ν	kinematic viscosity (m^2/s)
ρ	density (kg/m^3)
σ	Stefan-Boltzmann constant (w/m^2k^4)
ϕ	equivalence ratio
ψ	porosity (%)

Subscripts

$conv$	convection
$corr$	corrected
$critical$	critical
i	species
in	inner
ℓ	liquid
o	outer
rad	radiative
u	unburned gas
∞	ambient

Chapter 1

Introduction

1.1 Background and Motivation

As far back as 1875, the famous French writer, Jules Vernes, in his book "L'Ile Mystérieuse" predicted that water would replace coal as an energy source (Vernes, 1875). He suggested that water could be split into hydrogen and oxygen to provide an inexhaustible source of heat and light. Unfortunately, today this is not the reality that we live in. Hydrogen is not a primary energy source, but an energy carrier. Despite being the most abundant element in the universe, it exists on earth in its free form, H_2, in only minute quantities. It is bound to other atoms, such as carbon and oxygen, and energy must first be consumed to remove the hydrogen from, for example water, hydrocarbons or other organic matter.

Hydrogen contains more energy per unit mass than any other fuel and produces minimum emissions when combusted and essentially no emissions when electrochemically converted to electricity in a fuel cell. A fuel cell is a device that electrochemically converts hydrogen and oxygen into electricity, with the by-products being heat and water. Furthermore, hydrogen also has the potential to reduce governments' dependence on foreign fuels depending on how it is

generated. These are a few of the reasons why hydrogen is touted as the fuel of the future. However, in order for hydrogen to displace fossil fuels it must also be economical to produce, easy to store and get to market.

Globally, annual hydrogen consumption is currently around 5×10^{11} Nm^3 corresponding to around 2 % of primary energy demand (IAEA, 1999). Currently most hydrogen is produced from fossil fuels for industrial processes in petroleum refining, the fertiliser and other chemical industries, as well as fuel for the space shuttle's rocket engines. As environmental regulations have tightened in the petroleum refinery industry and the demand for cleaner distillates has increased, heavier streams are being hydrotreated. This has also increased the demand for hydrogen (Meyers, 1997).

Many studies have been conducted concerning future hydrogen demand, for example Barreto et al. (2003). However, it is difficult to forecast when hydrogen will comprise a significant share of the world energy market. Currently, numerous cities in North America, Europe and Japan are testing hydrogen fuel cell powered bus fleets. Prototype automobiles are also being tested in limited numbers. Iceland is ambitiously pursuing a goal of becoming the first country to replace their fossil fuel economy with a hydrogen economy. However, Iceland has vast thermal resources that can be harnessed to electrolyse water into hydrogen, whereas most other countries are not so fortunate.

There are several reasons why most other countries cannot immediately switch to a hydrogen economy, aside from economics. Most countries currently do not have sufficient renewable resources to produce enough hydrogen for their economy via electrolysis. Additionally, gaseous hydrogen only contains about one fifth of the energy of gasoline when stored at reasonable pressures ($\approx$ 600 bar). Problems exist using natural gas pipelines to transport hydrogen due to hydrogen embrittlement of the pipes and the very small size of the hydrogen molecule can lead to

significant leakage. Finally, making the transition to a hydrogen economy means converting the existing fossil fuel infrastructure that is already developed.

An alternative is to use a fuel reformer to extract hydrogen from existing fuels and alcohols. For example, a fuel cell powered automobile could use any number of fuels currently available, including methanol, ethanol, gasoline or even diesel. Such automobiles could operate more efficiently and produce fewer emissions, whilst creating a bridge between the future hydrogen economy and the present fossil fuel economy.

Aside from burning hydrogen directly in an engine or converting it to electricity in a fuel cell, research is also been conducted into burning fuels richly to produce a syngas ($CO + H_2$) and then combusting this mixture, with additional air, very lean, thereby negating NO_X emissions (Jamal and Wyszynski, 1994). Syngas demand is also increasing for use in the Fischer-Tropsch Synthesis (FTS) process to convert natural gas to liquid fuels. This demand is being driven by: (1) an increase in the known reserves of natural gas, (2) the need to monetize remote or stranded natural gas, (3) environmental pressure to reduce the flaring of gases and the desire to use cleaner fuels and (4) improvements in the FTS process, especially from the development of improved catalysts (Vosloo, 2001). Davis (2002) provides a good overview of the history and progress of the FTS process since Fischer and Tropsch discovered the production of liquid hydrocarbons from synthesis gas in 1923.

Although numerous technologies exist for producing hydrogen, the three main methods are steam reforming, autothermal reforming and partial oxidation (rich combustion). Partial oxidation and autothermal reforming processes have better dynamic responses and are more compact than a comparative steam reformer (Ahmed and Krumpelt, 2001; Ersoz et al., 2003; Meyer et al., 2000). Usually, they involve a catalyst which ensures good conversion, but a catalyst is prone

to poisoning and requires great care with the sulphur content of the fuel and with particulates. Additionally, the non-catalytic partial oxidation of methane produces syngas with a H_2/CO ratio less than two, which is close to the optimum needed by the Fischer-Tropsch process (Vosloo, 2001).

One of the most promising non-catalytic partial oxidation techniques is combustion inside a porous medium. This medium could be a fluidized or a stationary bed. In this thesis, stationary rich flames are stabilized in a compact two-layer burner comprising different porous materials.

1.2 Structure of this Chapter

The next section of this chapter provides a synopsis of the current status of existing hydrogen production technologies. Section 1.4.1 gives a more detailed review of the literature of combustion in porous media and where the current work contributes to the field. The final section of the chapter discusses the objectives of this thesis along with its structure.

1.3 Methods for Producing Hydrogen

While oil and gas are predominantly concentrated in one geographical location as illustrated by Fig. (1.1), hydrogen can be produced from numerous sources, many close to the end user. This results in reduced transportation costs, more stable energy prices and an increase in energy independence. This section describes the various sources and methods for producing hydrogen and aims to put into context the technique used in this thesis.

Fig. (1.2) illustrates the main pathways to produce hydrogen from primary energy sources. As an alternative to reforming the hydrocarbons and alcohols to

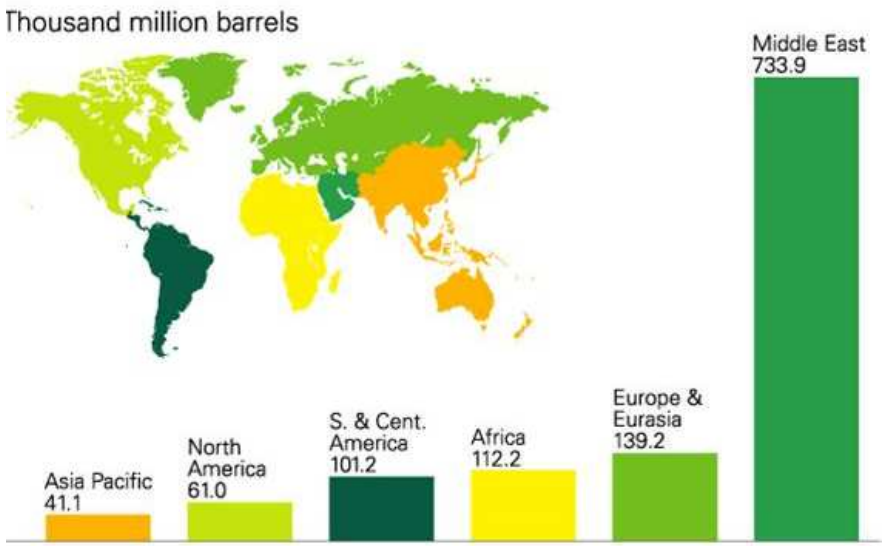

Figure 1.1: Proved world oil reserves at end of 2004 (BP, 2005). Note that this Excludes 174.5 billion barrels of proven oil sands reserves in Canada (Radler, 2004)

.

hydrogen, they could be combusted and the heat generated used to produce electricity to drive an electrolysis step to produce hydrogen. However, this method would be less efficient than producing hydrogen directly from the hydrocarbons. In the electrolysis process some of the energy required can also be provided by heat. The Rankine cycle is the most common thermodynamic cycle used to convert heat to electricity, but for some applications it could be replaced by the Sterling or Brayton cycle.

The process of *reforming* a primary energy source into a syngas or hydrogen can be broken down into four major subcategories:

1. Steam Reforming (SR)

2. Partial Oxidation (POX)

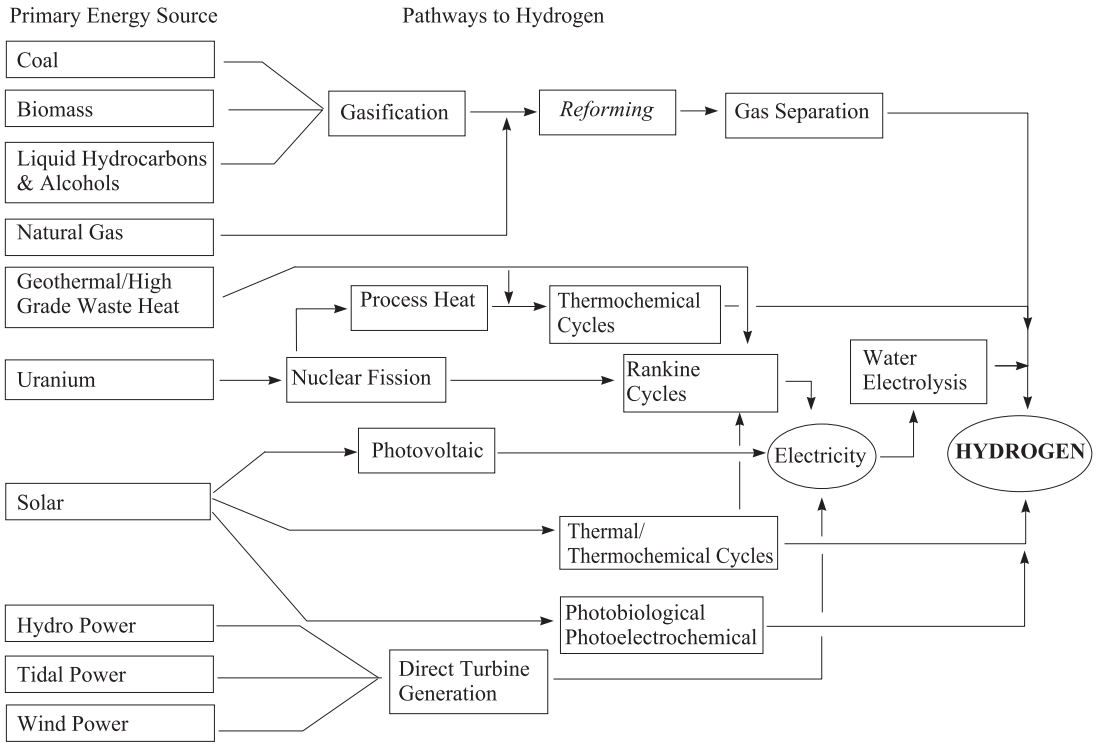

Figure 1.2: Pathways to hydrogen from primary energy sources.

3. Autothermal Reforming (ATR)

4. Pyrolysis

1.3.1 Steam Reforming

Steam reforming (SR) of natural gas is currently the cheapest method to produce hydrogen, accounting for half of the world's hydrogen production (Ewan and Allen, 2005). Such a method can convert light hydrocarbons and alcohols to hydrogen, with or without a catalyst via

$$\mathrm{C_nH_mO_p} + (\mathrm{n} - \mathrm{p})\,\mathrm{H_2O} \leftrightarrow \left(\frac{\mathrm{m}}{2} + \mathrm{n} - \mathrm{p}\right)\mathrm{H_2} + \mathrm{nCO}. \tag{1.1}$$

Most commercial applications use a nickel-based catalyst to enhance reaction rates at lower temperatures. Under these conditions, methane which is the main constituent of natural gas can be converted to a hydrogen rich gas reformate according to,

$$CH_4 + H_2O \leftrightarrow CO + 3H_2 \quad \Delta H = 206 \text{ kJ/mol.} \tag{1.2}$$

The second important reaction in a SR process is the water gas-shift reaction, which produces additional H_2 from water and fully oxidizes the CO to CO_2,

$$H_2O + CO \leftrightarrow H_2 + CO_2 \quad \Delta H = -41 \text{ kJ/mol.} \tag{1.3}$$

The reaction is exothermic, and equilibrium will favour low temperatures in accordance with Le Châtelier's principle. Since it is an equimolar reaction it will be unaffected by changes in pressure. When combining the steam reforming and water gas shift reactions, the net reaction, is endothermic. For methane this can be written as,

$$CH_4 + 2H_2O \leftrightarrow CO_2 + 4H_2 \quad \Delta H = 165 \text{ kJ/mol.} \tag{1.4}$$

To provide the necessary energy, a high temperature heat source is required, usually taking the form of an adjacent furnace that combusts a small portion of the feedstock. Typically, the overall efficiency of this process for methane is approximately 76 %. This gives a hydrogen yield, from methane on a volume basis of 2.4:1 (Simbeck and Chang, 2002). Typically, 1-2 % CO remains after the shift reaction (Hou et al., 2003). For use in a proton exchange membrane fuel cell (the most likely fuel cell for automobiles) the CO must be further reduced to about 50 ppm in a gas cleaning process to prevent poisoning the platinum catalyst (DuPont, 2002).

Steam reforming is a highly endothermic reaction, and reactor designs are generally limited by heat transfer, rather than reaction kinetics (Ahmed and Krumpelt, 2001). As a result, a relatively large reactor is required. Such a reactor has difficulties coping with rapid start-up and transient behaviour due to the indirect heat transfer across the reactor walls. This limits its attractiveness for mobile applications.

1.3.2 Partial Oxidation

In a partial oxidation (POX) reactor a sub-stoichiometric amount of air or oxygen is used to partially combust a hydrocarbon or alcohol. The reaction is exothermic and raises the reactants to a high temperature. Heavy hydrocarbons can be non-catalytically reformed at temperatures in excess of 1200 K. Since the high temperatures take the place of a catalyst, POX is not limited to the light, clean fuels reformed in a SR process. However, for lighter fuels the use of a catalyst can reduce substantially the operating temperature. The net reaction equation to reform a generic hydrocarbon or alcohol can be written as

$$\mathrm{C_nH_mO_p} + \left(\frac{\mathrm{n}}{2} - \frac{\mathrm{p}}{2}\right)\mathrm{O_2} \leftrightarrow \left(\frac{\mathrm{m}}{2}\right)\mathrm{H_2} + \mathrm{nCO}, \tag{1.5}$$

and for methane, the equation is

$$\mathrm{CH_4} + \frac{1}{2}\mathrm{O_2} \leftrightarrow 2\mathrm{H_2} + \mathrm{CO} \quad \Delta\mathrm{H} = -36 \text{ kJ/mol}. \tag{1.6}$$

As with SR, a water-gas shift reaction can be incorporated to increase hydrogen conversion and fully oxidize the CO to CO_2. Compared to a SR, a POX reactor is generally more compact and lighter as indirect (through wall) heat transfer is not required. The main disadvantage of partial oxidation is the dilution of the hydrogen by inert nitrogen, when combusting in air.

1.3.3 Autothermal

Autothermal-Reforming (ATR) is the coupling of POX with SR, thereby equilibrating the heat of both reactions allowing the process to be driven in an autothermal mode. ATR produces a more concentrated hydrogen gas stream than POX but less than pure steam reforming. The heat transfer between the two processes allows for an overall lower operating temperature than for a straight POX and a more compact reformer compared to a straight steam reformer. Furthermore, ATR offers a fuel processor compromise that results in the most flexibility in heat management, a higher H_2 concentration than the POX and a better transient response than SR (Berlowitz and Darnell, 2000). Despite its potential, ATR is the least developed of the three major reforming technologies, partially due to the careful thermal integration and tight controls that are required to ensure heat balance and temperature matching between the two reactions. Therefore, it will require substantial science and engineering efforts to bring its development up to the level of the SR and POX technologies.

1.3.4 Generic Fuel Conversion

SR, POX and ATR reforming are the main reforming techniques used to produce hydrogen. The following equation, published by Ahmed and Krumpelt (2001), is the idealized reaction stoichiometry for the conversion of a hydrocarbon or oxygenate fuel by any of the above three methods,

$$\begin{aligned} \mathrm{C_nH_mO_p} + x(\mathrm{O_2} + 3.76\mathrm{N_2}) + (y)\mathrm{H_2O}_\ell \\ \leftrightarrow n\mathrm{CO_2} + (z)\mathrm{H_2} + 3.76x\mathrm{N_2} \end{aligned} \tag{1.7}$$

where x is the molar ratio of oxygen to fuel. This ratio is important in determining a number of qualities. These are,

(a) the minimum water required to completely convert the carbon in the fuel to carbon dioxide,

$$y = 2n - 2x - p \tag{1.8}$$

(b) the maximum hydrogen yield,

$$z = 2n - 2x - p + \frac{m}{2} \tag{1.9}$$

(c) the maximum concentration (percent) of hydrogen in the reformate,

$$\frac{2n - 2x - p + \frac{m}{2}}{n + \left(2n - 2x - p + \frac{m}{2}\right) + 3.76x} \tag{1.10}$$

(d) the heat of reaction,

$$\Delta H_r = (n)\Delta H_{f,\mathrm{CO_2}} - (2n - 2x - p)\Delta H_{f,\mathrm{H_2O}} - \Delta H_{f,\mathrm{fuel}} \tag{1.11}$$

(e) the thermoneutral point, when

$$\Delta H = 0. \tag{1.12}$$

This is a total reaction where the fuel is converted to carbon dioxide. In reality, a mixture of carbon monoxide and carbon dioxide will be formed. In the subsequent water-gas shift reaction, the carbon monoxide will be fully oxidized to carbon dioxide. Fig. (1.3) plots the quantities of H_2, CO_2, N_2 and H_2O calculated from Eq. (1.7).

As is evident from the above equations, decreasing the oxygen to fuel ratio, x, results in an increasing demand for water to balance the equation. This also increases the hydrogen yield and concentration in the reformate. When $x = 0$, the equation reduces to the strong endothermic steam reforming reaction,

represented by Eq. (1.4) for methane. As x is increased the reaction becomes less endothermic until at $x = x_o$ the reaction becomes thermoneutral, x_o=0.44 for methane. Beyond this point, the reaction becomes increasingly exothermic. At $x = n - p/2$, which is 1 for methane, the feed contains sufficient oxygen to oxidize completely all the carbon to carbon dioxide, and no water is required.

At higher values [$x > n - p/2$], which is $x > 1$ for methane, the excess oxygen oxidizes the hydrogen to produce water. The heat of reaction is then determined by the phase of the water product. Finally, at stoichiometric combustion [$x = n + m/4 - p/2$], which is 2 for methane, all of the hydrogen and carbon are converted into water and carbon dioxide. Note that the equation is a mix of the SR reaction and the POX reaction at values of x between 0 and n (n=1 for CH_4).

Fig. (1.4) plots the effect of x on the lower heating value of the fuel and product H_2 as well as the efficiency of the idealized reforming process. When $x < x_0$, endothermic, additional fuel must be combusted to provide the required energy for the reaction. The maximum theoretical efficiency occurs at the thermoneutral point where $x = x_o$. For CH_4, this corresponds to a ϕ of 4.55 and 1.12 moles of H_2O per mole of CH_4.

The molar ratio of oxygen to fuel for the experiments conducted in this thesis was between $0.8 < x < 1.33$ with CH_4 as the fuel.

1.3.5 Pyrolysis

Pyrolysis is the endothermic thermal decomposition of organic material in the absence of oxygen. It is generally seen as the first step in steam gasification of biomass as noted by Piskorz et al. (1988), Marquevich et al. (1999) and Muradov (2001). However, research is also being conducted into a single stage process that has the potential to eliminate CO_2 emissions that the above methods suffer from,

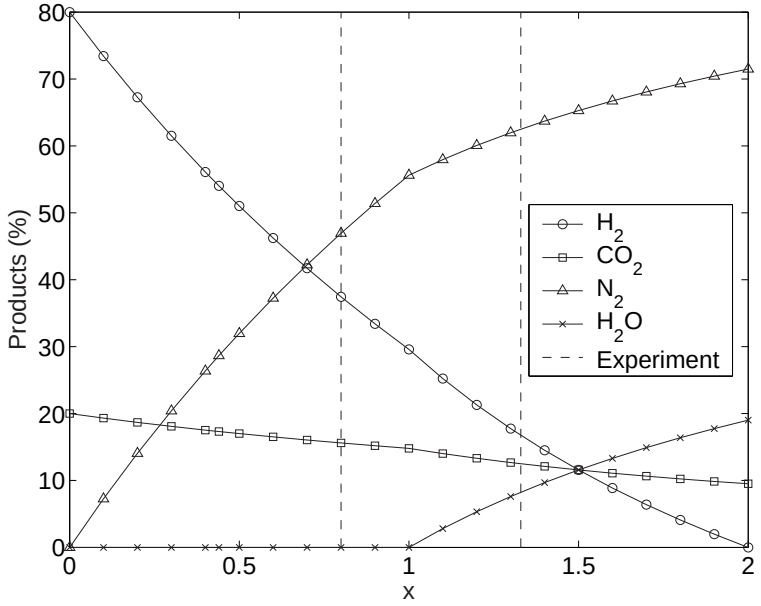

Figure 1.3: Products from the idealized autothermal conversion of methane.

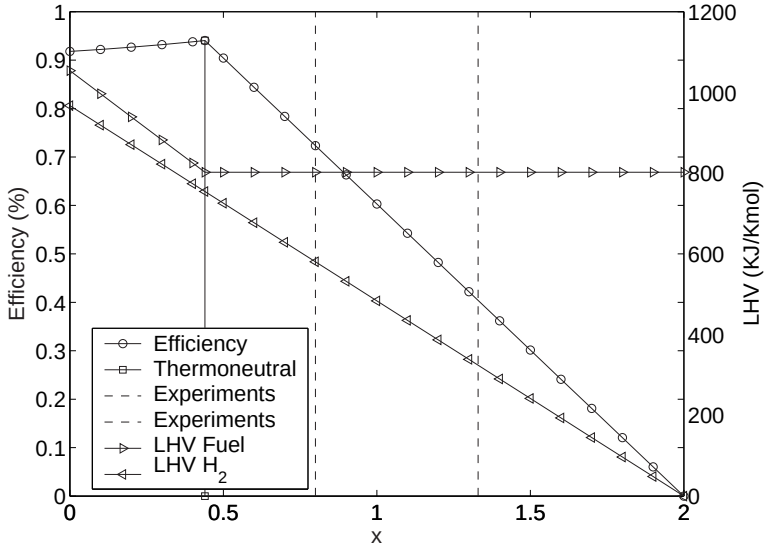

Figure 1.4: Efficiency of the idealized autothermal conversion of methane.

$$CH_4 \rightarrow C + 2H_2 \quad \Delta H = 75.6 \text{ kJ/mol.} \tag{1.13}$$

In this process, Muradov (1998) reports that catalytic pyrolysis of light liquid hydrocarbons over activated carbon yields 40-50 % H_2 gas by volume (with the balance being unreacted feedstock). The carbon is removed as a solid, sulfur and ash-free, product to be used in structural materials, soil amendment and environmental remediation. Muradov and Veziroglu (2005) estimate that this process becomes competitive with conventional methane SR at a carbon selling price of $100-300/ton.

1.3.6 Coal Processing

Gasification of coal is the oldest method of producing hydrogen. Many people in the 19th century burned a fuel called "town gas", currently known as syn-gas, which is a mixture of hydrogen and carbon monoxide. Typically, the coal is heated up to a temperature as high as 1260 °C in the presence of steam and air to partially oxidize the coal into a gas product. Based on a study by Simbeck and Chang (2002), coal gasification has an efficiency of 59 %, excluding sequestration (efficiency is defined in section 5.4). Due to larger world reserves and the geographical location of these reserves, new technologies for the gasification of coal are the object of intense research and development efforts. However since coal has a high carbon to hydrogen ratio, large amounts of carbon are released as a by-product. Additionally, sulphur and nitrogen compounds are also released, their quantities dependant on the composition of the fuel and gasification process used.

1.3.7 Sequestration

Although not actually a method to produce H_2, sequestration is one method to mitigate CO_2 emissions. Sequestration is the prevention of anthropogenic CO_2 emissions from reaching the atmosphere by capturing and storing the CO_2 in geological formations, for example, at the bottom of oceans and in aquifers. In general, it involves several steps: the capture of CO_2, pressurization, transportation and injection of liquid CO_2 into geological formations. At typical pressures and temperatures that exist in the ocean, CO_2 would exist as a liquid below 500 m. However, due to its relatively low density it would be positively buoyant in seawater down to depths of 3 000 m (Muradov and Veziroglu, 2005).

Audus et al. (1996) estimate the sequestration of CO_2 from a concentrated stream after pressure swing absorption adds approximately 25-30 % to the cost of hydrogen production and significantly more from diluted streams. The technical feasibility of a large scale, deep, saline aquifer has been proved by Statoil in the North Sea (in response to a \$50/ton carbon tax imposed by the Norwegian government). Another commercial technique currently used in the chemical industry, to remove CO_2 from flue gases, is Econamine FG process. It consumes 0.23 GJ per 1 GJ of primary energy when the feedstock is methane and 0.46 GJ per 1 GJ of primary energy when the feedstock is coal (Ewan and Allen, 2005).

Aside from the additional cost sequestration adds to hydrogen production, the long-term ecological consequences need to be addressed. Reservoirs need to be better understood with respect to their size, permanence and environmental impact. By way of example, in 1986, Lake Nyos in Cameroon erupted, releasing large quantities of CO_2 which killed over 1 700 people and 3 000 cattle by asphyxiation.

1.3.8 Electrolysis and Thermal Water Splitting

Electrolysis is the splitting of a water molecule with electricity to produce hydrogen and oxygen,

$$2H_2O \rightarrow O_2 + 2H_2. \tag{1.14}$$

The charge breaks the bond between the hydrogen and oxygen creating ions that form on two poles: the positively charged anode attracts the oxygen and the negatively charged cathode attracts the hydrogen. The main disadvantage of this process is that since the hydrogen is generated indirectly via electricity, efficiencies are relatively low, Ewan and Allen (2005) quote 70 %, while Yildiz and Kazimi (2005) quote 85-90 % for the water electrolysis process. The overall efficiency, including the power generation is closer to 25-35 %. As a result this process is currently only economically feasible in countries that have excess hydro-generating capacity or large thermal resources. As renewable energy resources such as solar and wind become more economical they will increasingly be harnessed to produce clean hydrogen.

Steam electrolysis is a variation of conventional electrolysis that uses high temperature steam to provide some of the energy to split the water and increase the overall efficiency of the process. Another approach to generating hydrogen is through solar-thermal which eliminates the need for an electrolyser. To dissociate water molecules using thermal energy, temperatures above 4000 K are required. Alternatively, using various catalysts this temperature can be reduced to less than 1000 K (Steinfeld, 2002). However, these last two processes are still in their infancy and currently do not produce appreciable amounts of hydrogen.

1.3.9 Thermochemical Cycles

Thermochemical water splitting uses chemicals such as bromine and iodine in the presence of heat to split water. One such example is Millennium Cell's and Daimler-Chrysler's minivan powered by hydrogen gas, separated from sodium borohydride and water in the presence of heat (Cropper, 2001).

Renewed interest in using nuclear power to generate electricity and more recently hydrogen, has resulted in several new high temperature reactor designs that are suitable for hydrogen production. Nuclear energy can be used to produce hydrogen in three ways:

- By using the electricity generated in a conventional water electrolysis process.
- By using both the electricity and high temperature heat in a combined high temperature steam electrolysis process.
- By using the high temperature heat in a thermochemical process.

Aside from the current methane SR technology that can be coupled to a nuclear source for near term hydrogen production, a recent study by Besenbruch et al. (2000) identified two thermochemical water splitting cycles with the highest commercial potential. These are the sulfur-iodine cycle (General Atomics) and the UT-3 cycle (University of Tokyo).

The sulfur-iodine (SI) cycle consists of three chemical reactions which yield the dissociation of water (Brown et al., 2003). These and their operating temperatures are,

$$I_2 + SO_2 + 2H_2O \rightarrow 2HI + H_2SO_4 \quad (120\ ^\circ C) \tag{1.15}$$

$$H_2SO_4 \rightarrow SO_2 + H_2O + \frac{1}{2}O_2 \quad (830 - 900\ ^\circ C) \tag{1.16}$$

$$2HI \rightarrow I_2 + H_2 \quad (300 - 450\ ^\circ C). \tag{1.17}$$

In this process all reagents are recycled and all reactions are fluid interactions. Water and high temperature heat are converted into H_2 and O_2. The disadvantages of this process are its high operating temperature combined with an aggressive chemical environment where sulfuric acid and hydrogen iodide are decomposed.

Ca-Br-Fe (UT-3) cycle involving solid-gas interactions can be represented by the following equations:

$$CaBr_2 + H_2O \rightarrow CaO + 2HBr \quad (730\ ^\circ C) \tag{1.18}$$

$$CaO + Br_2 \rightarrow CaBr_2 + \frac{1}{2}O_2 \quad (550\ ^\circ C) \tag{1.19}$$

$$Fe_3O_4 + 8HBr \rightarrow 3FeBr_2 + 4H_2O + Br_2 \quad (220\ ^\circ C) \tag{1.20}$$

$$3FeBr_2 + 4H_2O \rightarrow Fe_3O_4 + 6HBr + H_2 \quad (650\ ^\circ C) \tag{1.21}$$

The thermodynamics of these reactions has been proved favourable. However, the efficiency is limited to approximately 40 % due to the melting point of $CaBr_2$ at 760 °C (Hahn, 2004).

The two main disadvantages of using these cycles are the requirement for development of large scale plants necessitating large initial capital investment and the need to overcome the negative opinion the public has towards nuclear power.

1.3.10 Photobiological/Photoelectrochemical Processes

Photoelectrochemical processes use two types of electrochemical systems to produce hydrogen. In the first process, sunlight incident on a semiconductor electrode splits the water directly without the need for an external electrolyser (Bansal et al., 1999). In the second process soluble metal complexes are employed as

catalysts. When the soluble metal dissolves, it absorbs solar energy and produces an electrical charge that splits the water. Although these processes are less advanced than photovoltaics and the efficiencies are lower, so are the costs. The most advanced photoelectrochemical cell is based on the dye-sensitization of $n - T_iO_2$ and can achieve efficiencies in excess of 10 % (Polo et al., 2004).

Biological and photobiological processes can use algae and bacteria to produce hydrogen. Under certain conditions, pigments in specific types of algae can absorb solar energy. The enzyme in the cell acts as a catalyst to split the water molecules thereby producing hydrogen. Photosynthetic bacteria such as Rhodocyclus gelatinosus and Rhodospirillum rubrum can perform a water-gas shift reaction to produce H_2 and CO_2 in nearly stoichiometric quantities (Maness and Weaver, 1999). This technology also holds great promise, but it must overcome the problem of the sensitivity the enzyme systems have to the oxygen produced along with the hydrogen.

1.3.11 Gas Separation System

Carbon monoxide can be removed from the final gas stream by several different processes. Co-oxidation is a process where low levels of CO are oxidized in the presence of high concentrations of hydrogen over a noble catalyst according to

$$CO + \frac{1}{2}O_2 \rightarrow CO_2 \tag{1.22}$$

(Wagner and Takeda, 2001). Depending on the selectivity of the catalyst some H_2 will also be oxidized according to

$$H_2 + \frac{1}{2}O_2 \rightarrow H_2O. \tag{1.23}$$

The following processes are discussed in more detail in Meyers (1997). Methanation is a reaction that converts any residual carbon oxides back to methane using a small part of the H_2 product. It takes place at lower temperatures, 200 °C,

through a catalyst,

$$CO + 3H_2 \rightarrow CH_4 + H_2O. \tag{1.24}$$

At higher temperatures a strong exothermic reaction is also possible,

$$CO_2 + 4H_2 \rightarrow CH_4 + 2H_2O. \tag{1.25}$$

Gas can also be separated through membranes to a very high purity but currently only low flow rates are possible. Alternatively, pressure-swing adsorption (PSA) can purify the hydrogen rich stream by selectively adsorbing the other gases. This process is generally quite bulky and is only applicable to stationary plants.

1.3.12 Soot Produced by Partial Oxidation Combustion

Rich oxidation may result in particulate formation in many H_2 producing techniques. Air pollutants called particular matter include; soot, smoke, dust, dirt and liquid droplets emitted into the air by automobiles, factories, power plants and fires. Soot is carbonaceous particles formed during incomplete combustion. Soot particles are agglomerates of small, roughly spherical particles. Atmospheric particles have long been recognized to cause respiratory problems. Generally, the smaller the particle size the deeper it can penetrate into the lungs and the larger the adverse health effects. Soot can also have a significant effect on global warming. Hinds (1999) states that particulates in the stratosphere cool the troposphere and the earth's surface. However, soot has also been linked to an increase in the earth's surface temperature and therefore contributing to global warming (Jacobson, 2001). Particulate matter can be controlled, generally by forcing the particulate laden gas to change direction. As the gas changes direction, the momentum of the particles cause them to continue to travel in their previous direction, allowing the particles to be separated from the gas stream. Cyclones,

electrostatic precipitators, filters and wet scrubbers can all be used to reduce particulate matter escaping into the atmosphere, but all come at a cost in mass, efficiency and monetary expense. Avoiding soot formation is an important issue in POX and ATR technologies.

1.4 Porous Media Combustion

1.4.1 Overview of Porous Media Combustion

A premixed flame can be divided into two zones: a preheat zone, where little energy is released, and a thin reaction zone, where the majority of heat is released. In free flame laminar combustion, heat transfer in the upstream direction preheats the fluid up to an "ignition temperature". The temperature does not start increasing significantly until just before the reaction zone, see Fig. (1.5). A free premixed flame's propagation is largely dependent on the amount of heat transferred in the upstream direction and hence altering this mechanism will alter the flame speed.

The chemical reactions are concentrated in the reaction zone and the remainder of the combustion chamber only participates minimally in the chemical reactions. The combustion zone can be further divided into a thin region of very fast chemistry followed by a larger region of slower chemistry. Inside the fast region the fuel is broken down into many intermediate species. This region is driven by bimolecular reactions that provide the driving force for the flame to be self-sustaining: propagation of heat and radical species. Inside the slower reaction zone, three-body radical recombination reactions occur. At atmospheric pressure the fast reaction zone is less than a millimetre, while the slower reaction zone can extend several millimeters (Turns, 2000).

The high temperature and species gradients that exist in the thin fast reaction

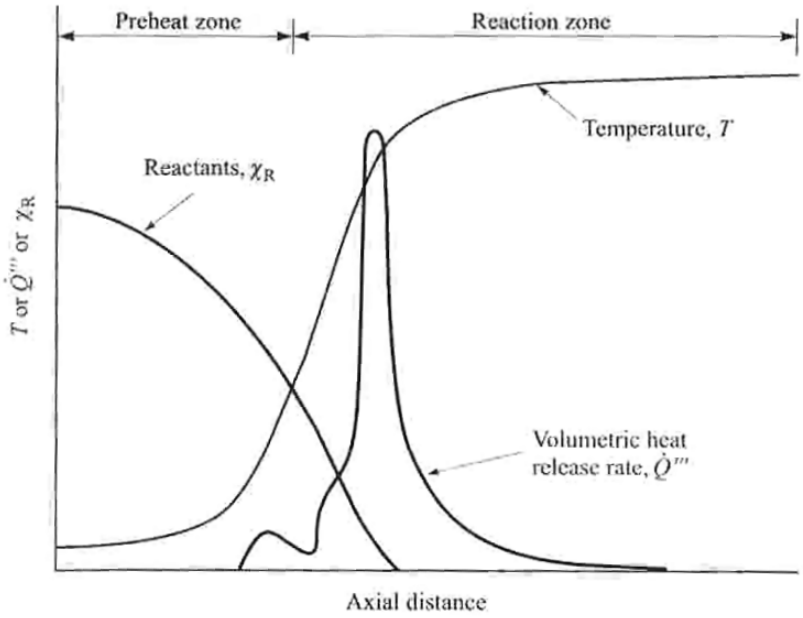

Figure 1.5: Laminar flame structure.

Turns (2000)

region transport heat to the incoming gases causing them to reach their ignition temperatures rapidly. In order to increase the heat transfer and make better use of the combustion chamber, turbulence can be used in the upstream gas mixture flow. However, highly turbulent flows can lead to stabilization problems, noise generation and high pressure losses. Another technique is to use a recuperator or a regenerator to transfer energy from the hot combustion products to the incoming air, as is illustrated in Fig. (1.6). Although this improves the efficiency of the system it increases its size and complexity. Additionally, depending on the feedstock, the channels inside the heat exchanger can clog up and become difficult to clean.

The theory of excess enthalpy burners, first promulgated by Egerton et al. (1963) and Weinberg (1971) in a theoretical study 40 years ago, introduced the

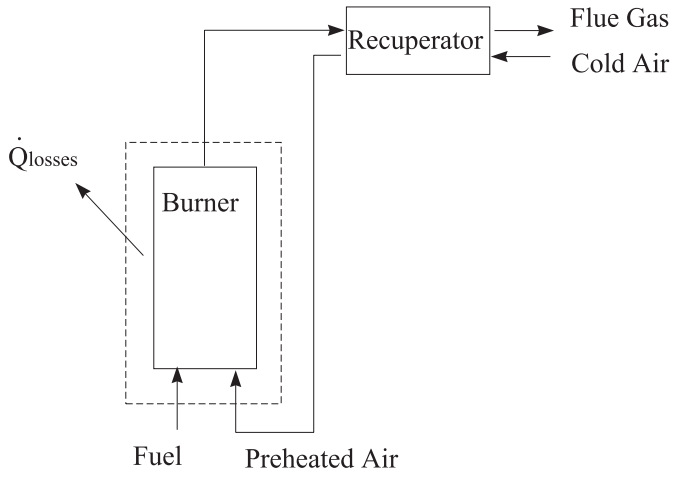

Figure 1.6: Schematic of burner with air preheated by recuperation.

concept of borrowing energy from a premixed flame in order to preheat the incoming reactants. The effect of this recuperation is a net transfer of enthalpy from the burned gas to the unburned gas. Weinberg recognized the advantages of achieving high combustion temperatures, such as high reaction rates, high thermodynamic efficiencies and the opportunity of producing endothermic products by sudden quenching. Other early research by Takeno and Sato (1979), proposed inserting a highly conductive porous solid into the flame to conduct heat from the solid to the incoming reactants.

An extension of this early research has led to the field of combustion in porous media. Combustion in porous media occurs inside the voids of the porous matrix. Energy is transferred to the solid by convection from the hot gases. Conduction and radiation through the solid porous medium, which has much higher thermal conductivity than the gas mixture and additionally radiates significantly, distributes some of this energy to the region upstream of the flame. This in turn transfers energy via convection to the incoming reactants. The porous matrix acts in essence as an integral preheater. This preheating allows for higher combustion

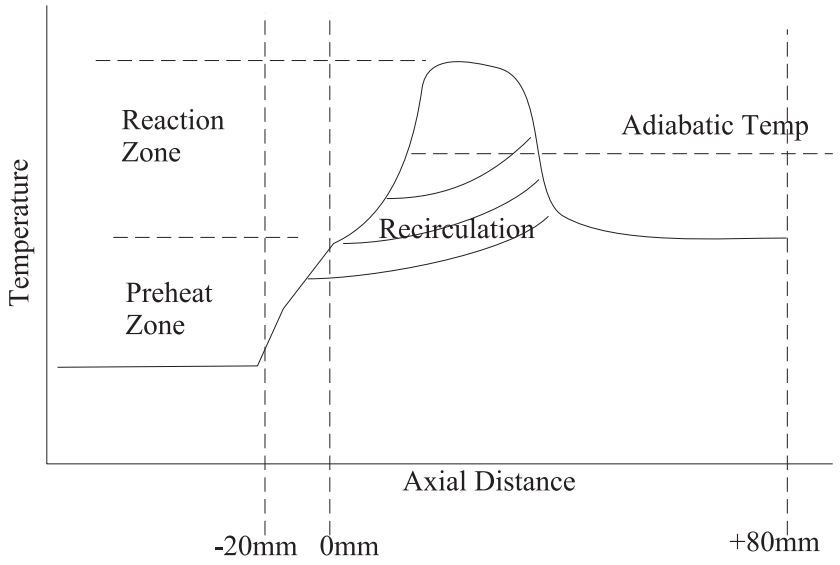

Figure 1.7: Enthalpy versus axial distance for an excess enthalpy flame. Adapted from Hardesty and Weinberg (1974).

temperatures and increased stability compared to a free premixed laminar flame. Locally, the flame zone may reach temperatures higher than the adiabatic flame temperature of the unburnt mixture, which gives the name "superadiabatic" to this combustion technology (Bingue et al., 2002; Diamantis et al., 2002; Drayton et al., 1998; Egerton et al., 1963; Hsu et al., 1993; Pedersen-Mjaanes et al., 2005; Zhdanok, 2003). However, the temperature at the exit of the burner cannot be higher, as this limit is imposed by the first law of thermodynamics. Fig. (1.7), adapted from Hardesty and Weinberg (1974), illustrates the concept of excess enthalpy burners. The dimensions are specific to the burners used in this thesis, -20 mm to 0 mm is the first layer of porous media and 0 to +80 mm is the second layer of porous media.

The properties of the porous matrix depend on the properties of the material being used as porous media. Ceramic foams, ceramic beads, ceramic rings, metal foils etc. can all be used as porous media. In the combustion region materials and

porous structures with maximized heat transport properties are advantageous to extend the reaction zone. Foam structures can have porosities (ψ) as high as 0.9,

$$\psi = \frac{free\,volume}{total\,volume}, \tag{1.26}$$

while spheres have a maximum random packing density of 0.64 or porosity of 0.36 (Weisstein, 1999). Typically, a packed bed of spheres has a porosity in the range of 0.36 to 0.43 (Nield and Bejan, 1992). Random packing density can be related to the porosity by the following equation,

$$packing\,density = 1 - \psi. \tag{1.27}$$

Foams have a lower optical thickness, up to 10 cavity space diameters, compared to approximately 2-3 diameters for spheres (Trimis et al., 1997). In Echigo (1982)'s experiments, screens having various optical thicknesses were placed in a circular duct through which heated air (800 °C) flowed. In his experiments it was shown that the upstream temperature increased with increasing optical thickness of the screen. Downstream temperatures were lower for increasing optical thickness, implying increased radiant losses from the gas to the porous media, in this case the screens. However, the conductivity of foams should be higher due to solid material bridges between the foams whereas for perfectly round spheres only a point contact exists between adjacent beads. Additionally, due to the higher porosity of foams, the pressure drop across the burner should be lower than with beads.

The porous medium can be a spouted, fluidized or stationary bed. This thesis investigates rich combustion in a fixed bed. Fig. (1.8) is a tree diagram of the various partial oxidation technologies, with the path leading to stationary combustion in a fixed bed outlined.

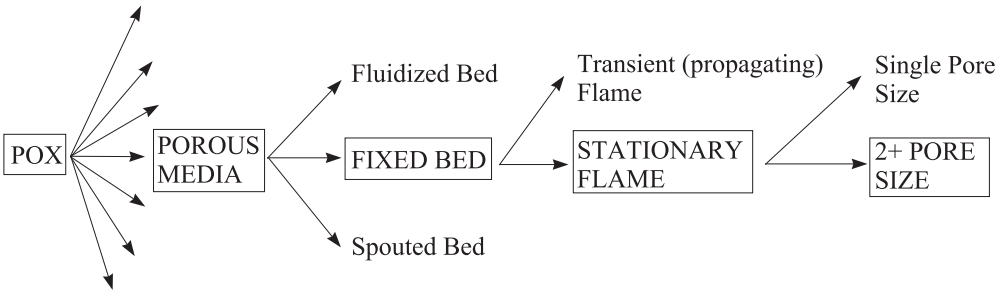

Figure 1.8: Porous media technologies.

1.4.2 Combustion in a Fluidized Bed

In a fluidized bed system, the incoming velocity of the gases is high enough to lift the particles. A spouted-bed combustor involves motion of solid inert (or catalytic) particles in a recirculatory manner, this technique has been used to stabilise rich flames of methane in order to produce syngas (Weinberg et al., 1988). In this study Weinberg was able to extend the upper flammability limit of methane by 40 % to an equivalence ratio of 2.34.

1.4.3 Transient Combustion in a Fixed Bed

Transient or filtration combustion inside a stationary, inert porous medium has also been used to produce syngas from methane at equivalence ratios exceeding the rich flammability limit (Bingue et al., 2002, 2004; Drayton et al., 1998; Zhdanok, 2003). In this technique, a confined wave is allowed to propagate along the solid, controlled by a periodical reversing of the reactants flow. In later tests the direction of wave propagation was controlled by varying the mass flow rates of reactants entering the system.

Hanamura et al. (1993) numerically investigated lean combustion in a similar reciprocating flow system. In these studies superadiabatic temperatures were also observed as was the ability to combust fuels with considerable lower calorific

values than are possible in a conventional combustion process.

In a further study, Bingue et al. (2004) looked at the effect of oxygen enrichment and depletion and inferred that peak hydrogen production was shifted toward higher equivalence ratios for successively higher concentrations of oxygen in the oxidizer stream. In addition to CH_4, Zhdanok (2003) looked at partial oxidation of kerosene as well as methane with several different types of porous media used as the packed bed materials. Bingue et al. (2002) and Slimane et al. (2002) studied hydrogen sulfide conversion to hydrogen. Slimane et al. (2004) studied the superadiabatic partial oxidation of H_2S numerically with the goal of optimizing the hydrogen yield.

The stored energy in the porous matrix is used to preheat the incoming reactants. The temperature of the combustion zone then becomes a function of not only the equivalence ratio and mass flow rate, but also the filtration velocity, reactor pressure, porous bead material and size. The reactors used in these experiments ranged in size from 430 mm in length by 38 mm I.D. to 622 mm in length and 257 mm in diameter. A disadvantage of this technique compared to a stationary flame system may be its relatively large size and high number of thermal cycles to which the porous media is subject.

1.4.4 Stationary Combustion in a Fixed Bed

In the stationary technique, a single piece of foam can be used to stabilize a flame, but this is limited by flashback when firing at low rates. Adding a second piece of foam with a smaller pore size upstream of the first piece acts as a stabilizing holder for the flame and prevents flashback (Hsu et al., 1993). The fine pores act as a flame arrestor by quenching the flame due to an increased diffusion of species and heat loss to the walls. Flame propagation is only possible when the rate of heat release from the reaction is higher than the rate of heat loss

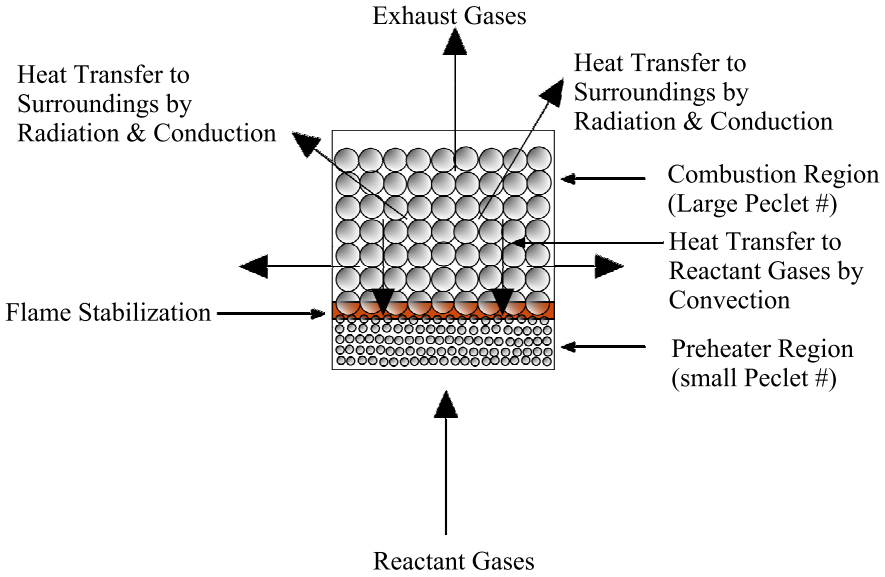

Figure 1.9: Operating principle of porous media combustion.

to the surroundings. Babkin et al. (1991) found that the minimum pore size to prevent quenching inside a porous medium is only possible when the Péclet number exceeds a certain limit, defined by

$$Pe = \frac{S_l d_m}{\alpha} \ . \tag{1.28}$$

By selecting a porous medium with a Péclet number less than the critical number for the upstream region and a Péclet greater than the critical number for the combustion region, the flame will be stabilized at the interface. Fig. (1.9) illustrates this concept.

A number of studies have examined lean and ultra-lean combustion of methane inside an inert porous media burner with two separate layers of ceramic foam (Barra et al., 2003; Barra and Ellzey, 2004; Delalic et al., 2000; Diamantis et al., 2002; Mathis Jr. and Ellzey, 2003; Mital et al., 1997; Smucker and Ellzey, 2004; Trimis et al., 1997; Trimis and Wawrzinek, 2003; Trimis and Durst, 1996; Zepter and Hustad, 2001). In these studies they observed elongated reaction zones and

flame stabilization at the interface between the fine and coarse pored ceramics. Howell et al. (1996) provides an excellent review of lean combustion in single and two layer PM burners up to 1996.

Several numerical models have been developed for single layer surface burners and two layer porous media burners operating in the lean regime with methane. Bouma and Goey (1999) developed a one-dimensional model for surface burners taking into account the heat transfer between the gas and the burner and the radiative properties of the ceramic material. The code was validated with experiments and they concluded that the influence of heterogeneous reactions is small so the ceramic foam burner can be regarded as chemically inert. A follow-up 1-D model by Lammers and de Goey (2003) concentrated on flame propagation and flashback inside a foam burner. The study showed that if the gas solid heat transfer, which heats up the burner, is greater than the radiative heat transfer, which cools the foam, then the material will gradually heat up and the flame will propagate through it.

Diamantis et al. (2002) have developed a one-dimensional, steady, numerical model, including the effects of solid to gas conduction, convection between solid and the gas, radiation and species diffusion with full chemistry using GRI 2.11 for planar premixed methane flames inside a two-layer porous media burner. They recognized that two distinct operating modes are possible: one with the flame stabilized at the surface and the other submerged in the upstream section of the porous media. An analysis of the energy balance within the burner revealed that enhanced flame speeds were primarily due to the preheating of the reactants. Their results predict that lean flames, ϕ=0.5, can also achieve temperatures exceeding the adiabatic flame temperature. However, at equivalence ratios close to stoichiometry flames do not experience superadiabatic combustion.

Barra et al. (2003) and Barra and Ellzey (2004) have also developed a 1-D

model for a two layer burner to attempt to quantify the amount of heat recirculation. They determined that the preheat zone for a flame in a porous media burner is approximately three times the size of the preheat zone for a laminar flame. Additionally, the closer to stoichiometric conditions the more dominant the radiation mode of heat recirculation becomes, due to higher temperatures.

Due to the enhanced heat transport to the reactants, the flame speeds can be considerably higher than those for a laminar free flame. Hsu et al. (1993), Zepter and Hustad (2001) and Mathis Jr. and Ellzey (2003) observed increased flame velocities for lean burning mixtures. Model results support experimental work by the above investigators that higher flame speeds and hence thermal loads are possible inside porous media.

As a result of the higher velocities, elongated reaction zones are then viable because enough energy can be transported against the incoming reactants to increase the mixture's velocity. Higher flame speeds offer the possibility of more compact burners but also extension of the combustion zone which increases flame stability and hence flammability limits.

Jugjai et al. (2002) and Jugjai and Polmart (2003) developed a two-layer porous media burner for first vaporizing and then combusting kerosene. Stable combustion with low emission of pollutants was achieved for equivalence ratios between 0.37 to 0.55.

Liu and Hsieh (2004) investigated combustion of liquefied petroleum gas in a three-layer burner with cooling tubes imbedded in the downstream layer. The transient response of the burner was investigated after decreasing the equivalence ratio from 0.394 to 0.286 by increasing the air flow rate. Steady state operating conditions were not attained again even after 1 200 s based on decreasing burner temperatures and increasing CO concentrations.

On the rich side, comparatively little research has been performed on station-

ary combustion in a fixed bed. Itaya et al. (2002) were successful in increasing the upper flammability limit of methane to a ϕ of 2.5, using a single piece of alumina foam inside a burner. In their experiments, a gas mixture was passed through a piece of ceramic and the flame stabilized on the surface. It was determined that adding a wire net after the foam at the burner's exit reduced radiative losses to the environment allowing stable operation at higher equivalence ratios.

The literature studied in the above paragraphs provides valuable information regarding the heat transfer mechanisms and flame propagation inside inert porous media. In summary, the principle advantages of combustion in non-catalytic porous media are:

- Higher flame temperatures resulting in higher flame velocities, leading to an increase in stability and extension of flammability limits.
- Several studies of transient combustion were able to increase the upper flammability limits and produce significant concentrations of syngas. This was also achieved by stationary combustion by Itaya et al. (2002) in a burner with a single piece of foam.
- Very high combustion efficiencies, leading to a more compact burner.
- Homogeneous heating of the matrix reducing hot and cold spots which are notorious for enhancing NO_X and CO_X emissions respectively.

1.5 Scope of Thesis

1.5.1 Objectives

In certain applications, e.g. in the automobile industry or in domestic systems, size, simplicity and longevity are of primary concern. Stationary combustion in

porous media may offer a solution to these concerns. Rich flames in two-layer burners have not been examined before, to the author's knowledge, and it is interesting to see if the advantages of these devices can be used for partial oxidation applications. In the present work, stationary rich flames are stabilized in a compact two-layer burner comprising different porous materials. Methanol, ethanol, kerosene, iso-octane, automotive grade petrol and bio-diesel, which are all potential fuels to be converted to H_2 in the transport sector, are tested. Methane, which is the major constituent of natural gas, is also tested as it is likely to have applications in stationary systems.

The specific objectives of this thesis are to:

1. Study the stability of flames inside several different types of porous media to examine the possibility of extending the upper flammability limits.

2. Examine the effectiveness of using this method to produce syngas from a variety of fuels.

3. Study the response of the burner to transients.

4. Test the robustness and operational lifetime of the porous media and burner.

1.5.2 Structure of Thesis

In order to meet these objectives, a range of experiments were performed. K and R-type thermocouples were used to record the temperature of the burner and its products at various locations over a range of operating conditions. Due to the limitations imposed by the porous matrix, only one optical technique was employed; a thermal imaging camera was used to determine the surface temperature of the beads at the exit of the burner and to determine the approximate location of the reaction within the burner. A commercial gas chromatograph (GC) was used to

measure the concentration of the product species produced by the burner during steady state operation. A Fast Thermal Conductivity Detector (TCD) was designed and constructed to measure on a continuous basis the H_2 produced from the burner during transients and start-up. Finally, a scanning mobility particle sizer (SMPS) was used to measure the amount of particulates produced by the burner.

The next chapter describes the apparatus and experimental techniques. Focus is placed on the gas chromatograph (GC), its configuration and calibration for the combustion products of interest. Furthermore, an uncertainty analysis is performed on the measurements taken during the experiments. Chapter 3 describes the Fast Thermal Conductivity Detector's design and calibration. Chapter 4 presents the flames behaviour and upper stability limits for the various fuels tested. The durability and robustness of the burner and ceramics are also examined. Furthermore, the particulates generated by the burner when combusting iso-octane and methane are measured by the SMPS. Chapter 5 describes the species concentrations obtained from the GC for steady state operation. These results are compared to NASA's Chemical Equilibrium code (CEA) (Gordon and McBride, 1994). Chapter 6 discusses the transient response of the burner as measured by the Fast Thermal Conductivity Detector. This thesis closes with a summary of the more important conclusions and with a discussion about the possible directions of future research.

Chapter 2

Experimental Methods

2.1 Structure of this Chapter

This chapter describes the apparatus used in the experiments, including the material properties of the burners and porous media (PM) tested. The procedure followed to obtain the results and the uncertainty analysis associated with the measurements is also discussed. Furthermore, the various instruments used to collect data from the experiments are presented. The exception is the Fast Thermal Conductivity Detector, which is discussed in a chapter unto itself, Chap. 3, as it was designed and fabricated in the Hopkinson Laboratory.

2.2 Apparatus Configuration

The apparatus used in these experiments with liquid fuels (methanol, ethanol, octane, kerosene and biodiesel) is illustrated in Fig. (2.1). The coordinate system for the burner (0,0) is located at the interface between the two pieces of porous media in the y-direction and at the centre of the burner in the x-direction. Liquid fuel was pumped by a gear pump to either a commercial fuel vapourizer or

a specially designed vapourizer for the heavier fuels, both are presented in Section 2.2.1. Dry air was supplied by the laboratory's compressor to the injector housing. The air flow rate was controlled and measured by a mass flow controller prior to entering the vapourizer for all tests except the methanol tests, where a rotameter was used. The vaporized fuel air mixture then entered the PM burner where it was combusted. The products exiting the burner were sampled by a water cooled probe and injected into a gas chromatograph (GC), Fast Thermal Conductivity Detector (TCD) or scanning mobility particle sizer (SMPS) via a vacuum pump.

The apparatus used for gaseous fuels (methane) is illustrated in Fig. (2.2). The only difference is that there is no vapourizer or fuel pump required and the fuel flow rate is controlled and measured by a mass flow controller. The conical and various straight tube burners used in these experiments can be interchanged with the liquid and gaseous apparatuses.

In order to minimize heat loss to the environment all of the burners were adequately insulated. A thin layer of alumina paper was inserted between the porous media and the burner wall to reduce heat loss and also to minimize gases leaking around the porous media. A high temperature ceramic insulation, Superwool607, was applied to the outside of the burner. Finally, a layer of Rockwool piping insulation was applied around the Superwool607. This data is tabulated in Table 2.1

The entire system was leak tested and a sample of uncombusted pure methane was introduced to the gas chromatograph to ensure that it was leak tight. Had it not been leak tight an O_2 and N_2 peak would be present on the GC printout as the sampling line from the burner to just before the GC is at negative pressure. Since the majority of tests were done at fuel rich conditions, where essentially no oxygen should be present in the products, it was easy to see on the gas chromatograph

Table 2.1: Properties of insulation material used in experiments. Properties obtained from the appropriate manufacturer.

Material	Thermal Conductivity ($W/m \cdot K$)	Thickness (mm)
Alumina paper	0.20 @ 1570 K	1.0
Superwool607	0.19 @ 1255 K	40-60
Rockwool	0.106 @ 670 K	50

plots if a leak had developed and to rectify it.

General lab safety precautions were followed throughout the project to minimise the risks associated with combusting liquid and gaseous fuels. Additionally, a local powered exhaust was used to remove any combustion products from the vicinity of the apparatus. A carbon monoxide sensor was used to periodically check for CO in the laboratory air. Polycarbonate plates were used as shielding around the burner. All gases were stored inside standard Air Product cylinders with the appropriate two stage regulators and additional shut-off valves. Only the minimum amount of fuel required to run a particular test was located near the apparatus, the rest was stored in a flammable containment cabinet in a separate room. Personal protection devices including goggles, face shield and heat resistant gloves were used when necessary. Safety precautions employed are described in greater detail in the Risk Assessment (A70) on file with the Department of Engineering, Health, Safety and Environmental Office.

2.2.1 Vapourizer

A commercial fuel vapourizer consisting of an injector housing and an electrically heated tube was used for methanol, ethanol and octane fuels. The amount of heat

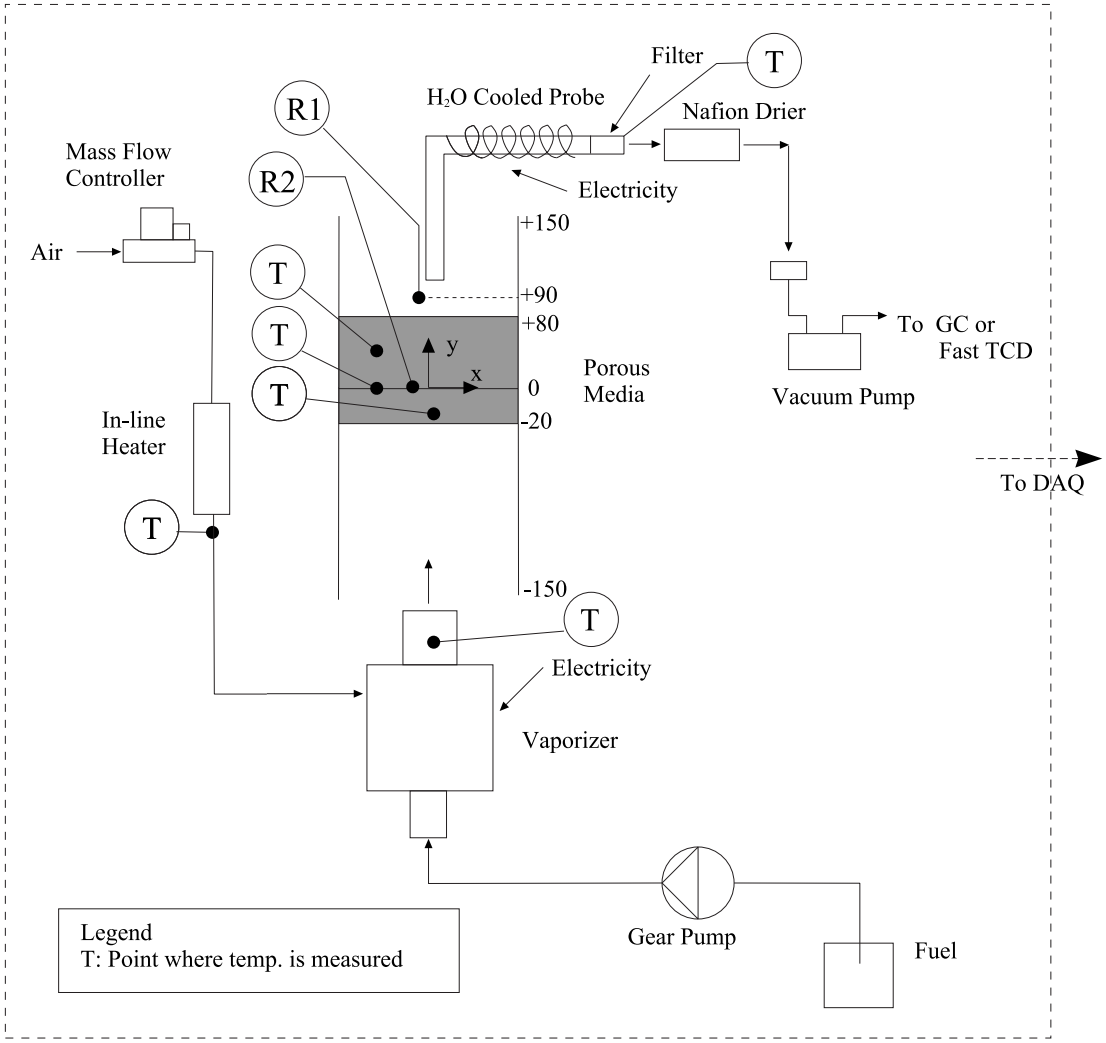

Figure 2.1: Schematic representation of experimental rig (straight-tube burner shown) for liquid fuels.

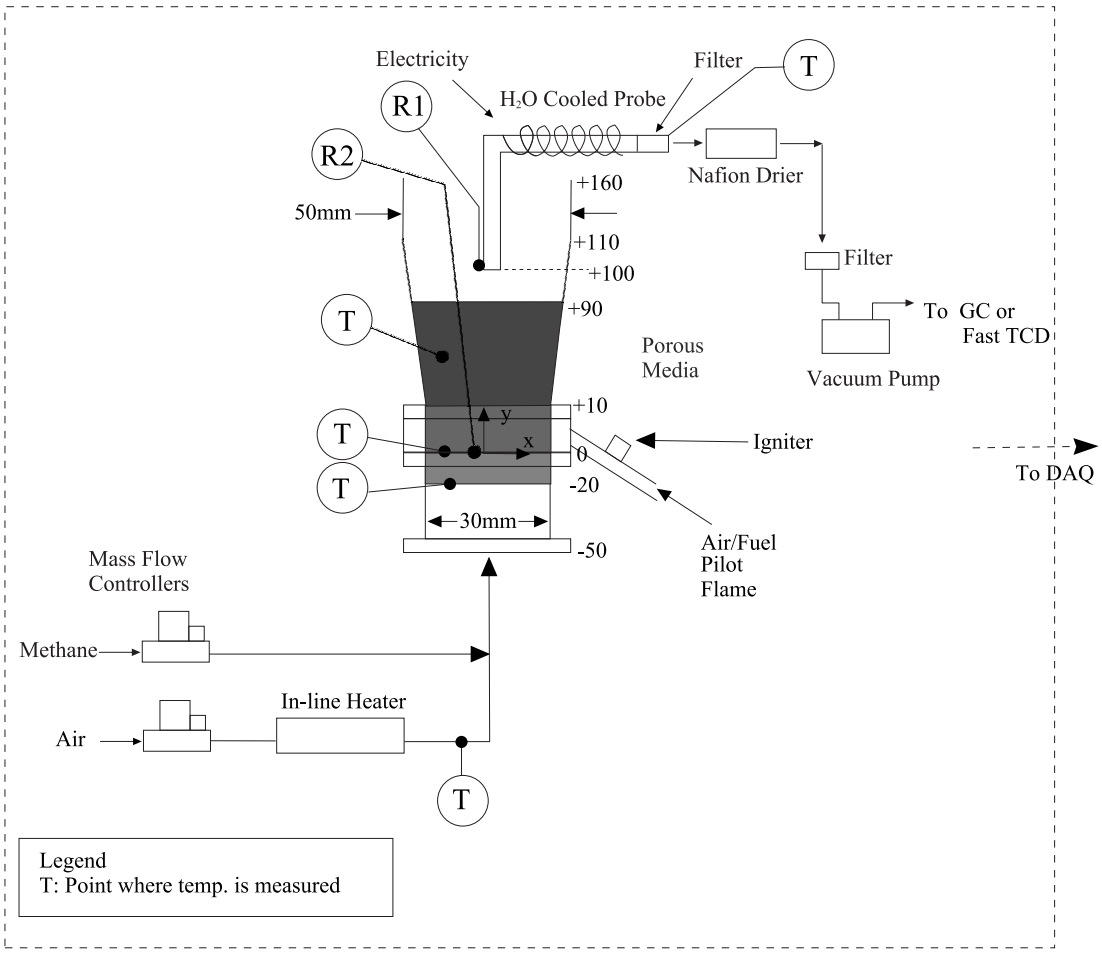

Figure 2.2: Schematic representation of experimental rig (conical burner shown) for gaseous fuels.

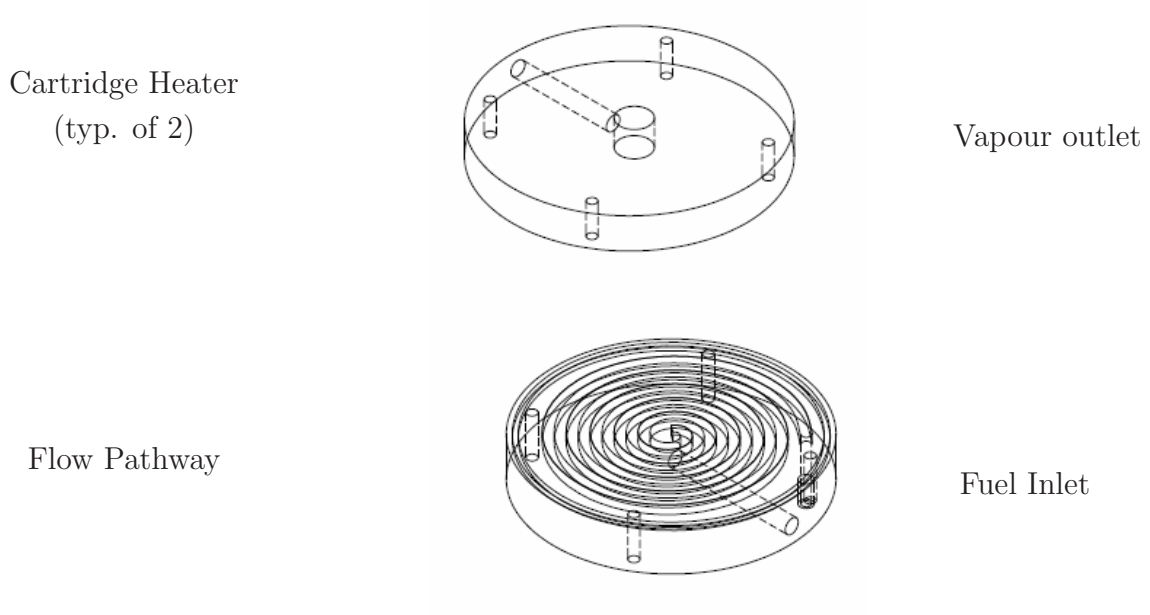

Figure 2.3: Schematic of serpentine vapourizer.

delivered by the vapourizer was controlled by a variable transformer. Within the injector housing, downstream of the injector, air holes are arranged to produce a strong swirl causing the fuel to centrifuge on the bore of the tube, where it will be evaporated.

A specifically designed vapourizer with a 1 m spiral flow pathway for longer residence time and higher operating temperatures was designed and constructed for use with the heavier fuels, kerosene and biodiesel. The vapourizer is illustrated in Fig. (2.3). Two 250 W cartridge heaters were used to heat the fuel up to a maximum temperature of 400 °C before exiting the vapourizer. A variable transformer was used to control the power dissapated in the cartridge heaters.

2.2.2 Straight-Tube Burners

Four different straight-tube burners were used during the course of the experiments. The important properties of these burners are summarized in Table 2.2. The first was a split stainless steel burner with an internal diameter of 29 mm, illustrated in Fig. (2.4a). This burner had a quartz window for viewing the location of the flame. The porous media was held inside the burner by set screws drilled through the side of the burner.

The second, more successful, burner was a quartz tube and is illustrated in Fig. (2.4b). Initially, the I.D. was 30.4 mm, but in later tests a larger I.D. of 50.0 mm was used. The third and fourth burners tested were similar in design to the quartz burner. An Al_2O_3 burner with an I.D. of 50 mm and a Kanthal® burner with an I.D. of 52.5 mm were tested. These burners are illustrated in Fig. (2.4c) and Fig. (2.4d), respectively. Kanthal® is a FeCrAlMo alloy, specifically designed for high temperatures and harsh environments. In these burners the porous media was supported by a stainless steel ring attached to the top of the vaporizing nozzle.

In all burners, alumina paper was wrapped around the porous media to prevent gases leaking around the edges and to absorb some of the thermal expansion. A fine mesh was placed at the exit of the vaporizing nozzle to act as a flame arrestor preventing flash back.

Table 2.2: Material properties of burners used in Experiments. 'Temp' is the upper continuous temperature that the materials can endure. Material properties are from Matweb (2006) and Sandvik (2006).

Material	Geometry	I.D. (mm)	Conductivity ($W/m \cdot K$)	Temp (K)	Fuels (Tested)	Fig.	Foams/Beads
SS-316	Split-tube	29	16.2-21.5	1198	CH_3OH	2.4a	F,B
Quartz	tube	30.4	1.4	1773	CH_4, CH_3OH, C_8H_{18}	2.4b	F,B
Quartz	tube	50.0	1.4	1773	CH_4, CH_3OH	-	B
Al_2O_3	tube	50.0	6.3-30	2023	CH_4	2.4c	F,B
Kanthal®	tube	52.5	12-32	1673	CH_4, CH_3OH, C_2H_5OH, C_8H_{18}, Jet-A, Biodiesel	2.4d	F,B
SS-316	conical	30-50	16.2-21.5	1198	CH_4, Biodiesel	2.5	B

2.2.3 Conical Burner

A burner with a varying cross-sectional area, from 30-50 mm, was designed to allow the flame to stabilize at different points in the axial direction. Some of its important properties are tabulated in Table 2.2 and it is illustrated in Fig. (2.5). Instead of igniting the fuel/air mixture at the exit of the burner, a pilot flame is introduced just downstream of the interface. A premixed CH_4/air mixture enters a 7 mm I.D. tube, is ignited by a spark traversing the gap between a pair of electrodes and stabilizes on a bluff body just prior to the entrance to the main burner. Once the pilot flame has heated the porous media to a sufficient temperature to maintain a reaction in the main burner, the air and CH_4 flows are shut-off and the flame stabilizes at the interface.

2.2.4 Porous Media

Tests were conducted using four different types of porous media inside the burner: cordierite foam, alumina foam, alumina beads and silicon carbide foam. Cordierite ceramics, $MgO - Al_2O_3 - SiO_2$, are composed of approximately 13.7 % MgO, 34.9 % Al_2O_3 and 51.4 % SiO_2. Cordierite is known for its extremely low heat expansion and high resistance to thermal shock. Fifteen percent of the earth's crust is composed of alumina, Al_2O_3, making it a very abundant and potentially inexpensive material. Alumina beads can be bought in one kilogram lots for around £20 kg^{-1}. Alumina has a higher thermal conductivity and melting point than cordierite but also a higher thermal expansivity and lower resistance to thermal shock which needs to be considered when selecting burner material. Silicon carbide, (SiC), is a hard material with good oxidation resistance and can be used in very high temperature environments. It has a low coefficient of expansion, a high thermal conductivity and melting point, but is also considerably more expensive than the other two materials. The properties of the porous media used

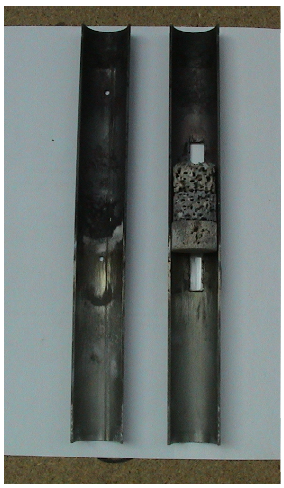

(a) Stainless steel burner.

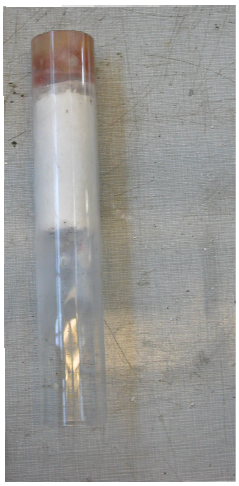

(b) Quartz burner.

(c) Al_2O_4 burner.

(d) Kanthal® burner.

Figure 2.4: Burners used in experiments.

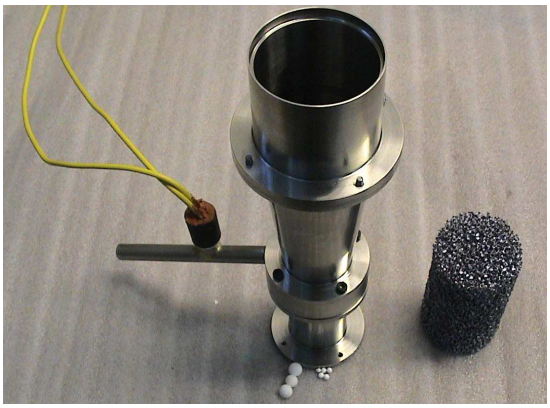

Figure 2.5: Photo of conical burner with integral igniter. SiC foam is to the right of the burner and differently sized Al_2O_3 beads are in the foreground.

in these experiments are summarized in Table 2.3.

2.2.5 Sampling Circuit

The gases exiting the burner are sampled through a water cooled probe. The probe was designed to: (1) aspirate the sample from the burner without disturbing the flow excessively by minimizing the probe's cross-sectional area and matching the burner exit velocity to the extraction rate, iso-kinetic sampling. (2) Deliver the sample at the probe exit without any appreciable change in chemical composition. Hence, the probe was constructed from stainless steel. (3) Freeze the reaction at the inlet of the probe by rapidly cooling it. Water from a reservoir was continually pumped into the tip of the probe via a peristaltic pump and the sample allowed to expand once entering the probe. (4) Prevent water vapour from condensing on the inside of the probe and maintain a temperature gradient across the drier. The downstream end of the probe was heated to maintain a temperature just above 100 °C as measured by a thermocouple at the exit of the probe. The probe is illustrated in Fig. (2.6). Section A-A shows a cross-sectional

Table 2.3: Properties of porous media used in the burners (Doceram, 2003; Goodfellow, 2003; Sembach, 2003). Where 'f' stands for foam and 'b' for beads.

Properties	Cordierite (f)	Al_2O_3(f)	SiC (f)	Al_2O_3(b)
Bulk density (g/cm^3)	2.1	3.9	2.9	3.9
Thermal expansivity ($10^{-6}K^{-1}$)	2-4	8.0	3-4	8.0
Thermal conductivity (W/mK)	1.2-2.5	6.3-30	12	6.3-30
Thermal shock resistance (ΔT)	300	250-270	-	-
Melting temperature (K)	1735	2370	2920-3220	2370
Upper continuous temp (K)	1570	1870-1970	-	1870-1970
Thickness (mm)	18.3	23.6	10-100	20-100
Porosity (%)	84-86	85-90	90-91	35-75
(pores per cm)	8, 16, 24	8, 24	4.8, 24	3.7-16.7[a]

[a]The average channel dimensions in a closely packed bed of spherical particles can be estimated as 0.3Φ, where Φ is the diameter of the sphere (Mare et al., 2000).

view of the inside of the probe revealing the two internal tubes used to extract the sample and deliver H_2O to the head of the probe.

Immediately after the probe a Nafion dryer was situated to remove any water from the sample prior to entering the vacuum pump and analysis instrumentation. Nafion is a semi-permeable membrane that absorbs water and some polar organic substances, including methanol and ethanol, but allows other substances to pass through unaffected making it an excellent choice for a water removal device.

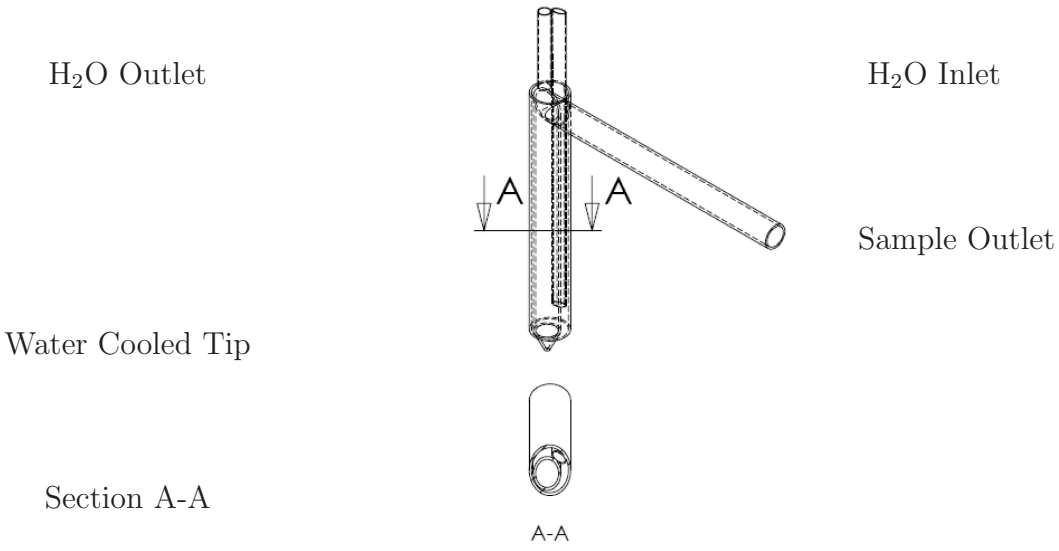

Figure 2.6: Schematic of the water cooled probe.

2.3 Flow Measurements

2.3.1 Rotameters

Two rotameters each with an accuracy of ± 2 % full scale deflection were used to measure the air flow entering the vapourizer for the tests conducted with CH_3OH. A rotameter works on the physical principle of drag, balancing the force of gravity against the force induced by the flowing medium on the bob. The meter is calibrated for a particular fluid, in this case air, at standard pressure and temperature. As a result any deviation from these conditions must be taken into account. The flow rate can be corrected using

$$Q_{corr} = Q \left[\frac{P}{P_{STD}} \frac{T_{STD}}{T} \right]^{0.5} \tag{2.1}$$

The first meter was used for flows in the range of 2.5 to 20 LPM. The second for flows less than 2.5 LPM. Due to the pressure drop through the vapourizer

and porous media a back pressure resulted at flows greater than 8 LPM. As a result these measurements must be corrected with Eq. (2.1), but have an error associated with the pressure gauge as well as the error from the flow meter itself. The pressure gauge has an accuracy class of 1.6 or is accurate to within ± 1.6 % of full scale deflection.

2.3.2 Mass Flow Controllers

All other fuels used Bronkhorst Hi-Tech mass flow controllers with a range of 1.4-70 LPM to measure the air flow rate. A similar Hi-Tech mass flow controller was used for CH_4 with a range of 0.2-10 LPM. The mass flow controllers have an accuracy of ± 0.5 % of the reading plus ± 0.1 % of full scale.

2.3.3 Liquid Fuels

The pump used to deliver the fuel to the vapourizer was a 180(GA) micro gear pump delivering 0.042 mL per revolution providing essentially a pulseless flow. The pump was calibrated a minimum of three times using a stopwatch and beaker for each fuel and apparatus configuration. After calibration, its accuracy is estimated to be within ± 2%.

2.4 Temperature Measurements

2.4.1 Infrared Camera

An infrared camera measures the emitted infrared radiation from an object. All objects above zero Kelvin, emit electromagnatic radiation that is a function of both the object's temperature and its emissivity. In addition, radiation also originates from the surroundings and is reflected in the object. Finally, the object's

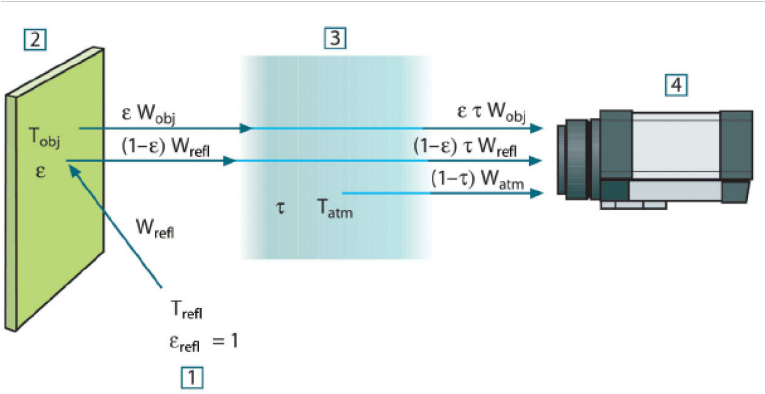

Figure 2.7: Schematic representation of the infrared camera. 1: Surroundings, 2: Object, 3: Atmosphere, 4: Camera. (ThermaCAM, 2003)

radiation and reflected radiation are influenced by the absorption of the atmosphere. Compensation for these additional radiation sources is performed on-line by the camera's software after the operator adds the reflected temperature, distance between the camera and the object and the relative humidity. The greater the difference in temperature between the target object and the environment the greater the accuracy of the measurement. Fig. (2.7) illustrates the general thermographic measurement situation, extracted from ThermaCAM (2003). The camera used in these experiments was borrowed from EPSRC and is a FLIR ThermaCAM SC3000 accurate to within $\pm$ 2% (Flir, 2000) with a 320 $\times$ 240 pixels resolution.

In using the infrared camera there are three main objectives. The first is to determine the surface temperature of the top most layer of beads exposed to the ambient environment, so that a convection/radiation balance can be performed on the thermocouple bead measuring the gas temperature above the burner. The second is to observe the uniformity of the surface temperature during both steady state operation and during transients. The final objective is to qualitatively

observe where, in the axial plane, the reaction stabilizes for different operating conditions.

The emissivity of a material will vary depending on its temperature and surface finish. Omega (1998) gives a range of 0.69-0.45 for alumina on Inconel between 427 °C and 1093 °C. The beads used in the burner for the tests conducted with the infrared camera are alumina beads with a coarse surface finish. One would expect the emissivity for the beads to be higher as the surface finish will not be as smooth (a highly polished surface has an emissivity less than 0.1) To obtain a more accurate emissivity, a calibration curve was plotted based on the emissivity of the beads at various known temperatures.

An alumina bead was attached to a 0.4 mm diameter nichrome wire and placed in a temperature controlled oven. The oven was heated to 10 °C above the desired temperature and the elements turned off allowing the oven to reach a uniform temperature. When the bead was removed and the oven door closed, to eliminate the high temperature source, four photos were taken of the bead immediately afterwards at one second intervals. At an oven temperature of 850 °C the following temperatures were recorded: 848, 848, 842, 840 °C. In four seconds the temperature dropped by 8 °C, similar temperature decreases were observed for all measurements. The oven door was open for less than three seconds. A conservative estimate for the temperature decline prior to the first photo is 6 °C as during most of this time the bead is partially exposed to radiation emitted from the oven. Therefore, when calculating the emissivity it was assumed that the bead's temperature was 6 °C lower than the oven temperature just prior to the first photo being taken.

The bead's emissivity was measured at temperatures ranging from 400 °C to 976 °C. The results are illustrated in Fig. (2.8). As expected the emissivity is higher for the beads tested than the value quoted by Omega. However, the

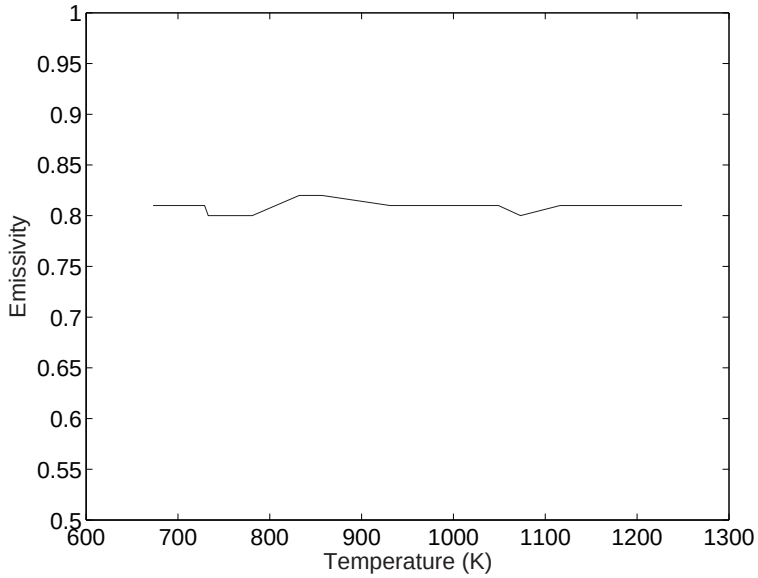

Figure 2.8: Calibration curve for Al_2O_3 beads as a function of temperature.

emissivity for this material does not appear to vary with temperature, instead it remains constant at 0.81 $\pm$ 0.01 over the temperature range tested. This agrees with Kant and Badarinath (1999) who state that the spectral emissivity for most non-metallic materials is almost independent of temperature. Metallic materials will oxidize at high temperatures making the object less reflective and therefore increasing its emissivity. However, the Al_2O_3 beads tested are inert and do not readily oxidize at the temperatures tested, leaving their surface layer and therefore emissivity relatively unaltered.

The amount of radiation emitted by a greybody, can be defined by the Stefan-Boltzmann formula

$$W = \epsilon \sigma T^4 \tag{2.2}$$

where ϵ is emissivity, σ is the Stefan-Boltzmann constant and T is the absolute temperature of the body.

The radiation emitted is much more sensitive to the temperature than the emissivity of the object. If we assume that our emissivity calibration curve is accurate to within ± 10% then the temperature measurement is accurate to within ± 2%.

2.4.2 Thermocouples

In these experiments the burner was instrumented with thermocouples (TC) as illustrated in Fig. (2.1 and 2.2). During all tests, an R-type TC was located 10 mm above the top layer of porous media. A sheathed R-type TC was inserted down through the beads to the interface between the two layers of porous media when beads were used as the porous media. All other TCs used are K-type thermocouples and are placed on the outside of the burner or embedded in the vapourizer.

The R-type thermocouple is accurate to within ± 1.5 °C from 0 to 600 °C and ± 0.0025·$|t|$ °C from 600 to 1600 °C. The K-type thermocouple is accurate to within ± 2.5 °C from -40 to 333 °C and ± 0.0075·$|t|$ °C from 333 to 1200 °C. At high temperatures the thermocouples will also have an error associated with radiation, this is especially true for the R-type thermocouples. This error is calculated in Section 4.4.1 after the burner's surface temperature has been measured with the infrared camera.

2.5 Species Concentration Measurements

2.5.1 Gas Chromatography

Gas chromatography is a method of continuous chemical separation of one or more individual compounds between a mobile phase (carrier gas) and a station-

ary phase. The gas mixture enters at the injector and its different components move along at different rates. The lower the vapour pressure of the component (higher boiling point), the longer it takes to elute through the stationary phase. For these experiments an AutoSystem XL Gas Chromatograph equipped with two columns (or stationary phases), a Flame Ionization Detector (FID) and a Thermal Conductivity Detector (TCD) was used to measure the composition of the products.

A porous polymer bead column (HeySep N) was used to separate out the permanent gases from the non-permanent gases. H_2, O_2, N_2 and CO elute very quickly in more or less one lump, closely followed by CH_4. After these gases have eluted onto the molecular sieve column, the valve is then switched to bypass the molecular sieve column prior to CO_2 coming off the porous polymer bead column. If the valve is not switched in time, CO_2 will poison the molecular sieve column. The permanent gases elute from the molecular sieve column quite quickly, before the first non-permanent gas comes off of the porous polymer bead column. The HeySep N column separates out the larger molecules including CO_2 and the various hydrocarbons C_2H_2, C_2H_4 and C_2H_6. The porous polymer bead column was a 1/8" inch in diameter and 5 metres long stainless steel column packed with HayeSep® N. The second column was a 1/8" inch in diameter and 1 metre long stainless steel column packed with molecular sieve 5A. The three gases used by the GC; hydrogen, zero air and the reference gas (argon) were all scientific grade gases (99.999 % pure). The gas chromatograph is illustrated in Fig. (2.9).

After the components exit the column they pass through the TCD. The TCD measures the difference between the thermal transfer properties of the gas and a reference gas. In this case argon was used as the reference gas. Its thermal conductivity is low compared to hydrogen's, 0.016 W/mK versus 0.17 W/mK

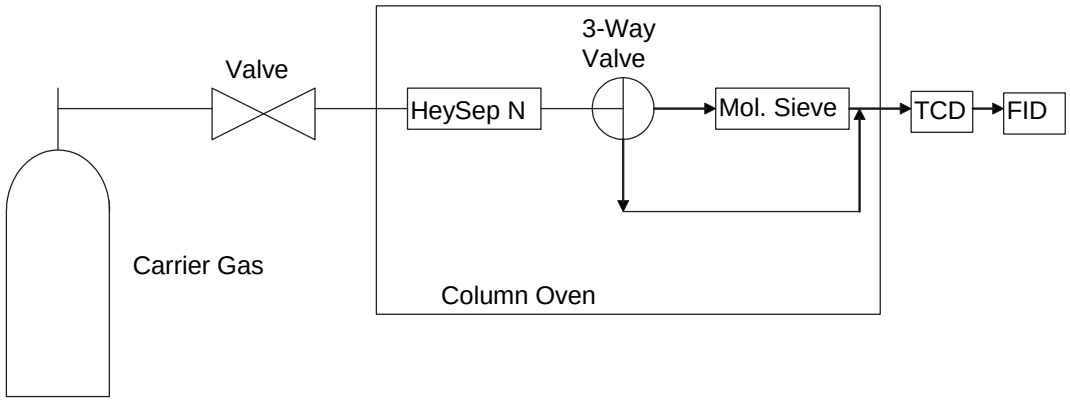

Figure 2.9: Schematic of a gas chromatograph.

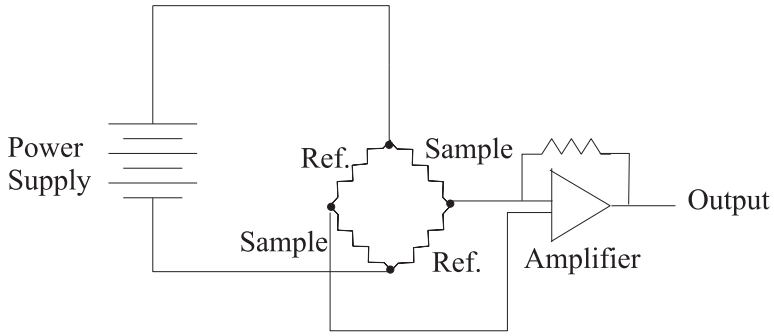

Figure 2.10: Simplified TCD diagram.

and also dissimilar to CO and CO_2 that were also measured with the TCD. The sample and reference filaments form two legs of a Wheatstone Bridge. A constant current is applied to the filament and as the sample passes through the detector, the resistance changes as the sample removes more or less heat than the reference gas. The response is universal since the detector responds to any compound that conducts heat. Minimum detection is 100-200 ppm. The test is also non-destructive, so that after the sample passes through the TCD it can then travel on to the FID. A typical TCD is illustrated in Fig. (2.10).

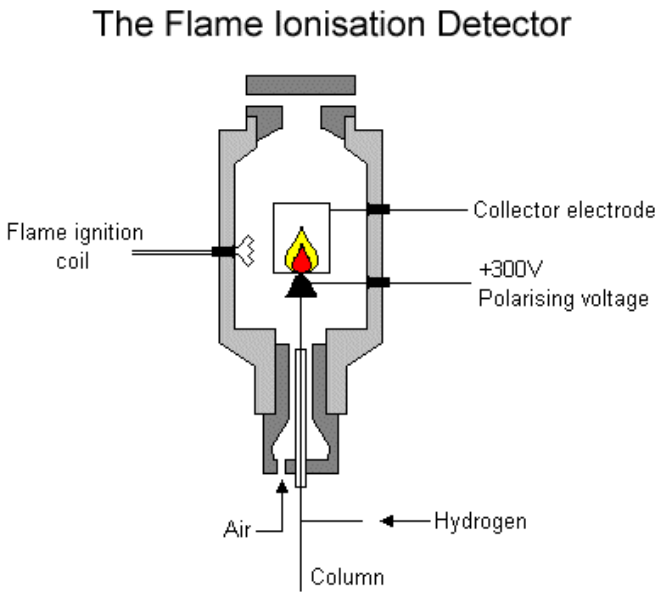

Figure 2.11: FID diagram. (Anonymous, 2002)

A high temperature hydrogen flame ionizes compounds as they elute from the TCD into the flame. These ions are collected in the flame by applying a positive potential to the FID jet and measuring the current at the collection electrode. The response is proportional to the concentration and is measured with an electrometer/amplifier. The FID is most sensitive to hydrocarbons and in these experiments was used to measure CH_4, C_2H_2, C_2H_4 and C_2H_6. The detector is destructive as the sample is combusted. A FID is illustrated in Fig. (2.11).

The GC was calibrated by passing two sets of calibration gases through the system. The first set contained: 1.98 % C_2H_6, 2.07 % CO_2, 19.92 % H_2, 10.09 % CO and 20.14 % CH_4. The second set contained: 2.00 % C_2H_2 and 1.97 % C_2H_4. Ideally the GC could have been calibrated using one set of gases, however concerns of a potential reaction occurring between either the ethane and the steel container or the acetylene and the aluminum container necessitated two different sets of gases. These concentrations were chosen as this is approximately what

was expected to be in the combustion products.

Fig. (B.1) and Fig. (B.2) in Appendix B are an example of a gas chromatograph printout of a calibration check on the GC. A mixture of 10 %, by volume, un-combusted methane with air was injected into the GC. The only components detected were 10.25 % methane and 0.001 % ethane. The amount of methane detected was well within the uncertainty of the flow meter and the small amount of ethane could have been a trace impurity in the methane cylinder (industrial grade 99.5 % purity).

The uncertainty associated with the gas chromatograph is harder to define than the uncertainty associated with the thermocouples and flow meters. The uncertainty is at least $\pm$ 2 % as this is the uncertainty associated with the calibration gases. The instrument's conditions are optimized by ensuring the following: (1) there are no leaks from the probe to the GC that the sample is extracted through, (2) the columns are giving good reproducible separations of the components, (3) there is no carryover of components or contamination, (4) all supplies of gas and power to run the system are stable and (5) the samples are being introduced in a standard reproducible way, i.e. all injected using the same technique, sample loop size, temperature and pressure.

After ensuring the above it is difficult to separate any uncertainty associated with the GC from uncertainty associated with the fuel and air delivery system. Repeating a test several times under the same conditions gave product compositions within the error bands associated with the flow meters.

2.5.2 Fast Thermal Conductivity Detector

Since the Fast Thermal Conductivity Detector is not a commercial product, but was designed and built in the laboratory a separate chapter is devoted to its design and calibration (Chap. 3).

2.5.3 Scanning Mobility Particle Sizer

Due to the large amount of unburnt hydrocarbons and soot that are formed during rich combustion, a scanning mobility particle sizer (SMPS) was used to measure the size and concentration of particles in the combustion products of octane and methane, as an example of a 'clean fuel'.

The SMPS consists of two stages: the classification and measurement stage. In the first stage a differential mobility analyser classifies charged particles according to their ability to transverse an electric field. Depending on their charge, positive or negative, particles are either attracted or repelled by a central column located inside the differential mobility analyser. Particles within a narrow band of electrical mobility diameter, exit through a slit at the end of the column and travel to the second stage. By varying the central column voltage, particles of different mobility are sent to the next stage, allowing a size distribution to be produced. In the second stage a condensation particle counter optically measures the concentration of the particles. Using a modified method for operating the instrument, the measurement time was on the order of a minute (Biskos, 2001).

2.6 Procedure

At the start of each experiment the vapourizer was heated to its operating point with just air passing through it. Once the vapourizer was above the vaporization temperature of the fuel (these temperatures are tabulated in Table 4.2) the fuel pump was activated and the pre-mixed air-fuel mixture flowed into the burner. The mixture was ignited with a butane torch at the burner's exit for all burners, except the conical burner where it was ignited at the interface. A mixture slightly richer than stoichiometric and a low mass flow rate was used so that the flame propagated into the porous medium. After the flame had stabilized at the

interface between the support layer and the combustion layer, the flow was held constant for several minutes to allow the burner to warm up.

After the warm up period, the flows were adjusted to their desired values for the experiment. After an additional period of several minutes the system reached thermal equilibrium, which can be deduced by constant thermocouple readings and a stationary flame front. At this point, a gas sample could be injected into the GC and the products' composition recorded by TotalChrom, the gas chromatograph's software or a sample could be re-routed to the SMPS. Alternatively, a transient could be introduced and the H_2 concentration measured by the Fast TCD. This method of operation is to be contrasted to filtration combustion (Bingue et al., 2002; Drayton et al., 1998; Zhdanok, 2003), where a propagating wave was induced. All data, temperatures, pressures and flow rates, were collected by a Data Acquisition System (DAQ).

2.7 Uncertainty Analysis

In all experimental work errors will creep into the data. Every measurement that is taken has some uncertainty associated with it. During this project every reasonable effort was made to keep errors to a minimum by regularly calibrating equipment, repeating various experiments, not indiscriminately discarding data, only varying one variable at a time and most importantly using great care and patience throughout the course of the project. Much of the error in a measurement can be eliminated by regular calibration. However, this will only improve its accuracy up to the precision of the instrument. The accuracy of an instrument indicates the deviation from a known input. The precision of an instrument indicates its ability to reproduce results with a given accuracy.

To assess the uncertainties contained in the data, an error analysis was per-

formed on both the air and fuel flow rates. The corrected air flow rate, Q_{corr}, is a function of the measured flow rate, Q, and the pressure, P. Using the method described in Kline and McClintock (1953) the uncertainty in the measurements can be calculated using

$$W_{Qcorr} = \left[\left(\frac{\partial Q_{corr}}{\partial Q} \omega_q \right)^2 + \left(\frac{\partial Q_{corr}}{\partial P} \omega_p \right)^2 \right]^{0.5} \tag{2.3}$$

where Q_{corr} is the corrected rotameter flow rate (including effects of pressure), ω_q is the error associated with the rotameter and ω_p is the error associated with the pressure gauge.

The uncertainty of the equivalence ratio, ϕ, is a function of the error associated with the rotameter, pressure gauge and fuel pump and can be calculated using

$$W_\phi = \left[\left(\frac{\partial \phi}{\partial Q_{Qcorr}} \omega_{Qcorr} \right)^2 + \left(\frac{\partial \phi}{\partial Q_{pump}} \omega_{Qpump} \right)^2 \right]^{0.5} \tag{2.4}$$

where ω_{Qcorr} is the error associated with the air flow measurement (corrected) and ω_{Qpump} is the error associated with fuel flow measurement.

The largest uncertainties are associated with the air rotameters (which were only used with CH_3OH), especially at low flow rates just prior to switching to the smaller rotameter. These low flow rates are associated with high equivalence ratios. A maximum uncertainty of $\pm$ 15 % at an air flow rate of 2.75 LPM was calculated. This corresponds to an overall uncertainty for ϕ of $\pm$ 16 %. At higher flow rates and lower equivalence ratios, the uncertainty decreases so that at a half scale deflection of 10 LPM the uncertainty associated with the rotameter has reduced to $\pm$ 7 % and the uncertainty associated with ϕ has reduced to $\pm$ 6.1 %.

The uncertainty associated with the mass flow controllers are much less. Using CH_4 as the fuel, at a ϕ of 1.5 and air flow rate of 20 LPM, the uncertainty for the air flow is $\pm$ 0.85 %. This corresponds to an overall uncertainty for ϕ of 1.5 ± 1.2 %. The accuracy of the measurement with the other fuels are somewhere

in between the CH_3OH and CH_4 results as no mass flow controller for these fuels was available.

The product species and the flames behaviour were reproducible within the uncertainty of the flow delivery system and measurement instruments as long as the following conditions were met:

- There were no leaks in any of the fuel, air or sampling lines to the GC.
- The burner's integrity had not been compromised.
- The porous media had not experienced significant degradation.
- The burner was insulated adequately.
- The flame had been stabilized at the interface between the two types of porous media prior to the flows being altered.

2.8 Chapter Summary

The apparatus and method followed for measuring the instantaneous temperatures, species concentrations and particle concentration are presented in this chapter. The burners were either straight-tube burners with constant cross-sectional area or of a conical design with a varying cross-sectional area. Cordierite, alumina, silicon carbide foams and alumina beads were used as the porous media. Several liquid and one gaseous fuel were tested inside the burners.

The steady state molar concentrations of H_2, O_2, N_2, CO, CO_2, CH_4, C_2H_2, C_2H_4 and C_2H_6 were measured by injecting a sample into a gas chromatograph via a water-cooled probe and vacuum pump. The Fast Thermal Conductivity Detector was used to measure the H_2 concentration on a continuous basis during transients. A SMPS instrument was used to measure the particulates from rich

combustion of octane and methane. Temperatures of the product mixture and burner were measured by various R and K-type thermocouples.

The uncertainty for temperatures, flow rates and equivalence ratios was calculated. The largest errors were associated with the early tests on methanol when only an air rotameter was available. Errors up to $\pm$ 16 % for ϕ were possible. These uncertainties were reduced to approximately $\pm$ 1.2 % when testing with methane. An error analysis for the R-type thermocouple is performed in Chapter 3 after the surface temperature of the burner is known. The expected uncertainties in the measurements are low enough to not affect the conclusions in future chapters.

Chapter 3

Fast Thermal Conductivity Detector Design

3.1 Structure of this Chapter

This chapter presents the theory of operation and the design of the Fast Thermal Conductivity Detector (TCD) which is used to measure H_2 during transient operation of the burner. In section 3.2 the theory behind measuring thermal conductivities of a gas mixture to determine its composition is introduced. In section 3.3 the design parameters and calibration of the instrument are discussed along with data manipulation and filtering, followed by the method used to calibrate the instrument. The chapter concludes with a brief section summarising the main results of this chapter. The results from the Fast TCD are presented in Chapter 6.

3.2 Theory of Fast TCD Operation

At start-up and during transients the H_2 concentration in the products can change much more rapidly than a Gas Chromatograph (GC) can detect. A method to measure hydrogen on a continuous basis was required in order to study the response of the burner to transients and during start-up. A search of the literature revealed that most commercial on-line hydrogen techniques use catalysts to measure low temperature H_2. Another approach is to use a thermal conductivity detector similar to the one used by the GC. Since H_2's thermal conductivity is almost an order of magnitude higher than the other major products expected in the exhaust gas, the hydrogen content should be measurable. In this technique the different gases will not be separated as they are in the GC, but their conductivity measured as a mixture. Hence, some accuracy will be sacrificed for speed.

In order to calculate the thermal conductivity of low pressure gases and gas mixtures at various temperatures a program was written in Matlab. The conductivity of the individual gases was calculated based on thermal conductivity coefficients taken from Todd and Young (2002); valid in the range of 273-1473 K. The gas mixture's thermal conductivity can be estimated using the Wassiljewa equation, eq. (3.1), with the Herning and Zipperer approximation, eq. (3.2), see Poling et al. (2001).

$$\lambda_m = \sum_{i=1}^{n} \frac{y_i \lambda_i}{\sum_{j=1}^{n} y_j A_{ij}} \tag{3.1}$$

where λ_m represents the thermal conductivity of the gas mixture, λ_i is the thermal conductivity of pure i, y_i and y_j are the mole fractions of components i and j and n is the number of components in the mixture. The function A_{ij} is given by

$$A_{ij} = \phi_{ij} = \left(\frac{M_j}{M_i}\right)^{1/2} \tag{3.2}$$

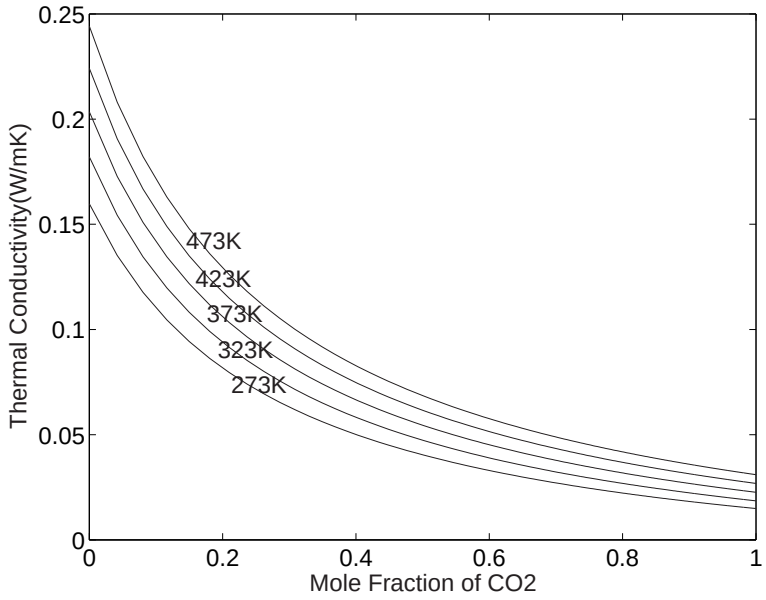

Figure 3.1: CO_2/H_2 Mixture Conductivity at different temperatures.

where ϕ_{ij} is the interaction parameter for gas-mixture viscosity and M is the molar mass of the individual molecules. The relation for estimating mixture thermal conductivities is also applicable to viscosities by substituting η for λ. Fig. (3.1) shows the conductivity for a CO_2/H_2 mixture at various temperatures. This result corresponds well to experimental data published by Todd and Young (2002).

3.3 Design of the Fast TCD

The Fast TCD detector measures the difference in thermal conductivity between a reference gas and the sample gas. The Fast TCD detector block is divided into two cells containing two filaments each. The physical device is presented in Fig. (3.2). One cell holds the sample pair of filaments and the other the reference pair connected in a Wheatstone bridge circuit. A constant current is applied to

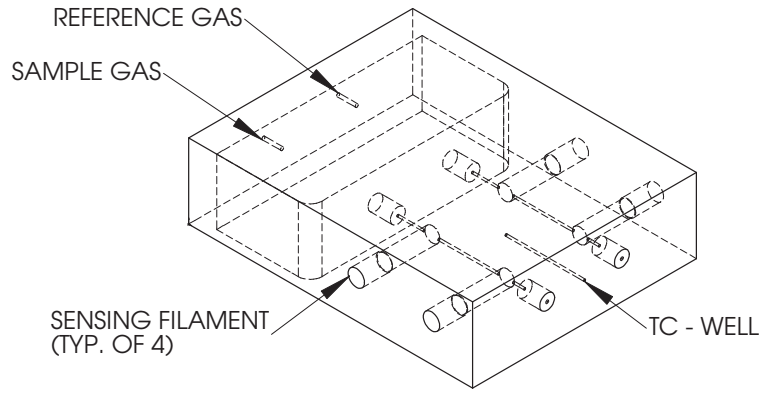

Figure 3.2: Fast TCD block diagram.

the filaments, which ensures a constant heat loss and hence a constant filament temperature. When a gas mixture is applied to the sample line, the thermal conductivity of the mixture changes, which causes a corresponding change in the heat dissipation rate from the filaments on the sample side. This leads to an imbalance in the Wheatstone bridge circuit which can be correlated to the conductivity of the new mixture.

There are five main variables that can impact the voltage signal corresponding to the thermal conductivity of a typical gas mixture that is likely to be sampled:

1. H_2 concentration and to a lesser extent CH_4 concentration.
2. Vapours condensing near the sensitive filaments.
3. Gas temperature.
4. Gas flow rate.
5. Gas pressure.

Hence, in order to accurately measure H_2 concentration the other variables need to be kept constant. The following section describes how these objectives were met and how the Fast TCD was designed to meet a limited budget.

3.3.1 Condensation Prevention

In order to prevent condensation inside the cavity of the Fast TCD, the temperature of the TCD needs to be greater than the boiling point of the product species with the highest boiling point, at atmospheric pressure. For methane oxidation this species is H_2O and the temperature therefore needs to be greater than 373 K. It is possible that it is advantageous to operate the Fast TCD at a temperature much higher than 373 K because the sensitivity of thermal conductivity of the mixture with respect to H_2 concentration may improve. The conductivity of H_2 in N_2, the two most abundant species expected in the gas mixture, are plotted in Fig. (3.3) for various temperatures. A 5 % increase in H_2 concentration equates to approximately a 10 % increase in the mixture's thermal conductivity for all the temperatures investigated. Thus, there appears to be little advantage in greatly exceeding this temperature as the sensitivity of the mixture with respect to thermal conductivity, does not improve with temperature. Therefore, the TCD block can be held at a constant 375 K with inexpensive off the shelf mat-heaters connected to a temperature controller. Another disadvantage of increasing the temperature too much beyond water's boiling point is that larger temperature gradients will be set-up between the centre of the block and the external envelope of the Fast TCD. Thus, potentially affecting the temperature of the gas within the sample or reference line differently.

A more conservative temperature to maintain the oven at would have been 380 K as the pressure in the tubing is above atmospheric pressure as there is some back pressure in the tubing, refer to Fig. (3.4). However this should not

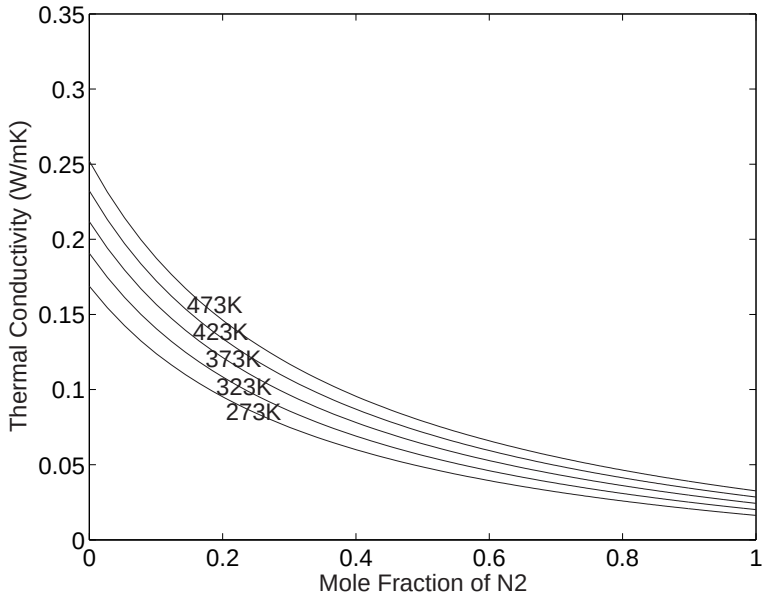

Figure 3.3: N2/H2 mixture conductivity at different temperatures.

have affected the results, as the sample is dried prior to entering the Fast TCD.

3.3.2 Gas Temperature Control

Ideally, the TCD block should be isothermal. To ensure an isothermal process, the sample gas and reference gas need to be at the same temperature as the block prior to reaching the filaments. To achieve this, industry standard Mat-heaters were attached to the top and bottom surfaces and the sides of the block were insulated with Superwool607. A compartment/oven was cut into the block upstream of the filaments and maintained at the same 375 K as the block. Tubing of the same diameter as the pathways leading to the filament chambers was coiled inside the oven. The following analysis allows the length of tubing required to bring the gas up to the block's temperature with a minimal pressure loss to be calculated. Fig. (3.5) illustrates the process of heating a fluid.

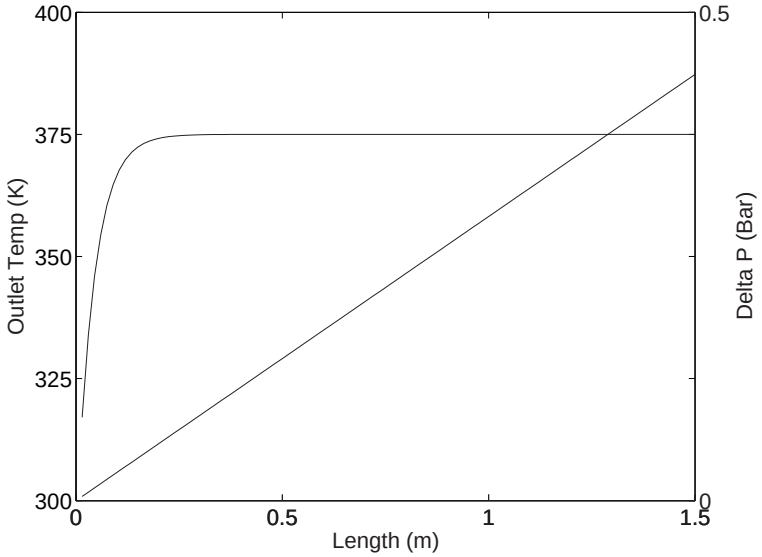

Figure 3.4: Fast TCD optimal length of tubing.

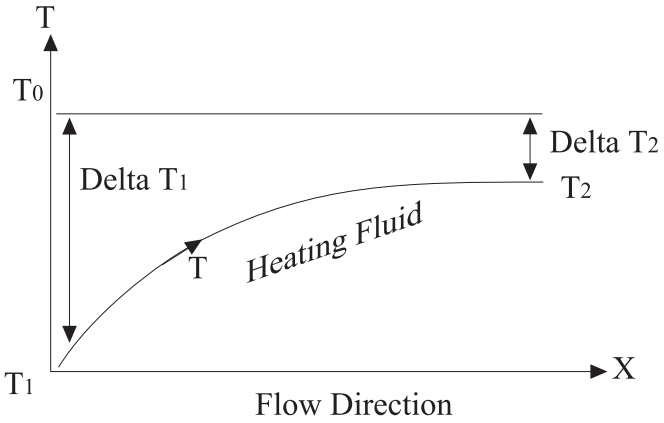

Figure 3.5: Heating a single phase fluid with the wall at a constant temperature.

Taking a heat balance for an element dx, where dQ_{wall} is the heat flux from the wall in length dx,

$$dQ_{wall} = q\pi Ddx = h\pi D(T_o - T)dx \tag{3.3}$$

and h is the heat transfer coefficient calculated for a single phase flow in a tube (Butterworth, 1977).

$$dQ_{fluid} = -\rho V C_p \frac{\pi D^2}{4} dT \tag{3.4}$$

where dQ_{fluid} is the heat flux from the fluid in length dx. The outlet temperature can be obtained by relating Eq. (3.3) and Eq. (3.4) and integrating from T_o to T

$$\int_{T_o}^{T} \frac{dT}{\rho V C_p D} = \int_{T_o}^{T} \frac{-4h}{\rho V C_p D} dx. \tag{3.5}$$

The pressure drop along the tube can be calculated for various flows by

$$\Delta P = \frac{2fL\rho V^2}{D_i}, \tag{3.6}$$

where the friction factor, for low Reynolds numbers (<2000) is given by

$$f = \frac{16}{Re}. \tag{3.7}$$

A Reynolds number of approximately 1 600 was calculated for an 80 % N_2 - 20 % H_2 mixture. The outlet temperature versus length of tubing and pressure loss versus length of tubing are plotted in Fig. (3.4). The temperature at the exit of the tube tends towards the oven temperature with an exponential decay rate proportional to the tubing length. The tube needs to be a minimum of approximately 0.4 m in length to ensure that the exit temperature is equivalent to the oven's temperature. The pressure drop increases linearly with the length of tube. A conservative length of 1 m was selected as any variation in inlet

Table 3.1: Thermal conductivity of major product species at 375 K.

Species	Conductivity ($W/m \cdot K$)
H_2	0.2042
CH_4	0.0458
H_2O	0.0249
CO_2	0.0228
CO	0.0309
N_2	0.0316
O_2	0.0323

temperature will affect the measurements accuracy and a slightly higher pressure will not impact the performance or cost of the instrument.

3.3.3 Gas Mixture Control

The major products in the syngas generated in this study are H_2, CO, N_2 and smaller amounts of CO_2. Since N_2 is inert and has a thermal conductivity very similar to that of CO, it was chosen as the reference gas. Table (3.1) tabulates individual thermal conductivities for expected product species at 375 K. Although H_2O is a significant product species of rich-combustion and has a lower thermal conductivity than the reference gas, it can be removed with the Nafion Drier prior to reaching the TCD, as was done with the GC measurements. CH_4 has a thermal conductivity approximately 50 % higher than N_2, but as presented in Chapter 4, CH_4 is not a major product species except when the flow rates are too low at high ϕ. Therefore, the tests, presented in Chapter 6, avoid this operating regime when possible.

3.3.4 Gas Flow Rate and Pressure Loss

A sensitive differential pressure transducer was connected between the reference and sample circuit to verify that the flow rates are constant at the start of each test. The tubing downstream of the filament sensors is open to atmosphere, so the pressure in the filament housings can be assumed to be atmospheric as the pressure loss to the exit is minimal, thereby ensuring that the pressure in the two circuit legs are equal.

3.3.5 Electrical and Filament Sensor Design

At the heart of the Fast TCD is a Wheatstone Bridge incorporating four temperature sensitive, electrically heated, platinum filament sensors for sample analysis. The circuit is illustrated in Fig. (3.6). Filament R1 and R4 are exposed to the sample gas and filament R2 and R3 to the reference gas. An alternative circuit can be imagined where each leg only has one filament, however by having two filaments per leg, the sensitivity of the circuit is doubled. Arranging the filaments in a Wheatstone Bridge additionally eliminates any noise that the power supply may be generating.

All four filaments are designed to be physically identical, although in reality differ slightly due to difficulties in manufacturing. To account for these differences BC184 is used to initially balance the circuit with N_2 flowing through both cells. In the first instance this was not enough to balance the circuit so a second potentiometer, Pot 2, was added to the right of BC184 to pull the bridge's voltage either up or down. The distance between the two filaments in the same cell was calculated based on maintaining a laminar flow at the entrance to each filament cavity, ensuring that the heat transfer from the two filaments in series would be similar. The Reynolds number was calculated using

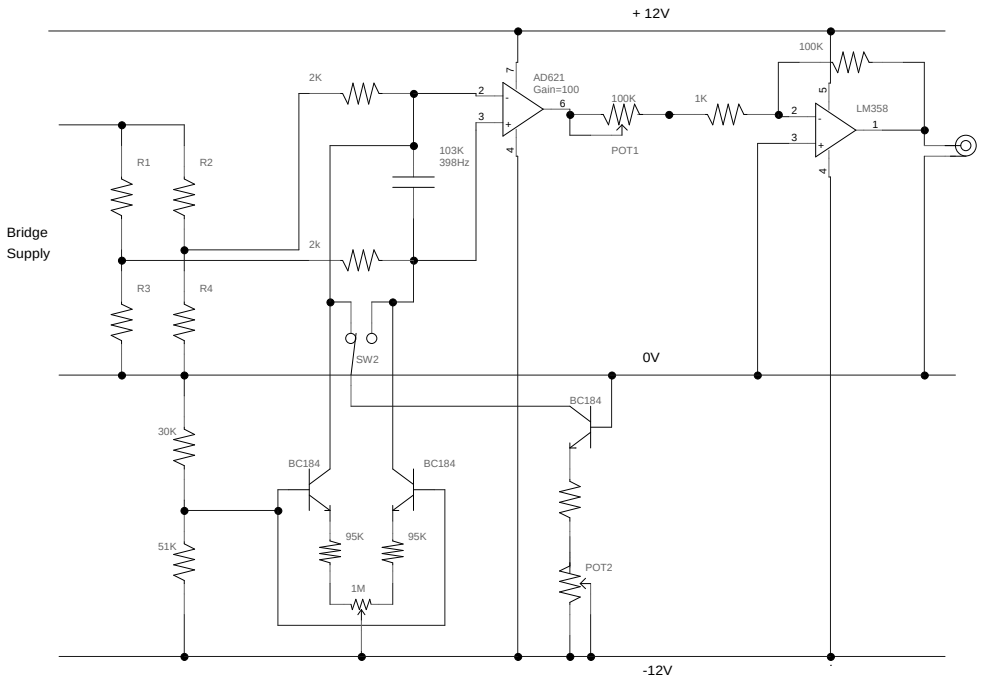

Figure 3.6: Fast TCD electrical circuit diagram.

$$Re = \frac{\rho_g u_g D_g}{\mu_g} \tag{3.8}$$

where the diameter of the gas passage, D_g, is 1 mm, and μ_g is the viscosity of the gas calculated for the reference gas and the gas mixture, 80 % N_2, 20 % H_2 based on the Herning and Zipperer approximation.

Three different filament housings were considered, see Fig. (3.7). Fig. (3.7a) shows the first, a direct-type design, where the filament is placed directly in the flow. Fig. (3.7b) shows the second, a diffused-type, where the filament is placed

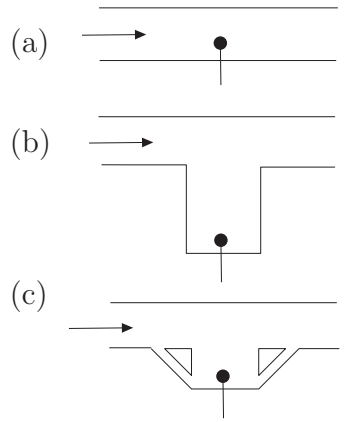

Figure 3.7: Schematic representation of (a) direct-type, (b) diffused-type and (c) semi-diffused TCD filament housing.

outside of the flow and the filament detects gas which diffuses from its main path. The final type, see Fig. (3.7c), is a semi-diffused design and is a cross between the previous designs. A portion of the gas diffuses from the main pathway and flows directly past the filament. Direct-type designs have higher sensitivity and respond quicker to changes, but at the expense of stability due to flow fluctuations around the filaments. Initially, a semi-diffused design was selected as a compromise, but due to manufacturing difficulties the indirect diffused-type housing (b) was used as shown in the TCD block diagram (Fig. 3.2).

3.3.6 Results Interpretation

By effectively measuring the change in resistance of the heated filament, the change in thermal conductivity of the sample gas may be determined. Fig. (3.8) is a photograph of one of the four filaments. Any change in species concentrations causes an imbalance in the Wheatstone Bridge, producing an electrical signal proportional to the change. Calibrating the TCD with known mixtures of H_2 and N_2 or air, allows the concentration of H_2 in the sample gas to be inferred.

Figure 3.8: Photograph of filament.

The output signal from the Wheatstone Bridge is amplified 100 fold by op-amp 621. A second amplifier, LM358, controlled by the potentiometer (POT1) could increase the amplification by another multiple of 100. However, for the tests conducted in this project its gain was set to one, resulting in a total amplification of 100. The output signal, ranging from -10 to 10 V, is taken from the BNC Output and sent to the data acquisition (DAQ) system for further processing.

Temperatures, flow rates, pressure differential between the two TCD channels and the Fast TCD signal were all routed to the DAQ system. The sampling frequency for the temperatures and flow rates was 1 Hz. The Fast TCD signal was sampled at 10 Hz and the median value of this signal was calculated every second and stored. The median value was used in preference to the mean value as it is less sensitive to outlying points. All the data presented in Chapter 6 has had this filter applied as a minimum.

3.4 Calibration

Now that the previous sections have discussed how to minimise changes or hold constant four out of the five variables, the conductivity of the sample mixture can

be compared to a known gas mixture and the concentration of hydrogen deduced. The Fast TCD was calibrated using two calibration gas cylinders of 10.08 % and 25.61 % H_2 in N_2. Additional calibrations were carried out using the mass flow controllers to control the amount of H_2 in air at flow rates similar to those in the experiments. During experiments, a sample was periodically sent to the GC to confirm the Fast TCD's analysis.

The circuit was balanced so that with N_2 flowing through both cells an output of +2 V was produced. The higher the voltage supplied to the bridge the more sensitive the filaments will be to a change in hydrogen concentration, but the shorter the lifetime of the filaments will be due to the higher current. It was determined that a supply voltage of 4.5 V, at minimum gain, was sufficient to allow full scale output deflection (8-20 V) corresponding to a hydrogen concentration between 8 % and 30 %.

In Fig. (3.9) air was held constant at 10 LPM, while H_2 was increased incrementally from 1.0 LPM in steps of 0.1 LPM to 3.5 LPM. This corresponds to H_2 concentrations of 9.09 % to 25.9 %. Each step was held for 60 seconds. The voltage was averaged over 56 seconds (the 4 seconds immediately following the adjustment of the H_2 flow was not averaged) and plotted on the graph. We may also conclude from this figure that the time response of the instrument is at worst 60 seconds, which is an order of magnitude better than the GC.

It takes a sample approximately 0.8 seconds from the time it enters the sampling probe to the time it exits the Fast TCD, based simply on the volume of the tubing and housing assembly divided by the flow rate. The actual time for the original sample to completely exit the Fast TCD is longer due to the time for the new sample to replace the original sample inside the filament housing.

The average voltage at each step is plotted on Fig. (3.10) and a 4th order polynomial is fit to the data. The circles on the plot represent the two calibra-

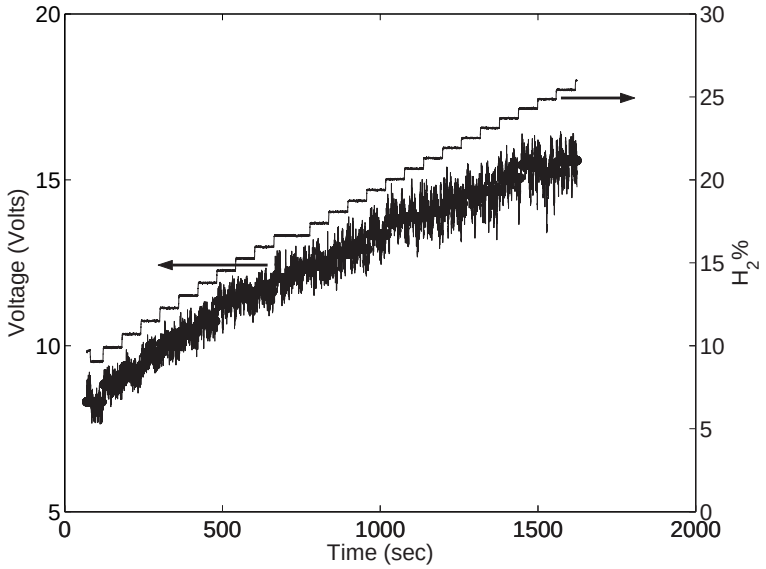

Figure 3.9: Calibration using step change in H_2 concentration with a 60 second hold between successive steps.

tion cylinder mixtures at 10.08 % and 25.61 %. This is the calibration curve that unknown mixtures will be compared against to determine their hydrogen concentration. The equation for the 4th order polynomical fit is

$$M_{H_2} = 0.00028831x^4 - 0.025102x^3 + 0.71717x^2 - 5.9219x + 21.8394 \qquad (3.9)$$

where M_{H2} is the H_2 concentration.

The amount each individual point deviates from the mean is plotted in Fig. (3.11). As the H_2 concentration increases, so does the error associated with the output voltage. A histogram of the above errors, Fig. (3.12), results in a steep Gaussian distribution ranging from -1.5 V to +1.2 V, centred around 0.

Since errors are random and have positive and negative values, the Root Mean Square or RMS error is calculated, rather than the worst case minimum and maximum error. RMS error is calculated using the following expression

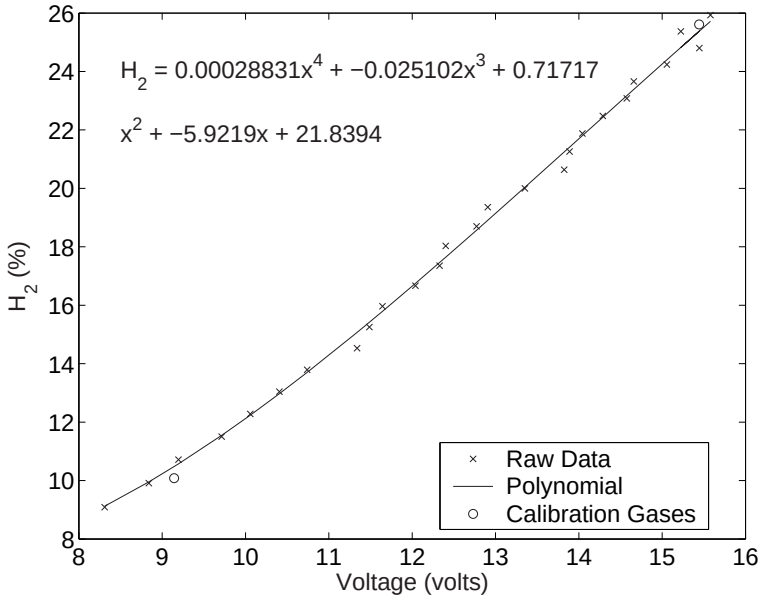

Figure 3.10: 4th order polynomial fit to FAST TCD calibration.

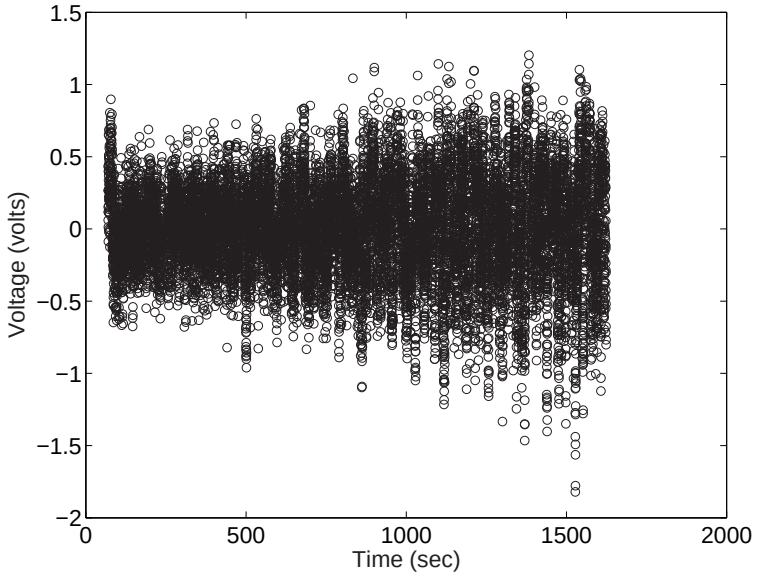

Figure 3.11: Error at 10,11,12,..,26 % H_2 concentration.

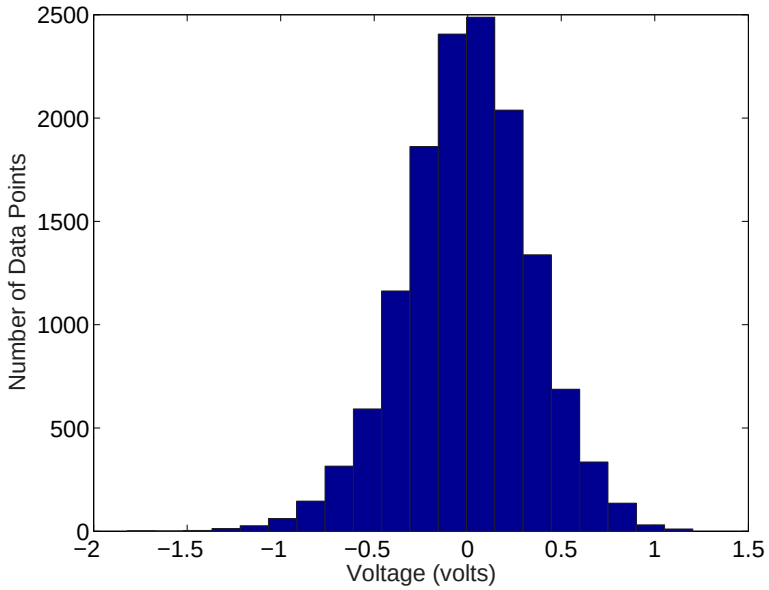

Figure 3.12: Error distribution.

$$E_{rms} = \sqrt{\frac{1}{n}\sum_{i=1}^{n} E_i^2} \tag{3.10}$$

where E is the error associated with each data point and n is the number of data points.

Fig. (3.13) shows that the RMS error is less than 0.5 V for all cases. The absolute error is proportional to output voltage. To determine if the relative error increases with voltage, the Signal to Noise Ratio (SNR) is calculated

$$\text{SNR} = 20\text{Log}\left(\frac{\text{Signal voltage}}{\text{Noise voltage, rms}}\right). \tag{3.11}$$

Fig. (3.14) illustrates that there is no definite trend relating the relative error to voltage. The SNR varies from approximately 25 to 40, with the exception of the data from the 9 % concentration, which is barely large enough to isolate the actual signal from the noise.

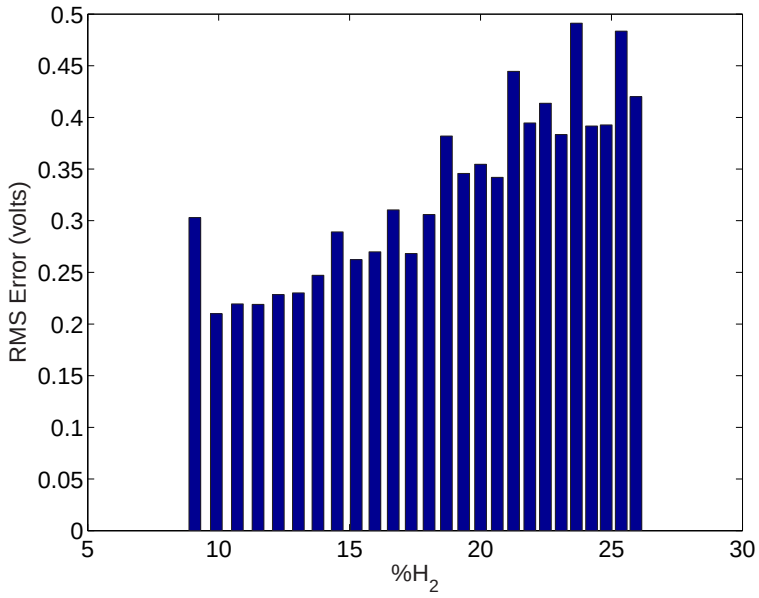

Figure 3.13: RMS error.

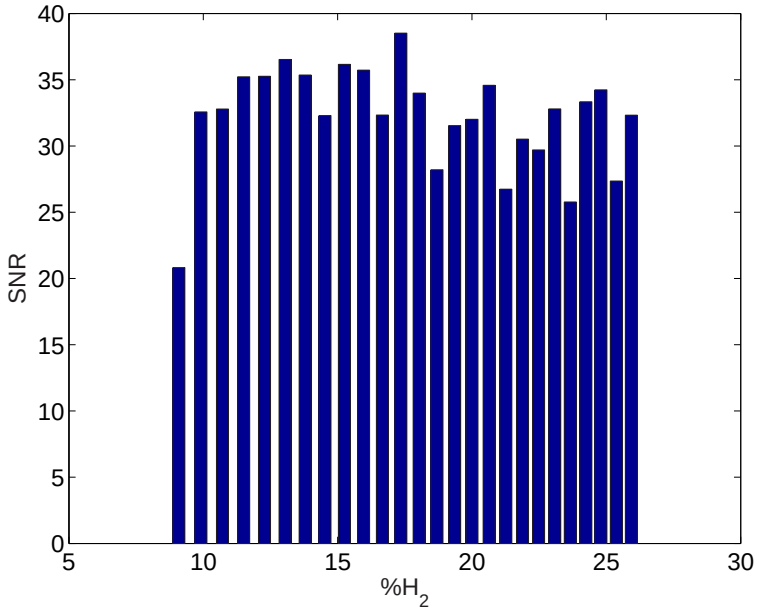

Figure 3.14: Signal to noise ratio (SNR).

3.5 Chapter Summary

A Fast TCD was designed and constructed to measure H_2 on a continuous basis. The instrument was designed to minimize the factors that affect the thermal conductivity of a gas mixture, except its composition. It was calibrated against known gas mixtures from the mass flow controllers and also against calibration gas mixtures. Accuracy was sacrificed for speed of measuring the gas mixture's composition in comparison to the GC. The SNR was calculated to range from 25 to 40, sufficiently high enough to isolate the actual signal from the noise. Transient response data of the burner as measured by the Fast TCD is presented in Chapter 6.

Chapter 4

Global Behaviour and Stability Limits

4.1 Structure of this Chapter

This chapter discusses the global behaviour and stability of the methane, methanol, ethanol, octane, petrol, kerosene/Jet A-1 and biodiesel in the porous media (PM) burners. Section 4.2 describes the preliminary tests performed with methanol prior to selecting the burners' final configuration. Section 4.3 discusses how the flames behaved inside the porous media burner for the various fuels tested. Section 4.4 presents the results obtained from the infrared camera, including the uniformity of the burner's surface temperature. The error associated with R1 due to radiation absorbed and reflected by the thermocouple bead at high temperatures is also calculated and discussed. In the next section, the particulates diameter and concentration are measured for rich octane and methane flames. Section 4.7 discusses the durability and operational lifetime of the PM and the materials the burners were constructed from. The chapter closes with a summary of the most important findings presented in this chapter.

4.2 Preliminary Results

Initially, a single piece of 18.3 mm thick cordierite was used inside the steel burner (Fig. 2.4a) to carry out a set of feasibility tests. All experiments in this section were conducted inside various burners with 30 mm I.D. All preliminary tests were performed with methanol as the fuel. It should be noted that in these tests the UFL was considered to be the richest flame that could be stabilized. During these tests the flammability limits of methanol were not extended. This can be attributed to insufficient burner insulation, failing of the ceramic cement and only a single piece of foam resulting in a surface stabilized flame without the advantages of a submerged flame inside the porous media.

In the second set of tests a piece of 60 PPI cordierite was placed upstream of a 40 PPI cordierite and secured in place by alumina paper instead of ceramic cement. The flame stabilized on the surface of the top piece of ceramic but would not penetrate further down. In this instance the flame could not propagate into the ceramic because it was losing more heat to its surroundings than it was generating. Or put another way, the *Pé* number was too low to allow the flame to propagate into the ceramic. The top piece of foam was replaced with a 10 PPI piece of cordierite and in this case the flame stabilized at the interface between the two ceramics.

The quartz window of the first burner cracked after only a couple of thermal cycles due to the differing thermal expansivity of the stainless steel burner ($16 - 18\text{x}10^{-6}$ K^{-1}) and quartz window ($0.75\text{x}10^{-6}$ K^{-1}). The cracks are visible in Fig. (4.1). Another problem with the first burner was that the split tube design leaves egress routes for air to enter the burner or gas to escape. An all-steel burner constructed without a split was considered but rejected, since being able to see the location and colour of the flame is important for the purposes of this experiment. As a result a quartz tube burner was selected due to its transparency,

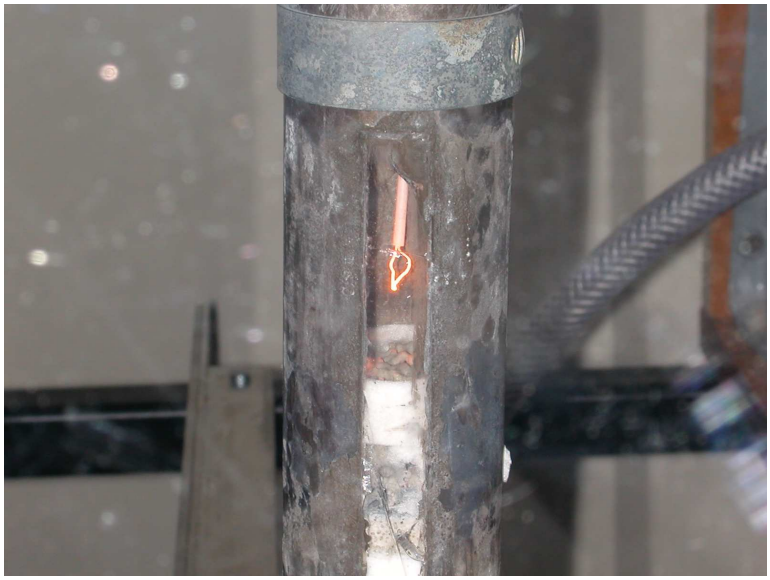

Figure 4.1: Methanol flame with crack visible in quartz window.

high softening temperature (1800 K) and excellent thermal shock characteristics (Mindrum Precision, 2003).

The ceramic was transferred into the new quartz burner and an attempt to repeat the second set of tests in the steel burner failed. The flame would not enter the 10 PPI top piece of ceramic. It was assumed that this was because the radiative heat losses were too excessive through a transparent burner. This hypothesis was proven correct when 40 mm of Superwool insulation was added to the outside of the burner and the flame stabilized once again at the interface between the two ceramics. However, after several more thermal cycles the flame became increasingly difficult to stabilize at the interface. Inspection of the cordierite revealed that the centre of the top piece had melted. Materials' durabilities are discussed in greater detail in Section 4.7.

Tests in the same burner using one 60 PPI piece of alumina foam as the flame holder and one 20 PPI piece of alumina downstream of it produced results similar

to the latest cordierite tests. The flame would stabilize at the interface but it was not possible to extend the flammability limits much beyond the UFL of 4.1 (Turns, 2000). In these tests, each piece of alumina had a thickness of 23.6 mm.

At the lower flow rates the reaction was losing more heat to its surroundings than it was generating and the flame would gradually fade and then disappear. At the higher flow rates the flame front would start moving up towards the surface and blow off would occur. It should be noted that at low flow rates and conditions closer to stoichiometric conditions, the reaction could generate enough heat to penetrate the bottom piece of ceramic and flashback would occur.

A wire net was placed over the exit of the burner, to determine if the limit could be increased further as was done by Itaya et al. (2002). A slight improvement was noticed, indicating that radiative heat losses from the surface of the 20 PPI piece of ceramic were still excessive.

Next a second piece of 20 PPI alumina foam was added on top of the single piece of 60 PPI foam. In this set-up the flame still stabilized at the interface between the fine and coarse ceramic. This resulted in more radiant heat being trapped inside the burner, increasing the energy available to heat the incoming gas mixture. Tests of this configuration increased the UFL to 6.0. In this instance placing a metal screen over the exit produced no improvement. Hence, this configuration of a single piece of 60 PPI alumina foam and two 20 PPI pieces of alumina foam without a metal screen at the outlet was used for the remainder of the ceramic foam tests.

At this point, 50 mm of rockwool insulation was added to the existing insulation. This configuration was used for the remainder of the tests and was summarized in Table (2.1). With the increased insulation the UFL was extended to 9.3. The flame's stability increased compared to the previous test for both higher and slower flow rates due to less heat being lost to the surroundings.

This ends the preliminary testing section. All future tests were conducted inside a fully insulated burner with a sufficient upper layer of porous material to minimise radiative heat losses from the top layer of foam or beads to the environment.

4.3 Global Behaviour and Stability Limits

Table (4.1) summarizes all the major tests completed in this thesis. 'Envelope' is the stable operating limits for the burner. 'Behav.' is the general behaviour of the flame inside the porous media encompassing where the flame stabilizes, the time to reach the interface and the upper flammability limit achievable. Beads and foams refer to the type of PM used in the tests. H_2O is the addition of water in either vapour, injected as steam with the methane, or liquid form, mixed with the ethanol. Δh refers to tests where the height of the sampling probe above the burner was varied. A number of tests were also carried out with methane during non-steady state, transient, conditions. All results except for the biodiesel, were compared to equilibrium results calculated using CEA.

Table (4.2) tabulates the important properties of the fuels tested. The densities of the fuels are at one atmosphere and 20 °C. 'Temp'. is the temperature of the fuel/air mixture entering the burner and is the temperature used in the following chapter for the equilibrium calculations using NASA's CEA code. Due to the reluctance of the biodiesel manufacturer to release the exact composition of their fuel an average molecular formula was assumed based on information from Martinez (2006).

In these experiments, it was observed that if the flame is extinguished by a momentary interruption of fuel or oxidant, it can be immediately re-started by simply restoring the fuel and oxidant flows. A PM burner has a large enough

Table 4.1: Major tests conducted on fuels. Where Δh equates to changing the height of the probe in relation to the surface of the burner.

Fuel	Envelope	Behav.	Beads	Foams	H_2O	Δh	Transients	CEA
CH_4	-	X	X	X	X	X	X	X
CH_3OH	X	X	X	X	-	X	-	X
C_2H_5OH	-	X	X	-	X	-	-	X
C_8H_{18}	-	X	X	X	-	-	-	X
Jet-A	-	X	X	X	-	-	-	X
Biodiesel	-	X	X	-	-	-	-	-

thermal mass, especially true for the beads, that it will maintain its temperature above the auto-ignition temperature of the fuel for a significant amount of time after the flame has been extinguished. This is particularly important for devices that may experience severe transients or unsteady conditions, such as changing power requirements for an on-board reformer for an automobile.

4.3.1 Methane

Methane, CH_4, is the simplest hydrocarbon and is the main constituent of natural gas. The main source of methane is extraction from geological deposits, however it can also be generated by the fermentation of organic matter. In the latter case it can be considered a sustainable fuel. CH_4 was tested as a potential feedstock to our burner, due to its ready wide-spread use as a primary energy source, high hydrogen to carbon ratio and its potential to be generated sustainably.

In these experiments, methane flames were stabilized up to an equivalence ratio of 2.5, considerably higher than the upper flammability limit for a laminar

Table 4.2: Properties of fuels tested. Fuel properties obtained from Turns (2000) and API (1976) at 20 °C and 1 atmosphere, unless otherwise noted.

	Methane	Methanol	Ethanol	Octane /Petrol	Kerosene /Jet A-1	Biodiesel
Formula	CH_4	CH_3OH	C_2H_5OH	C_8H_{18}	$C_{12}H_{23}$ [a]	$C_{17}H_{32}O_2$ [b]
Mol. Wt. (kg/Kmol)	16.04	32	46	114.23	167	268
Density (kg/m^3)	0.6581	791	790	700	792	883
LHV (MJ/kg)	50.0	21.1	26.4	44.8	43.7	36.0
A/F St. (kg/kg)	17.1	6.46	9.0	14.7	14.9	12.4
UFL	1.64	4.08	3.35	3.8-4.2	4.65	N.A.
Temp (K)	293	353	373	403	573	583

[a] Molecular make-up obtained from NASA's thermodynamic database (McBride et al., 2002).

[b] Molecular make-up obtained from Martinez (2006).

free flame (1.64). Richer, transient flames were also observed, where the combustion wave would propagate downstream at a velocity on the order of 10^{-5} m/s, in agreement with Babkin et al. (1991).

In one set of experiments, inside a 50 mm quartz burner, the flame became unstable and started to oscillate while emitting a thumping sound. This phenomenon was most pronounced around stoichiometric conditions over a wide range of flow rates. Removing the insulation revealed that the quartz envelope had become compromised as there were several holes close to the interface between the two bead layers. Similar results were recreated in a burner with a single hole in it, used for a TC probe. It was deduced that the hole allowed air to enter and exit the burner, presumably driven by the unsteady components of pressure and heat release from the combustion process. The only time thermoacoustic instabilities were present was when a hole, allowing air to enter and exit the system, close to the point of highest heat release was introduced either by design or accident.

4.3.2 Methanol

The remainder of the fuels tested are all liquid fuels. Combusting liquid fuels within porous media burners has several advantages over burning the fuels in an open flame. The porosity provides a convoluted path for the fuel to travel, exposing it to a homogenous hot matrix without cold boundaries ensuring droplet vaporization and contributing to complete combustion. As shown by Jugjai et al. (2002) and Jugjai and Polmart (2003) a compact design is possible as a separate vaporizer is not necessary. In our tests liquid fuels were first vaporized by either a separate commercial vaporizer or the specially designed vaporizer, presented in Section 2.2.1.

Methanol, CH_3OH, is the simplest of the alcohols and is viewed as a potential

energy carrier for the automobile industry. Historically, it has been generated as a by-product of the distillation of wood. Today, most is produced synthetically from methane. It is an intrinsically pure product, has a higher flame velocity and wider flammability limits, but is less energy dense compared to petrol.

Methanol flames would stabilize between the two differently sized pored ceramics. The UFL of methanol was increased from 4.1 to 6.1 inside the foam burner and to 9.3 inside the bead burner. Based on a LHV of 21.6×10^6 J/kg for CH_3OH, a firing range of 135 kW/m^2 to 2670 kW/m^2 was attained at an equivalence ratio of 3.8. This corresponds to a turndown ratio of 20:1. This high turndown ratio is possible because of the wide range of gas mixture speeds that the flame can stabilize at (eg. Fig. 4.2). Trends suggest that even greater turndown ratios would be possible closer to stoichiometric conditions due to the broadening of the operating envelope, as has been observed for lean flames by Hsu et al. (1993) and also predicted by numerical models (Diamantis et al., 2002).

A plot of laminar flame speeds versus ϕ for methanol and octane, Fig. (4.3), based on a derivation from Metghalchi and Keck (1982), can be compared to flame speeds inside the porous media: unfortunately the correlation is only valid for ϕ = 0.8-1.4. Appendix A has more details on the formulas used to calculate the velocities for the above figure. At a ϕ of 1.4, the laminar flame speed is 35 cm/s. Egolfopoulos et al. (1992) performed a detailed kinetic model to calculate the laminar flame speeds for methanol and validated it against experiments. At a slightly higher inlet temperature of 368 K, at a ϕ of 1.9, they determined the laminar flame speed for methanol to be approximately 23 cm/s. Both studies confirmed that flame speeds decrease with increasing ϕ.

Comparing these results to our results plotted in Fig. (4.2), at a higher ϕ of 3.8, where one would expect lower velocities, we observe a flame velocity ranging from less than 5 cm/s to as high as 55 cm/s. Therefore, demonstrating that

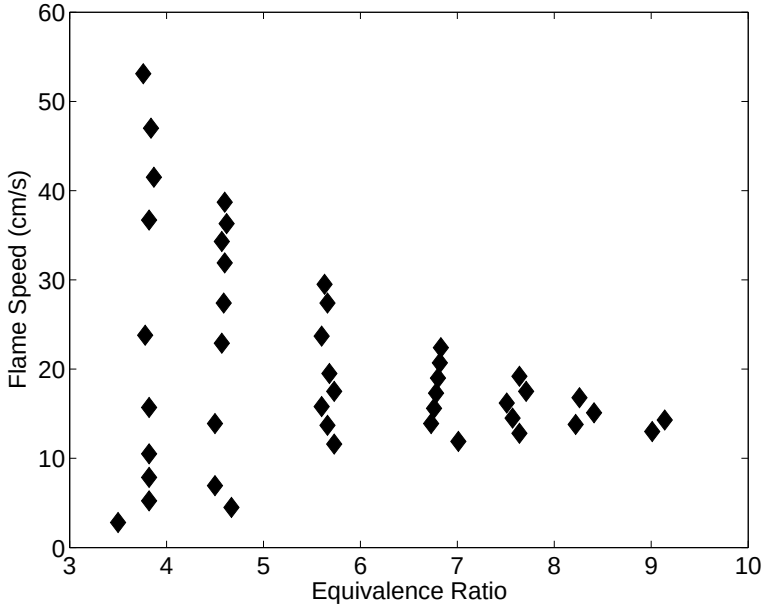

Figure 4.2: Operating envelope of methanol flame inside the bead burner.

higher flame velocities are possible in stationary porous media combustion, in agreement with Sathe et al. (1990), Diamantis et al. (2002), Zepter and Hustad (2001) and Mathis Jr. and Ellzey (2003)

4.3.3 Ethanol

Ethanol, C_2H_5OH, is also an alcohol. Ethanol, unlike methanol, is non-toxic. Throughout history it has been primarily used as the intoxicating ingredient in alcoholic beverages. Its other main use, one which is increasing rapidly, is a fuel in the transportation sector. Ethanol can be produced from a variety of biological sources that contain sugar, starch or cellulose. An ethanol water mix of 96 % ethanol by volume is possible with fractional distillation. To produce pure ethanol, neat ethanol, a more complex, expensive process is required. In this set of experiments, both neat ethanol and ethanol/water mixtures were tested.

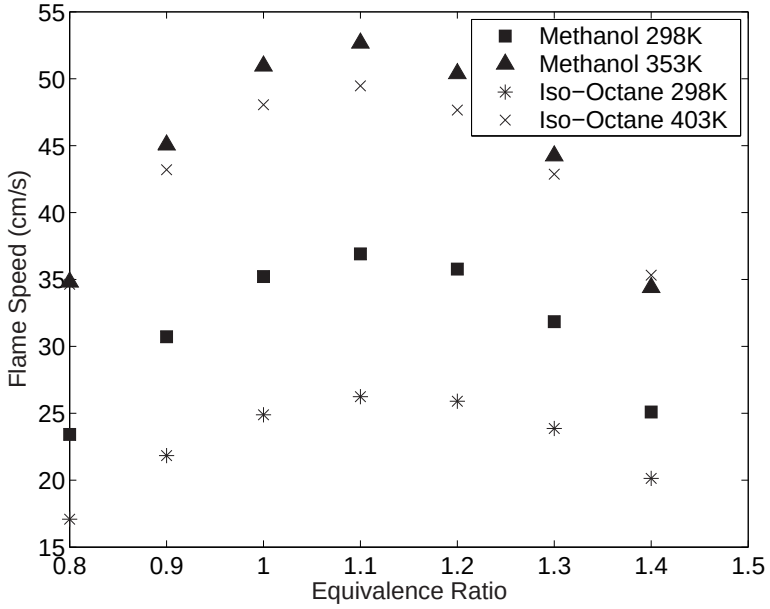

Figure 4.3: Laminar flame speeds based on Metghalchi and Keck (1982).

Neat C_2H_5OH, 90 % C_2H_5OH and 67 % C_2H_5OH (by volume) were tested in the 52.5 mm I.D. Kanthal® burner. The upper flammability limit was extended from 3.35, for a laminar free flame, to a ϕ above 4.0. It was observed that the time for the system to reach thermal equilibrium increased with increasing H_2O fraction. No soot was observed for any of the tests conducted with C_2H_5OH.

4.3.4 Iso-Octane and Petrol

Petrol or gasoline is the primary fuel in the transportation sector. It is a mixture of hundreds of hydrocarbons with the bulk of the mixture comprised of between 5 and 12 carbon atoms per molecule. In addition, a large range of additives are added to the fuel to enhance certain performance characteristics. Petrol's composition is not static and changes with the seasons as well as with geographic area. 2,2,4-Trimethyl pentane or Iso-octane is an isomer of octane, C_8H_{18}, with

a designated octane number of 100. It is used as a standard for determining the octane number of fuels. It is used in these experiments since its composition and chemical make-up are known and remain constant.

Iso-octane and petrol both behaved similarly to the other fuels tested and stabilized at the interface. However, compared to a methane or an alcohol flame which only takes a couple of minutes to enter the foam, the two hydrocarbon fuels took approximately 10 minutes to warm up the foam enough to propagate into it. This can be partially explained by iso-octane's large quenching diameter, approximately 4 mm compared to 1.5 mm for methanol and 2.0 mm for methane (Glassman, 1996). However once stable, the upper flammability limit for the fuels could be attained. At equivalence ratios above 2.0 soot exiting the burner was visible, especially so for the petrol. The soot accumulated on the thermocouple and turned the ceramics from white to black. However, the soot could be removed by burning a mixture with excess oxygen for several minutes.

4.3.5 Kerosene (Jet-A)

Like petrol, aviation fuel is a mixture of many different hydrocarbons. Additionally, additives, which are fuel-soluble chemicals are added in small amounts to enhance or maintain fuel properties. Almost all jet fuel is made from petroleum, but recently the Fischer-Tropsch process has been used to manufacture a synthetic jet fuel blend (Bacha et al., 2000).

Kerosene was tested in the 52.5 mm I.D. Kanthal® burner consisting of a 20 mm (4.8 pores/cm-90 % porosity) SiC support layer and a 100 mm (24 pores/cm-91 % porosity) SiC upper layer. In these tests, the UFL was extended to approximately a ϕ of 5.0. The flame would propagate to the interface in 2-3 minutes, when operated close to stoichiometric conditions, and be accompanied by a high pitched hum. Once at the interface the flows were adjusted to their

desired rich setting and the hum ceased.

A second set of tests was conducted in the same burner filled with 30 mm of Al_2O_3 desiccant beads as the support layer and 80 mm of 4.6-5.0 solid Al_2O_3 beads as the top layer. In these tests the UFL was also extended to 5.0, however it took considerably longer for the flame to propagate to the interface, on the order of 30 minutes. In both sets of tests some soot formed on the porous matrix, although not as much as in the octane tests.

4.3.6 Biodiesel

Biodiesel refers to any diesel-equivalent biofuel usually produced from renewable resources such as vegetable oils, tallow and waste oils and fats. It is produced by mixing a vegetable oil or fat with an alcohol (generally methanol) in the presence of a catalyst to produce fatty acids (methyl ester) and glycerine. Biodiesels are biodegradable and non-toxic and are increasingly blended with conventional diesel.

Initial tests were conducted in the 52.5 mm I.D. Kanthal® burner filled with 30 mm of 2-3 mm desiccant Al_2O_3 beads and 80 mm of 4.6-5.0 mm solid Al_2O_3 beads. However, the burner tended to clog up with large amounts of residual deposits when the fuel cooled between exiting the vapourizer and reaching the surface of the burner where it was ignited. The carbon could be oxidized and removed with a lean acetylene and oxygen flame. Fig. (4.4) and Fig. (4.5) illustrate the residual deposits at the intake to the burner before and after the lean C_2H_2 burn. To overcome this problem, the conical burner was designed where the mixture could be ignited at the interface instead of the surface of the porous media. This burner is illustrated in Section 2.2 and is filled with the same porous media as the Kanthal® burner was.

To further reduce the amount of residual deposits, the burner was operated

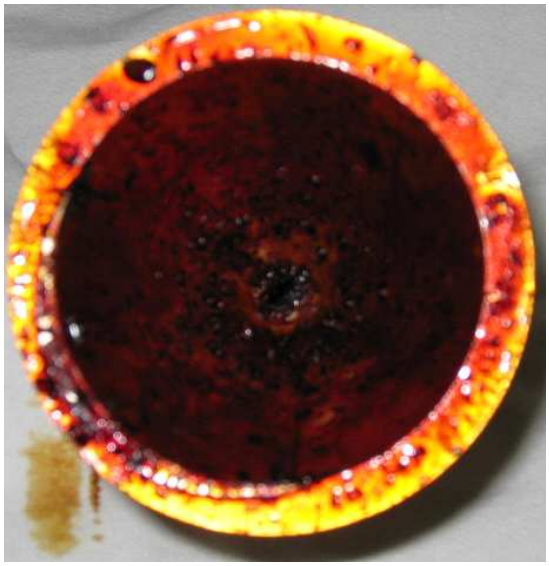

Figure 4.4: Residual deposits left by biodiesel on entrance adapter to burner.

Figure 4.5: Adapter to burner after lean acetylene/oxygen flame.

with CH_4 for five minutes during warm-up and for five minutes during cool down. In these tests a flame could be stabilized at a ϕ up to 3.0 at the interface between the two different porous mediums. Several tests were carried out where the vaporized biodiesel was mixed with CH_4. This increased the stability of the flame and tended to reduce the amount of deposits inside the burner.

4.4 Temperature Measurements

This section presents temperature measurements from the thermal imaging camera. The camera was positioned 600 mm from the burner's surface at an angle (θ) of 74.1° to the horizontal, to avoid the excessively high temperatures directly above the burner. The camera in relation to the burner is illustrated in Fig. (4.6). As a result the pictures are skewed in the vertical direction and L102 appears shorter than L101. In order to assist the reader, the figures of the surface of the burner have been stretched in the y-direction to make L101 and L102 equal. Since the bottom of line L102 is closer to the camera, equally spaced gradients on the line will increase as the line is traversed moving towards the top of the picture. Fig. (4.7) is a photograph, in the visible light spectrum, from the same location as the thermal images were shot. As can be seen the burner's insulation is also being imaged by the thermal camera. In Fig. (4.8) through Fig. (4.11) the Max T, Min T, Avg T and Stdev relate to circle AR01. AR01 has a diameter of approximately 38 mm (the burner's diameter is 52.5 mm) and L101 and L102 are 100 mm in length. The top layer of beads is 35 mm below the upper edge of the burner.

The average surface temperature of the beads is approximately 220-300 °C higher than the temperature recorded by the R-type thermocouple 10 mm above the surface of the beads for an equivalence ratio of 2.5 at various flow rates. The

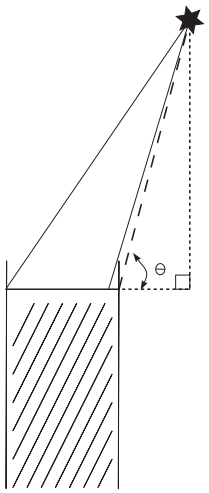

Figure 4.6: Schematic illustration of camera in relation to burner.

data is tabulated in Table (4.3). R1 is the raw temperature recorded by the R-type thermocouple 10 mm above the surface of the top layer of beads.

As the flow rates are increased, the surface temperature of the beads increases due to the increase in energy released by the reaction and as the reaction zone stabilizes further downstream of the interface. These temperatures are used in section (4.4.1) to calculate the difference between the thermocouple bead and the actual gas temperature 10 mm above the burner's surface.

The standard deviation of the temperature across the burner's surface is only 19.3 °C rising to 30.6 °C as the flow rates are increased and the average temperature increases, inside AR01, from 887 °C to 1015 °C. In steady state operation the burner's surface temperature is relatively uniform (± 100 K). Fig. (4.12) to (4.15) plot the temperature profile across the burner's surface in the x and y axis. L101 traverses left to right and L102 traverses top to bottom. In the plots the burner extends between 24 mm to 76.5 mm, as shown by the vertical lines, and is centred at 50.3 mm on the x-axis. The increase in temperature of L102 at approximately 83 mm is the radiation being emitted from the top of the burner

Figure 4.7: Visible image of burner from same location as infrared images were shot.

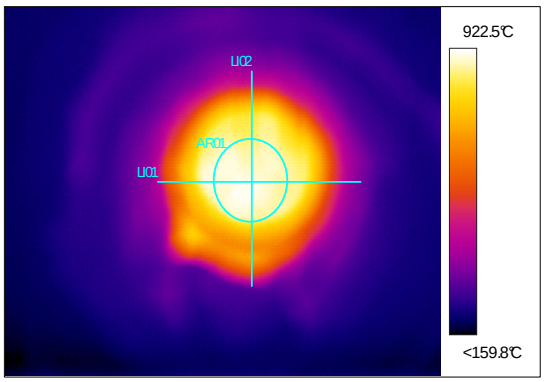

Figure 4.8: Surface temperature at ϕ=2.5, fuel=1.5 LPM.

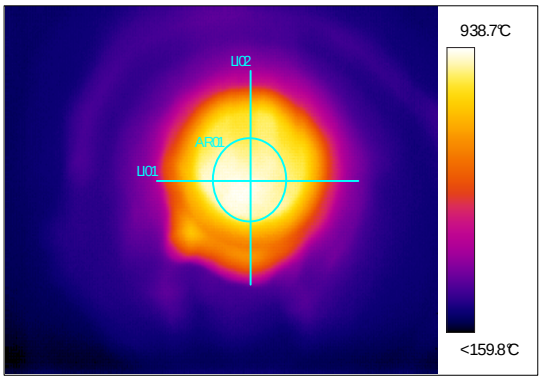

Figure 4.9: Surface temperature at ϕ=2.5, fuel=2.5 LPM.

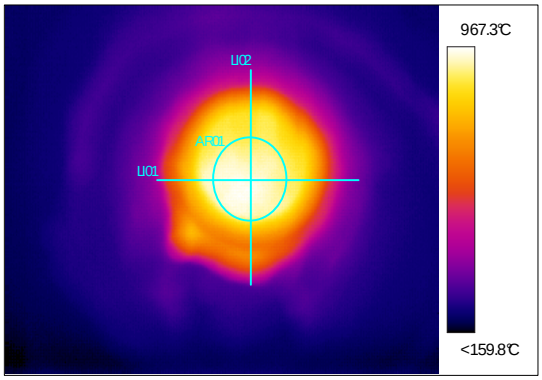

Figure 4.10: Surface temperature at ϕ=2.5, fuel=3.5 LPM.

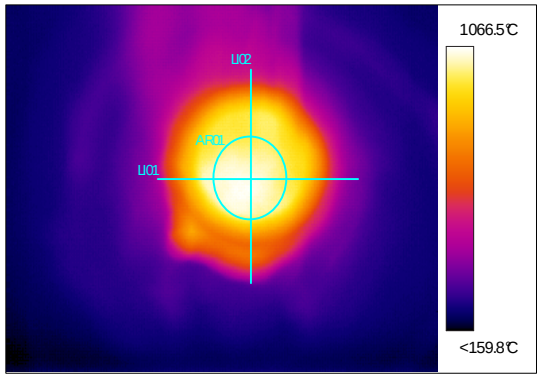

Figure 4.11: Surface temperature at ϕ=2.5, fuel=4.5 LPM.

Table 4.3: Surface bead temperatures at ϕ=2.5

Fuel (LPM)	Air (LPM)	Max T (°C)	Min T (°C)	Avg T (°C)	Stdev (°C)	R1 (°C)
1.5	5.7	926	799	887	19.3	667
2.5	9.5	943	816	898	22.8	676
3.5	13.2	972	841	923	25.3	687
4.5	17.0	1071	922	1015	30.6	721

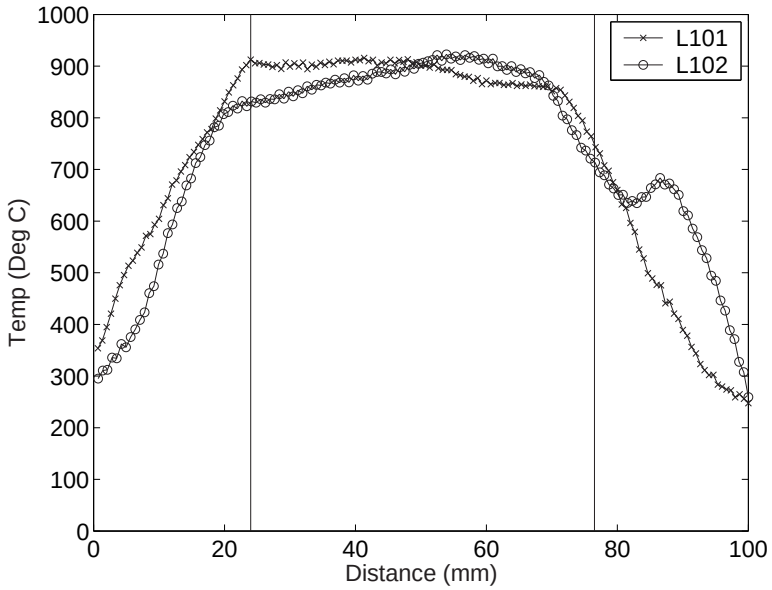

Figure 4.12: Surface temperature at ϕ=2.5, fuel=1.5 LPM.

wall as the insulation stopped about 10 mm below the exit plane of the burner. As the flow rate of CH_4 is increased to 4.5 LPM the flame becomes less stable and will eventually traverse downstream to the exit of the burner. In Table (4.3) the standard deviation at this flow rate is considerably higher than at the lower, more stable, flow rates. In Fig. (4.15) it can be seen that the surface uniformity of the temperature has likewise decreased.

Table (4.4) and Fig. (4.16) show the beads' surface temperature during start-up for a $\phi = 0.8$ and fuel flow rate of 1.0 LPM. R1 is the thermocouple located 10 mm above the surface beads and R2 is at the interface between the two different layers of beads. At 44 minutes the reaction zone was slightly above the interface. As the flame propagates towards the interface the surface temperature decreases and becomes more uniform. The temperature difference between R1 and the surface also decreases as the thermocouple bead is exposed to less emitted radiation from the surface. This radiation/convection balance is described in

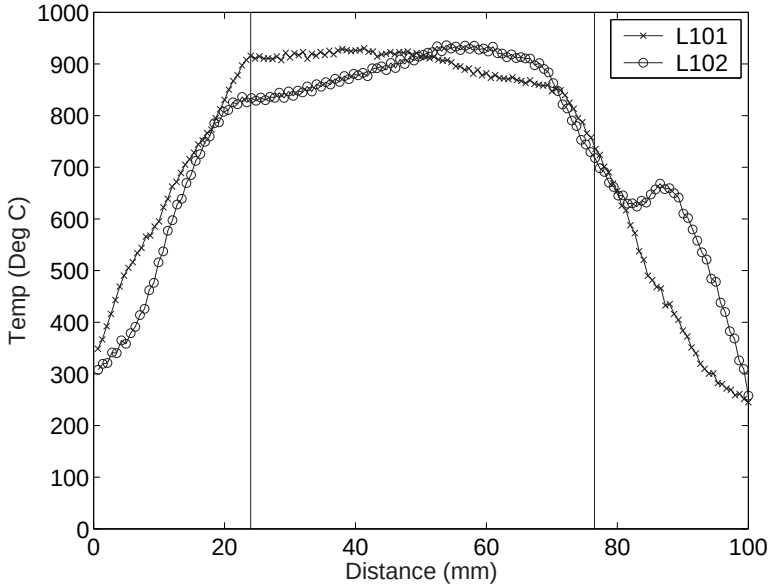

Figure 4.13: Surface temperature at ϕ=2.5, fuel=2.5 LPM.

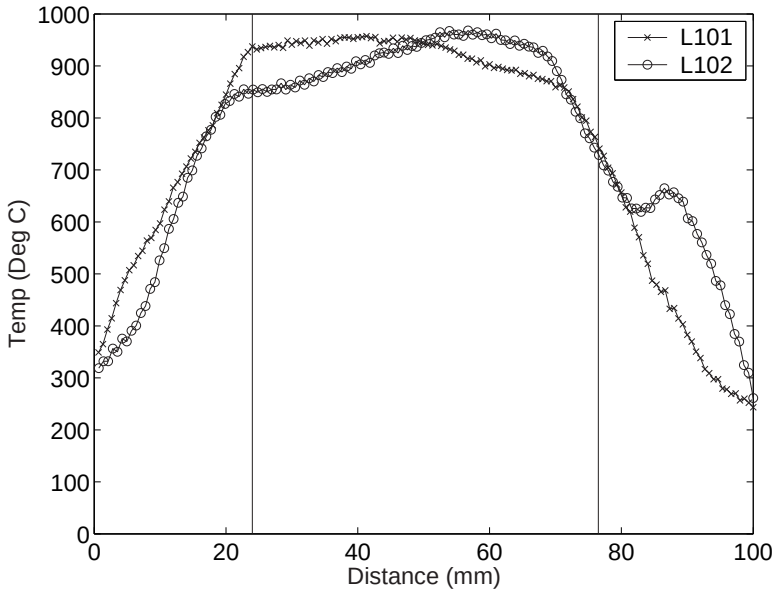

Figure 4.14: Surface temperature at ϕ=2.5, fuel=3.5 LPM.

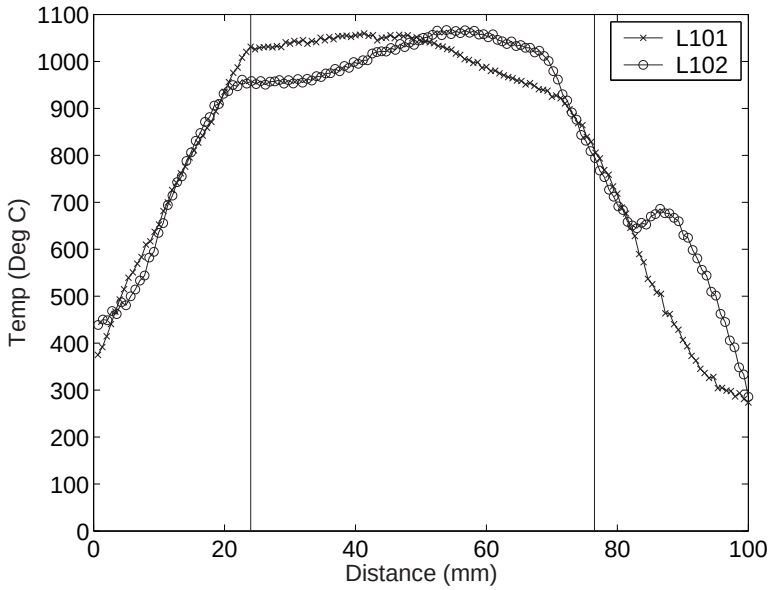

Figure 4.15: Surface temperature at ϕ=2.5, fuel=4.5 LPM.

more detail in section (4.4.1).

To meet the third objective, of determining where the reaction stabilizes in the axial plane for different conditions, a rectangular window was cut into the burner's insulation. This is a qualitative measurement as the emissivity of Kanthal® is not known with great accuracy and a calibration was not done for various temperatures (an emissivity of 0.81 was assumed based on information from www.kanthal.com). L101 and L102 are 100 mm, the same length as for previous measurements. The same coordinate system as defined in Fig. (2.1) and Fig. (2.2) is used for orientation. L101, which is at approximately the interface, crosses L102 at 0 mm in the y-direction. L102 extends to +75 mm which is approximately 5 mm below the termination of the top layer of porous media. Fig. (4.20) shows the burner with the rectangle cut in the insulation and L101 and L102 superimposed on the image.

At zero seconds the equivalence ratio has just been changed from 0.8 to 1.8 by

Table 4.4: Surface bead temperatures at ϕ=0.8 during start-up.

Time (Minutes)	Max T (°C)	Min T (°C)	Avg T (°C)	Stdev (°C)	R1 (°C)	R2 (°C)
20	1139	862	1034	76	771	51
28	1027	780	935	62	711	112
37	936	735	864	46	658	227
44	870	691	810	41	620	716

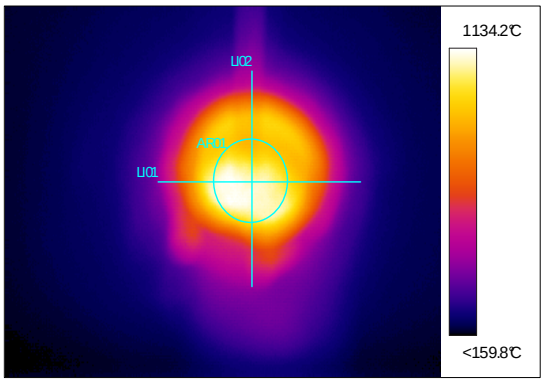

Figure 4.16: Surface temperature at ϕ=0.8, fuel=1.0 LPM and 20 minutes.

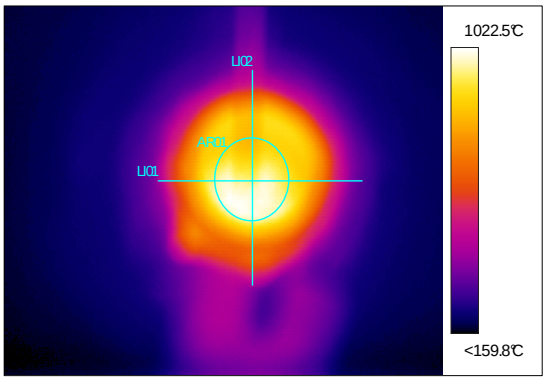

Figure 4.17: Surface temperature at ϕ=0.8, fuel=1.0 LPM and 28 minutes.

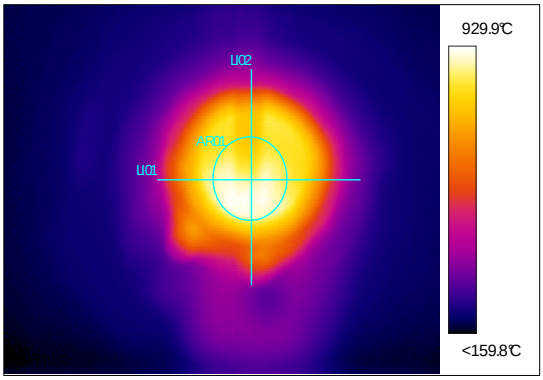

Figure 4.18: Surface temperature at ϕ=0.8, fuel=1.0 LPM and 37 minutes.

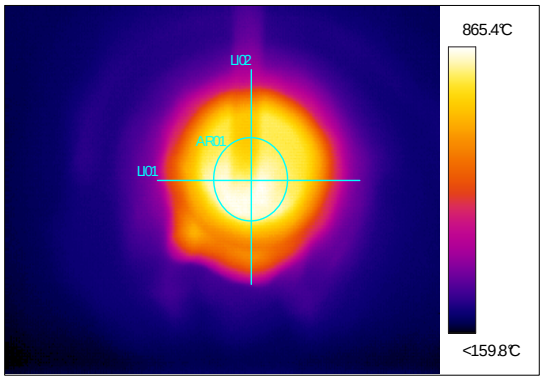

Figure 4.19: Surface temperature at ϕ=0.8, fuel=1.0 LPM and 44 minutes.

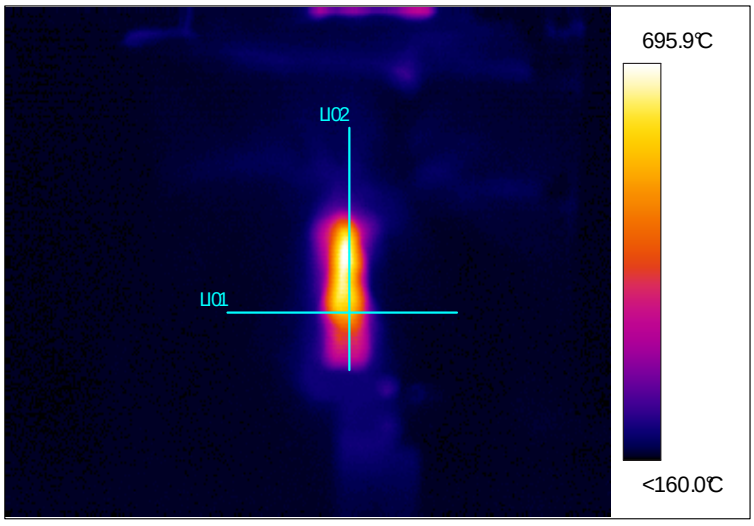

Figure 4.20: Image taken at 5 seconds for ϕ=1.8, fuel=2.5 LPM.

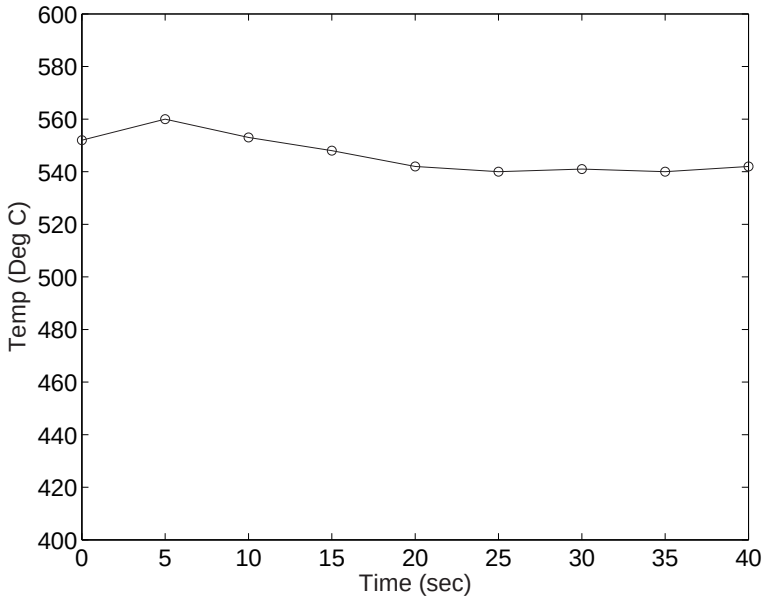

Figure 4.21: Max temperature at interface (L01) for ϕ=1.8, fuel=2.5 LPM with respect to time.

increasing the fuel flow rate. As is illustrated in Fig. (4.21) the maximum temperature first increases as the reaction releases more energy, but then decreases and levels off as the flame moves and then re-stabilizes further downstream. The time to re-establish equilibrium is actually less than indicated by this figure because we are measuring the temperature of the outside of the Kanthal®, not the temperature of the reaction. As a result there is a time delay associated with the thermal inertia of the Kanthal®.

Fig. (4.22) is the temperature profile along L102, the horizontal line along the interface. The vertical line on the left is the approximate termination of the insulation at the top of the slit and the vertical line on the right is the bottom of the slit. It can be seen that at 0 mm where L101 and L102 cross the temperature is higher at 5 seconds than at 40 seconds as was illustrated in Fig. (4.21). However, the point of maximum temperature remains constant at approximately 53 mm

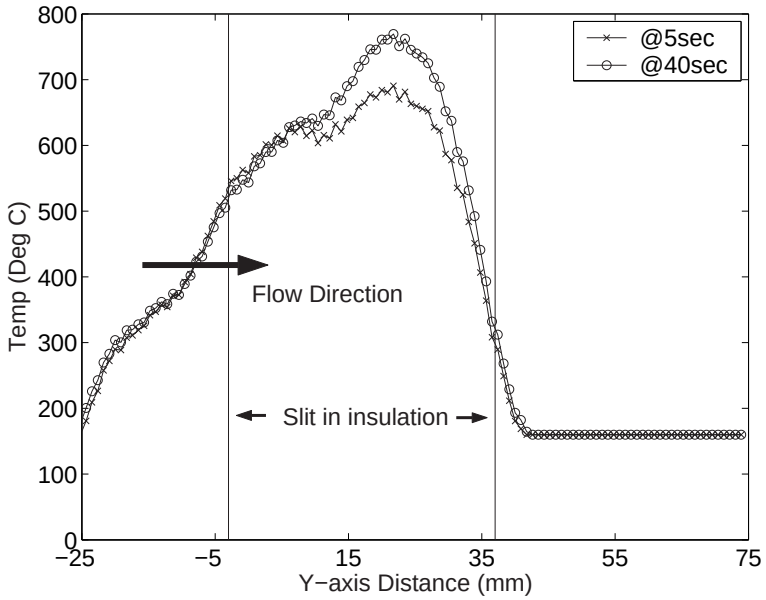

Figure 4.22: Temperature profile at 5 and 40 seconds for (L02) for ϕ=1.8, fuel=2.5 LPM along Y-axis.

making it impossible to determine the distance the reaction zone has moved.

A steep temperature gradient starting at -3 mm, where the slit begins, exists. This is the result of a large amount of energy being transported in the upstream direction and used to preheat the incoming mixture. Qualitatively these results agree with theoretical results of Diamantis et al. (2002) and experimental results from Drayton et al. (1998) and Zhdanok (2003). The sudden decrease in temperature at approximately 37 mm is where the hole in the insulation terminates.

4.4.1 Radiation Correction for R-Type Thermocouple

The thermocouple itself is very accurate, $\pm$ 1.5 °C from 0 to 600 °C and $\pm$ 0.0025·|t|°C from 600 to 1600 °C. However, a thermocouple measures the temperature of the thermocouple bead, which may vary from the actual temperature of the gas

stream at high temperatures where radiation losses and gains must be balanced with conduction and convection heat transfer. The following calculations assume: (1) no evaporation (i.e. the thermocouple is dry), (2) the thermocouple is isothermal, (3) the system is at equilibrium and (4) conduction losses along the thermocouple wire are negligible. A large thermal gradient between the thermocouple wire and bead did not exist as both were in a moving gas stream at approximately the same distance above the ceramic. To minimise conduction errors, the thermocouple leads exposed to the local temperature should be at least 10 times longer than the diameter of the wire (Murray, 1994), as it is in this case.

The thermocouple and its surroundings can be broken down into four main areas: (1) The burner surface, (2) the thermocouple bead, (3) the ambient environment and (4) the walls of the burner. This is illustrated in Fig. (4.23). The energy emitted by the burner and absorbed by the thermocouple bead is calculated by

$$Q_{12} = \sigma \varepsilon_1 A_1 F_{12} T_1^4 \alpha_2 \tag{4.1}$$

where σ is the Stefan-Boltzmann constant equal to 5.669x10^{-8} W/m^{2}K^4, ε_1 is the fraction of energy emitted by the burner, A_1 is the surface area of the burner, F_{12} is the fraction of energy emitted by the burner that strikes the thermocouple bead, T_1 is the temperature of the burner's surface and α_2 is the fraction of energy absorbed by the thermocouple bead.

All of the above variables can either be measured or looked up in reference books except for the shape factor, F_{12}, which must be calculated. The shape factor from the thermocouple bead to the other three surfaces must be unity since the thermocouple is completely surrounded by these three shapes. The shape factors can be calculated using the following formulas:

$$F_{2\to4} = \frac{2\pi RL}{2\pi RL + 2\pi R^2} \tag{4.2}$$

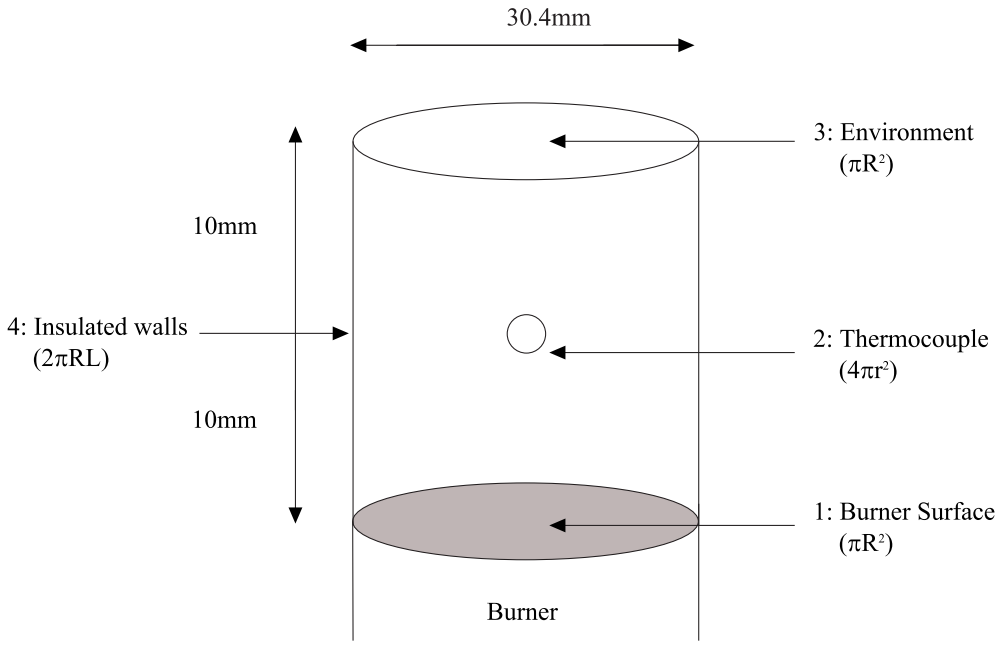

Figure 4.23: Location of thermocouple bead with respect to burner.

Through symmetry

$$F_{2\to1} = F_{2\to3} = \frac{1 - F_{2\to4}}{2} \tag{4.3}$$

Through reciprocity

$$F_{3\to2} = F_{1\to2} = \frac{A_2}{A_1} F_{2\to1} \tag{4.4}$$

$$F_{4\to2} = \frac{A_2}{A_4} F_{2\to4} \tag{4.5}$$

The Nusselt Number, (Nu), for forced convection flow past a sphere may be calculated using Eq. (C.6) which is valid for:

$3.5 < Re < 8 \times 10^4$

$0.7 < Pr < 380$

$$Nu = 2 + (0.4Re^{0.5} + 0.06Re^{0.67})Pr^{0.4} \tag{4.6}$$

where Re is defined as

$$Re = \frac{VD}{\nu}. \tag{4.7}$$

The convective heat transfer coefficient may be solved for using,

$$h = \frac{kNu}{D} \tag{4.8}$$

where k is the thermal conductivity of air and D is the diameter of the thermocouple bead.

Using the above equations the net energy absorbed by the thermocouple can be calculated. Eq. (4.9) can then be used to balance the energy absorbed from radiation to the energy removed by convection, hence calculating the actual temperature of the gas stream around the thermocouple.

Since conduction along the wire is assumed to be negligible, setting the energy due to radiation equal to the energy due to convection, the temperature of the gas can be solved for

$$Q_{rad} = Q_{conv}. \tag{4.9}$$

Tests conducted in section 4.4, Table (4.3) and Table (4.4) reveal that the surface temperature is generally between 1100-1300 K and the bead temperature (R1) approximately 200 K lower. This agrees with results from Diamantis et al. (2002) who calculated that the burner surface temperature should be less than 1500 K. The inside average surface temperature of the walls were estimated to be approximately half of the burner's surface temperature.

Fig. (4.24) illustrates the thermocouple error versus the temperature of the thermocouple bead. R1 generally read between 900-1100 K for tests presented in this paper, corresponding to a thermocouple reading 16-31 K lower than the actual flame temperature. In this configuration, the error due to radiation and

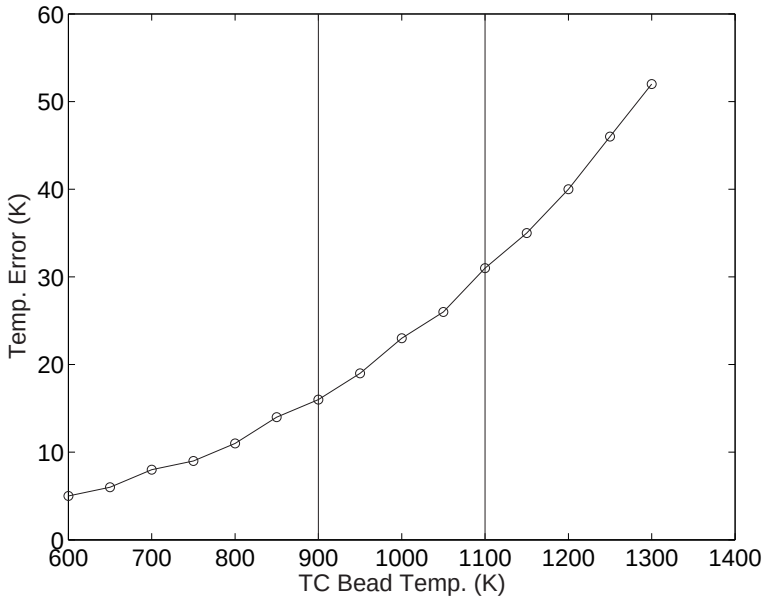

Figure 4.24: Thermocouple error due to radiation and convection.

convection is minimal. Therefore, temperature readings used throughout the remainder of this paper are the raw temperature readings not corrected for radiation and convection errors, unless specifically stated.

A more complicated calculation was performed on R2. This study is presented in Appendix D. It was determined that the gas temperature R2 was measuring could be up to 200 K higher than the temperature of the thermocouple bead at equivalence ratios close to one. As the equivalence ratio is increased the gas, ceramic beads and thermocouple temperatures converge.

4.5 Particulates

Due to the large amount of unburnt hydrocarbons and soot that can be formed during rich combustion, a scanning mobility particle sizer, SMPS, was used to measure the size and concentration of particles in the combustion products of

octane and methane, the latter as an example of a 'clean fuel'.

Fig. (4.25) plots the particle concentration versus particle size for unfiltered ambient lab air. Fig. (4.26) is a plot during start-up at an equivalence ratio of 0.8. The concentration of particles generated is higher than that found in the ambient air until the flame has propagated halfway into the first layer of porous media. As the flame approaches the interface and starts to stabilize, the soot present in the exhaust decreases below the amount found in the lab ambient air. It is not known at this point why more soot is produced for the propagating flame than the stationary flame. Once the flame reaches the interface it then switches from transient combustion to stationary combustion and generates very little soot. The fact that the burner is producing less soot than that found in the ambient air is a good indication that the burner combined with a clean fuel, methane, produces very little particulate matter. It also demonstrates the inertness and robustness of the Al_2O_3 beads as they are not degrading and producing particulates. The burner's exhaust contains less particulate matter than the ambient lab air as the burner is using filtered air from the lab's compressor as an oxidant, not the unfiltered lab air.

At steady state conditions for a $\phi = 1.5$ essentially no soot is produced, particulate concentration is considerably lower than in the ambient lab air, as is illustrated in Fig. (4.27). Three tests at the same operating conditions demonstrate the repeatability of the burner during steady state operation. Similar results were observed for a $\phi = 2.0$, Fig. (4.28) with approximately a 30 % increase in particulate concentration.

As the equivalence ratio is increased to 2.5 the amount of particulates produced substantially increases as can be seen in Fig. (4.29). Soot formation is most prominent at very low and high fuel flow rates. At low flow rates, 0.8 LPM, temperatures are not high enough to allow all the fuel to react, so unburnt fuel

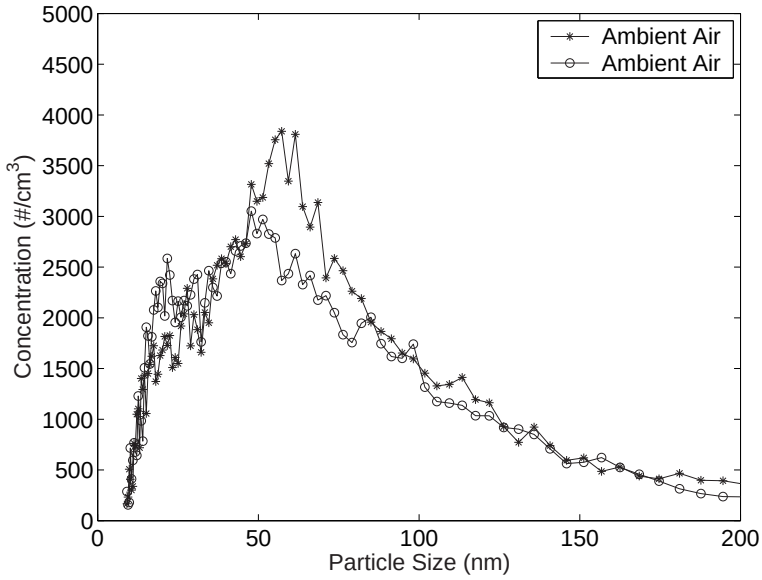

Figure 4.25: Particle number concentration versus size for unfiltered ambient lab air

and oxygen exist in the exhaust gases. This is explained in more detail in Section (5.3.1). As the fuel flow rate is increased to 4.5 LPM the flame starts to propagate upstream towards the burner's exit resulting in more soot.

During steady state operation methane combusted in a porous media burner produces very little particulate matter. The trend is for particulate concentration to increase with increasing ϕ. During transients when the flame front is propagating in either the upstream or the downstream direction (filtration) particulate concentration can increase by more than two orders of magnitude. This may be one advantage of stationary combustion in porous media compared to filtration combustion in porous media.

In order to determine the mass concentration of soot generated the particle's volume and effective density must be known. One such method to calculate the effective density has been described by Maricq and Xu (2004). They performed

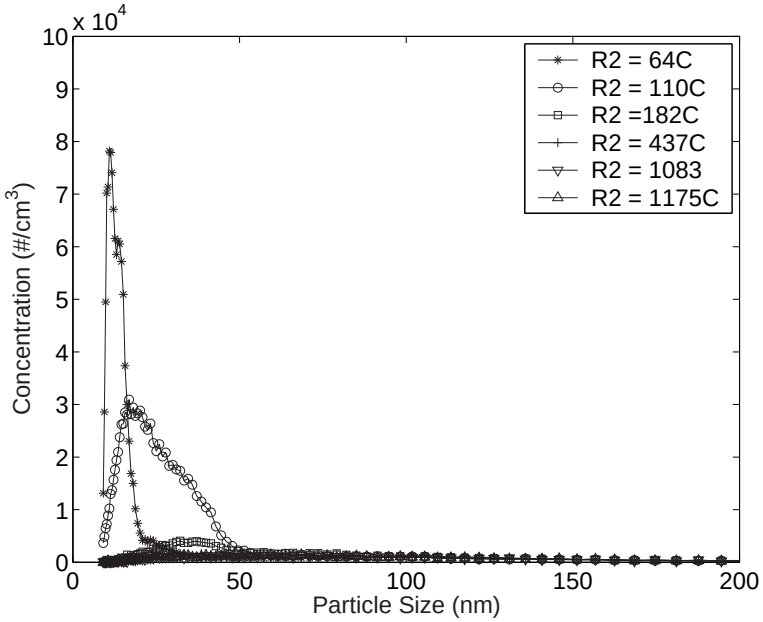

Figure 4.26: Particle number concentration versus size for methane at $\phi = 0.8$ during start-up. R2 is the temperature at the interface between the two different sizes of beads.

measurements to determine both a particle's mobility diameter and its aerodynamic diameter. The two measures of size are related via the particle effective density, which is defined as

$$\rho_e(d_m) = \frac{\rho_0 C_c(d_a) d_a^2}{C_c(d_m) d_m^2} \tag{4.10}$$

where $\rho_0 = 1$ g/cm^3, C_c is the Cunningham slip correction (Hinds, 1999), d_m and d_a denote mobility and aerodynamic diameter, respectively. Mobility diameter is the diameter of a sphere with the same aerodynamic drag as the particle. Mobility diameter gives no information about the particle's mass or density. The aerodynamic diameter, measured by impaction instruments, is the diameter of a sphere of unit density with the same mass.

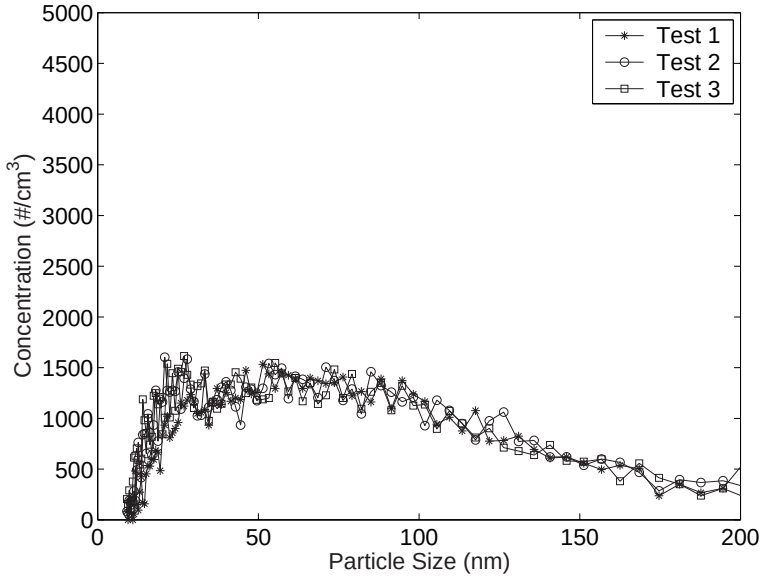

Figure 4.27: Particle number concentration versus size for methane during steady state operation at $\phi = 1.5$, fuel = 4.0 LPM

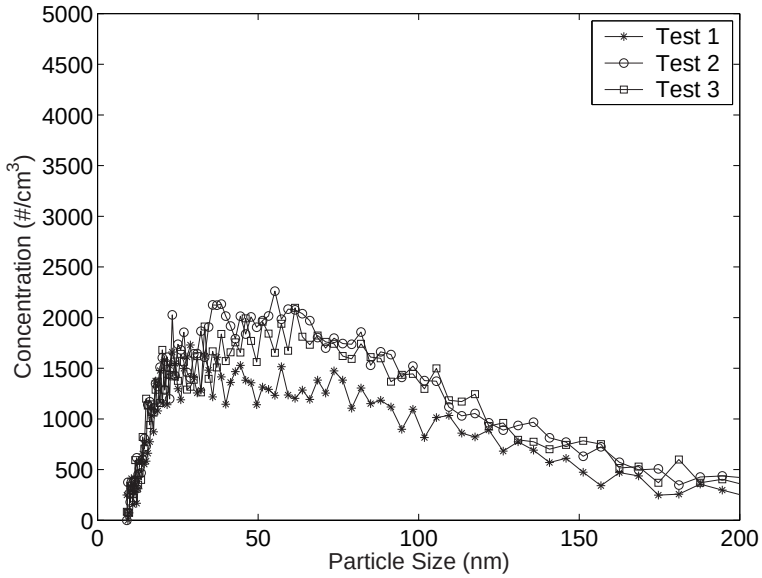

Figure 4.28: Particle number concentration versus size for methane during steady state operation at $\phi = 2.0$, fuel = 5.0 LPM.

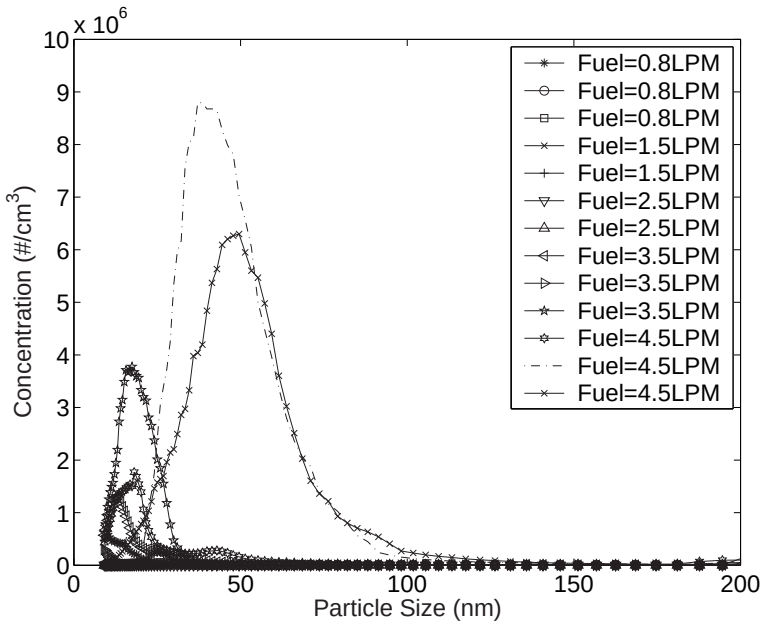

Figure 4.29: Particle number concentration versus size for methane at $\phi = 2.5$ for the fuel flow rates indicated with air adjusted accordingly.

In these tests they determined that soot, whether generated by a rich premixed ethylene flame or emitted by diesel or spark ignition engine, shows a characteristic steep decline in effective density as the particle's diameter increases. Specifically, tests of a premixed ethylene flame at a ϕ of 2.08, produced an effective density of 1.2 g/cm^3 at 30 nm and 0.3 g/cm^3 at 200 nm. Larger particles are an agglomerate of smaller particles, resulting in some void space and therefore a lower effective density. The principle observation from this study is the relative insensitivity of soot effective density to its source. Virtanen et al. (2002) and Virtanen et al. (2004) using a different measurement technique also found that the effective density of agglomerated particles decreases with increasing particle size. Furthermore, they determined that the type of fuel, they tested a low sulfur and a high sulfur content diesel fuel, had a minimal effect on particle density.

Using the above data for ethylene, an equation can be fit to the data, $\rho_e(d_m) = 15.39x^{-0.7252}$ where x is in nm and $\rho_e(d_m)$ is in g/cm^3, and used to calculate the density at different diameters. Maricq and Xu (2004) also took high resolution images of primary particles and determined an upper limit of 2 g/cm^3. In our calculations this maximum density is assumed for any particles smaller than 16 nm in diameter. Converting the x-axis to a mass concentration and summing the products of the x and y axis gives us the mass concentration in grams per cubic centimetre of exhaust gas (g/cm^3).

Table (4.5) tabulates the mass concentration at the different flow rates measured in Fig. (4.29). The mass concentration is converted to a mass flux by multiplying it by the velocity of the exhaust gases at the sampling location (R1). The general trend is for the soot mass concentration and mass flux to increase with flow rate. As presented in Section 4.4, higher mass flow rates correspond to higher temperatures. Higher temperatures will produce more radicals leading to an increase in soot nuclei (Tuovinen, 2002). The last three rows are particularly interesting as the mass flux increases by more than an order of magnitude from the first measurement taken at 4.5 LPM to the second and third measurements. At this flow rate and high ϕ we are at the edge of the operating envelope for methane and in the final two measurements the flame has transitioned to transient mode. The trend of increasing soot with flow rate is captured in Fig. (4.30). The exception to this trend, is the higher concentration of particulates at the lowest firing rate, when large amounts of unburnt fuel is present.

Plots of the number concentration of particles versus size at various equivalence ratios for iso-octane are illustrated in Fig. (4.31) and Fig. (4.32). At stoichiometric conditions the amount of particles detected is negligible, as would be expected since all the carbon is being oxidized. The overall trend, in agreement with the methane results, was for the particle number concentration and particle

Table 4.5: Mass concentration for methane soot experiments at $\phi = 2.5$

Fuel (ml/min)	Air (L/min)	ϕ	Mass Concentration (g/cm^3)	Mass Flux ($g/s \cdot cm^2$)
0.8	3.0	2.5	8.5×10^{-11}	9.2×10^{-10}
0.8	3.0	2.5	1.9×10^{-11}	2.1×10^{-10}
0.8	3.0	2.5	1.1×10^{-11}	1.2×10^{-10}
1.5	5.7	2.5	6.8×10^{-12}	1.3×10^{-10}
1.5	5.7	2.5	7.1×10^{-12}	1.3×10^{-10}
2.5	9.5	2.5	8.0×10^{-12}	2.6×10^{-10}
2.5	9.5	2.5	1.2×10^{-11}	4.0×10^{-10}
3.5	13.2	2.5	1.9×10^{-10}	9.5×10^{-9}
3.5	13.2	2.5	2.1×10^{-11}	1.0×10^{-9}
3.5	13.2	2.5	5.8×10^{-10}	2.9×10^{-8}
3.5	13.2	2.5	4.1×10^{-9}	2.0×10^{-7}
4.5	17.0	2.5	6.7×10^{-10}	4.4×10^{-8}
4.5	17.0	2.5	9.3×10^{-9}	6.1×10^{-7}
4.5	17.0	2.5	8.1×10^{-9}	5.3×10^{-7}

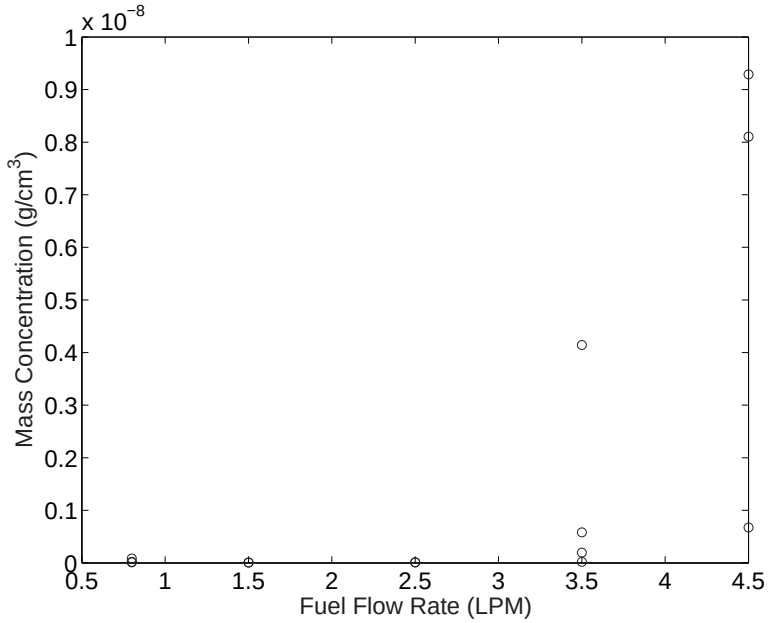

Figure 4.30: Mass concentration for methane soot experiments at $\phi = 2.5$ and increasing flow rates

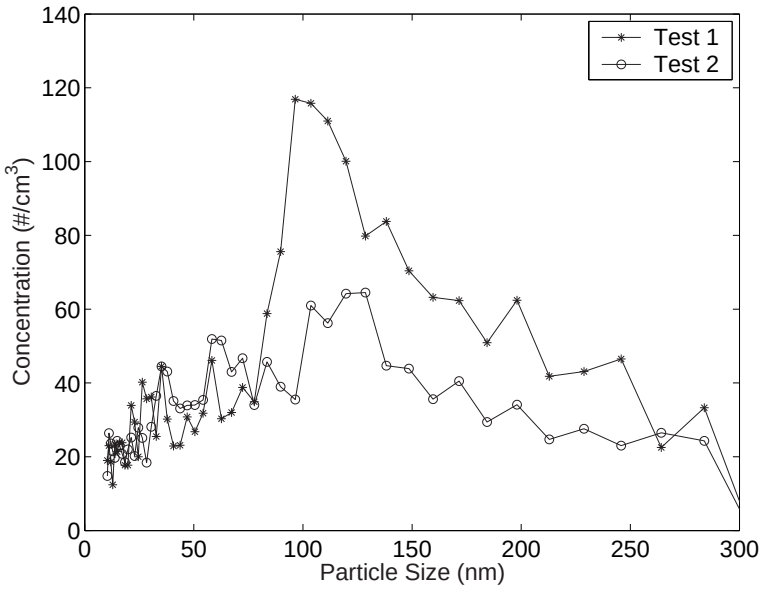

Figure 4.31: Particle number concentration versus size for octane at a ϕ of 1.0 in a foam burner.

size to increase with ϕ as the reaction moved further away from completion. However, at a ϕ of 2.0 the particle concentration detected was approximately twice as high as at a ϕ of 2.5. Converting this to a mass per unit volume and mass flux, using the same method as for the methane, revealed that more soot by mass was still being formed at a ϕ of 2.5. Mass concentration and mass flux of particles for the octane tests are tabulated in Table (4.6).

The mass flow rate of reactants at a ϕ of 1.5 and 2.5 are similar, while the mass flow rate of reactants at a ϕ of 2.0 is approximately 70 % higher. Although at a ϕ of 2.0 the particle concentration was higher than at a ϕ of 2.5, the mass flux of particles was essentially equal for the two tests. This test illustrates that by varying the residence time of the gases inside the combustion zone the particle concentration and particle size can be affected. Keeping ϕ constant and decreasing the mass flow rate, decreased the particle concentration but increased

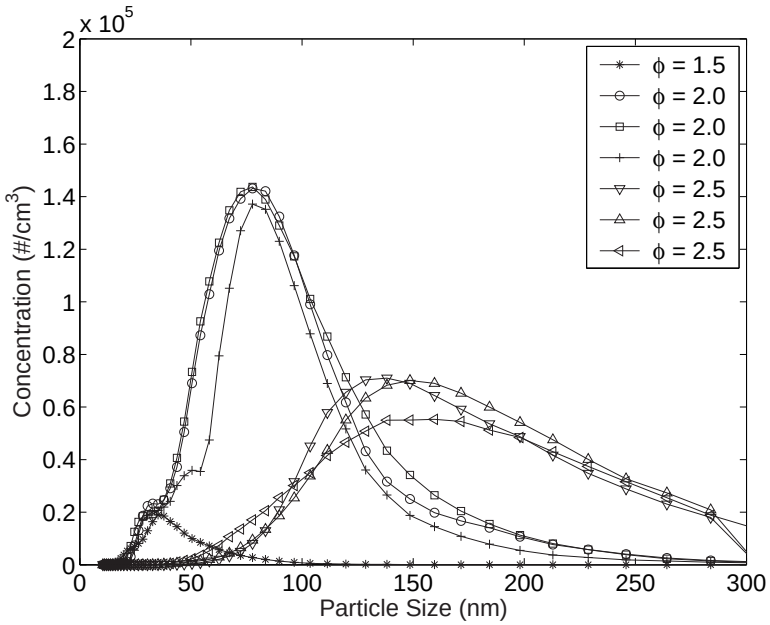

Figure 4.32: Particle number concentration versus size for octane at various ϕ in a foam burner.

Table 4.6: Mass concentration for octane soot experiments

Fuel (ml/min)	Air (L/min)	ϕ	Mass Concentration (g/cm^3)	Mass Flux ($g/s \cdot cm^2$)
1.25	10.0	1.0	1.0×10^{-12}	1.1×10^{-10}
1.25	10.0	1.0	6.6×10^{-13}	7.4×10^{-11}
1.25	6.6	1.5	9.9×10^{-12}	6.5×10^{-10}
1.75	7.0	2.0	4.4×10^{-10}	3.2×10^{-8}
1.75	7.0	2.0	4.8×10^{-10}	3.5×10^{-8}
1.75	7.0	2.0	3.4×10^{-10}	2.5×10^{-8}
1.25	4.0	2.5	7.6×10^{-10}	2.9×10^{-8}
1.25	4.0	2.5	8.1×10^{-10}	3.1×10^{-8}
1.25	4.0	2.5	8.4×10^{-10}	3.3×10^{-8}

the particle size.

In summary, during stationary operation, the mass flux of particulates at a $\phi = 2.5$ for octane is approximately an order of magnitude higher than that for methane. This is a conservative estimate as a ϕ of 2.5 for octane is well within the upper flammability limits, whereas for methane 2.5 is well outside its rich limit. However, once the methane flame transitions to transient mode it produces considerably more soot than a stationary flame for octane. This attests to the importance of operating the burner in its stationary mode to minimise particulate production. No tests were conducted for a transient octane flame.

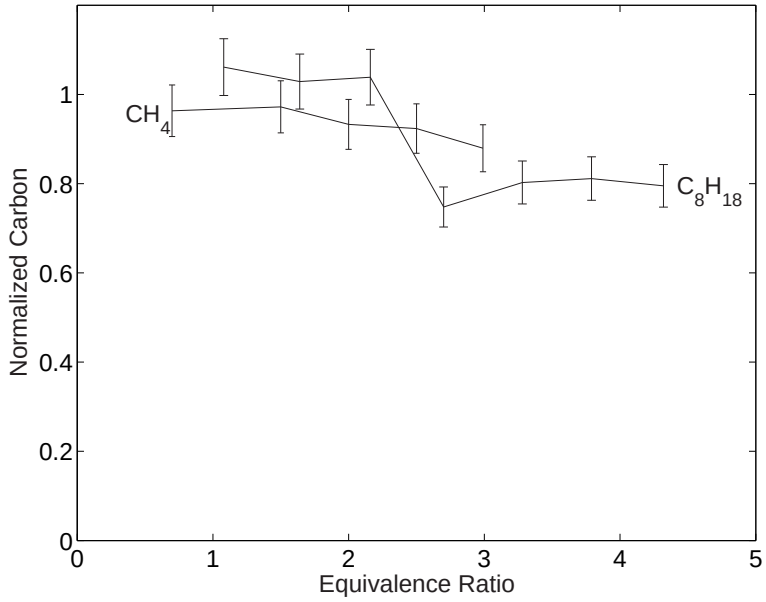

Figure 4.33: Carbon balance for CH_4 and C_8H_{18}. Performed using method presented Appendix D

4.6 Carbon Balance

Performing a carbon balance with the measured species reveals that at higher equivalence ratios not all the carbon is accounted for in the measured products. The carbon balance is performed in Appendix D. The results for CH_4 and C_8H_{18} are plotted in Fig. (4.33). A small percentage of carbon is unaccounted for in the product species measured by the GC for CH_4 at ϕ greater than 2. However, only about 80 % of the carbon in the product species for C_8H_{18} is accounted for for ϕ greater than 2.5.

To determine if some of this carbon is tied up in soot produced by the rich flame, the mass fluxes in Table 4.5 and Table 4.6 are converted to mass flow rates by multiplying by the burner's cross-sectional area. This reveals that in the worst case scenario, high flow rate and a propagating flame, only 2.3 $\times 10^{-4}$ kg

(230mg/kg of fuel)of soot per kg of CH_4 (230 mg/kg of fuel) is produced from the CH_4 flame. The octane flame produces 1.5×10^{-5} kg of soot per kg of C_8H_{18}. Although some soot accumulates inside the burner during rich C_8H_{18} combustion it is unlikely to be significantly more than the mass of the particulates in the exhaust. These numbers are insignificant, by three orders of magnitude, to account for the missing carbon. Therefore, at higher equivalence ratios the missing carbon must be tied up in higher hydrocarbons not measured by the GC.

4.7 Materials Durability

The combustion temperatures of PM burners can be made relatively low by burning lean in the warm-up cycle and rich during the operation cycle. However, temperatures are still high enough to cause rapid degradation to fine porous structures. The other mode of failure is from cracking due to thermal fatigue or thermal shock. Orenstein and Green (1992) examined the thermal shock characteristics of several open-cell ceramic foams by immersing heated specimens in oil and water at pre-quench temperatures up to 1500 °C. Thermal shock resistance was strongly dependant on pore size, increasing with increasing pore size.

The quartz burner proved to be very robust and showed no signs of degradation even after 100 plus hours of testing and over 200 complete thermal cycles, from ambient temperature to operating temperature with CH_3OH as the fuel. However, the quartz melted near the interface after a couple of hours of testing with CH_4. The adiabatic flame temperature for CH_3OH near its UFL (4.1) is 1000 K compared to 1800 K for CH_4 near it UFL (1.64).

Several burners made out of the same materials as the Al_2O_3 beads, Al_2O_3 were also tested with CH_4. Al_2O_3 has a much higher melting temperature than quartz and would expand and contract at a rate similar to the PM. However,

these burners failed due to thermal shock after several hours of testing. Although not attempted, placing the burner inside a stainless steel sleeve for mechanical strength may have increased the life expectancy for this burner.

The conical stainless steel burner, endured approximately 50 hours of testing without failing. However the inside of the burner, especially near the interface where the highest temperatures are present, experienced scaling and wall thinning.

The final burner material tested was made out of Kanthal® which as mentioned in Chapter 2 is a FeCrAlMo alloy, especially designed for high temperature operation. This burner showed no degradation after a total of several hundred hours of testing with all the fuels used in this thesis.

As can be seen from Fig. (4.34) the inside of the top piece of cordierite foam sustained the most damage, as would be expected since this is where the reaction is occurring. The axial surface is essentially intact suggesting that a large temperature gradient exists extending from the centre out towards the walls of the vessel. These test were carried out in the preliminary stages with a 30 mm I.D. quartz burner with insufficient insulation.

Cordierite failed due to its melting temperature being exceeded. Alumina foam with its higher operating point did not melt or charr, but still suffered serious damage. After about 20 hours of testing it became more difficult to stabilize the flame at the ceramic interface. When attempting to remove the foam from the burner it started to crumble Fig. (4.35). This can be explained by two mechanisms: (1) because its thermal coefficient of expansion is approximately ten times higher than that of quartz, stresses build up in the foam during expansion and contraction, and (2) sudden thermal gradients within the material due to ignition, cooling down periods, and changes in equivalence ratios can cause weakening or fracturing within the material. This is more pronounced in the alumina as it has

Top piece

Bottom piece

Figure 4.34: Damaged pieces of cordierite.

a lower thermal shock resistance than cordierite.

The solid alumina beads appeared to suffer no degradation even after 100 plus hours of testing. Unlike the foams, which were held rigidly in place, the beads were free to move around inside the quartz burner. As a result the same stresses caused by thermal cycles did not build up inside the beads making them considerably more robust.

However, it was observed that the desiccant beads would lose mass over time. After approximately 1100 minutes of testing and 26 thermal cycles, beads that had an initial diameter of between 3.5-4.0 mm had decreased in size to between 2.6-3.2 mm. The solid beads experienced no degradation after a similar amount of time in the burner.

The materials tested in these experiments are claimed to be inert by the manufacturers. At high temperatures and large surface areas, such as with the

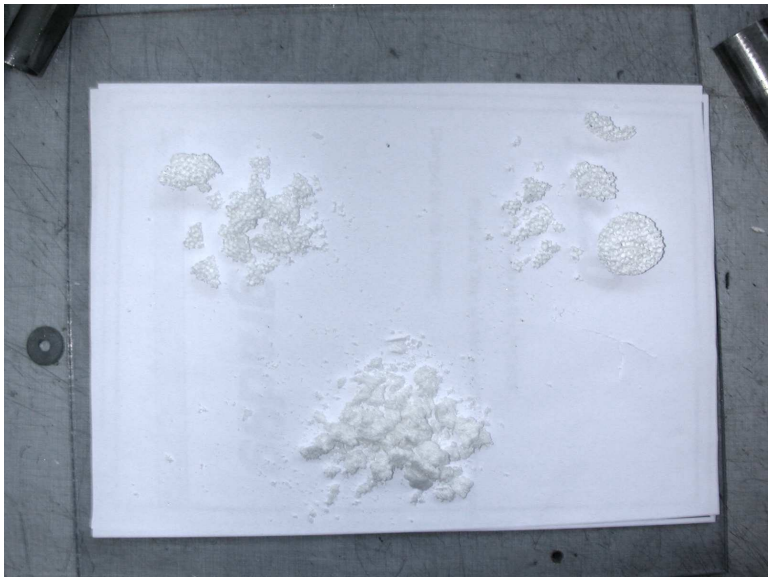

Figure 4.35: Damage to alumina.

desiccant beads, some catalytic activity may be present. However, no degradation in performance over time was observed for the experiments conducted. In general, catalytic activity would decrease with time especially when being used with the Jet-A kerosene as it contains some sulfur which is known to poison catalysts. Therefore, it is assumed that catalytic activity, if present at all, plays only a minimal role in these experiments.

It can be concluded that generally beads will have a longer operational lifetime than foams as they are less susceptible to thermal stresses. Furthermore, solid beads due to their higher structural integrity will degrade less than desiccant beads. It should be noted that the lifetime of the ceramic foams can be extended by selecting a burner material that has a similar thermal expansion rate and minimizing rapid changes in operating temperature.

4.8 Chapter Summary

The main observation from the preliminary tests were, firstly, the importance of sufficient insulation to minimize heat loss and increase flame stability and hence extend the upper flammability limits. Secondly, the large thermal mass of the PM burner allowed a flame to be re-ignited after a disruption in either oxidant or fuel by simply restoring the fuel and oxidant flows.

Steady rich flames of methane, methanol, ethanol, iso-octane, petrol, kerosene (Jet A) and biodiesel were stabilized at the interface between two differently sized pored ceramic foams or differently sized ceramic beads over a range of equivalence ratios. The UFL of methane, methanol, ethanol and Jet A were increased by combustion inside the porous media. At a minimum, the conventional rich flammability limits for octane was also reached. Since the free-flame UFL for biodiesel was unknown a meaningful comparison could not be made. A large operating envelope was also observed, making high turndown ratios possible.

An infrared imager was used to determine the surface temperature of the top layer of beads inside the burner. The burner's surface temperature will increase with increasing flow rates and is approximately 200 K higher than the thermocouple reading (R1) located 10 mm above the surface. A radiation/convection balance was done on the thermocouple bead and it was calculated that R1 underestimates the exhaust gases temperature by approximately 16-31 K.

No soot or carbon deposits were visible for methane, methanol, ethanol or kerosene. However, for octane, petrol and biodiesel soot was visible at higher equivalence ratios. In addition biodiesel left residual deposits around the entrance to the burner and exit of the vapourizer. Results from the SMPS, revealed that running on filtered lab air, CH_4 combusted inside the PM burner has fewer particulates than the ambient lab air up to an equivalence ratio of 2.0, under steady state conditions. At higher equivalence ratios and also during transients

the particulate count increases drastically. At a ϕ of 2.5 the mass concentration of particulates for C_8H_{18} is an order of magnitude greater than that for CH_4 at a ϕ of 2.5 during steady state combustion.

Finally, it can be concluded that beads will have a longer operational lifetime than foams as they are less susceptible to thermal stresses and solid beads will outlast desiccant beads. Quartz and stainless steel are adequate materials to manufacturer the burner from for lower temperatures. However, the best material, over a wide range of fuels, to manufacturer the burner from is Kanthal®.

Chapter 5

Product Composition

5.1 Structure of this Chapter

In this chapter, we present measurements of the major product species, H_2, CO, CO_2, N_2 and the minor product species, CH_4, C_2H_2, C_2H_4, C_2H_6, O_2 present in the syngas. Methane, the major constituent of natural gas, is tested as are methanol, neat ethanol, ethanol mixed with water and biodiesel, all of which can be considered sustainable fuels. In addition, kerosene (Jet-A) aviation fuel, iso-octane and petrol are also tested as they are two of the main fuels used in today's transport sector. All of these results except for biodiesel are compared with equilibrium predictions using the code described in the next section.

5.2 Equilibrium Calculation

The species concentrations discussed in this chapter are compared to NASA's well-established equilibrium calculation code, CEA. Zeleznik and Gordon (1968), Svehla and McBride (1973), Gordon and McBride (1994), McBride and Gordon (1996) and Gordon and McBride (1999) have made great strides in developing

methods and computer programs to solve for the final chemical equilibrium compositions, as well as thermodynamic and transport properties of mixtures. The latest version, used in this thesis, is called CEAII (Chemical Equilibrium and Application II) by McBride and Gordon (1996) in 1996 and updated in 2002 by McBride et al. (2002).

The code is based upon the free-energy minimization formulation. The effects of chemical kinetics or finite reaction rates are not considered. Thermodynamic data for more than 2 000 chemical species (including gases, liquids, solids and ions) are provided with the program for a temperature range of 300 to 5000 K. This data originates form the JANAF Thermochemical Tables (Chase et al., 1985) and from data generated at NASA Lewis Research Center. More information about the program is available from $http://www.grc.nasa.gov/WWW/CEAWeb$.

5.3 Steady State Species Concentrations

5.3.1 Methane

Fig. 5.1 plots the adiabatic flame temperature of methane, calculated by the equilibrium code CEA, at various ϕ against the temperature at the burner's exit (R1) and the maximum temperature at the interface (R2). It is evident that for equivalence ratios greater than 1.5 superadiabatic combustion is occurring. The temperature at the exit of the burner is also considerably lower than the temperature at the interface as the product species lose heat to the porous matrix as they traverse downstream from the reaction. Drayton et al. (1998) also observed similar superadiabatic temperatures for ultra-rich and ultra-lean operation inside their filtration combustion burner.

As illustrated in Fig. (5.2), up to an equivalence ratio of 2.0 the experimental results follow equilibrium predictions quite well with both H_2 and CO increasing

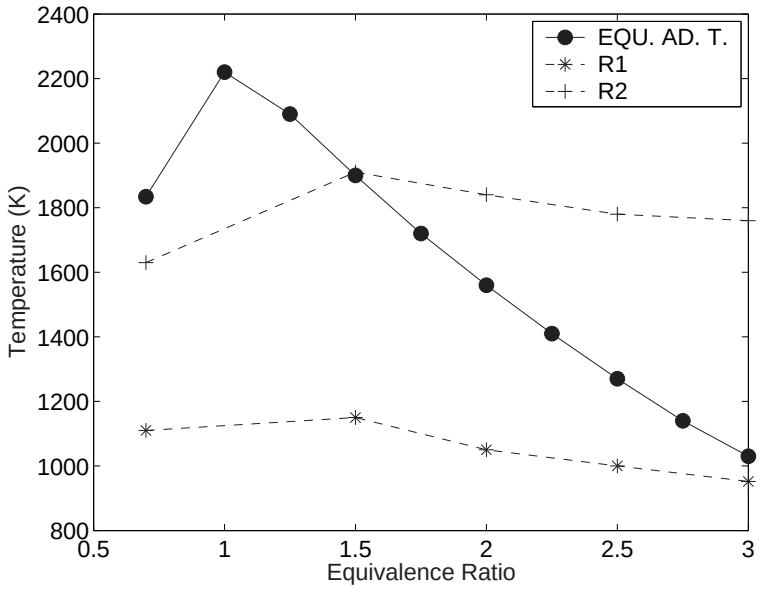

Figure 5.1: Calculated adiabatic methane temperatures and temperatures achieved in burner filled with 20 mm of 2-3 mm and 80 mm of 6-7 mm Al_2O_3 beads

while CO_2 decreases. Up to a ϕ of 2.0, 100 % of the methane was consumed. At ϕ greater than 2.0, some methane was present in the products, but no other hydrocarbons were detected. At $\phi > 2.5$, the products had moved away from equilibrium. As the H_2 and CO concentration dropped off considerably, CH_4 concentration increased.

Fig. (5.3) illustrates that at $\phi = 2.0$, as the mass flow rate is increased the reaction moves closer to equilibrium. At a ϕ of 2.5 the result is similar, except the reaction never completely reaches equilibrium as the flame blows off prior to attaining equilibrium, see Fig. (5.4). CH_4 and CO_2 initially increase with mass flow rate for both $\phi = 2.0$ and $\phi = 2.5$ before starting to decrease. Comparing this to Fig. (5.5) where major equilibrium product species are plotted against temperature, CH_4 and H_2 never increase together, demonstrating that the prod-

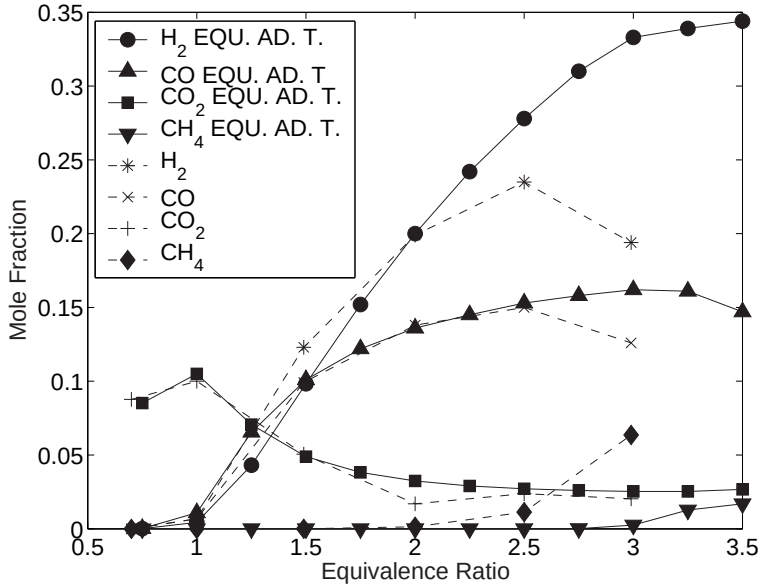

Figure 5.2: Equilibrium species concentrations for methane compared to experimental results from the 50 mm burner filled with 20 mm of 2-3mm and 80 mm of 3-3.5 mm desiccant Al_2O_3 beads at various ϕ.

ucts are not at chemical equilibrium. However, at a higher mass flow rate of 3.0 $\times 10^{-4}$ kg/s at a $\phi = 2.5$, changing the probe height above the burner does not change the concentration of product species, indicating that at this higher flow rate the products have reached chemical equilibrium, albeit at a temperature less than the adiabatic temperature.

At low flow rates a large percentage of the methane and oxidant does not participate in the reaction. Figs. (4.12)-(4.15) illustrate that a temperature gradient exists near the walls of the burner, the temperature near the walls at the burner's surface is significantly lower for the lower firing rates. This lower temperature combined with quenching on the walls of the burner allows CH_4 penetration and prevents the products from reaching equilibrium resulting in a lower H_2 yield for the lower mass flow rates.

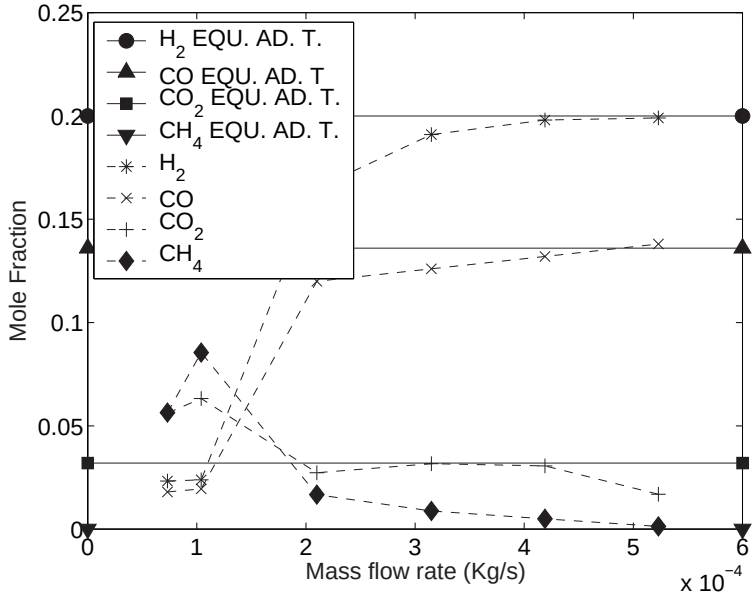

Figure 5.3: Equilibrium species concentrations for methane compared to experimental results from the 50 mm burner filled with 20 mm of 2-3 mm and 80 mm of 3-3.5 mm desiccant Al_2O_3 beads at a ϕ of 2.0.

As the flow rate is increased the temperature of the burner becomes higher and the reaction moves towards equilibrium. The higher burner surface temperatures are tabulated in Table (4.3) for a ϕ of 2.5. The average temperature of the surface beads increases from 887 °C to 1015 °C and the minimum temperature increased from 799 °C to 927 °C. The minimum temperature is actually lower than 799 °C as the circle the temperatures were extracted from does not extend completely to the burner's walls.

In an effort to understand the generation of hydrocarbons observed in the products, equilibrium calculations were performed at various temperatures. As illustrated in Fig. 5.5, CH_4 is only generated at temperatures less than 1000 K along with an increase in H_2O and a corresponding decrease in H_2 and CO. This change in product species can be attributed to the reverse steam reforming reac-

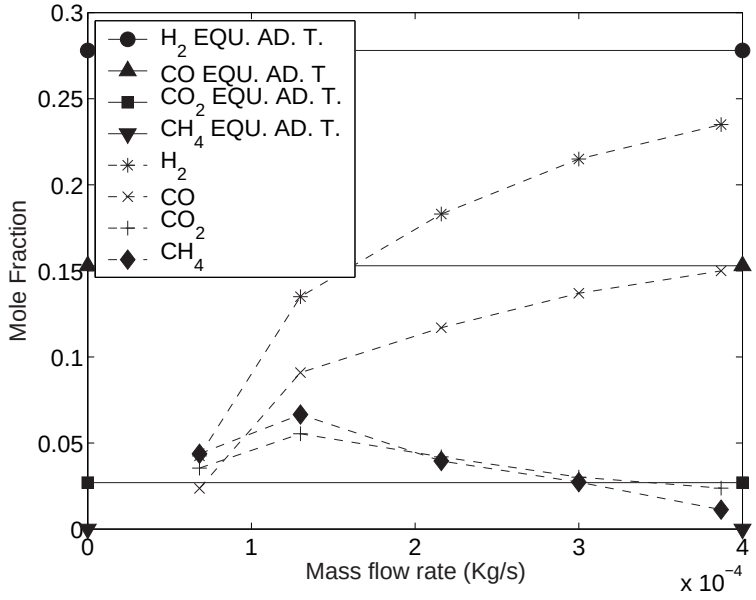

Figure 5.4: Equilibrium species concentrations for methane compared to experimental results as a function of the flow rate from the 50mm burner filled with 20 mm of 2-3 mm and 80 mm of 3-3.5 mm desiccant Al_2O_3 beads at a ϕ of 2.5.

tion $CH_4 + H_2O \leftrightarrow CO + 3H_2$ becoming important. However, during these tests the products' temperature remained considerably above this critical temperature. Hence, the significant CH_4 concentrations measured at lower mass flow rates are due to finite rate kinetic effects or quenching at the walls, rather than the reverse steam reforming reaction.

Various studies have shown that the conversion of CH_4 to H_2 occurs in two stages: initially a fast partial oxidation process that accounts for most of the H_2, followed by a slower steam reforming process. The initial process is exothermic and supplies the heat required to drive the second, endothermic, reaction (Dhamrat and Ellzey, To appear; Drayton et al., 1998; Naidja et al., 2003).

In order to determine if there is an optimal length of burner for the steam reforming reaction, the height where the sample was extracted from the burner

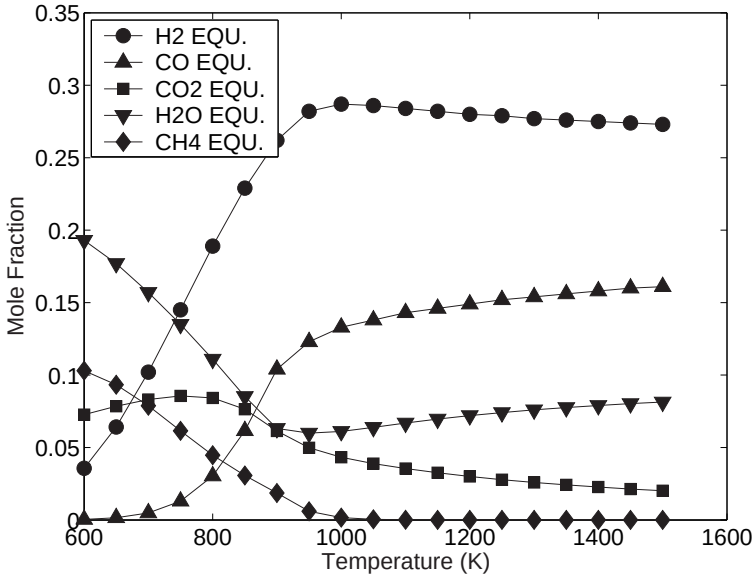

Figure 5.5: Calculated equilibrium product species (dry) for methane at various temperatures at $\phi = 2.5$ and inlet air/fuel at 293.15 K.

was varied. Changing the height of the sample probe above the burner, at a ϕ of 2.5, did not produce any discernable trends in the products' concentrations, indicating that the reaction had reached steady state. The major product species for varying heights are illustrated in Fig. (5.6). The surface of the burner is at +70 mm and the interface between the two bead layers is at 0 mm. It appears that both the partial oxidation and steam reforming reaction reach equilibrium in 20 mm. In the first 10 mm, -5 to +5 mm, the methane starts to be converted into syngas. The bulk of the fuel is converted in the next 10 mm, +5 to +15 mm. At -5 mm all the fuel is still present, however at +5mm the fuel present has decreased from 20.0 % to 15.8 % and 7.7 % O_2 is still present from an initial 16.6%. After this point no O_2 is present until the probe is 10 mm above the surface (+80 mm), at this point 8.3 $\times 10^{-2}$ % becomes entrained in the exhaust gases from the surrounding air.

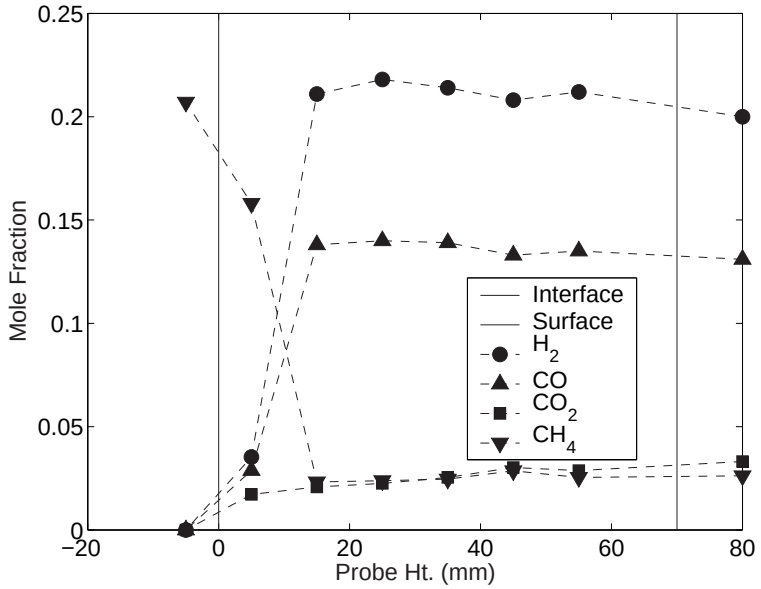

Figure 5.6: Species concentrations from a methane flame inside the 52.5 mm burner consisting of 30 mm of 2-3 mm and 70 mm of 3.5-4.0 mm desiccant beads. Sampling probe height varied from 10 mm above the surface to 5 mm below the interface. All measurements taken at $\phi = 2.5$, $\dot{m}_{fuel} = 3.0 \times 10^{-4}$ kg/s.

Computational results from Fay et al. (2005) indicate that the steam reforming reaction plays a much more significant role in H_2 production than the water-gas shift reaction. However, with additional H_2O injected into the system it may be possible to drive this reaction forward producing more H_2 and oxidizing some of the CO to CO_2 (generally the water-gas shift reaction is performed in the presence of a catalyst). Although not tested, a third and fourth layer of catalysed beads could be added to the burner to drive the steam reforming and water-gas shift reactions in the presence of steam.

In order to determine if simple steam addition in the presence of inert beads would drive these reactions forward, several tests were carried out using burner configurations illustrated in Fig. (5.7) and Fig. (5.8). In these configurations,

steam was either injected with the fuel, Fig. (5.7), or 70 mm above the interface, Fig. (5.8). The steam was produced by vapourizing water in the spiral vapourizer presented in Section 2.2.1. In both instances 100 mm of 4.6-5.0 mm non-catalytic Al_2O_3 beads were used as the porous medium. The amount of steam injected was varied from 0.9 to 1.4 moles of H_2O per mole of CH_4.

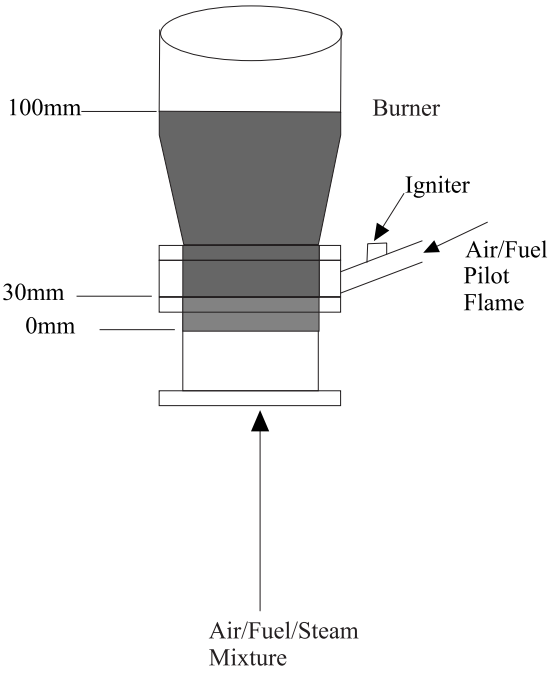

Figure 5.7: H_2O injected with the fuel and air mixture.

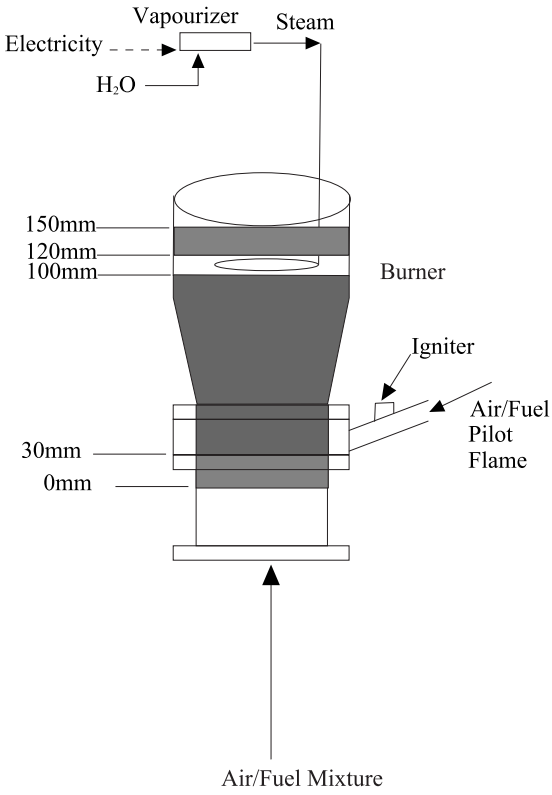

Figure 5.8: Steam injected 70 mm above the interface.

The results from these experiments are illustrated in Fig. (5.9). There was no apparent benefit to steam addition as both H_2 and CO production decreased with steam addition. Peak temperatures decreased by approximately 200 K for the steam addition experiments. These lower temperatures resulted in slower kinetics impeding the amount of H_2 produced. For these tests steam addition in

the presence of non-catalytic beads did not enhance H_2 production.

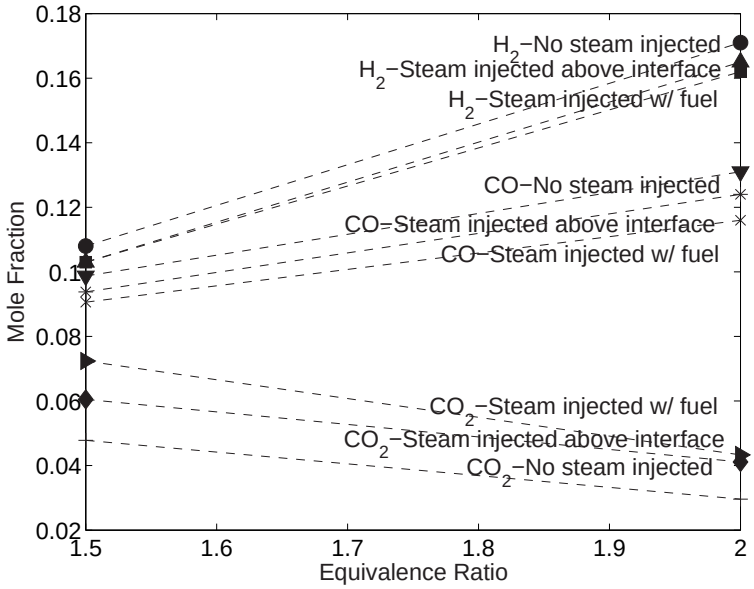

Figure 5.9: Experimental methane results with steam injected 70 mm above the interface or injected with the fuel into the 50 mm burner, 30 mm of 2-3 mm desiccant beads and 100 mm of 4.6-5.0 solid Al_2O_3 beads.

Numerical results complied by Drayton et al. (1998) reveal that the steam reforming reaction is very temperature sensitive. At temperatures of 1200 °C to 1300 °C reaction times are on the order of 10^2 seconds compared to 10^{-1} seconds at 1600 °C. The steam addition in our experiments had the effect of lowering the temperatures to under 1300 °C for all tests. At this temperature the residence time of the reactants inside the burner is insufficient (< 1 sec) to drive the steam reforming reaction forward. Although not tested, the opportunity still exists to use the excess heat downstream of the reaction in conjunction with catalysed beads to drive these reactions forward.

Fig. (5.10), (5.11) and (5.12) compare species concentrations from 50 mm burners comprising 80 mm of 4.6-5.0 mm, 6.0-7.0 mm and 7.5-9.0 mm diameter

solid Al_2O_3 beads, respectively, to the equilibrium code. Similar to previous tests, the product species concentrations followed the equilibrium predictions up to a ϕ of 2.0 or 2.5 before starting to diverge. Similar tests performed with SiC foam revealed a much narrower operating range out to a ϕ of 2.0. A test at a ϕ of 2.0 at different mass flow rates revealed that the trend of higher H_2 production at higher flow rates as observed with the beads holds true for the foams as well. Fig. (5.13) illustrates this data.

Fig. (5.14) summarizes the results for H_2 production from the previous four figures and compares these results to the desiccant bead burner. The highest amount of hydrogen produced was when the desiccant beads where used as the porous media, the lowest when the silicon carbide foam was used as the porous media. The temperature of the exhaust gases at the point of extraction, 10 mm above the top layer of porous media, was approximately 200 K lower for the foam burner at the same operating conditions as the bead burner. Although not shown on this plot, the desiccant beads also had the largest operating envelope and the silicon carbide foam the narrowest. It is speculated that the desiccant beads, with their large porous surface area, result in better heat transfer between the solid and gas, which increases the superadiabatic effect and hence fuel conversion. However, in these tests it is difficult to make a direct comparison between the beads and foams as the two materials themselves are different. The beads are alumina and the foams are silicon carbide. Direct comparisons between beads and foams of the same material are performed in the next section with CH_3OH as the fuel.

In contrast, Fay et al. (2005) observed higher mole fractions of H_2 from a burner filled with 3.9 PPC reticulated yttria stabilized zirconia (YZA) compared to an Al_2O_3 packed bead burner. In these experiments the burner was operated in filtration combustion mode, not in stationary mode. They explained the

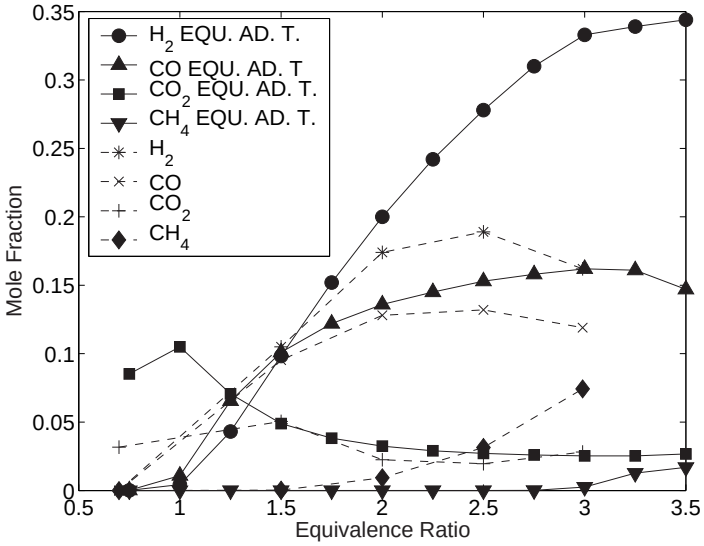

Figure 5.10: Equilibrium species concentrations for methane compared to experimental results from the 50 mm burner filled with 20 mm of 2-3 mm of desiccant beads and 80 mm of 4.6-5.0 mm solid Al_2O_3 beads at various ϕ.

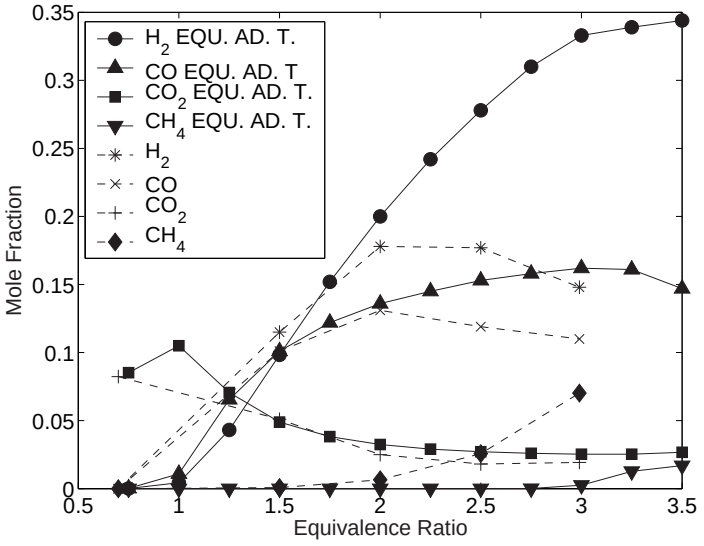

Figure 5.11: Equilibrium species concentrations for methane compared to experimental results from the 50 mm burner filled with 20 mm of 2-3 mm od desiccant beads and 80 mm of 6-7 mm solid Al_2O_3 beads at various ϕ.

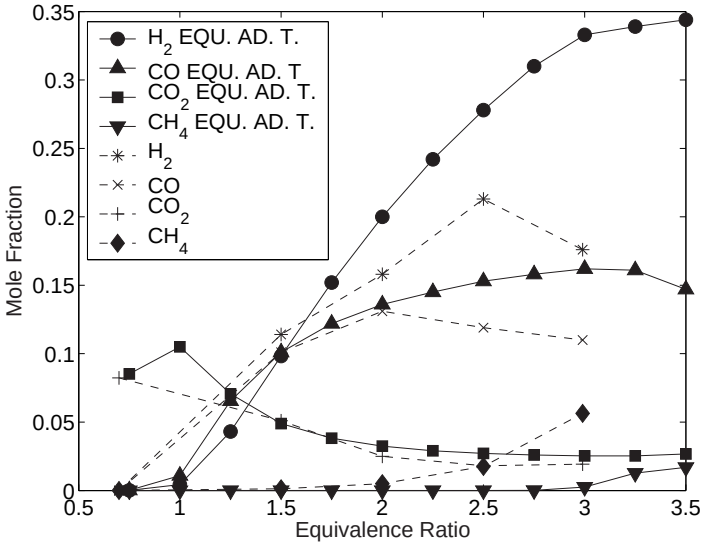

Figure 5.12: Equilibrium species concentrations for methane compared to experimental results from the 50 mm burner filled with 20 mm of 2-3 mm of desiccant beads and 80 mm of 7.5-9 mm solid Al_2O_3 beads at various ϕ.

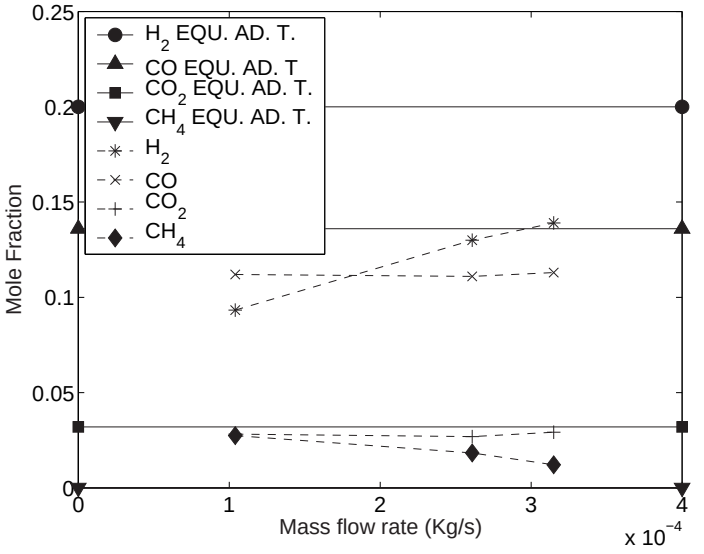

Figure 5.13: Equilibrium species concentrations for methane compared to experimental results from the 50 mm burner, 20 mm of SiC foam (24 pores/cm) and 100 mm of SiC foam (4.8 pores/cm) at a ϕ of 2.0.

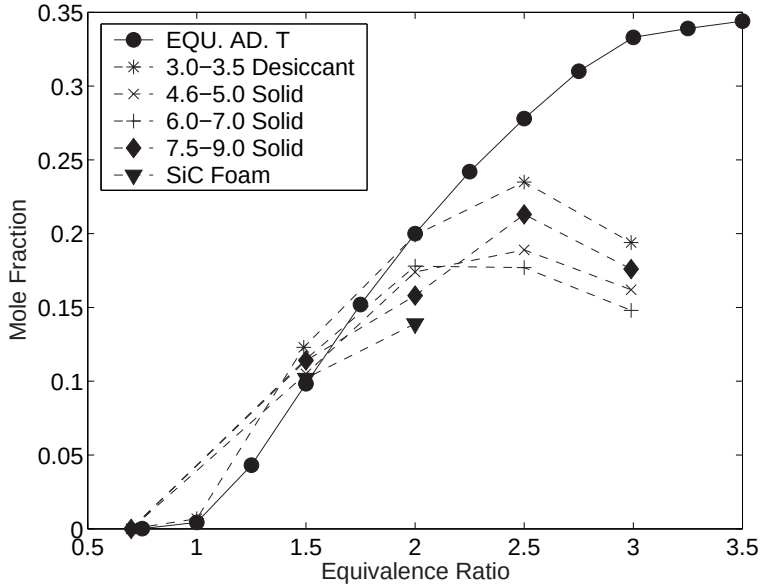

Figure 5.14: Comparison of hydrogen concentrations from the 50 mm burners tested above.

better performance of the foams on temperatures approximately 100 K higher in the YZA burner, particularly in the reaction zone where the steam reforming reaction is prevalent. One explanation may be that they were comparing the two burners at equal interstitial velocities, since the foam has a higher porosity, equal interstitial velocities equate to a higher mass flow rate (approximately twice as high) for the foam burner compared to the bead burner. In our tests we observed higher conversions at higher mass flow rates. However, it is difficult to make an exact comparison as we used a silicon carbide foam while they used a YZA foam.

Yoshizawa et al. (1988) analytically showed that the temperature profiles and burning velocities were highly dependant on the radiative properties of the porous matrix. According to their model, the absorption coefficient is the single most important property governing the flame's behaviour. An increase in the surface area per unit volume increases the absorption coefficient which increases

the interphase heat transfer. This helps explain the larger extension of the rich flammability limit observed with the desiccant beads versus the solid beads. However, it should be noted that in Diamantis et al. (2002) model conduction plays a major role in preheating the incoming gases and on the flames behaviour. In general, foams should have a higher thermal conductivity than beads due to the solid material bridges between the pores, whereas spherical beads only have a point contact between adjacent beads.

5.3.2 Methanol

Fig. 5.15 compares the adiabatic flame temperature of methanol, calculated by the equilibrium code CEA, with the temperature of the measured products. It is evident that the products are below the adiabatic temperature, especially at low ϕ. This is attributed to higher radiation heat losses from the burner at low ϕ. It is also probable that superadiabatic temperatures have been reached for both burners at a ϕ of 4.0, since at the point of measurement the products have already lost some heat to their surroundings and still have temperatures higher than the adiabatic flame temperature.

Fig. (5.16) and Fig. (5.17) show that up to an equivalence ratio of 3.0, in the foam burner, and approximately 6.0 in the bead burner, the mole fraction of hydrogen increases with increasing equivalence ratio while the mole fraction of carbon dioxide decreases, in agreement with the equilibrium calculations. No hydrocarbons were measured in the products at equivalence ratios less than 2.5. Changing the height of the sampling probe above the ceramic, at a ϕ of 2.5, did not result in any significant change in the product species or produce any discernable trends. This is a good indication that the products have reached chemical equilibrium by the time they exit the ceramic. However, it appears that at higher equivalence ratios the reaction has moved away from equilibrium (e.g.

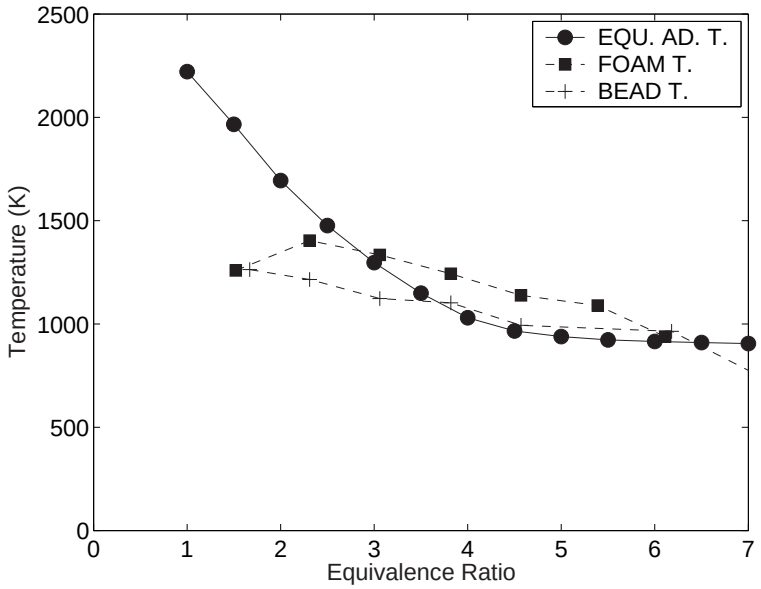

Figure 5.15: Calculated adiabatic methanol flame temperature compared to product temperature measured at burner exit. $\dot{m}_{fuel}$ was 4.6×10^{-2} g/s for all ϕ, except at ϕ=4.0 for the foam burner and at ϕ=6.5 for the bead burner where $\dot{m}_{fuel}$ was 3.6×10^{-5} kg/s.

Fig. 5.16 for H_2 and Fig. 5.17 for CO and CO_2). At a ϕ of 8, the largest mole fraction of hydrocarbons detected was methane, 0.6 %, with minute amounts of other hydrocarbons, not enough to account for the low (relative to equilibrium calculations) concentration of hydrogen measured.

It is assumed that the missing H_2 is tied up in either H_2O or CH_3OH. The nafion drier removes both H_2O and CH_3OH, which are polar molecules, prior to the gases being measured in the GC. Un-reacted fuel in the exhaust products at ultra high equivalence ratios would agree with CH_4 results, where significant quantities of un-reacted CH_4 was also detected at very high ϕ. It is speculated that this is a result of lower overall temperatures, especially near the walls resulting in quenching of the reaction and unburnt fuel penetrating into the exhaust

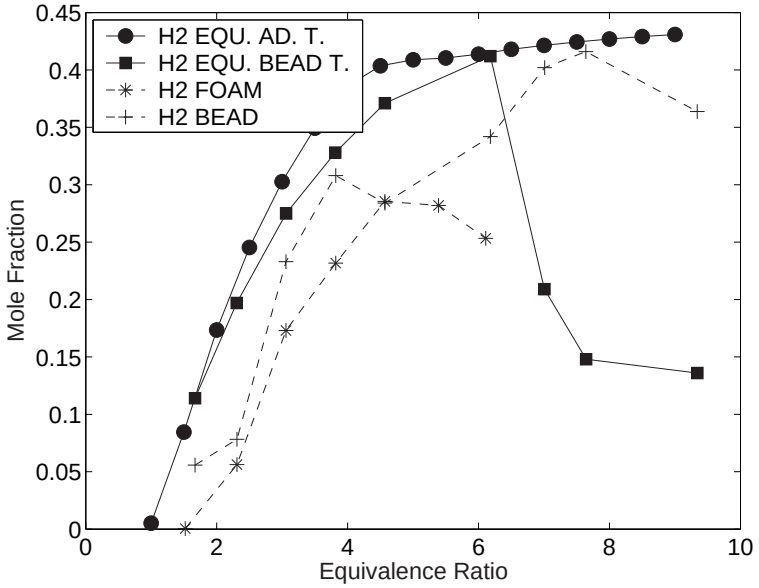

Figure 5.16: Equilibrium H_2 species concentrations for methanol compared to experimental results in the 30 mm burner. The black circles depict the H_2 mole fraction calculated at the adiabatic flame temperature, while the black squares depict the H_2 mole fraction calculated at the temperature measured by the R-type thermocouple. $\dot{m}_{fuel}$ was 4.6×10^{-5} kg/s for all ϕ, except at ϕ=4.0 for the foam burner and at ϕ=6.5 for the bead burner where $\dot{m}_{fuel}$ was 3.6×10^{-5} kg/s.

gases. This conjecture is consistent with the lower temperature measured close to the walls, Figs. (4.8 - 4.11).

In order to explore the deviation from equilibrium at very rich equivalence ratios, the CEA code was run with a set temperature equal to the measured one. The H_2 concentration thus calculated is also plotted in Fig. (5.16), revealing that the measured composition lies between the two equilibrium calculations. This implies that the products in our tests could be at a chemical equilibrium, just at a temperature lower than the adiabatic temperature. Changing the probe's height above the burner at low equivalence ratios had no effect, however at higher

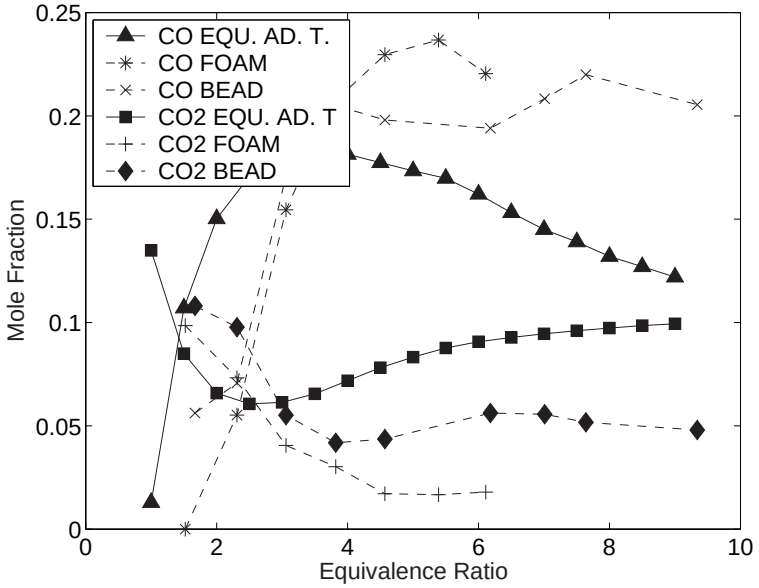

Figure 5.17: Equilibrium CO and CO_2 species concentrations for methanol compared to experimental results in the 30 mm burner. $\dot{m}_{fuel}$ was 4.6×10^{-5} kg/s for all ϕ, except at ϕ=4.0 for the foam burner and at ϕ=6.5 for the bead burner where $\dot{m}_{fuel}$ was 3.6×10^{-5} kg/s.

ϕ the species concentrations changed slightly indicating that chemical equilibrium had not been reached. At lower equivalence ratios, the high temperatures imply that equilibrium conditions are reached quicker, while the flames at very rich ϕ are probably influenced by the fact that residence times are not long enough to attain equilibrium.

Running the equilibrium code at ultra high ϕ over a wide range of temperatures produced no CH_3OH in the product species, but at lower temperatures some of the fuel was converted to CH_4, as illustrated in Fig. (5.18). The presence of small amounts of hydrocarbons observed in methanol flames is consistent with equilibrium expectations. The equilibrium composition of methanol products at $\phi = 3.0$ shows an increase in H_2O and CH_4 mole fractions at temper-

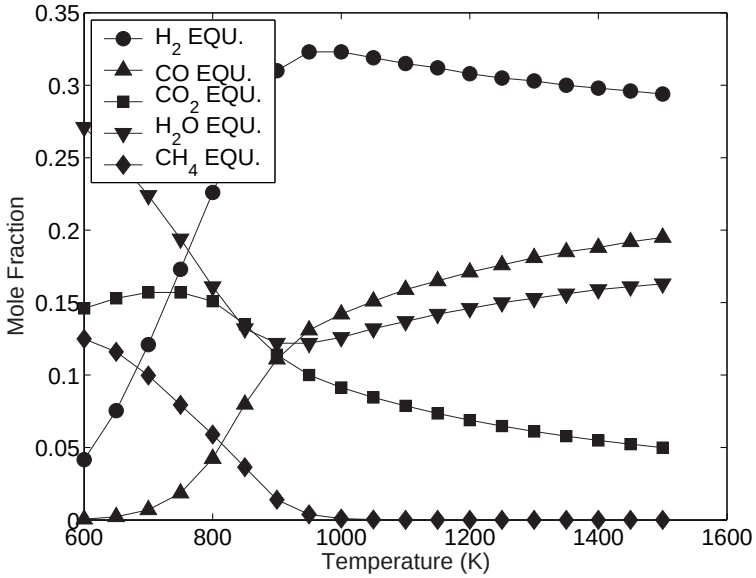

Figure 5.18: Calculated equilibrium product species (dry) for methanol at various temperatures at $\phi = 3.0$, inlet Air/fuel at 353.15 K.

ature below 950 K with a corresponding decrease in CO and H_2. This change in product species can be attributed to the reverse steam reforming reaction $CH_4 + H_2O \leftrightarrow CO + 3H_2$ becoming important.

The measured temperatures of the products for the range of operation of the foam burner was always above this critical temperature and minimum methane was measured. For $\phi > 6.5$ the bead burner products could fall below 950 K and small amounts of methane were indeed detected. Fig. (5.18) suggests that to maximize the H_2 yield the product temperatures should not drop below 950 K.

5.3.3 Ethanol

Neat ethanol, 90 % ethanol/ 10 % H_2O and 67 % ethanol/ 33 % H_2O (by volume) were combusted in the 52.5 mm Kanthal® burner. Ethanol diluted with H_2O was also tested as it is considerably more economical than anhydrous ethanol.

The burner consisted of 20 mm of 2-3 mm Al_2O_3 desiccant beads as the support layer and 80 mm of 3-3.5 mm Al_2O_3 desiccant beads acting as the combustion layer.

In Fig. (5.19) it can be seen that the products start to deviate from the equilibrium results at ϕ of 2.0. H_2 production is considerably less than the predicted equilibrium results with a large portion of H_2 being tied up in CH_4. CO is also considerably less, with the missing carbon in CO_2 and the CH_4. No coke was noticed over the range of ϕ tested, nor was there a significant concentration of minor species.

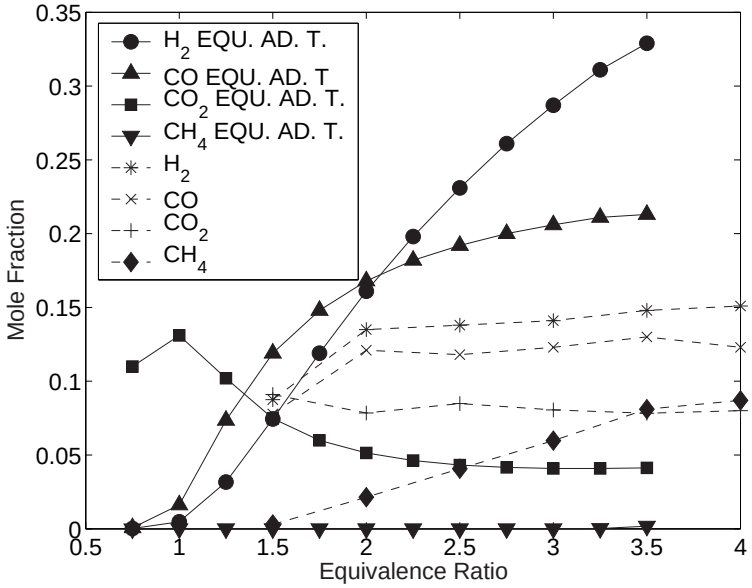

Figure 5.19: Equilibrium species concentrations (dry) for neat ethanol compared to experimental results from the 52.5 mm burner filled with 20 mm of 2-3 mm and 80 mm of 3-3.5 mm desiccant Al_2O_3 beads at various ϕ.

Fig. (5.20) and Fig. (5.21) show the results from the 10 % and 33 % H_2O blends respectively. Similarly to the neat ethanol, the products deviate from equilibrium predictions and large amounts of CH_4 are also present.

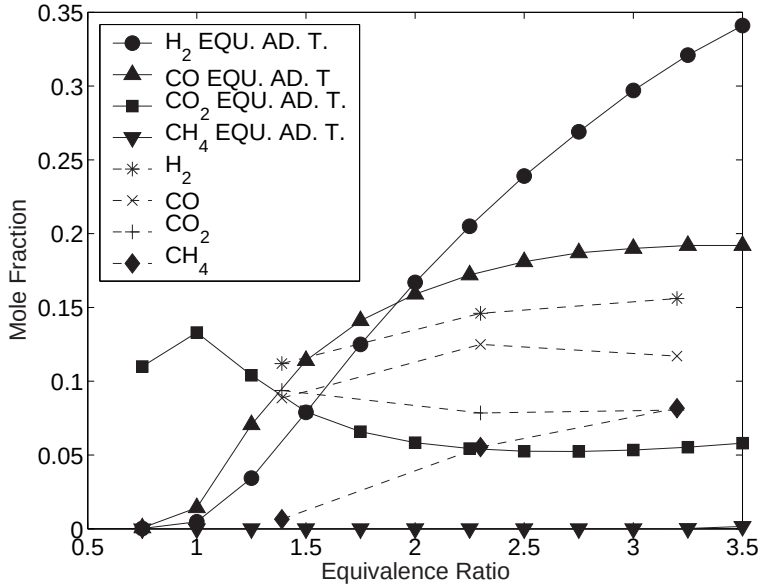

Figure 5.20: Equilibrium species concentrations (dry) for 90 % ethanol, 10 % H_2O (by vol.) compared to experimental results from the 52.5 mm burner filled with 20 mm of 2-3 mm and 80 mm of 3-3.5 mm desiccant Al_2O_3 beads at various ϕ.

The large amounts of CH_4 agree with Galvita et al. (2001) who studied syngas production inside a two-layer fixed-bed catalytic reactor. They observed improved H_2 production at higher temperatures. However, it should be noted that as they were using a catalyst, they were operating at much lower temperatures than in our experiments. Additionally, Fishtik et al. (2000), Cavallaro and Freni (1996) and Vasudeva et al. (1996) state that H_2, CO, CO_2 and CH_4 are the usual set of species produced from steam reforming of ethanol.

As illustrated in Fig. (5.22), equilibrium predictions at a ϕ of 3.0 over a range of temperatures, show H_2 production peaking around 1000 K. Additionally, CH_4 decreases to almost zero by 1000 K. CO increases with temperature, while CO_2 decreases. In all of the tests the reaction temperature was above 1000 K indicating

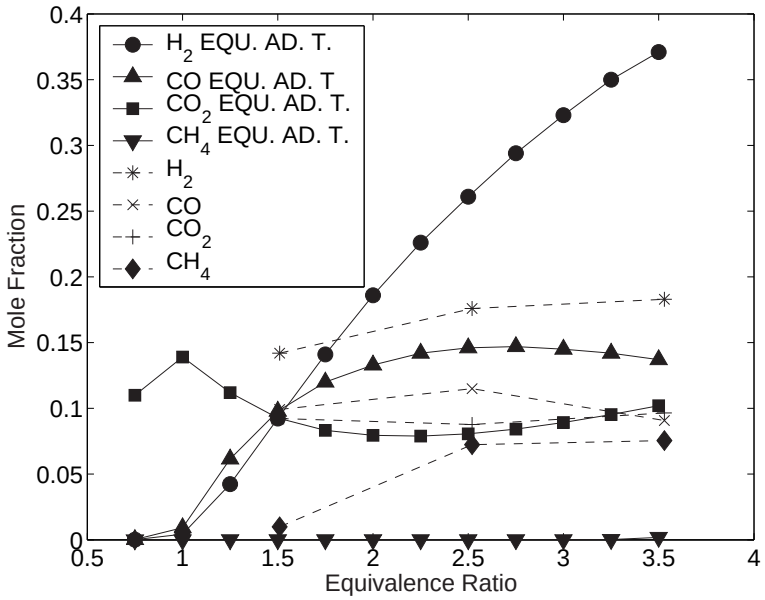

Figure 5.21: Equilibrium species concentrations (dry) for 67 % ethanol, 33 % H_2O (by vol.) compared to experimental results from the 52.5 mm burner filled with 20 mm of 2-3 mm and 80 mm of 3-3.5 mm desiccant Al_2O_3 beads at various ϕ.

that the products did not reach equilibrium. The large amount of CH_4 measured can be attributed to finite kinetic effects and not equilibrium being reached at a lower temperature than the adiabatic temperature.

These results can be partially explained by work described by Fishtik et al. (2000). Based on equilibrium calculations they determined that at low water concentrations ethanol decomposes according to

$$2C_2H_5OH = 3CH_4 + CO_2 \tag{5.1}$$

and

$$2C_2H_5OH = CH_4 + CO + H_2 \tag{5.2}$$

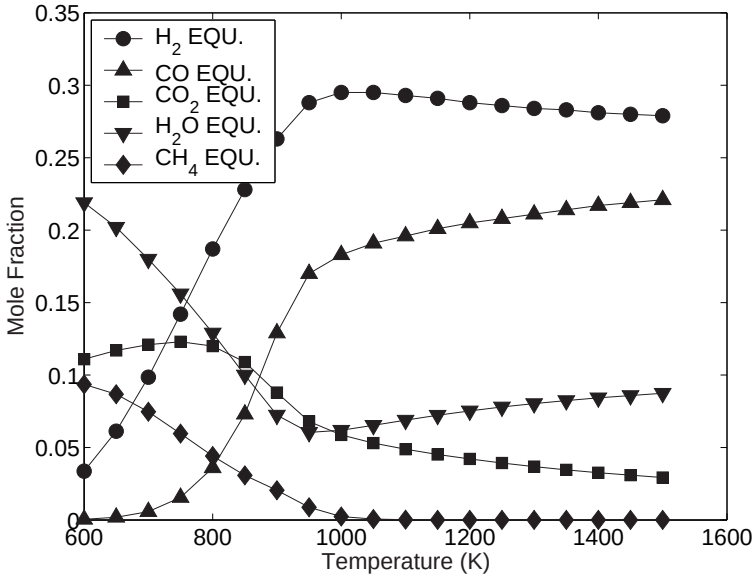

Figure 5.22: Calculated equilibrium product species (dry) for ethanol at various temperatures at ϕ=3.0, inlet Air/fuel at 383.15 K.

to produce methane. The first reaction is dominant at lower temperatures and the second is favoured at higher temperatures.

In our experiments, the reaction attained its highest temperature with the neat ethanol and its lowest with the 67/33 % C_2H_5OH/H_2O blend. At a ϕ of approximately 2.5, the amount of CH_4 present in the products for neat, 10 % and 33 % blends respectively was 4.1 %, 5.5 % and 7.2 %. This agrees with Fig. (5.22) that the amount of CH_4 present should decrease with the temperature of the reaction.

Similarly to the other fuels tested, as the mass flow rate was increased while holding the equivalence ratio constant, the amount of H_2 also increased, see Fig. (5.23). However, unlike methane and methanol the major product species never reached the amounts predicted by the CEA code.

Fig. (5.24) compares the H_2 produced from the three forms of ethanol to the

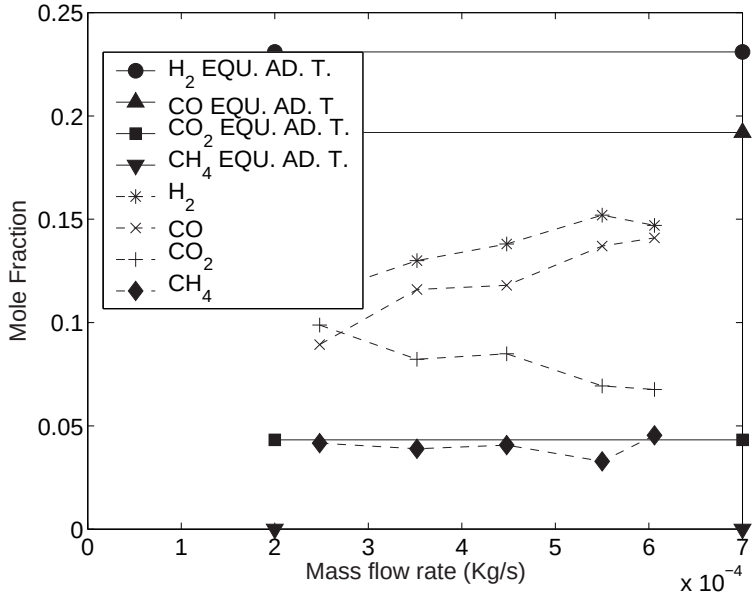

Figure 5.23: Equilibrium species concentrations (dry) for neat ethanol compared to experimental results from the 52.5 mm burner filled with 20 mm of 2-3 mm and 80 mm of 3-3.5 mm desiccant Al_2O_3 beads at $\phi = 2.5$.

CEA code. H_2 production increases with H_2O addition for both equilibrium and experimental results. Similarly, Fig. (5.25) compares CO for the same conditions as the previous plot. CO decreases with increasing H_2O concentration.

As H_2O concentration and temperature are increased the preferred steam reforming reaction,

$$2C_2H_5OH + 3H_2O = 2CO_2 + 6H_2 \tag{5.3}$$

can be made predominant. Increasing the ratio of H_2O to C_2H_5OH also increases the water-gas shift and methane steam reforming reactions,

$$CO + H_2O = CO_2 + H_2 \tag{5.4}$$

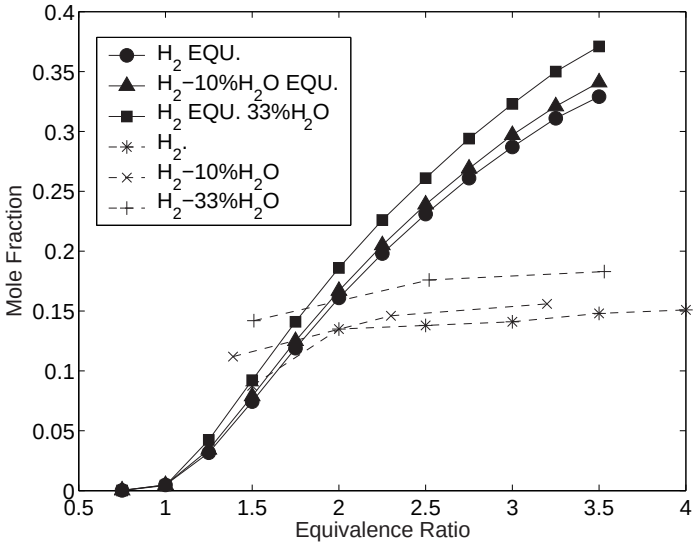

Figure 5.24: H_2 species concentrations compared to equilibrium results (dry) for neat, 90 %, 33 % ethanol from the 52.5 mm burner filled with 20 mm of 2-3 mm and 80 mm of 3-3.5 mm desiccant Al_2O_3 beads at various ϕ.

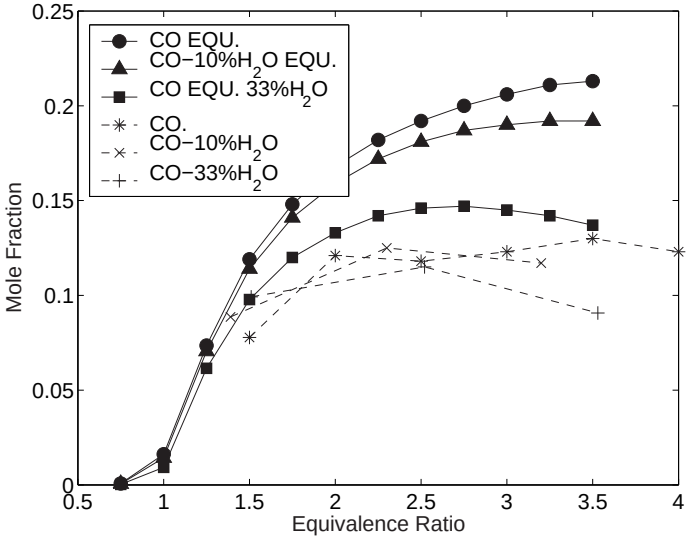

Figure 5.25: CO species concentrations compared to equilibrium results (dry) for neat, 90 %, 33 % ethanol from the 52.5 mm burner filled with 20 mm of 2-3 mm and 80 mm of 3-3.5 mm desiccant Al_2O_3 beads at various ϕ.

$$CH_4 + H_2O = CO_2 + 4H_2 \tag{5.5}$$

producing more H_2 and CO_2 and consequently less CO and CH_4. In these tests H_2 production increased with H_2O concentration from 14.8 % to 18.3 % and CO_2 increased from 8.7 % to 9.7 % at a ϕ of 3.5. Likewise at a ϕ of 3.5, CO decreased from 13.0 % to 9.1 % and CH_4 decreased from 8.1 % to 7.6 %.

However at a ϕ of 1.5 and 2.5, the results are not as easily explained. H_2 increases with H_2O and CO_2 increases slightly, but CO remains relatively unchanged and CH_4 actually increases slightly. As H_2O increases so did the quantities of C_2H_2, C_2H_4 and C_2H_6. In these instances the extra hydrogen goes into both H_2, CH_4 and the C_2s making it impossible to explain the results with just the methane steam reforming and water-gas shift reactions.

These results illustrate the importance of operating the burner at an optimal temperature, mass flow rate and the effect fuel dilution with H_2O can have on the H_2 conversion process.

5.3.4 Octane and Petrol

The composition of the products obtained with octane and petrol were equivalent within the accepted uncertainty of the measurements. Hydrogen production peaked at 10 % for petrol and at a slightly higher 11 % for octane, much lower than the equilibrium values (Fig. 5.26). When the equivalence ratio was increased beyond approximately 1.5 the actual hydrogen mole fraction started to diverge from the hydrogen predicted by the equilibrium code. Soot was visible at ϕ above 2.0 for petrol and above 3.0 for octane. The soot from the octane flame was measured and the results are presented in Section 4.5.

Fig. (5.27) shows that in contrast to CH_3OH and to a greater extent than CH_4 and C_2H_5OH, with the exception of CH_4 as a product species, significant

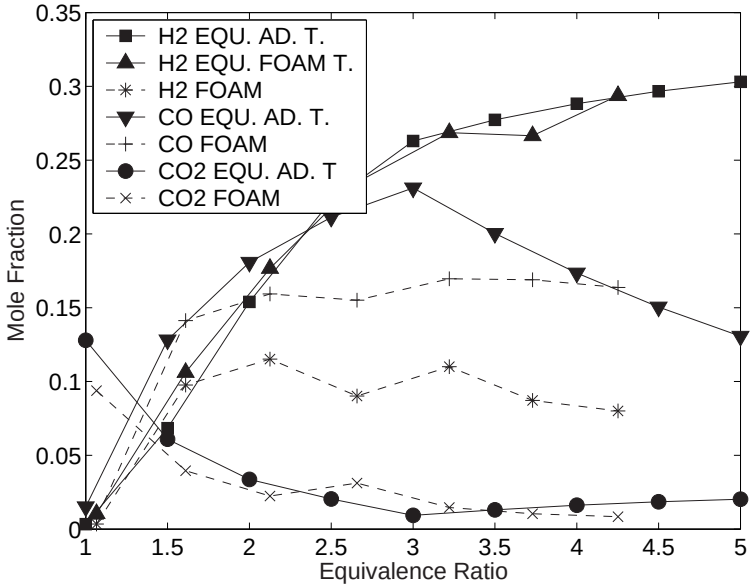

Figure 5.26: Equilibrium H_2, CO and CO_2 species concentrations for octane compared to experimental results. EQU. AD. T. is the species concentration calculated with the equilibrium code at the adiabatic flame temperature. EQU. FOAM T. is the species concentration calculated with the equilibrium code at the temperature measured by the R-type thermocouple. $\dot{m}_{fuel}$ for all ϕ was 1.5×10^{-5} kg/s.

amounts of hydrocarbon species were present in the products. Methane, acetylene and ethylene were the most abundant hydrocarbons detected by the GC. Methane started to increase at a ϕ of 1.5 and continued to increase with increasing ϕ. Acetylene increased rapidly from a ϕ of 1.5, peaked at a ϕ of 2.0 and then slowly decreased thereafter. Ethylene started increasing at a ϕ of 2.5 and also continued to increase with ϕ. Equilibrium cannot explain the presence of these higher hydrocarbons. Fig. (5.28) shows that for a ϕ of 3.0, the steam reforming reaction becomes important for C_8H_{18} combustion at temperatures below 1100 K. However, during these tests the temperature at the point of extraction and there-

fore also the reaction temperature remained above 1100 K. Therefore, since such high values cannot be generated by an equilibrium reaction, it is evident that the results are influenced by finite rate kinetics. Measurements at higher and lower flow rates are necessary to elucidate this point further.

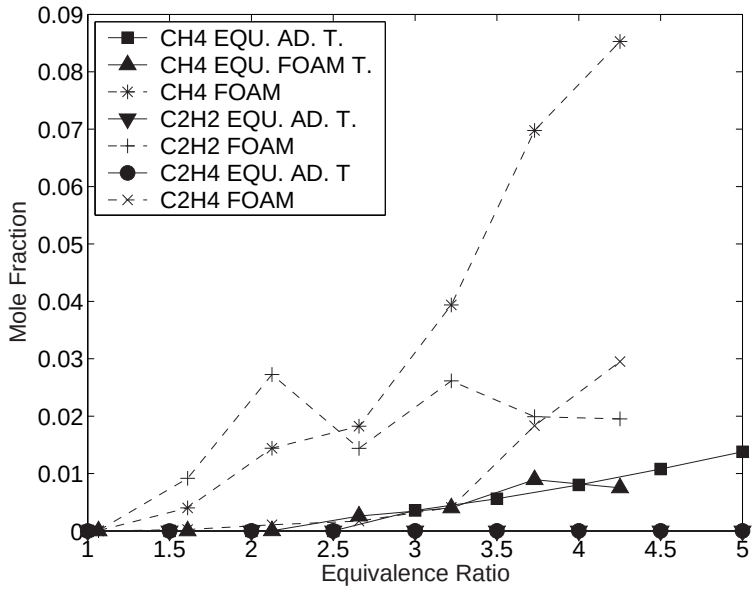

Figure 5.27: Equilibrium CH_4, C_2H_2 and C_2H_4 species concentrations for octane compared to experimental results. EQU. AD. T. is the species concentration calculated with the equilibrium code at the adiabatic flame temperature. EQU. FOAM T. is the species concentration calculated with the equilibrium code at the temperature measured by the R-type thermocouple. $\dot{m}_{fuel}$ for all ϕ was 1.5×10^{-5} kg/s.

Using petrol as fuel it was observed that as the distance separating the probe and ceramics changed, the products's composition also changed (Pedersen-Mjaanes, 2003). When the probe height was increased the mole fraction of H_2, CO and minor hydrocarbon species all decreased, while the mole fraction of CO_2 increased. This is because the residence time and/or temperature were not long

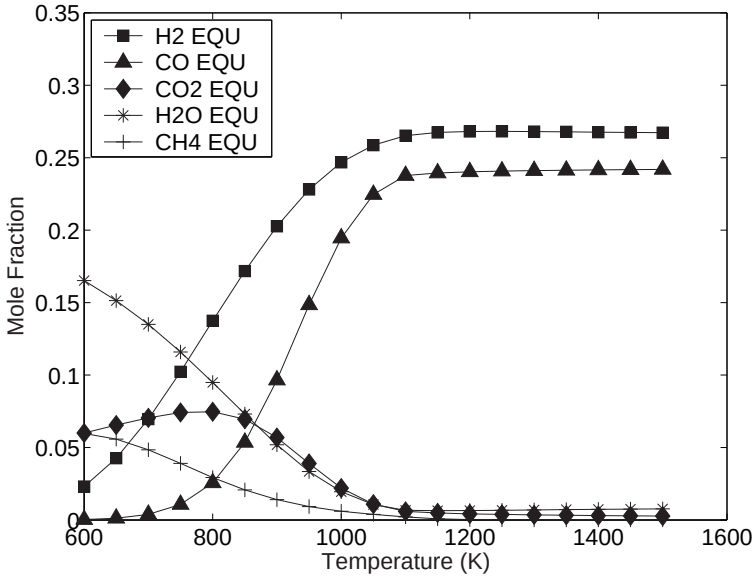

Figure 5.28: Calculated equilibrium product species for octane at various temperatures at ϕ=3.0.

or high enough for the system to attain chemical equilibrium at the outlet of the burner. As the distance increased, the reaction moved closer to completion as more species became oxidized. This has future implications as for determining the ideal length of the burner and ideal location to extract the syngas.

5.3.5 Kerosene

Kerosene ($C_{12}H_{23}$) or more specifically Jet-A fuel was reformed in the 52.5 mm Kanthal® burner. As is illustrated in Fig. (5.29), H_2 and CO production peaked at a ϕ of 2.5 after which hydrocarbons became increasingly abundant. Similar to octane, the complex chemistry of the fuel was not reformed fully to H_2 resulting in large quantities of CH_4 and C_2H_4.

Similar to the other fuels tested, increasing the mass flow rate, increased the H_2 production until the flame became unstable and started to move towards the

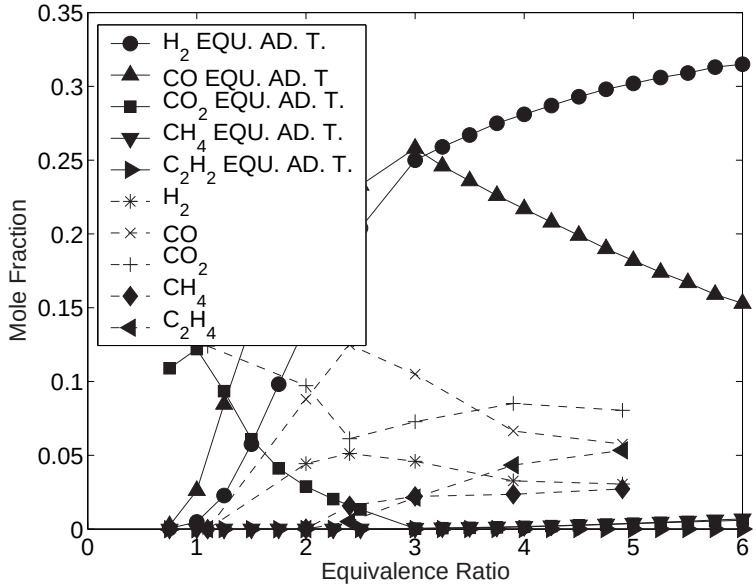

Figure 5.29: Equilibrium species concentrations for Jet-A fuel compared to experimental results for the 52.5 mm burner comprising two layers: (1) 100 mm SiC, 4.8 pores/cm-90 % porosity and (2) 20 mm SiC (24 pores/cm-91 % porosity) at various ϕ.

exit of the burner. Fig. (5.30) plots these results for a ϕ of 2.5 inside a burner filled with SiC foam.

This test was repeated for a burner filled with 20 mm of 2-3 mm desiccant Al_2O_3 beads and 80 mm of 4.6-5.0 solid Al_2O_3 beads as illustrated in (5.31). Higher mass flow rates were possible even though the porosity is considerably lower, resulting in even higher flame speeds. Both H_2 and CO increased to higher levels than observed in the SiC burner. As before, the beads proved to have a wider operating envelope and are capable of producing higher concentrations of syngas than the foams.

Fig. (5.32) plots the main product species over a range of ϕ for the bead burner. In comparison to Fig. (5.29), higher concentrations of H_2 and CO are observed,

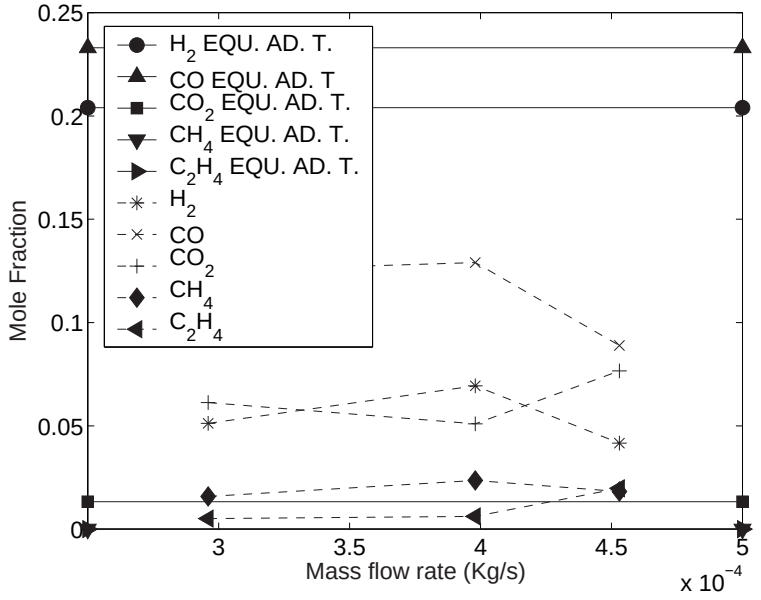

Figure 5.30: Equilibrium species concentrations for Jet-A fuel compared to experimental results for the 52.5 mm burner comprising two layers: (1) 100 mm SiC, 4.8 pores/cm-90 % porosity and (2) 20 mm SiC, 24 pores/cm-91 % porosity, at ϕ=2.5.

but the overall trend is similar as production of syngas peaks at approximately a ϕ of 3.0 before decreasing as CH_4 and C_2H_4 become more abundant.

5.3.6 Biodiesel

Neat biodiesel ($C_{17}H_{32}O_2$) and neat biodiesel mixed with methane were reformed in the conical burner (Fig. 2.5). The product species, as measured by the GC, are plotted in Fig. (5.33). Similarly, to the other complex fuels, octane and Jet-A, the bonds in the biodiesel proved difficult to break. The majority of the carbon became tied up in CO and CO_2 with minimal amounts tied up in CH_4 and the C_2s. Since all the carbon can not be accounted for, it is likely (although

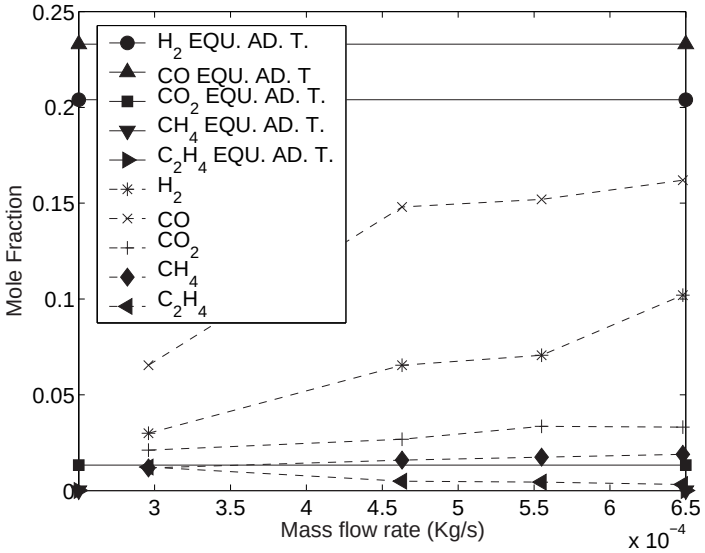

Figure 5.31: Equilibrium species concentrations for Jet-A fuel compared to experimental results for the 52.5 mm burner comprising two layers: (1) 80 mm of solid 4.5-5.0 mm dia. Al_2O_3 and (2) 20 mm of 2-3 mm desiccant Al_2O_3 at ϕ=2.5.

not measurable) that significant quantities also remain trapped in the un-reacted fuel.

The biodiesel was also injected into the burner with CH_4 in an attempt to raise the temperature of the reaction and convert more of the fuel to H_2. In these tests, for equivalent ϕ based on only the ratio of air to biodiesel, the exit temperature to the burner was approximately 100 K higher. The amount of H_2 and CO produced in these tests is plotted in Fig. (5.34). As can be seen, H_2 increased considerably and CO increased even more. The additional CH_4 drove the methane steam reaction forward producing more CO and H_2. Although not plotted, the amount of CO_2 present in the product species decreased significantly which supports the argument that the methane steam reaction was at least partially responsible for the improved performance with the addition of CH_4. In terms of kW, the ratio

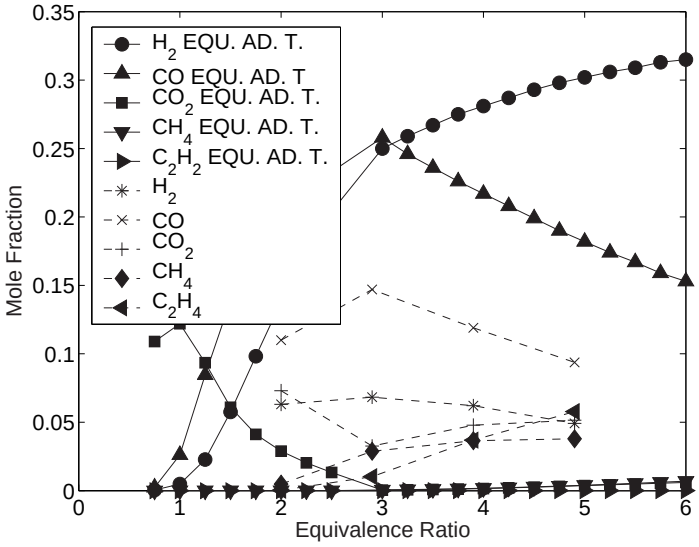

Figure 5.32: Equilibrium species concentrations for Jet-A fuel compared to experimental results for the 52.5 mm burner comprising two layers: (1) 80 mm of solid 4.5-5.0 mm dia. Al_2O_3 and (2) 20 mm of 2-3 mm desiccant Al_2O_3 at various ϕ.

of biodiesel to CH_4 varied from 4.3 to 5.4.

5.4 Discussion

In summary, the theoretical optimal ϕ for H_2 production from methane is 4.0 based simply on balancing the reaction of fuel and oxygen to give only CO and H_2 as products. However, in these tests the H_2 production was maximized between $2.0< \phi <2.5$. The maximum amount of hydrogen produced from methane was 24 % by volume at a ϕ of 2.5. The other major product apart from nitrogen was 15 % CO which can be used in an additional water-gas shift reaction and converted to CO_2 and H_2. Hydrogen production increases with increasing ϕ as the reaction moves further away from completion. As ϕ increases, the amount

of nitrogen is decreasing which accounts for part of the higher molar fraction of hydrogen in the products. Therefore, the burner may have a higher efficiency of converting the energy inside the fuel to energy stored in H_2 at a lower ϕ than the maximum ϕ achievable. Defining the function of the burner as that of converting a fuel to H_2, and assuming that the CO produced can help convert the H_2O to H_2 in a future water-gas shift reaction, then the efficiency of the burner can be given by

$$\eta = \frac{\dot{m}_{H_2} LHV_{H_2} + \dot{m}_{CO} LHV_{CO}}{\dot{m}_{fuel} LHV_{fuel}}. \tag{5.6}$$

A similar definition was used by Hagan et al. (2000) and Ahmed and Krumpelt (2001), where the LHV of H_2 produced was divided by the LHV of fuel to calculate conversion efficiency (which implies that the water-gas shift reaction has taken place). This assumption seems reasonable as CO conversion efficiencies greater than 90 % in WGS reactors are achievable as demonstrated by Maiya et al. (2000) and Batista et al. (2005). The highest conversion efficiency of methene to syngas, based on Eq. (5.6), was 55 % (24 % H_2) at a ϕ between 2.0 and 2.5 inside the Al_2O_3 burner and 37 % (14 % H_2) inside the SiC foam burner. A summary of the major results for the fuels tested is tabulated in Table (5.1).

Hydrogen production peaked at a ϕ of 2.5 for all the bead burners, except the 6.0-7.0 mm AL_2O_3 burner where the H_2 peaked between a ϕ of 2.0-2.5. The peak conversion at a ϕ of 2.5 agrees with experimental and computational results reported by Fay et al. (2005) in a filtration type burner. In a similar burner, Bingue et al. (2004) determined H_2 production to be maximum between $2< \phi <3$.

These results are similar to those obtained earlier with a smaller foam burner, 30 mm I.D., where the conversion efficiency was 36 % (12 % H_2). In these tests, the richest flammability limit reached was 1.84 inside an Al_2O_3 foam burner

compared to approximately 2.0 in the larger diameter SiC foam burner. These results are plotted in Fig. (5.35) and show the experimental results following equilibrium predictions for increasing H_2 and CO with ϕ and decreasing CO_2 with increasing ϕ albeit at a reduced rate. Methane and acetylene mole fractions increased from 0.4 % at a ϕ of 1.55 to over 1.0 % at a ϕ of 1.84. Increasing the mass flow rate resulted in higher temperatures that drove the reaction towards equilibrium producing less CH_4 and C_2H_2 which increased the H_2 yield.

In addition to the higher conversion efficiencies, a higher upper flammability limit was also achievable with the bead burners in comparison to the foam burners. In general the beads outperformed the foams and there was little change in increasing the size of the burner. Although, the smaller I.D. burner will have greater heat loss per unit volume, adequate insulation appears to be sufficient to offset this effect. However, changing the insulation configuration around the burner so that heat loss was not at a minimum, decreased the burner's conversion efficiency significantly. The effect was more pronounced on the smaller I.D. burner as it has a larger surface area per unit volume than the larger I.D. burner. The latter results reinforce the suggestion that heat losses are at least partly responsible for the burner's non-equilibrium behaviour during lower firing rates.

Hydrogen production is theoretically maximum at a ϕ of 3.0 when using CH_3OH as the feedstock. In these tests H_2 conversion efficiency was highest in a wide range of equivalence ratios between $3.9 < \phi < 7.8$. The 30 mm bead burner had the highest conversion efficiency of 61 %, followed closely by the 50 mm bead burner at 57 %, which is well within the measurement error associated with these tests. Once again, the foam burner was observed to have the poorest conversion efficiency of 35 %.

Also in these tests both the foams and beads were Al_2O_3, reinforcing the evidence from the CH_4 tests that the beads are a better porous media to maximize

H_2 production and extended UFLs.

The theoretical optimal equivalence ratio for C_2H_5OH conversion is 6.0, well above the UFL. However, in these tests the highest ϕ tested was 4.0. The maximum conversion efficiency for neat ethanol occurred between a ϕ of 2-2.5. As observed with the previous fuels, H_2 and CO increase with ϕ. As ϕ was increased, CH_4 became a major product species and at a ϕ of 4.0 reached 8.7 %. C_2H_4 also increased and reached 2.2 % of the product species at a ϕ of 4.0.

Increasing the mass flow rate, at a ϕ of 2.5, increased H_2 production and reduced the concentration of CH_4 in the products. Examining chemical equilibrium results over a range of temperatures revealed that CH_4 decreases with increasing temperature. In these tests as the mass flow rate was increased, more energy was released by the reaction resulting in higher temperatures inside the burner reducing the amount of CH_4 in the products.

Diluting the fuel with H_2O increased the burner's performance as the steam reforming reaction (5.3) became dominant and the water-gas shift (5.4) and methane steam reforming (5.5) reactions were driven forward. It is hypothesized that the lower temperatures induced by the dilution with H_2O increases the effects of finite rate kinetics resulting in more C_2s being formed and moving the reaction further away from equilibrium. The conversion efficiencies increased from 29 % to 37 % as the fuel was diluted with 33 % (by volume) of H_2O. The main results for C_2H_5OH are tabulated in Table (5.1).

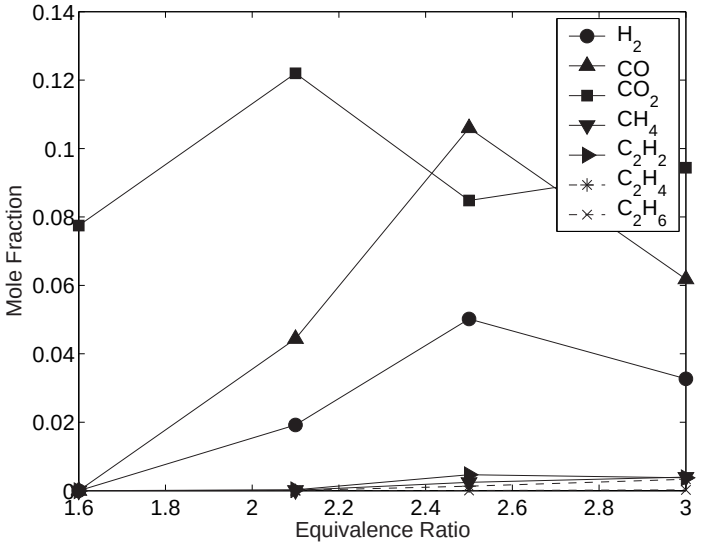

Figure 5.33: Species concentrations using biodiesel inside the conical burner comprising two layers: (1) 80 mm of solid 6.0-7.0 mm dia. Al_2O_3 and (2) 30 mm of 2-3 mm desiccant Al_2O_3 at various ϕ.

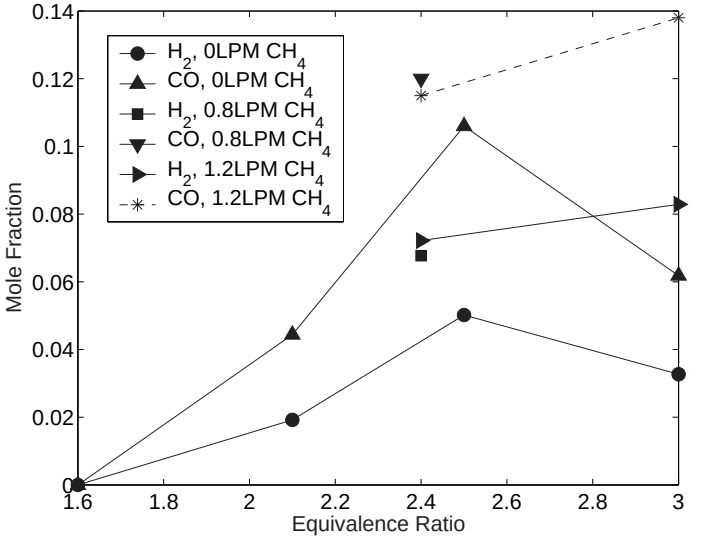

Figure 5.34: Species concentrations using biodiesel mixed with CH_4 inside the conical burner comprising two layers: (1) 80 mm of solid 6.0-7.0 mm dia. Al_2O_3 and (2) 30 mm of 2-3 mm desiccant Al_2O_3 at various ϕ.

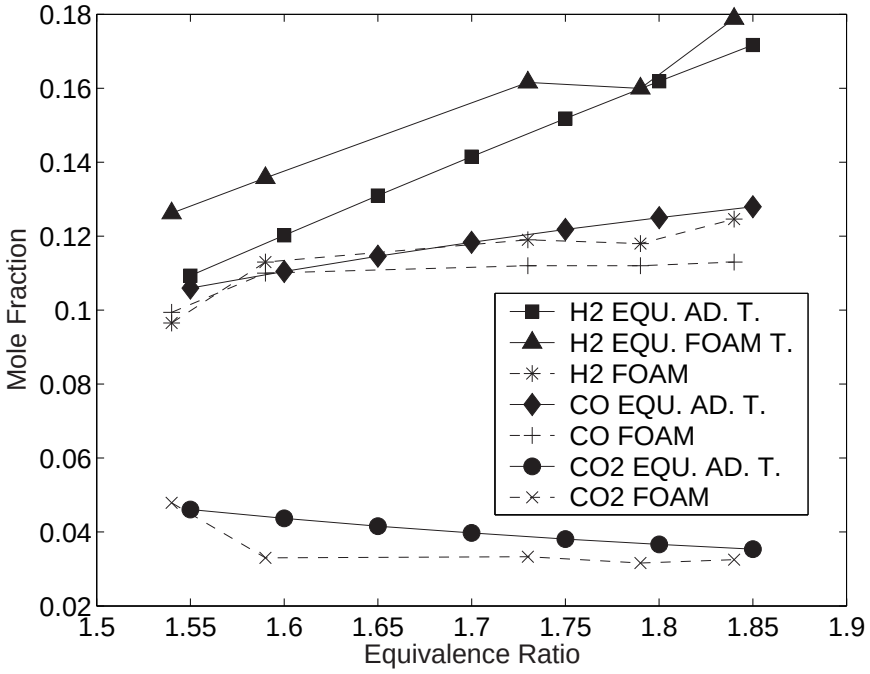

Figure 5.35: Equilibrium H_2, CO and CO_2 species concentrations for methane compared to experimental results. EQU. AD. T. is the species concentration calculated with the equilibrium code at the adiabatic flame temperature. EQU. FOAM T. is the species concentration calculated with the equilibrium code at the temperature measured by the R-type thermocouple. $\dot{m}_{fuel}$ for ϕ=1.55 to ϕ=1.75 was 6.6×10^{-6} kg/s and $\dot{m}_{fuel}$ for ϕ=1.80 and ϕ=1.85 was 5.5×10^{-6} kg/s.

Table 5.1: Maximum equivalence ratios and conversion efficiencies reached in the foam and bead burners.

Fuel	Free Flame [a]	Optimal ϕ	Al [b] Foam	Al Beads	SiC Foam	η (%) [c]	η (%) [d] included
	(UFL)	(Theoretical)	(UFL)	(UFL)	(UFL)	(foam/beads)	(beads)
Methane	1.64	4.0	1.84	2.5	-	37/55	42
Methanol	4.08	3.0	6.2	9.5	-	35/61	49
100 % Ethanol	3.35	6.0	-	4+	-	-/39	28
90 % [e] Ethanol	NA	-	-	3.2+	-	-/41	30
67 % [f] Ethanol	NA	-	-	3.5+	-	-/48	37
Iso-Octane	3.8-4.2	3.125	4.3	-	-	34/-	20
kerosene	4.65	2.96	-	4.9+	4.9	20/28	16
Biodiesel	NA	3.2	3.0	-	-	-/15	10

[a] Data from Refs. (Turns, 2000) and (API, 1976).

[b] Al is short for Al_2O_3. The Al_2O_3 foam was used in the 30 mm burner and the SiC foam in the 50 mm burner.

[c] Maximum efficiency as defined by Eq. (5.6).

[d] Maximum efficiency with only H_2 used in numerator of Eq. (5.6).

[e] 10 % H_2O by volume.

[f] 33 % H_2O by volume.

The petrol and Iso-octane experiments only achieved a conversion efficiency of 34 % at a ϕ of 1.7. The theoretical optimal ϕ for H_2 production is 3.125. The temperatures were not high enough and/or residence times long enough to approach equilibrium conditions resulting in a large amount of H_2 remaining trapped in CH_4, C_2s and soot deposits. In order to make this a viable technology for extracting H_2 from petrol the considerable amounts of H_2 trapped in the hydrocarbons needs to be recovered.

No other tests on reforming petrol or octane in an inert porous media could be located in the archival literature. However, work by Kirwan et al. (2002) on a catalytic POX reactor produced 20 % H_2 and 21 % CO after a 30 second warm-up period at an airflow rate of 1.5×10^{-3} kg/s and 15 % H_2 and 15 % CO at an airflow rate of 2.5×10^{-3} kg/s. The tests in this thesis, with non-catalytic PM, achieved a maximum H_2 concentration of 11 % with a CO concentration of 17 %.

The theoretical optimal equivalence ratio for kerosene ($C_{12}H_{23}$) conversion is 2.96, well within the UFL. In these tests H_2 production was maximized at $2.5< \phi <3.0$. Similar to the octane tests considerable amounts of H_2 remained trapped in CH_4 and C_2H_4. No soot was visible during these tests.

Zhdanok (2003) ran several tests with kerosene inside a quartz burner in filtration combustion mode and also determined the optimal conversion efficiency to be around a ϕ of 3.0. Relatively large quantities of CH_4 were observed at high equivalence ratios in the order of 4-5 %, approximately twice as much as we observed. In contrast to our tests, in Zhdanok's experiments C_2H_4 never increased beyond 1 %.

H_2 production peaked at a ϕ of approximately 2.5 for the biodiesel, less than the theoretical maximum of 3.2. Similarly to the other complex fuels, large amounts of hydrogen remained trapped in CH_4 and the C_2s. The peak efficiency achievable with neat biodiesel was 15 %, increasing to 18 % when CH_4

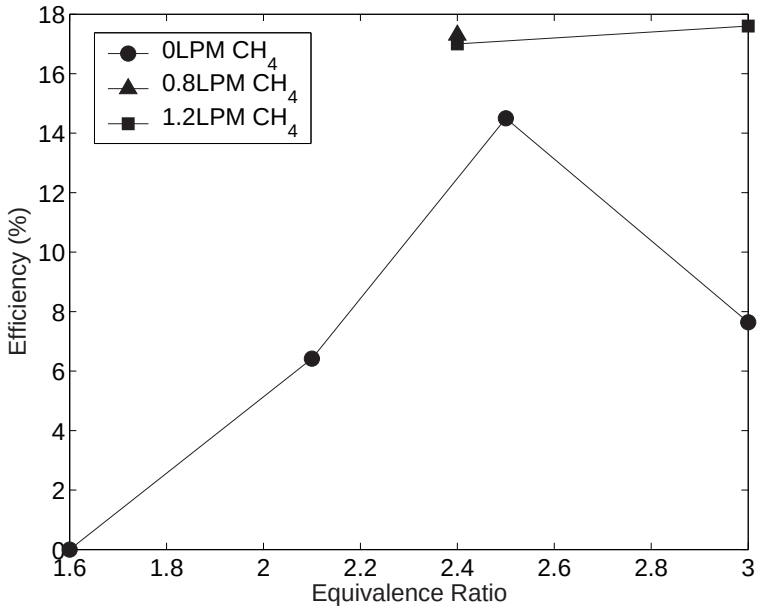

Figure 5.36: Conversion efficiencies using neat biodiesel and biodiesel mixed with CH_4 inside the conical burner comprising two layers: (1) 80 mm of solid 6.0-7.0 mm dia. Al_2O_3 and (2) 30 mm of 2-3 mm desiccant Al_2O_3 at various ϕ.

was injected with the biodiesel.

Fig. (5.36) presents the conversion efficiencies for the biodiesel burner with and without CH_4 added. As expected the efficiency increases with CH_4 addition. However, it should be noted that at no time did the efficiency approach that of pure CH_4.

5.5 Chapter Summary

The general trend for all the fuels tested was for H_2 production to initially increase with ϕ. After the flame became unstable and started to propagate downstream, H_2 production would decrease. Increasing the mass flow rate, at a constant ϕ pushed the product species closer to equilibrium producing more H_2. At high mass

flow rates, at least for methane and methanol, changing the probe's height above the burner did not affect the product species indicating that the products had reached equilibrium, but at a temperature lower than the adiabatic temperature. Extracting the sample from different points in the axial direction within the CH_4 burner revealed that most of the fuel conversion takes place within the first 20 mm after the interface (at least for CH_4). The function of the remaining 60 mm of PM is to minimize radiation heat transfer to the environment. At the lower flow rates, the lower temperatures combined with quenching on the walls allowed CH_4 penetration and reduced the concentration of syngas produced.

CH_4 and CH_3OH achieved the highest conversion efficiencies of 55 % and 61 % respectively. The more complex fuels, octane, kerosene and biodiesel, did not achieve the same conversion efficiencies as the simpler fuels and significant amounts of the H_2 remained trapped in CH_4 and the C_2s. Finally, the beads were able to extend the UFLs further than the foams and also produced higher concentrations of H_2 in the products. However, the time for the flame to propagate to the interface and stabilize is an order of magnitude longer for the beads than the foams.

Chapter 6

Transient Response

6.1 Structure of this Chapter

This chapter presents the results obtained by using the Fast TCD described in Chapter 3. The first section explains the method and burner used to take the measurements described in this chapter. Section 6.3 presents the burner's response to transients with methane as the fuel. It also describes the response time of the foam and bead burners and the response time of the Fast TCD. The final section summarizes how the Fast TCD can be used to measure hydrogen on a continuous basis.

6.2 Experimental Conditions

The apparatus used for these experiments is illustrated in Fig. (2.2). A single burner with two different PM configurations was used in these experiments. In its initial configuration the burner was the 52.5 mm I.D. Kanthal® burner filled with 30 mm of 2-3 mm desiccant Al_2O_3 beads as the flame support layer and 80 mm of 3.5-4.0 mm desiccant Al_2O_3 beads for the combustion layer. In the

second configuration, the beads were replaced with a support layer of 20 mm SiC (24 pores/cm 91 % porosity) and a 75 mm SiC (4.8 pores/cm 90 % porosity) combustion layer. A third layer of 20mm of 2-3mm desiccant beads was added beneath the foam support layer to reduce the chances of flashback occurring. The Kanthal® burner is illustrated in Fig. (2.4d).

The burner was brought to thermal equilibrium by combusting a CH_4/air mixture at a ϕ of 0.8. Once thermal equilibrium was attained the flows were adjusted to the desired rates and the transient introduced by readjusting either the CH_4 or air flow rate to the desired setting.

6.3 Transient Response of Methane Burner

6.3.1 Time Delay Associated with Fast TCD and Burner

There is a time response to transients associated with the equipment and the combustion process itself. The time delay can be broken down into four parts:

1. The time for the mass flow controllers (MFCs) to reach steady state.
2. The physical time response for the burner to adjust to the new operating conditions.
3. The time for the new mixture to reach the Fast TCD.
4. The time for the Fast TCD to respond to the new sample mixture.

In order to determine this time delay, two tests were conducted. Both tests were carried out inside the first burner which consisted of two layers of desiccant Al_2O_3 beads. In the first test, a lean flame was stabilized at the interface between the two different layers of beads. Next a transient was introduced by changing the equivalence ratio from 1.5, at 183.0 seconds, to 1.75 by ramping the air flow rate

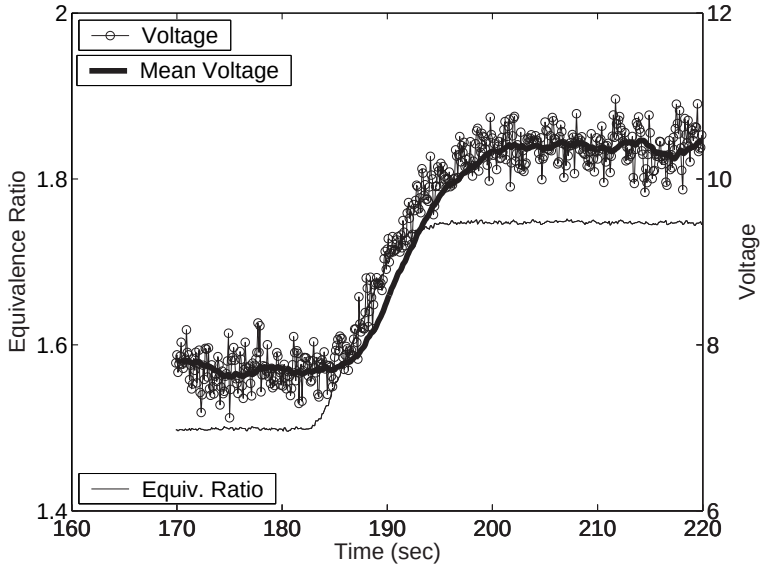

Figure 6.1: Time delay associated with Fast TCD and PM burner.

down over a period of 9 seconds, as is illustrated in Fig. (6.1). If a step change had being introduced, the minimum response time of the mass flow controllers to reach a new equilibrium would have been 2.4 seconds as measured in other tests. The dark solid line is the moving average of the preceding 32 points (3.2 seconds) of the output signal. However, a large change in a steady state signal, such as we are introducing here, should be detected almost instantaneously albeit with a gentler gradient. In this instance, the moving average starts to increase at 185.5 seconds, 2.5 seconds after the H_2 flow rate was changed. It takes a gas sample approximately 0.8 seconds to reach the filaments in the Fast TCD from the inlet of the sampling probe. Subtracting the 0.8 seconds from the 2.5 second delay results in 1.7 seconds to be accounted for in the actual Fast TCD and burner's response. Therefore, it can be deduced that the physical response of the burner to the new flow conditions is considerably faster than 1.7 seconds. These time delays are tabulated in Table (6.1).

Table 6.1: Time delays associated with Burner and Fast TCD.

Condition	Time
Time for H_2 to Δ after MFCs have Δ	2.5 sec
Time for sample to reach Fast TCD	0.8 sec
Time of burner and Fast TCD response	1.7 sec
Time of burner response	$<$ 1.7 sec

Re-establishing equilibrium conditions takes appreciably more time. The moving average reaches steady state at approximately 201.5 seconds. Accounting for the 3.2 second delay inherent in the moving average technique, and the 0.8 seconds for the sample to reach the filaments, the TCD does not reach equilibrium for 5.5 seconds after the flows have reached steady state. The gas in the filament housing is replaced by the new mixture by recirculation and random diffusion of gas molecules. Since the inlet and exit are relatively small, 0.79 mm^2, compared to the housing's volume, 1 260 mm^3, this process takes time for the gas to be replaced by the new mixture. As mentioned earlier, a semi-diffused housing would have resulted in a quicker response time for the Fast TCD.

The response time of the burner can be removed from the equation by sampling an un-ignited gas mixture and varying its composition. Thereby, allowing the response time of the Fast TCD to be measured. In this test, a mixture containing approximately 9.7 % H_2 (by volume) was introduced into the system. Once steady state was reached, the H_2 concentration was reduced to 9.1 % over a 1.7 second time interval. As can be seen from Fig. (6.2), the transient is introduced at 80.8 seconds by decreasing the H_2 flowing through the mass flow controller. After 82.5 seconds, an interval of 1.7 seconds, the flow has stabilized. The voltage moving average (thick line) starts to decrease at 82.7 seconds and

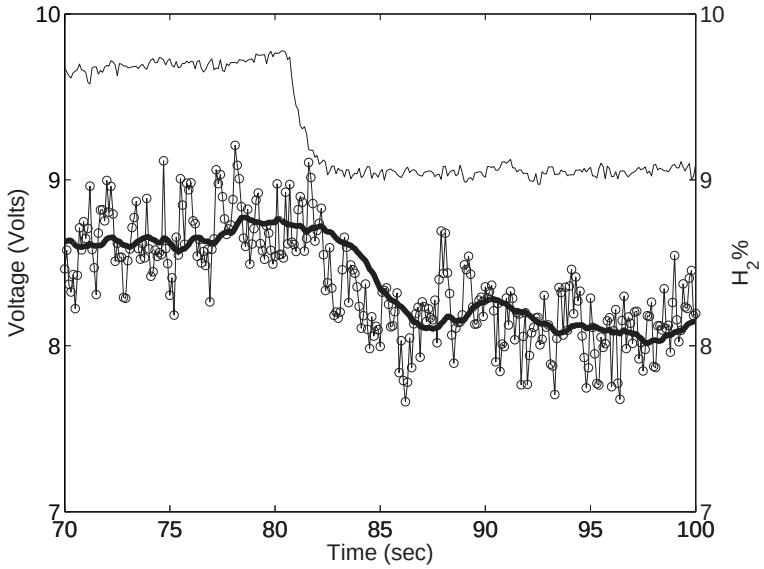

Figure 6.2: Time delay associated with Fast TCD.

Condition	Time
Time for H_2 to Δ after MFCs have Δ	1.9 sec
Time for sample to reach Fast TCD	0.8 sec
Initial time response of Fast TCD	1.1 sec

Table 6.2: Time delays associated with Fast TCD

reaches equilibrium at approximately 94.0 seconds. Subtracting the 0.8 seconds it takes the sample to reach the TCD reveals that the TCD has an initial response time of 1.1 seconds. The time for the TCD to reach equilibrium is approximately 7.5 seconds, based on subtracting the 3.2 and the 0.8 seconds from the difference in time between the TCD's steady state signal and the mass flow controllers steady state signal. These time delays are tabulated in Table (6.2).

These tests demonstrate that the Fast TCD has an initial response time of approximately 1 second after the sample has reached the filament housing. The

burner has an initial response time on the order of 0.5 seconds. It takes considerably longer for the original sample to be replaced by the new sample inside the filament housing. In these tests the Fast TCD reached equilibrium between 6.0 and 7.5 seconds after the sample entered its housing. In the first test, the burner appeared to reach equilibrium, with respect to H_2 production, quite quickly, but later tests illustrate that it can take considerably longer depending on the operating conditions and transient introduced.

6.3.2 Response of Burner to Transients

In the following tests the burner's response to a step increase in equivalence ratio by either decreasing the air flow rate or increasing the fuel flow rate, while keeping the other flow rate constant are studied.

Fig. (6.3) plots the output voltage from the Fast TCD for step changes in ϕ, keeping the mass fuel rate constant at 3.18×10^{-5} kg/s. Fig. (6.4) fits Eq. (3.9) to the voltage in the previous figure to convert it to a H_2 concentration. In addition, a 32 point moving average is applied to smooth the data. Up to an equivalence ratio of 2.0 the hydrogen output is stable. At higher ϕ, H_2 peaks quickly and then starts to decline. The H_2 decrease is steeper with increasing ϕ.

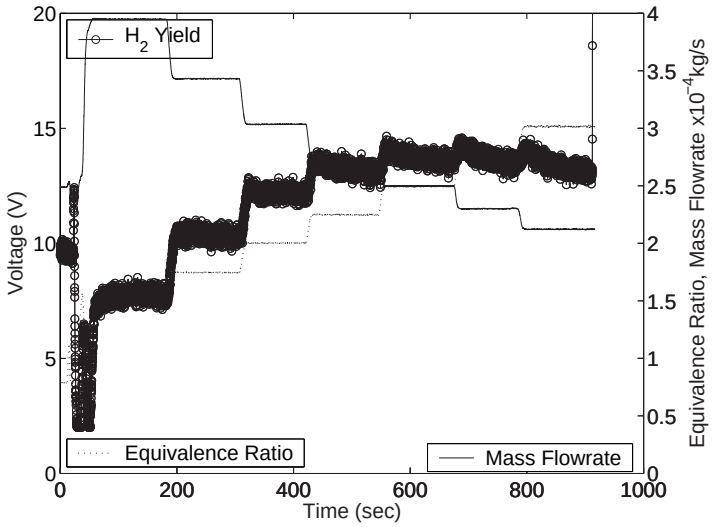

Figure 6.3: Voltage output from Fast TCD for methane. Fuel rate held constant at $\dot{m}_{\text{fuel}} = 3.18\times10^{-5}$ kg/s, while decreasing air flow rate. Mass flow rate on second y-axis is the total mass flow rate of air and fuel.

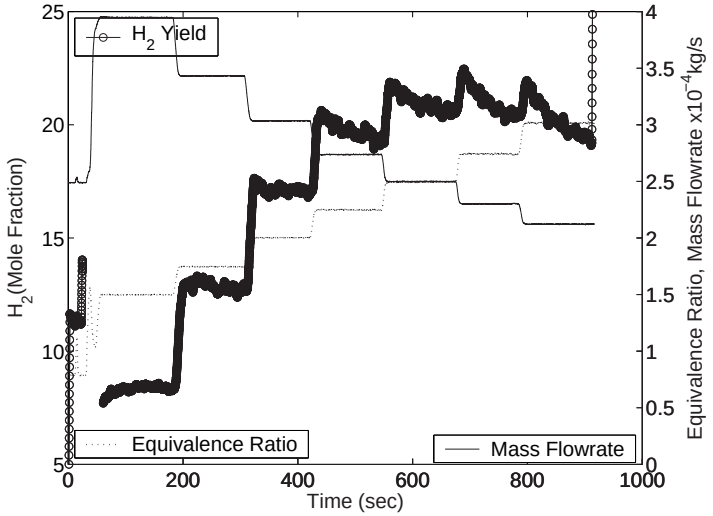

Figure 6.4: Measured hydrogen concentration using Fast TCD for methane. Fuel rate held constant at $\dot{m}_{\text{fuel}} = 3.18\times10^{-5}$ kg/s, while decreasing air flow rate. Data is from the same test used in Fig. (6.3).

The next two tests repeat the previous test except at higher mass flow rates in order to investigate the effect of higher firing rates on H_2 production. In Fig. (6.5) the mass flow rate of fuel has been increased to 3.84×10^{-5} kg/s. H_2 production remains stable up to a ϕ of 2.25 and even at 2.5 levels off after a 30 second decline. In Fig. (6.6) the mass flow rate of fuel is increased to 4.39×10^{-5} kg/s. This extends the flame's stability out to a ϕ of 2.5. Increasing the fuel flow rate past this amount resulted in the flame moving towards the exit at lower equivalence ratios. An increase in the mass flow rate is able to delay instabilities until higher equivalence ratios and produces more H_2 up to a mass flow rate of 4.39×10^{-5} kg/s or 4.0 LPM in a 52.5 mm I.D. burner packed with the above mentioned porous media.

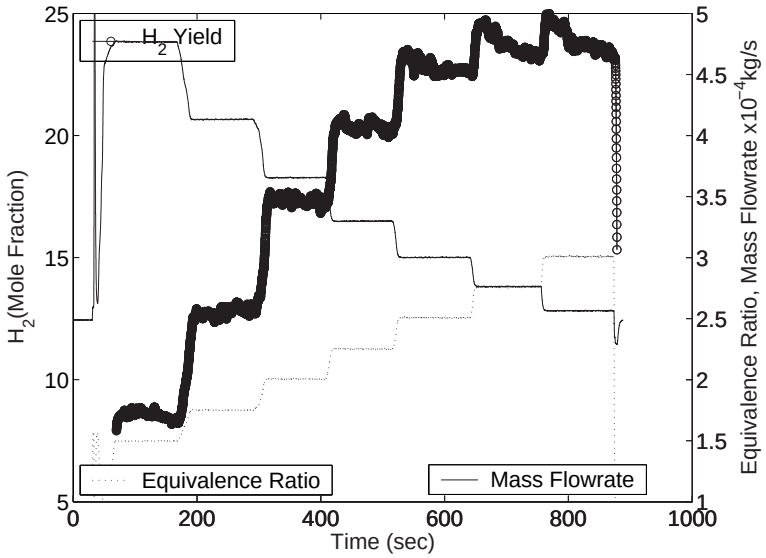

Figure 6.5: Measured hydrogen concentration using Fast TCD for methane. Fuel rate held constant at $\dot{m}_{\text{fuel}} = 3.84\times10^{-5}$ kg/s, while decreasing air flow rate. Mass flow rate on second y-axis is the total mass flow rate of air and fuel.

The next two tests kept the air flow rate constant and varied the fuel flow

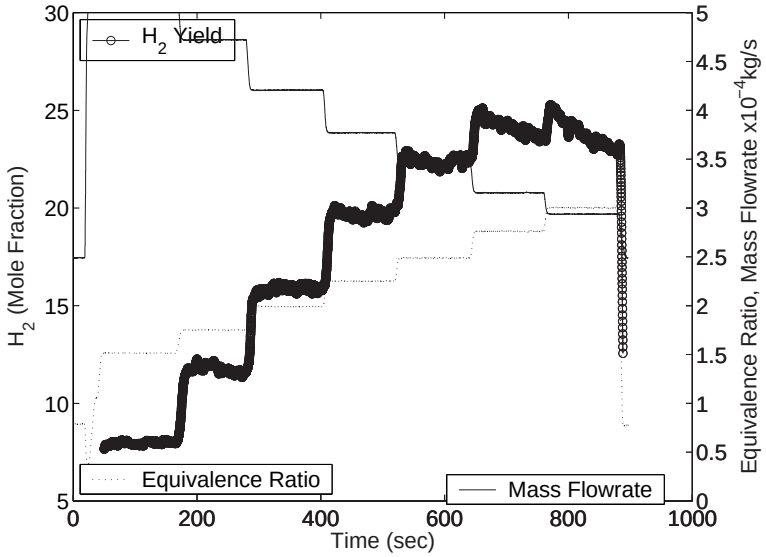

Figure 6.6: Measured hydrogen concentration using Fast TCD for methane. Fuel rate held constant at $\dot{m}_{\text{fuel}} = 4.39\times10^{-5}$ kg/s, while decreasing air flow rate. Mass flow rate on second y-axis is the total mass flow rate of air and fuel.

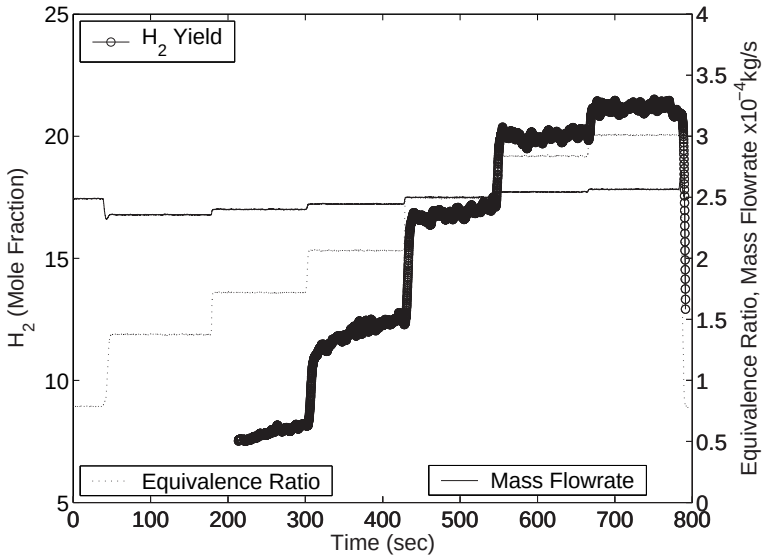

Figure 6.7: Measured hydrogen concentration using Fast TCD for methane. Air rate held constant at $\dot{m}_{air} = 2.18\times10^{-4}$ kg/s, while increasing fuel flow rate. Mass flow rate on second y-axis is the total mass flow rate of air and fuel.

rate. The main difference between these tests and the previous ones is that now the total mass flow rate remains relatively unchanged as ϕ is increased. In the previous tests the mass flow rate was increased, while the energy into the system remained constant. In Fig. (6.7) and Fig. (6.8) hydrogen production is unstable for a ϕ less than 2.5. In both tests after the equivalence ratio is set, H_2 increases with time. As will be shown in later figures it takes several minutes for H_2 production to level off. Comparing H_2 production at $\phi = 2.75$ in Fig. (6.8) to Fig. (6.6), where the mass flow rate is the same for both tests, it can be seen that when the air flow rate is being decreased, H_2 production peaks quickly at a higher value and then declines towards the stable value. If the total mass flow rate is high enough equilibrium will be reached quicker when the mass flow rate is held constant, by just changing the fuel flow rate.

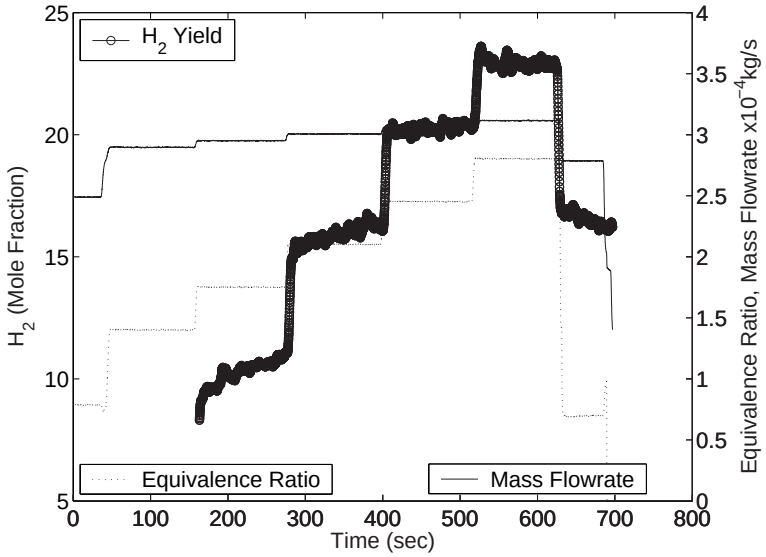

Figure 6.8: Measured hydrogen concentration using Fast TCD for methane. Air rate held constant at $\dot{m}_{air} = 2.68{\times}10^{-4}$ kg/s, while increasing fuel flow rate. Mass flow rate on second y-axis is the total mass flow rate of air and fuel.

Stable H_2 production is very dependant on having a sufficient mass flow rate of reactants to generate enough heat to ensure a stable reaction takes place across the entire cross-sectional area of the burner. Section 4.4 presented the higher temperatures measured across the burner's surface at higher mass flow rates. Increasing the mass flow rate increases the stability of the reaction and hence H_2 production as was discussed in Chapter 5.

Fig. (6.9) and Fig. (6.10) plot the results for $\phi = 2.0$ and $\phi = 2.5$, respectively, as the mass flow rate is ramped up in step increments. The dip in equivalence ratio is caused when the air is ramped up followed by the methane being ramped up. During these transients the burner and Fast TCD are very responsive in that the measured concentration of H_2 being produced follows the rapid change in ϕ. The overall trend is for H_2 production to increase with mass flow rate. Once again the higher the mass flow rate the shorter the time period for the H_2 production to reach steady state.

The next set of experiments compares the response time of the bead burner to a foam burner comprising three layers. The Al_2O_3 bead burner is the same as used in the previous tests. The SiC foam burner has a bottom layer of 20 mm of 2-3 mm Al_2O3 beads, a second support layer of 20 mm of SiC foam sits on top of the first layer. The top layer is a 75 mm thick layer of SiC foam. The Al_2O_3 beads are essentially a back-up layer to prevent the flame from flashing back. The flame still stabilizes in-between the two layers of SiC.

Fig. (6.11) shows the temperature of the SiC burner at various locations during a typical start-up. R1 is located 10 mm above the top layer of beads, K1 through K3 are located on the outside of the Kanthal® burner. K1 is in the middle of the top layer, K2 is at the interface between the two pieces of SiC and K3 is located at the interface between the two bottom layers. Once the flame reaches the interface the equivalence ratio is increased from 0.85 to 2.0 by increasing the

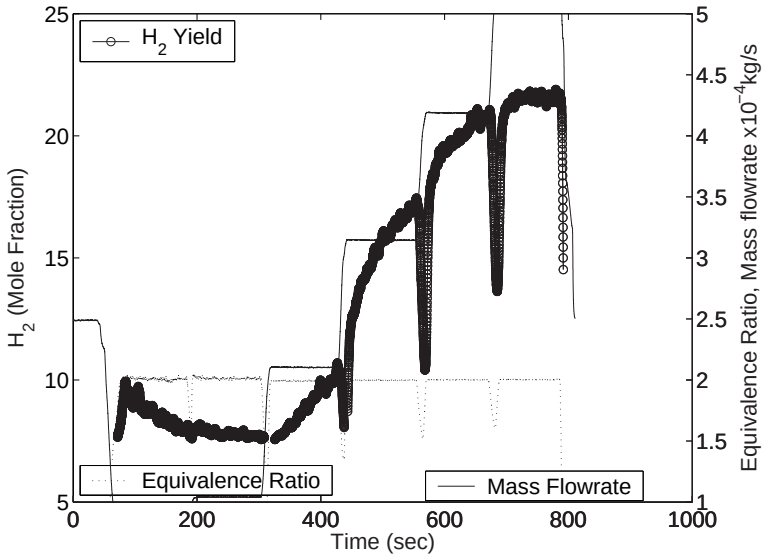

Figure 6.9: Measured hydrogen concentration using Fast TCD for methane. $\phi =$ 2.0, fuel and air flow rate increased. Mass flow rate on second y-axis is the total mass flow rate of air and fuel.

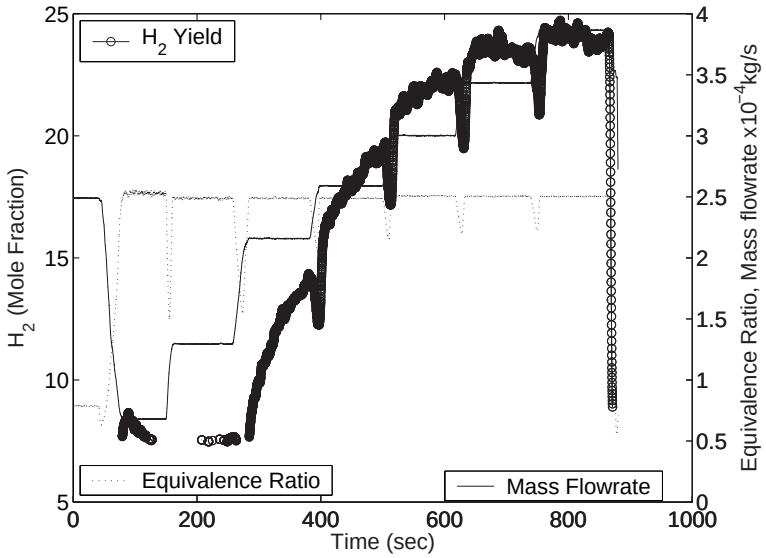

Figure 6.10: Measured hydrogen concentration using Fast TCD for methane. ϕ = 2.5, fuel and air flow rate increased. Mass flow rate on second y-axis is the total mass flow rate of air and fuel.

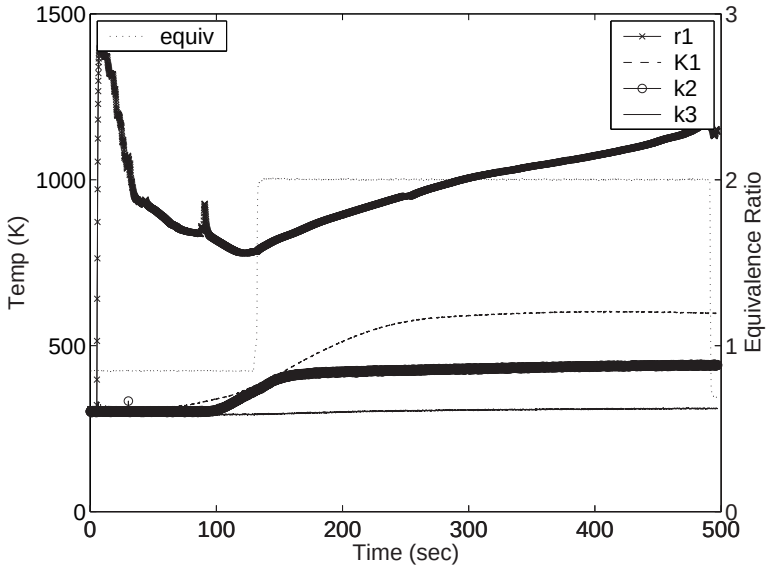

Figure 6.11: Start-up time for SiC foam burner with methane as fuel.

fuel flow rate.

Fig. (6.12) shows the temperature of the Al_2O_3 burner at various locations during a typical start-up. R1, K1 and K2 are in the same locations as for the foam burner. R2 is located inside the burner at the interface between the two different sized layers of beads. R1 is the thick line decreasing from 1200 K. R2 is the second thick line increasing from ambient temperature and reaching an asymptote at approximately 1600 K when the flame reaches the interface.

It only takes 120 seconds for the reaction to propagate to the interface in the foam burner. However, it takes approximately 45 minutes for the flame to reach the interface inside the bead burner.

Fig. (6.13) plots the corresponding results from the Fast TCD for the SiC foam burner (Fig. 6.11 plots the corresponding temperatures). Comparing these results, it can be seen that H_2 production tracks the change in ϕ and stabilizes quickly. K1 and K2 appear to take several minutes to reach equilibrium, but

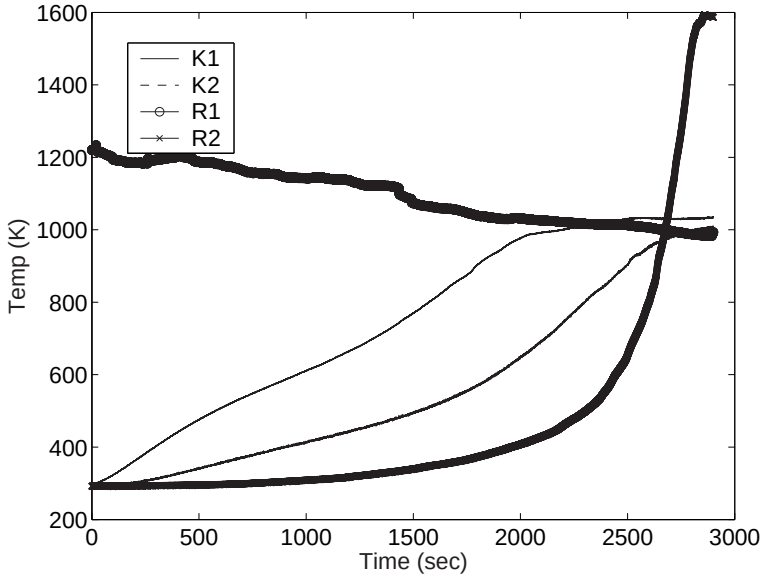

Figure 6.12: Start-up time for AL_2O_3 bead burner with methane as fuel.

they are measuring the temperature of the outside wall of the burner not the temperature of the reaction. R1 continues to increase as the downstream portion of the porous matrix absorbs more heat.

Fig. (6.14) and Fig. (6.15) plot the response of a warmed up SiC burner to an increase in ϕ. Fig. (6.15) has a higher mass flow rate than Fig. (6.14) and as expected reaches a higher H_2 peak and also settles at a higher H_2 production concentration.

These two tests are compared to similar tests using the bead burner, as plotted in Fig. (6.16) and Fig. (6.17). Interestingly both plots show a continuous increase in H_2 production prior to levelling off at a constant value instead of the peak and then decline to a stable point as observed for the SiC burner. As observed in Chapter 5, the steady state hydrogen production is considerably higher for the bead burner than for the SiC burner. H_2 production peaked in the foam burner with the lower flow rate after approximately 80 seconds, this decreased to 70

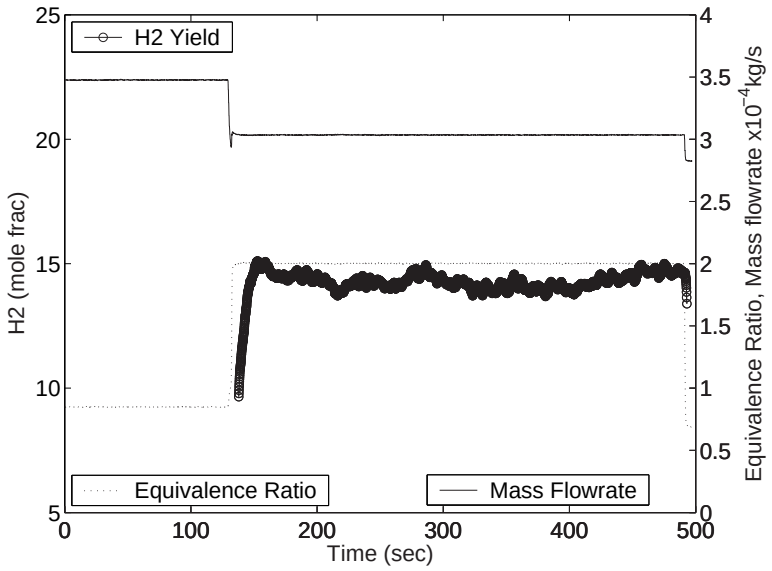

Figure 6.13: Effect on H_2 production when increasing ϕ from 0.85 to 2.0 by increasing fuel flow from $\dot{m}_{fuel} = 1.65\times10^{-5}$ kg/s to 3.18×10^{-5} kg/s, same test as performed in Fig. (6.11).

seconds as the mass flow rate was increased in the second test. At the same mass flow rates, it took the bead burner approximately 500 seconds to approach an asymptote at the lower flow rate and approximately 150 seconds at the higher flow rate.

A final test with this configuration was performed, where the ϕ was increased rapidly to 2.5. As is illustrated in Fig. (6.18) a similar result as to the other two tests in the bead burner was observed except with the H_2 concentration being higher.

6.4 Chapter Summary

The Fast TCD was able to measure the concentration of H_2 in a gas mixture as discussed in Chapter 3. The burner itself has an initial response time on the order of 0.5 seconds. The TCD's response is slower due to the time it takes the new gas mixture to diffuse into the filament housing and replace the previous gas composition. Its initial response is on the order of 1 second, however it takes approximately 7 seconds to reach steady state, depending on the operating conditions. A quicker response would be possible with either a semi-diffused or direct filament housing, although some stability in the signal would be sacrificed.

The burner reaches steady state conditions after a transient has been introduced quicker with increasing mass flow rates. The higher mass flow rates of reactants produce more heat resulting in shorter times to reach steady state operating conditions. H_2 output is also less disturbed when the fuel flow rate is varied instead of the air flow rate when moving to a different equivalence ratio. The burner is more easily unbalanced by a change in mass flow rate than the energy being released by the reaction.

The foam burner reaches equilibrium much faster than the bead burner with its larger thermal inertia. A flame will propagate to the interface within 120 seconds as opposed to over 30 minutes for the bead burner. In the foam burner H_2 production will peak and then level off to a lower stable concentration as ϕ is increased, whereas in the bead burner H_2 production will increase and then level off, there is no dip. As observed with the GC measurements in Chapter 5, the bead burner produces higher concentrations of H_2 than the foam burner.

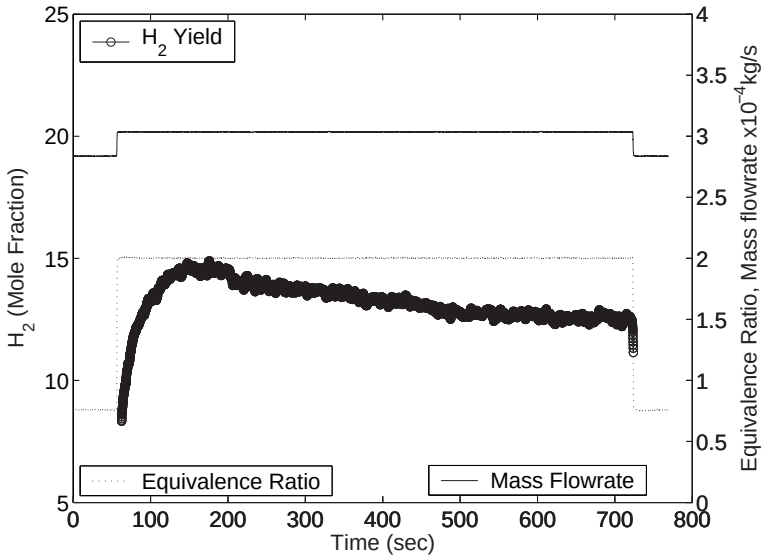

Figure 6.14: Response of SiC foam burner to a sudden change in ϕ from 0.75 to 2.0 by increasing fuel flow from $\dot{m}_{\text{fuel}} = 1.21\times10^{-5}$ kg/s to 3.18×10^{-5}kg/s. Mass flow rate on second y-axis is the total mass flow rate of air and fuel.

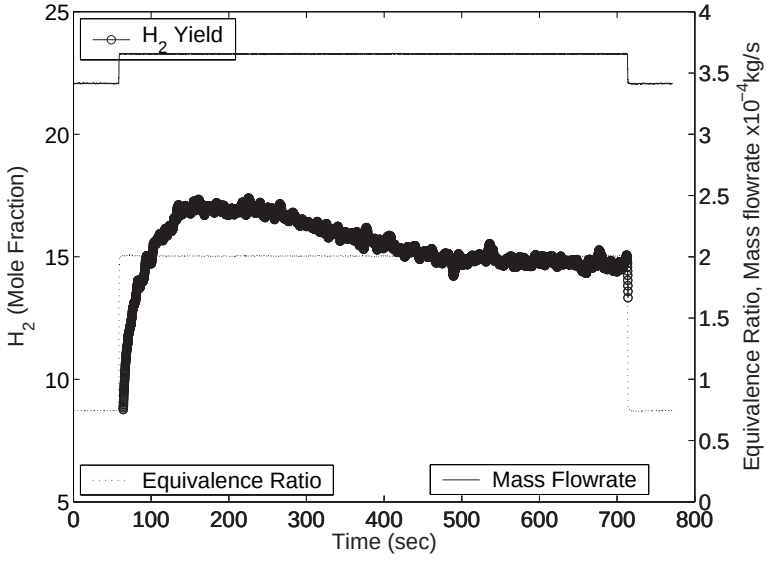

Figure 6.15: Response of SiC foam burner to a sudden change in ϕ from 0.75 to 2.0 by increasing fuel flow from $\dot{m}_{\text{fuel}} = 1.43\times10^{-5}$ kg/s to 3.84×10^{-5} kg/s. Mass flow rate on second y-axis is the total mass flow rate of air and fuel.

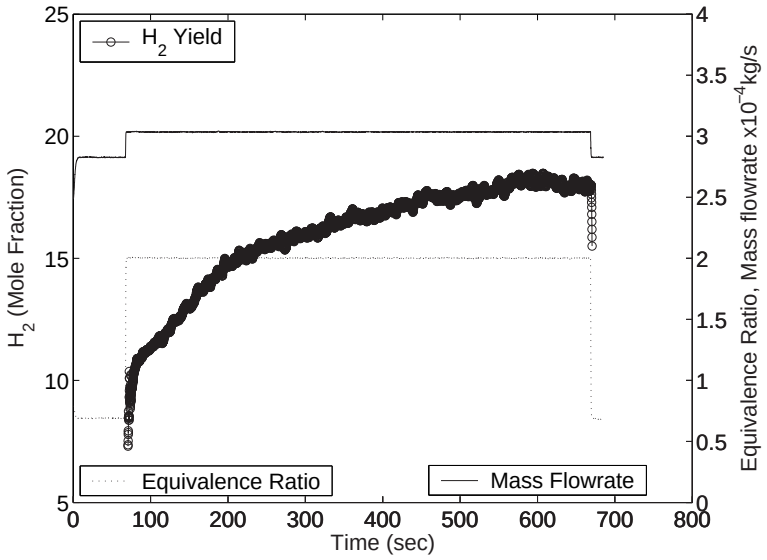

Figure 6.16: Response of bead burner to a sudden change in ϕ from 0.7 to 2.0 by increasing fuel flow from $\dot{m}_{\text{fuel}} = 1.10\times10^{-5}$ kg/s to 3.18×10^{-5} kg/s. Mass flow rate on second y-axis is the total mass flow rate of air and fuel.

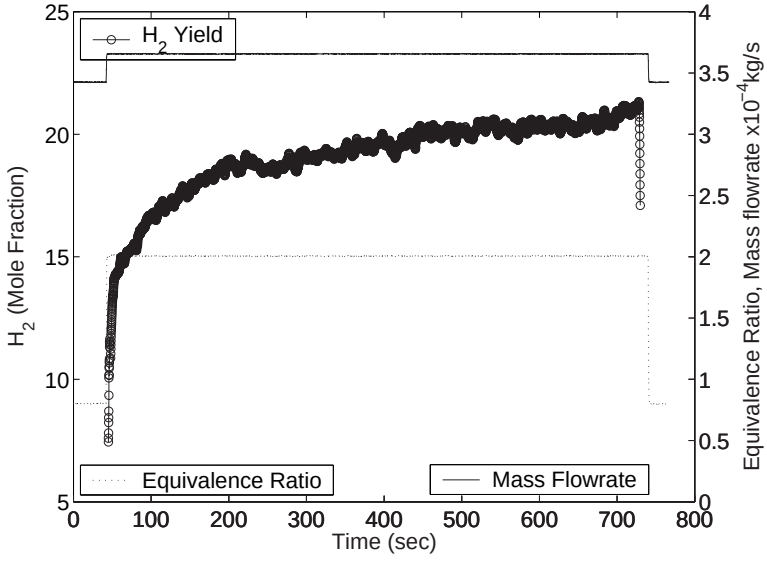

Figure 6.17: Response of bead burner to a sudden change in ϕ from 0.8 to 2.0 by increasing fuel flow from $\dot{m}_{\text{fuel}} = 1.54\times10^{-5}$ kg/s to 3.84×10^{-5} kg/s. Mass flow rate on second y-axis is the total mass flow rate of air and fuel.

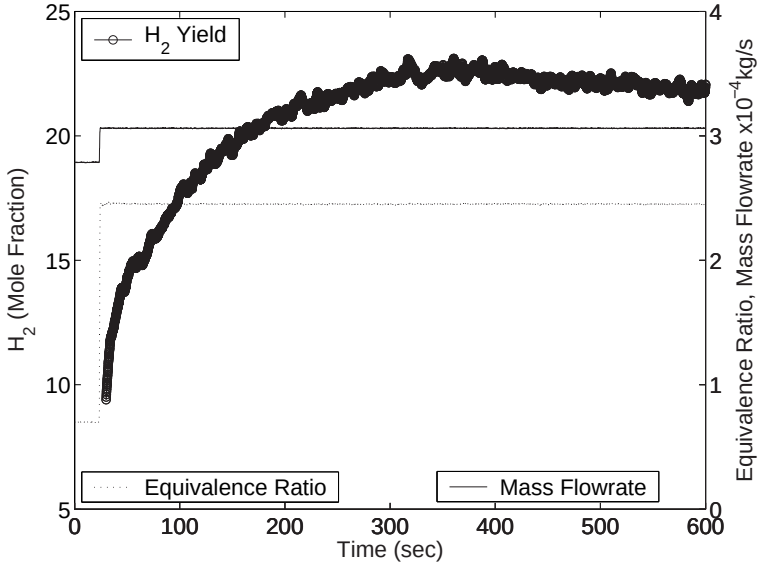

Figure 6.18: Response of bead burner to a sudden change in ϕ from 0.7 to 2.5 by increasing fuel flow from $\dot{m}_{\text{fuel}} = 1.10\times10^{-5}$ kg/s to 3.84×10^{-5} kg/s. Mass flow rate on second y-axis is the total mass flow rate of air and fuel.

Chapter 7

Summary and Suggestions for Further Research

7.1 Summary and Conclusions

The objectives of this thesis were to study the stability of stationary rich flames inside different types of inert porous media and to examine the possibility of extending the upper flammability limits. In addition, the overall effectiveness of this method to produce syngas from a variety of fuels and the burner's response to transients was investigated. The final objective was to test the robustness and operational lifetime of the porous media and burners.

In order to meet these objectives a range of experiments were performed. The apparatus was instrumented with K and R-type thermocouples to record the temperature of the burner and exhaust gases at various locations. In addition, a thermal imaging camera was used to determine the surface temperature of the beads at the exit of the burner and to determine the approximate location of the reaction within the burner. A commercial gas chromatograph calibrated to

measure $H_2, O_2, N_2, CO, CO_2, CH_4, C_2H_2, C_2H_4$ and C_2H_6 was used to determine the concentration of product species in the burner's exhaust. A Fast Thermal Conductivity Detector was designed and fabricated to measure H_2 in the exhaust gases from the burner on a continuous basis, especially during transients and start-up. Finally, a scanning mobility particle sizer was employed to measure the amount of particulates exiting the burner. All of the product species from the various fuels, except for biodiesel were compared to equilibrium calculations from the CEA code.

The large thermal mass of the PM burner allowed a flame to be re-ignited after a disruption in either oxidant or fuel by simply restoring the fuel and oxidant flows. The size of the burner was also determined to be scalable. There was no significant differences between the behaviour and H_2 production from the 30 mm and 50 mm I.D. burners as long as both were sufficiently insulated. Burners that did not have adequate insulation lost too much energy to the environment resulting in poorer flame stability.

Steady rich flames of methane, methanol, ethanol, iso-octane, petrol, kerosene (Jet A) and biodiesel were stabilized at the interface between two differently sized pored ceramic foams or differently sized beads over a range of equivalence ratios. The UFL of methane, methanol, ethanol and Jet A were increased by combustion inside the porous media. At a minimum, the conventional rich flammability limits for octane and petrol were also reached. Since the free-flame UFL for biodiesel was unknown a meaningful comparison could not be made.

A large operating envelope was also observed, making high turndown ratios possible. If the reactants' flow is increased the flame will propagate downstream away from the fine pored ceramic where more heat will be released, resulting in increased preheating of the reactants. The increased mass flow rate will also increase the amount of energy being released by the reactants. Both these mech-

anisms increase the flame's velocity and act as a restoring force on the flame, moving it back towards the interface. We have observed experimentally the predictions by Diamantis et al. (2002) that the self restoring force is only applicable in approximately the first half of the porous matrix. If a positive disturbance is introduced in the downstream section of the matrix the flame will propagate to the exit and blow-off will occur, with a slowly-moving combustion wave.

Steam was injected with the CH_4 in one set of experiments to determine if it was possible to enhance the methane steam reforming and water-gas shift reactions without a catalyst. However, these tests did not improve H_2 production. Without a catalyst, the residence time was too short and the temperatures too low to greatly affect the reactions.

An infrared imager was used to determine the surface temperature of the top layer of beads inside the burner. The burner's surface temperature would increase with increasing flow rates and is approximately 200 K higher than the thermocouple reading (R1) located 10 mm above the surface. In these tests a temperature gradient of up to $\pm$ 100 K was observed across the burner. A radiation/convection balance was done on the thermocouple bead and it was calculated that R1 underestimates the exhaust gases temperature by approximately 16-31 K.

The general trend for all the fuels tested was for H_2 production to initially increase with ϕ. After the flame became unstable and started to propagate downstream, H_2 production would also decrease. Increasing the mass flow rate, at a constant ϕ pushed the product species closer to equilibrium. At high mass flow rates, at least for methane and methanol, changing the probe's height above the burner did not affect the product species concentrations, indicating that the products had reached equilibrium, but at a temperature lower than the adiabatic temperature. At the lower flow rates, the lower temperatures combined with quenching on the walls, due to the temperature gradient across the burner,

allowed CH_4 penetration and reduced the fuel converted to syngas. The more complex fuels, octane, kerosene and biodiesel, did not achieve the same conversion efficiencies as the simpler fuels and significant amounts of the hydrogen remained trapped in CH_4 and the C_2s. Extracting the product species from rich CH_4 combustion at different points in the axial direction revealed that most of the fuel conversion takes place within the first 20 mm after the interface.

The Fast TCD was able to measure the concentration of H_2 in a gas mixture as discussed in Chapter 3 and Chapter 6. The burner itself has an initial response time on the order of 0.5 seconds. The TCD's response is slower due to the time it takes the new gas mixture to diffuse into the filament housing and replace the previous gas composition. Its initial response is on the order of 1 second, however it takes approximately 7 seconds to reach steady state, depending on the operating conditions.

The burner reaches steady state conditions after a transient has been introduced, quicker with increasing mass flow rates. H_2 output is also less disturbed when the fuel flow rate is varied instead of the air flow rate when moving to a different equivalence ratio. The burner is more easily unbalanced by a change in mass flow rate than the energy being released by the reaction.

The foam burner reaches equilibrium much faster than the bead burner with its larger thermal inertia. A flame will propagate to the interface within 120 seconds as opposed to over 30 minutes for the bead burner. In the foam burner H_2 production will peak and then level off to a lower stable concentration as ϕ is increased, whereas in the bead burner H_2 production will increase and then level off, there is no dip. In agreement with the GC measurements in Chapter 5, the bead burner produces higher concentrations of H_2 than the foam burner.

No soot or carbon deposits were visible for methane, methanol, ethanol or kerosene. However, for octane, petrol and biodiesel soot was visible at higher

equivalence ratios. In addition biodiesel left residual deposits around the entrance to the burner and exit of the vapourizer. Results from the SMPS, revealed that running on filtered lab air, CH_4 combusted inside the PM burner has fewer particulates than the ambient lab air up to an equivalence ratio of 2.0, under steady state conditions. At higher equivalence ratios and also during transients the particulate count increased drastically. At a ϕ of 2.5 the mass flux of particulates for C_8H_{18} is an order of magnitude greater than that for CH_4 operating at steady state at a ϕ of 2.5.

It can be concluded that beads will have a longer operational lifetime than foams as they are less susceptible to thermal stresses and solid beads will last longer than desiccant beads. Quartz and stainless steel are adequate materials to manufacturer the burner from for lower temperatures. However, the best material, over a wide range of fuels, to manufacturer the burner from is Kanthal®. The Kanthal® burner showed no signs of stress or degradation after enduring over 100 hours of testing with various fuels.

The maximum conversion efficiencies for CH_4 was 55 %, for CH_3OH 61 %, for C_2H_5OH 37 %, for C_8H_{18} 34 %, for kerosene 28 % and for biodiesel 15 %. These conversion efficiencies were based on comparing the LHV of H_2 and CO in the products to the LHV of the fuel. Considerable amounts of CH_4, C_2H_2 and C_2H_4 were measured in the combustion products of octane, petrol, kerosene and biodiesel at higher equivalence ratios which cannot be explained by equilibrium conditions, hence suggesting finite rate effects.

These results show that stationary rich combustion inside a porous medium can be used to reform liquid and gaseous fuels into syngas. This particular burner produces the highest concentrations of H_2 at high mass flow rates operating in the stationary mode. Once the flame starts to propagate in either direction, H_2 concentration decreases and particulate concentrations increase.

Specifically for the materials and fuels tested, the support layer (lower) should be 20-30 mm thick consisting of Al_2O_3 beads with a diameter $2 \leq \theta < 3$. The combustion layer (upper) for CH_4 and CH_3OH should be between 60-70 mm of Al_2O_3 beads with a diameter $3 < \theta \leq 9$ (9 mm being the largest diameter beads tested). The support layer for the other fuels tested should be the same. The combustion layer also use the same diameter beads but should be greater than 80 mm in length in order for the exhaust gases to approach chemical equilibrium.

Quick startup times, compact size and high turn down ratios make it a potential candidate for the next generation fuel cell powered automobile. In addition, its scalability and ability to process various fuels translates into applications in the stationary power industry.

7.2 Suggestions for Further Research

Further research should include more experimental tests and also modelling. On the experimental side, the probe's height should be varied for all the fuels tested, not just CH_4, to determine the optimal length of porous media in the combustion zone. A catalyzed third layer of porous media can also be added to decrease the temperature and residence time of the reactants required in order to drive the H_2O-gas shift and steam reforming reactions.

On the modelling side, a full kinetic model of the chemistry for rich combustion would be most beneficial in helping to understand current experimental results and improving the design of future burners. Ideally, a two dimensional model should be created as there are temperature gradients in the radial direction within the burner. As was seen, these gradients can affect the performance of the burner, especially when operating with very rich mixtures at low mass flow rates. This code should then be validated against the experimental results from this thesis.

Appendix A

Flame Speed Correlations

In free flames, flame temperature and laminar velocity are a function of the equivalence ratio and the initial pressure and temperature of the incoming reactants. In porous media they are also dependent on flow velocity and porous particle diameter. At steady state conditions, the laminar flame velocity is equal to the flow speed of the reactants in the free area space divided by the porosity of the porous media.

Metghalchi and Keck (Metghalchi and Keck, 1982) experimentally determined laminar flame speeds for several fuels at various fuel-air mixtures and temperatures. A modified version of their most useful correlation for calculating laminar flame speeds over a range of temperatures and equivalence ratios is given below

$$S_L = S_{L,ref} \left(\frac{T_u}{T_{u,ref}} \right)^{\gamma} \tag{A.1}$$

The subscript ref refers to standard temperature and pressure conditions.

$$S_{L,ref} = M_M + B_2(\phi - \phi_M)^2 \tag{A.2}$$

and

$$\gamma = 2.18 - 0.8(\phi - 1) \tag{A.3}$$

the constants B_M, B_2 and ϕ_M depend on fuel type and are given in Table (A.1).

Table A.1: Values for B_M, B_2 and ϕ_M used with Eq.(A.3).

(Metghalchi and Keck, 1982)

Fuel	ϕ_M	B_M (cm/s)	B_2 (cm/s)
Methanol	1.11	36.92	-140.51
Isoctane	1.13	26.32	-84.72

Appendix B

GC Sample Printouts

Software Version	: 6.2.0.0.0:B27	Date	: 23/07/2003 12:14:49
Sample Name	:	Data Acquisition Time	: 13/05/2003 12:19:14
Instrument Name	: Autosystem	Channel	: A
Rack/Vial	: 0/0	Operator	: HAAKON
Sample Amount	: 1.000000	Dilution Factor	: 1.000000
Cycle	: 1		

Result File : C:\TCDATA\Test Data3\13May03_A001.rst
Sequence File : C:\TCDATA\Sequence\28mar.seq

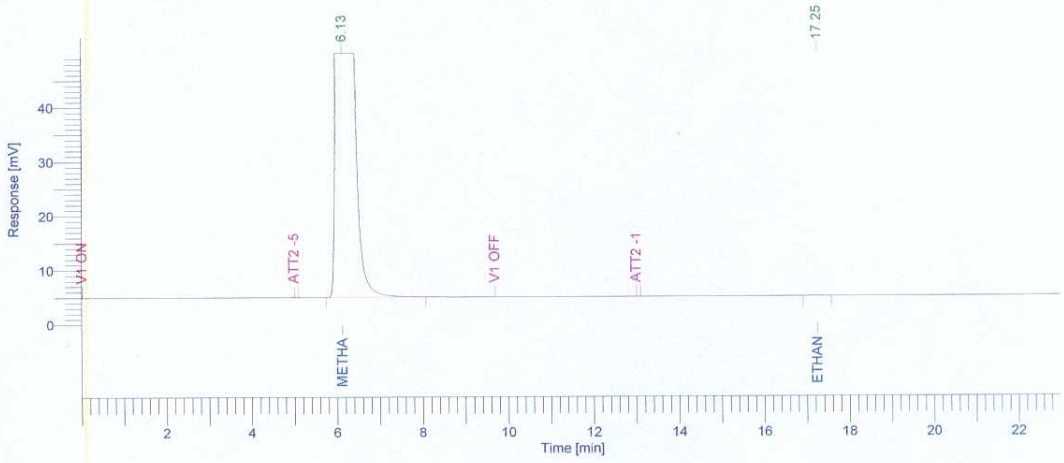

FID GAS ANALYSIS REPORT

Peak #	Component Name	Time [min]	Area [uV*sec]	% Concentration
1	METHANE	6.130	6409080.19	10.2521
-	ETHYLENE	14.655	0.00	0.0000
2	ETHANE	17.254	1121.63	0.0010
-	ACETYLENE	20.131	0.00	0.0000
			6410201.82	10.2530

Missing Component Report

Component	Expected Retention (Calibration File)
ETHYLENE	14.655
ACETYLENE	20.131

Figure B.1: GC FID printout of unlit 10% methane in air mixture.

Software Version	: 6.2.0.0.0:B27	Date	: 23/07/2003 12:16:00
Sample Name	:	Data Acquisition Time	: 13/05/2003 12:19:14
Instrument Name	: Autosystem	Channel	: B
Rack/Vial	: 0/0	Operator	: HAAKON
Sample Amount	: 1.000000	Dilution Factor	: 1.000000
Cycle	: 1		

Result File : C:\TCDATA\Test Data3\13May03_B001.rst
Sequence File : C:\TCDATA\Sequence\28mar.seq

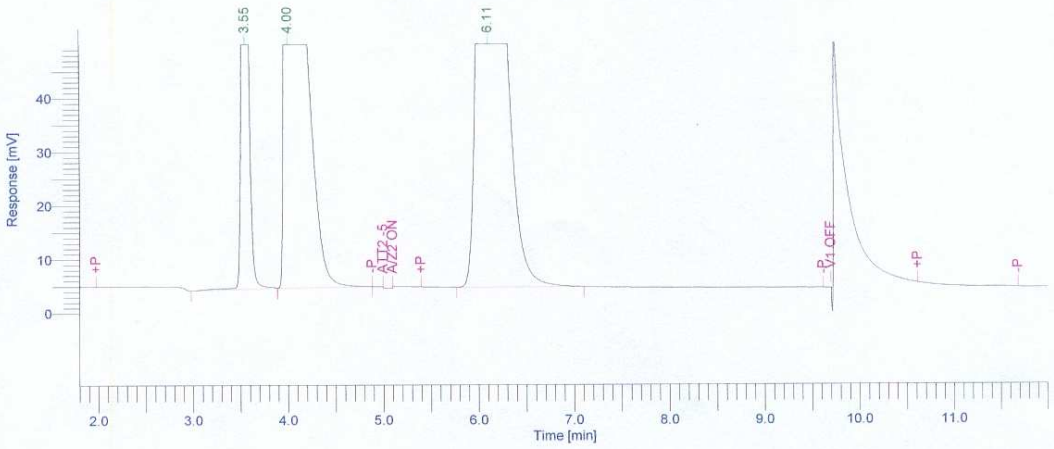

TCD GAS ANALYSIS REPORT

Peak #	Component Name	Time [min]	Area [uV*sec]	% Concentration
-	HYDROGEN	2.651	0.00	0.0000
-	CO	8.356	0.00	0.0000
-	CO2	11.236	0.00	0.0000
			0.00	0.0000

Missing Component Report

Component	Expected Retention (Calibration File)
HYDROGEN	2.651
CO	8.356
CO2	11.236

Figure B.2: GC TCD printout of unlit 10% methane in air mixture.

Appendix C

R2 Radiation Correction

R2 is an R-type mineral insulated thermocouple (TC) located at the interface between the two layers of beads (y=0 mm). See Fig. (2.1) and Fig. (2.2). The purpose of R2 is to measure the temperature of the gas in the voids of the porous media. However, due to radiation from the gases and surrounding porous media, conduction along the TC and to the porous media and convection between the TC and the gas, the temperature of the TC bead may be at a different temperature than the gas. The following analytical and numerical model investigates the energy balance between the TC bead and its surroundings.

Fig. (C.1) illustrates the geometry around the TC bead and control volume used. There are three bodies: (1) thermocouple (TC), (2) ceramic beads (CER) and (3) gas (GAS). There is heat transfer between the gas and ceramic beads via radiation and convection. Radiation and convection also exist between the gas and the TC. The ceramics will radiate and convect heat to and from the TC. Additionally, the TC will loose heat to the environment via conduction along its length. Finally, the gas will be heated by the enthalpy of combustion, Q_{IN}, generated from the fuel and oxidant. Fig. (C.2) illustrates the three modes of heat transfer within the control volume described above.

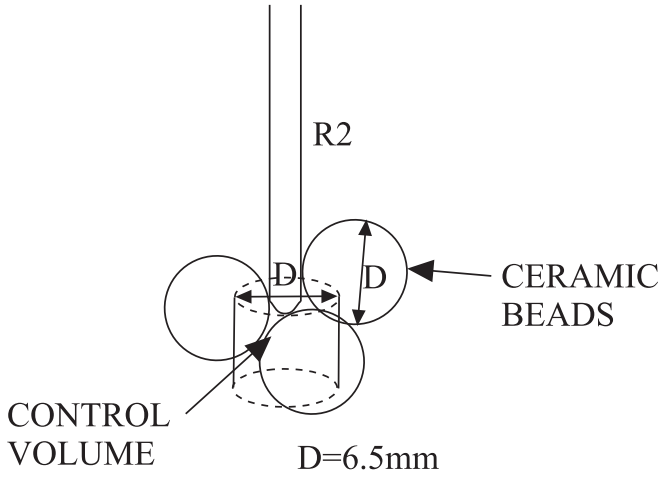

Figure C.1: Control volume for radiation, convection and conduction between the gas, thermocouple and ceramic beads.

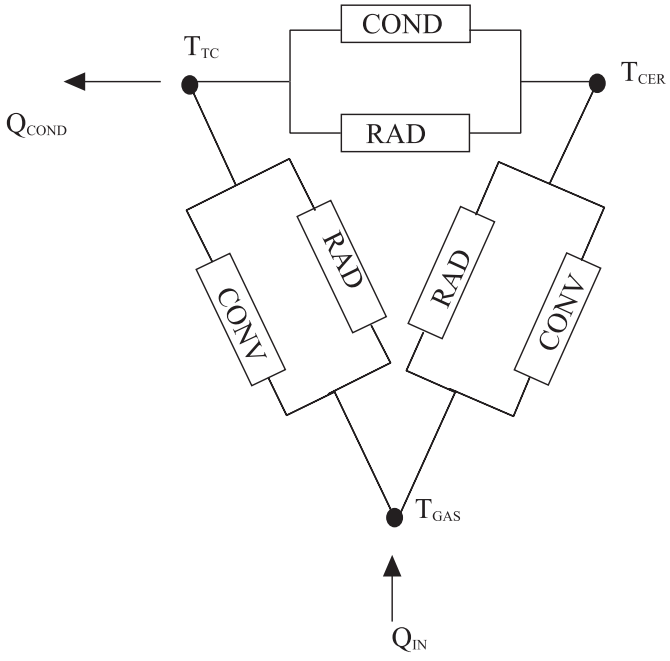

Figure C.2: Radiation, convection and conduction between the gas, thermocouple and ceramic beads.

In order to perform an energy balance on the TC bead the following assumptions are made:

- Heat of combustion is uniform across burner.
- The TC bead is at the same temperature as the TC sheath.
- The contact area between the beads and the TC are small compared to the void space around the TC.

Assuming that the contact area between the TC and ceramic beads is small, the radiation transfer between the TC and ceramic beads will dominate. The number of equations can be reduced further if either $Q_{rad} >> Q_{conv}$ or $Q_{conv} >> Q_{rad}$. The radiation exchange between two bodies can be written as

$$q_{rad} = \frac{\sigma T_{CER}^4 - \sigma T_{TC}^4}{(1-\epsilon_{CER})/(A_{CER}\epsilon_{CER}) + 1/(A_{CER})(F_{CER\rightarrow TC}) + (1-\epsilon_{TC})/(A_{TC}\epsilon_{TC})} \tag{C.1}$$

where ϵ is the emissivity of the three bodies. $\epsilon_{CER} = 0.81$ as was calculated in Section 2.4.1. ϵ_{TC} is estimated to be the same as it is made of a similar material. The emissivity of the gas is estimated to be between 0.01 and 0.04 (Vollmer et al., 2004). Eq. (C) was derived from (Ozisik, 1985).

$F_{CER\rightarrow TC}$ is the view factor from the ceramic to the TC. Since the TC only 'sees' ceramic beads, $F_{CER\rightarrow TC} = 1$. $F_{TC\rightarrow CER}$ can be calculated through reciprocity,

$$F_{CER\rightarrow TC} = \frac{A_{TC}}{A_{CER}} F_{TC\rightarrow CER} \tag{C.2}$$

The equation for the amount of energy transferred via convection from the gas to the ceramic is

$$q_{conv} = A_{CER}(T_{GAS} - T_{CER})h \tag{C.3}$$

and from the gas to the TC is

$$q_{conv} = A_{TC}(T_{GAS} - T_{TC})h \tag{C.4}$$

The convective heat transfer coefficient may be solved for using,

$$h = \frac{kNu}{D} \tag{C.5}$$

where k is the thermal conductivity of air and D is the diameter of the thermocouple bead.

The Nusselt Number, (Nu), for forced convection flow past a sphere may be calculated using Eq. (C.6) which is valid for:

$3.5 < Re < 8 \times 10^4$

$0.7 < Pr < 380$

$$Nu = 2 + (0.4Re^{0.5} + 0.06Re^{0.67})Pr^{0.4} \tag{C.6}$$

where Re is defined as

$$Re = \frac{VD}{\nu}. \tag{C.7}$$

The enthalpy of combustion is calculated using

$$\mathrm{Q_{IN}} = \sum_{\mathrm{prod}} \mathrm{n_i h_i} - \sum_{\mathrm{reac}} \mathrm{n_i h_i} \tag{C.8}$$

where the number of moles of the product species are calculated in Appendix D. The enthalpy of combustion is illustrated in Fig. (C.3). As the ϕ is increased, less energy is released as the amount of energy being tied up in product species also increases.

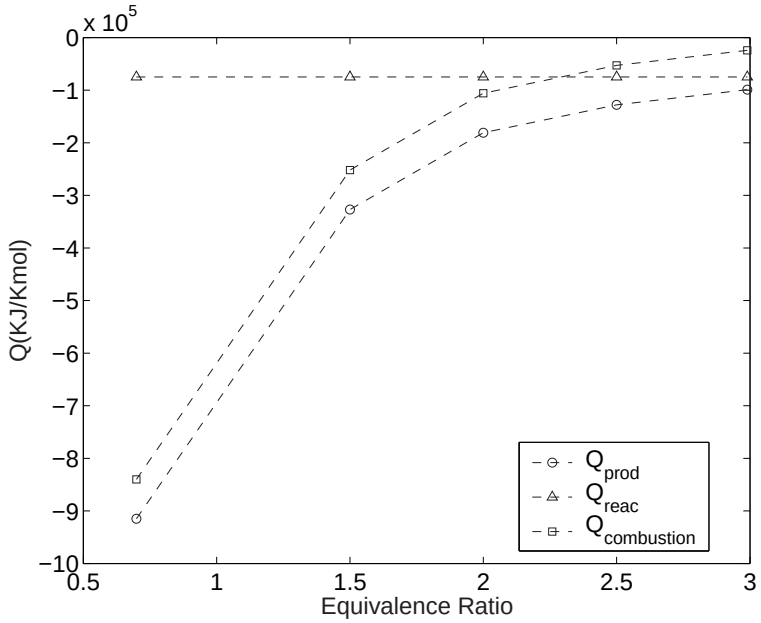

Figure C.3: Enthalpy of combustion for methane using experimental data from 7.5-9.0 mm bead test.

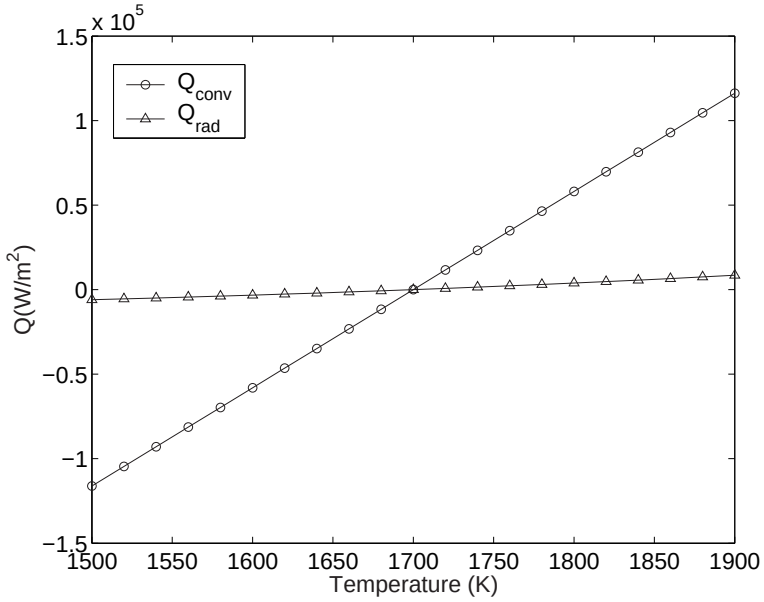

Figure C.4: Comparison of energy transfer by radiation versus convection.

Fig. (C.4) compares the amount of energy being transferred via convection versus the amount through radiation. The majority of energy transferred is through convection not radiation. According to studies performed by Vollmer et al. (2004), the emissivity (ϵ) for a hot gas or flame is between 0.1-0.4. Using the higher value still results in the majority of energy been transferred via convection. Therefore, by ignoring the amount of energy being transferred by radiation from the gas, Fig. (C.2) can be simplified to Fig. (C.4).

Performing an energy balance at the GAS node gives

$$q_{in} = q_{GAS \rightarrow CER} + q_{GAS \rightarrow TC} \tag{C.9}$$

and at the CER node

$$q_{GAS \rightarrow CER} = q_{CER \rightarrow TC}. \tag{C.10}$$

where $q_{CER \rightarrow TC}$ is the radiation term defined by Eq. (C) and the other terms are

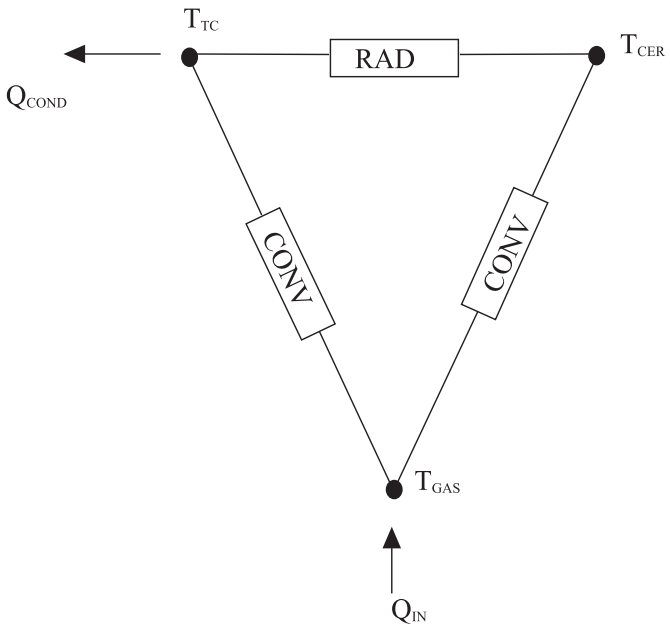

Figure C.5: Major sources of heat transfer between the three bodies.

convective.

This equation can be solved numerically. In this example a methane flame was combusted at the interface between 20 mm of 2-3 mm Al_2O_3 beads and 80 mm of 7.5-9.0 mm Al_2O_3 beads in the 52.5 mm I.D. Kanthal® burner . The data used in these calculations is compiled in Table C.1.

The results are plotted in Fig. (C.6). The TC has the largest errors associated with it for lower equivalence ratios corresponding to higher temperatures and higher enthalpies of combustion. As Q_{IN} decreases the temperatures of the TC, ceramic beads and the gas converge.

Table C.1: Data used in R2 calculations

Fuel (LPM)	Air (LPM)	ϕ	R2(Raw) K
1.5	20.3	0.7	1595
4.0	25.2	1.5	1738
5.0	20.0	2.0	1526
4.5	17.0	2.5	1526
3.0	9.5	3.0	1543

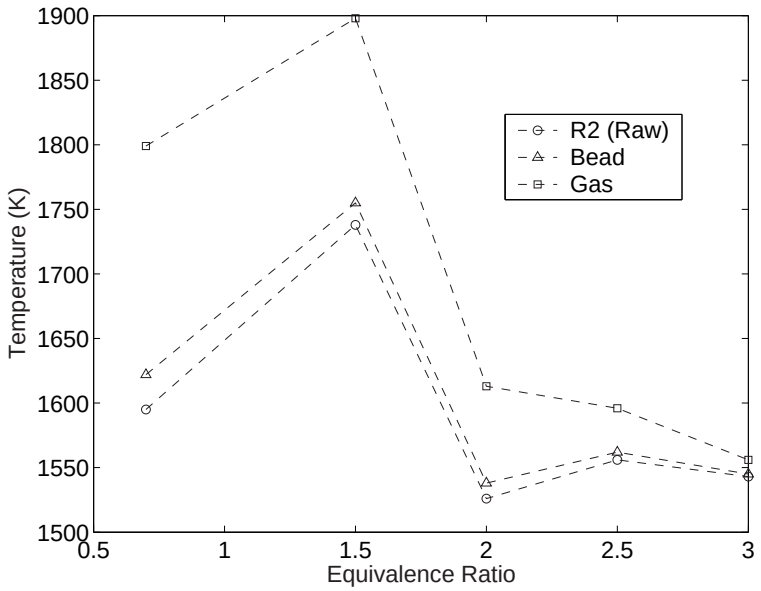

Figure C.6: Calculated temperature of gas and ceramic (beads) compared to raw, R2, temperature measurement.

Appendix D

Carbon Balance

The gas chromatograph measures the mole fractions of the following product species $CO_2, CO, H_2, O_2, N_2, CH_4, C_2H_4, C_2H_4 \text{and} C_2H6$ after the H_2O has been removed. In order to perform a carbon balance the mole fractions must first be converted to moles. The following generic formula represents the various hydrocarbon fuels tested,

$$\begin{aligned} C_xH_y + \frac{a}{\phi}(O_2 + 3.76N_2) \rightarrow a_1CO_2 + a_2CO + a_3H_2O + a_4H_2 + a_5O_2 \\ + \frac{3.76a}{\phi}N_2 + a_6CH_4 + a_7C_2H2 + a_8C2H4 + a_9C_2H_6 \end{aligned} \quad \text{(D.1)}$$

where a = x + y/4 and the variables a1 through a9 are in moles.

Rewriting this equation in mole fractions gives the following 9 equations:

$$XCO_2 = a_1/(a_1 + ... + a_9 + 3.76a/\phi) \quad \text{(D.2)}$$

$$XCO = a_2/(a_1 + ... + a_9 + 3.76a/\phi) \quad \text{(D.3)}$$

$$X\mathrm{H_2} = \mathrm{a_4}/(\mathrm{a_1} + ... + \mathrm{a_9} + 3.76\mathrm{a}/\phi) \tag{D.4}$$

$$X\mathrm{O_2} = \mathrm{a_5}/(\mathrm{a_1} + ... + \mathrm{a_9} + 3.76\mathrm{a}/\phi) \tag{D.5}$$

$$X\mathrm{N_2} = \frac{3.76\mathrm{a}}{\phi}/(\mathrm{a_1} + ... + \mathrm{a_9} + 3.76\mathrm{a}/\phi) \tag{D.6}$$

$$X\mathrm{CH_4} = \mathrm{a_6}/(\mathrm{a_1} + ... + \mathrm{a_9} + 3.76\mathrm{a}/\phi) \tag{D.7}$$

$$X\mathrm{C_2H_2} = \mathrm{a_7}/(\mathrm{a_1} + ... + \mathrm{a_9} + 3.76\mathrm{a}/\phi) \tag{D.8}$$

$$X\mathrm{C_2H_4} = \mathrm{a_8}/(\mathrm{a_1} + ... + \mathrm{a_9} + 3.76\mathrm{a}/\phi) \tag{D.9}$$

$$X\mathrm{C_2H_6} = \mathrm{a_9}/(\mathrm{a_1} + ... + \mathrm{a_9} + 3.76\mathrm{a}/\phi) \tag{D.10}$$

However, only 8 of the 9 equations are independent as the mole fractions add up to unity. Replacing the equation for $\mathrm{N_2}$ with an independent ninth equation relating the average mass of the products (MW_{prod}) to the number of moles results in 9 equations and 9 unknowns. This equation can be written as

$$n = \frac{m}{MW_{prod}} \tag{D.11}$$

where MW_{prod} calculated based on the measured mole fractions of the product species. Assuming mass is conserved in the reaction and all of the reactants are converted into products (soot is assumed to be negligible as calculated in Section 4.5) then m is equivalent to the mass of the reactants.

These 9 linear equations can now be solved simultaneously using the following matrices:

$$[A]^{-1}[B] = [C] \tag{D.12}$$

where $[A], [B]$ and $[C]$ are defined as

$$[\mathrm{A}] = \begin{pmatrix} X_{CO_2}-1 & X_{CO_2} & X_{CO_2} & X_{CO_2} & X_{CO_2} & X_{CO_2} & X_{CO_2} & X_{CO_2} & 0 \\ X_{CO} & X_{CO}-1 & X_{CO} & X_{CO} & X_{CO} & X_{CO} & X_{CO} & X_{CO} & 0 \\ X_{H_2} & X_{H_2} & X_{H_2}-1 & X_{H_2} & X_{H_2} & X_{H_2} & X_{H_2} & X_{H_2} & 0 \\ X_{O_2} & X_{O_2} & X_{O_2} & X_{O_2}-1 & X_{O_2} & X_{O_2} & X_{O_2} & X_{O_2} & 0 \\ X_{CH_4} & X_{CH_4} & X_{CH_4} & X_{CH_4} & X_{CH_4}-1 & X_{CH_4} & X_{CH_4} & X_{CH_4}0 & \\ X_{C_2H_2} & X_{C_2H_2} & X_{C_2H_2} & X_{C_2H_2} & X_{C_2H_2} & X_{C_2H_2}-1 & X_{C_2H_2} & X_{C_2H_2} & 0 \\ X_{C_2H_4} & X_{C_2H_4} & X_{C_2H_4} & X_{C_2H_4} & X_{C_2H_4} & X_{C_2H_4} & X_{C_2H_4}-1 & X_{C_2H_4} & 0 \\ X_{C_2H_6} & X_{C_2H_6} & X_{C_2H_6} & X_{C_2H_6} & X_{C_2H_6} & X_{C_2H_6} & X_{C_2H_6} & X_{C_2H_6}-1 & 0 \\ 1 & 1 & 1 & 1 & 1 & 1 & 1 & 1 & 1 \end{pmatrix}$$

[B] =

$$\begin{pmatrix} a1 \\ a2 \\ a4 \\ a5 \\ a6 \\ a7 \\ a8 \\ a9 \\ a3 \end{pmatrix}$$

and

[C] =

$$\begin{pmatrix} -X_{CO_2} * 3.76 * a/\phi \\ -X_{CO} * 3.76 * a/\phi \\ -X_{H_2} * 3.76 * a/\phi \\ -X_{O_2} * 3.76 * a/\phi \\ -X_{CH_4} * 3.76 * a/\phi \\ -X_{C_2H_2} * 3.76 * a/\phi \\ -X_{C_2H_4} * 3.76 * a/\phi \\ -X_{C_2h_6} * 3.76 * a/\phi \\ (MW_{fuel} + a/\phi * (MW_{O_2})/MW_{prod}) \end{pmatrix}$$

The GC can measure each gas to within ±2%. Taking the RMS of the error associated with each species containing carbon results in the carbon balance being accurate to within ±6%. This error is calculated using the following formula,

$$Error = (E_{CO_2}^2 + E_{CO}^2 + E_{CH_4}^2 + 2E_{C_2H_2}^2 + 2E_{C_2H_4}^2 + 2E_{C_2H_6}^2)^{0.5}. \qquad \text{(D.13)}$$

Bibliography

S. Ahmed and M. Krumpelt. Hydrogen from hydrocarbon fuels for fuel cells. *International Journal of Hydrogen Energy*, 26:291–301, 2001. 1.1, 1.3.1, 1.3.4, 5.4

Anonymous. Gas chromatography. Technical report, Sheffield Hallam University, http://www.shu.ac.uk/schools/sci/chem/tutorials/chrom/gaschrm.htm, 2002. 2.11

API. Alcohols: A technical assessment of their application as motor fuels. Technical Report No. 4261, American Petroleum Institute, 1976. (document), 4.2, *a*

H. Audus, O. Kaarstad, and M. Kowal. Decarbonization of fossil fuels: hydrogen as an energy carrier. In *Proceedings of the 11th World Hydrogen Energy Conference*, page 525, Stuttgart, Germany, 1996. 1.3.7

V. S. Babkin, A. A. Korzhavin, and V. A. Bunev. Propagation of premixed gaseous explosion flames in porous media. *Combustion and Flame*, 87:182–190, 1991. 1.4.4, 4.3.1

J. Bacha, F. Barnes, M. Franklin, L. Gibbs, G. Hemighaus, N. Hogue, D. Lesnini, J. Lind, J. Maybury, and J. Morris. Technical review aviation fuels. Technical report, Chevron Products Company, 2000. 4.3.5

A. Bansal, J. Beach, R. Collins, O. Khaselev, and J. A. Turner. Photoelectrochemical based direct conversion systems for hydrogen production. U.S. DOE Hydrogen Program Review, 1999. 1.3.10

A. Barra, G. Diepvens, J. Ellzey, and M. Henneke. Numerical study of the effects of material properties on flame stabilization in a porous burner. *Combustion and Flame*, 134:369–379, 2003. 1.4.4

A. Barra and J. Ellzey. Heat recirculation and heat transfer in porous burners. *Combustion and Flame*, 137:230–241, 2004. 1.4.4

L. Barreto, A. Makihira, and K. Riahi. The hydrogen economy in the 21st century: a sustainable development scenario. *International journal of Hydrogen Energy*, 28:267–284, 2003. 1.1

M. Batista, E. Santiago, E. Assaf, and E. Ticianelli. Evaluation of the water-gas shift and *co* methanation processes for purification of reformate gases and the coupling to a pem fuel cell system. *Journal of Power Sources*, 145:50–54, 2005. 5.4

P. J. Berlowitz and C. P. Darnell. Fuel choices for fuel cell powered vehicles. In *Fuel Cell Technology for Vehicles*, volume PT-84 of *SAE International Progress in Technology Series*, pages 45–55, 2000. 1.3.3

G. Besenbruch, L. Brown, J. Funk, and S. Showalter. High efficiency generation of hydrogen fuels using nuclear power. In *OECD/NEA information exchange meeting on Nuclear Production of Hydrogen*, Paris, France, 2000. 1.3.9

J. P. Bingue, A. V. Saveliev, A. A. Fridman, and L. A. Kennedy. Hydrogen production in ultra-rich filtration combustion of methane and hydrogen sulfide. *International Journal of Hydrogen Energy*, 27:643–649, 2002. 1.4.1, 1.4.3, 2.6

J.P. Bingue, A.V. Saveliev, and L.A. Kennedy. Optimization of hydrogen production by filtration combustion of methane by oxygen enrichment and depletion. *International Journal of Hydrogen Energy*, 29:1365–1370, 2004. 1.4.3, 5.4

G. Biskos. Calibration modification of the fast aerosol spectrometer. Technical report, Eng. Dept. University of Cambridge, 2001. 2.5.3

P. Bouma and L. De Goey. Premixed combustion on ceramic foam buners. *Combustion and Flame*, 119:133–143, 1999. 1.4.4

BP. Putting energy in the spotlight - bp statistical review of world energy. Technical report, British Petroleum Co, London, United Kingdom, 2005. 1.1

L. Brown, G. Besenbruch, R. Lentsch, K. Schultz, J. Funk, P. Pickard, A. Marshall, and S. Showalter. High efficiency generation of hydrogen fuels using nuclear power - final technical report for the period august 1, 1999 through september 30, 2002, prepared under the neri program grant no. defg0399sf21888 for the us department of energy. Technical report, 2003. 1.3.9

D. Butterworth. *Introduction to Heat Transfer*. Engineering Design Guides. Oxford University Press, 1977. 3.3.2

S. Cavallaro and S. Freni. Ethanol steam reforming in a molten carbonate fuel cell: a preliminary kinetic investigation. *International Journal of Hydrogen Energy*, 21(6):465–469, 1996. 5.3.3

M. Chase, C. Davies, J. Downey, D. Frurip, R. McDonald, and A. Syverud. Janaf thermochemcial tables, 3rd ed. *Journal of Physical and Chemical Reference Data*, 14, 1985. 5.2

M. Cropper. Chrysler develops fuel cell van using novel hydrogen storage technology. *Fuel Cell Today*, Dec. 2001. 1.3.9

B. Davis. Overview of reactors for liquid phase fischer-tropsch synthesis. *Catalysis Today*, 71:249–300, 2002. 1.1

N. Delalic, N. Ganic, and M. Likic. Experimental study on combustion in a porous media. In *Euro Conference - Renewable Technologies for Sustainable Development*, Medeira Island, Portugal, 2000. 1.4.4

R. Dhamrat and J. Ellzey. Numerical and experimental study of the conversion of methane to hydrogen in a porous media reactor. *Combustion and Flame*, To appear. 5.3.1

D. J. Diamantis, E. Mastorakos, and D.A. Goussis. Simulations of premixed combustion in porous media. *Combustion Theory and Modelling*, 6:383–411, 2002. 1.4.1, 1.4.4, 4.3.2, 4.3.2, 4.4, 4.4.1, 5.3.1, 7.1

Doceram. http://www.doceram.com/e/ mat1.htm. Internet, 2003. 2.3

M. K. Drayton, A. V. Saveliev, L. A. Kennedy, A. A. Fridman, and Y. Li. Syngas production using superadiabatic combustion of ultra-rich methane-air mixtures. *Proc. Comb. Inst.*, Twenty-Seventh Symposium on Combustion:1361–1367, 1998. 1.4.1, 1.4.3, 2.6, 4.4, 5.3.1, 5.3.1, 5.3.1

DuPont. Private phone conversation with dupont, 2002. 1.3.1

R. Echigo. Effective energy conversion method between gas enthalpy and thermal radiation and application to industrial furnaces. In *Proceedings 7th International Heat Transfer Conference*, volume VI, pages 361–366, Munich, 1982. 1.4.1

A. Egerton, K. Gugan, and F.J. Weinberg. The mechanism of smouldering in cigarettes. *Combustion and Flame*, 7(63-78), 1963. 1.4.1

F. Egolfopoulos, D. Du, and C. Law. A comprehensive study of methanol kinetics in freely-propagating and burner-stabilized flames, flow and static reactors, and shock tubes. *Combustion Science and Technology*, 83:33–75, 1992. 4.3.2

A. Ersoz, H. Olgun, S. Ozdogan, C. Gungor, F. Akgun, and M. Tlrls. Autothermal reforming as a hydrocarbon fuel processing option for pem fuel cell. *Journal of Power Sources*, 118(1-2):384–392, 2003. 1.1

B. Ewan and R. Allen. A figure of merit assessment of the routes to hydrogen. *International Journal of Hydrogen Energy*, 30:809–819, 2005. 1.3.1, 1.3.7, 1.3.8

M. Fay, R. Dhamrat, and J. Elllzey. Effect of porous reactor design on conversion of methane to hydrogen. *Combustion Science and Technology*, 177:2171–2189, 2005. 5.3.1, 5.3.1, 5.4

I. Fishtik, A. Alexander, R. Datta, and D. Geana. A thermodynamic analysis of hydrogen production by steam reforming of ethanol via response reactions. *International Journal of Hydrogen Production*, 25:31–45, 2000. 5.3.3, 5.3.3

Flir. *ThermaCAM SC 3000 Specifications*. Flir Systems, 2000. 2.4.1

V. Galvita, G. Semin, V. Belyaev, V. Semikolenov, P. Tsiakaras, and V. Sobyanin. Synthesis gas production by steam reforming of ethanol. *Applied Catalysis A: General*, 220:123–127, 2001. 5.3.3

I. Glassman. *Combustion*. Academic Press, San Diego, 3rd edition, 1996. 4.3.4

Goodfellow. http://www.goodgellow.com/csp/active/gfmaterialinfo.csp. Internet, 2003. 2.3

S. Gordon and B. McBride. Thermodynamic data to 20,000 k for monatomic gases. Technical Report NASA/TP-1999-20853, 1999. 5.2

S. Gordon and B.J. McBride. Computer program for calculation of complex chemical equilibrium compositions and applications. Part I: Analysis NASA RP-1311, 1994. 1.5.2, 5.2

M. Hagan, W. Northrop, B. Bowers, J. Rumsey, and S. Prabhu. Automotive fuel processing for PEM fuel cells. In *Fuel Cell Technology for Vehicles*, volume PT-84 of *SAE International Progress in Technology Series*, pages 103–110, 2000. 5.4

D. Hahn. Design features of advanced sodium-cooled fast reactor kalimer-600. In *2004 international congress on advances in nuclear power plants*, Pittsburgh, PA, USA, 2004. ICAPP2004. 1.3.9

K. Hanamura, R. Echigo, and S. Zhdanok. Superadiabatic combustion in a porous medium. *International Journal of Heat and Mass Transfer*, 36(13):3201–3209, 1993. 1.4.3

D. Hardesty and F. Weinberg. Burners producing large excess enthalpies. *Combustion Science and Technology*, 8:201–214, 1974. (document), 1.7, 1.4.1

W. Hinds. *Aerosol Technology: Properties, Behavior, and Measurement of Airborne Particles*. John Wiley & Sons, Inc, New York, 2nd edition, 1999. 1.3.12, 4.5

Z. Hou, B. Yi, H. Yu, Z. Lin, and H. Zhang. Co tolerance electrocatalyst of $PtRu - H_xMeO_3/C(Me = W, Mo)$ made by composite support method. *Journal of Power Sources*, 123:116–1125, 2003. 1.3.1

J. Howell, M. Hall, and J. Ellzey. Combustion of hydrocarbon fuels within porous inert media. *Progress in Energy and Combustion Science*, 22(2):121–145, 1996. 1.4.4

P. Hsu, W. Evans, and J. Howell. Experimental and numerical study of premixed combustion within nonhomogenous porous ceramics. *Combust. Sci. and Tech.*, 90:149–172, 1993. 1.4.1, 1.4.4, 1.4.4, 4.3.2

IAEA. Hydrogen as an energy carrier and its production by nuclear power. Tecdoc-1085, Report IAEA, 1999. 1.1

Y. Itaya, T. Oyashiki, and M. Hasatani. Hydrogen production by methane-rich combustion in a ceramic burner. *Journal of Chemical Engineering of Japan*, 35(1):46–56, 2002. 1.4.4, 4.2

M. Z. Jacobson. Strong radiative heating due to the mixing state of black carbon in atmospheric aerosols. *NATURE*, 409(6821):695–697, 2001. 1.3.12

Y. Jamal and M. Wyszynski. On-board generation of hydrogen-rich gaseous fuels - a review. *International Journal of Hydrogen Energy*, 19(7):557–572, 1994. 1.1

S. Jugjai and N. Polmart. Enhancement of evaporation and combustion of liquid fuels through porous media. *Experimental Thermal and Fluid Science*, 27: 901–909, 2003. 1.4.4, 4.3.2

S. Jugjai, N. Wongpanit, T. Laoketkan, and S. Nokkaew. The combustion of liquid fuels using a porous medium. *Experimental Thermal and Fluid Science*, 26:15–23, 2002. 1.4.4, 4.3.2

Y. Kant and K. Badarinath. Determination of effective emissivity and temperature over inhomogeneous land surfaces - results from field campaign. *Current Science*, 77(11):1348–1351, 1999. 2.4.1

J. Kirwan, A. Quader, and M. Grieve. Fast start-up on-board gasoline reformer for near zero emissions in spark-ignition engines. Technical Report 2002-01-1011, Society of Automotive Engineers, Inc., 2002. 5.4

S. J. Kline and F. A. McClintock. *Experimental Methods for Engineers*, volume 75, pp.3. McGraw Hill, New York, 1953. 2.7

F. Lammers and L. de Goey. A numerical study of flash back of laminar premixed flames in ceramic-foam surface burners. *Combustion and Flame*, 133:47–61, 2003. 1.4.4

J.F. Liu and W.H. Hsieh. Experimental investigation of combustion in porous heating burners. *Combustion and Flame*, 138:295–303, 2004. 1.4.4

P. Maiya, T. Anderson, R. Mieville, J. Dusek, J. Picciolo, and U. Balachandran. Maximizing h_2 production by combined partial oxidation of ch_4 and water gas shift reaction. *Applied Catalysis A:General*, 196:65–72, 2000. 5.4

P. Maness and P. F. Weaver. Biological hydrogen from fuel gases and from water. U.S. DOE Hydrogen Program Review, 1999. 1.3.10

L. Mare, T.A. Mihalik, G. Continillo, and J.H.S. Lee. Experimental and numerical study of flammability limits of gaseous mixtures in porous media. *Experimental Thermal and Fluid Science*, 21:117–123, 2000. *a*

M. Maricq and N. Xu. The effective density and fractal dimension of soot particles from premixed flames and motor vehicle exhaust. *Journal of Aerosol Science*, 35:1251–1274, 2004. 4.5, 4.5

M. Marquevich, S. Czernik, E. Chornet, and D. Montan. Hydrogen from biomass: Steam reforming of model compounds of fast-pyrolysis oil. *Energy & Fuels*, 13: 1160–1166, 1999. 1.3.5

I. Martinez. Fuel properties. http://imartinez.etsin.upm.es/, 2006. 4.3, *b*

W. M. Mathis Jr. and J. L. Ellzey. Flame stabilization, operating range, and emissions for a methane/air porous burner. *Combustion Science and Technology*, 175:825–839, 2003. 1.4.4, 4.3.2

Matweb. Matweb material property data. Technical report, Automation Creations, Inc., www.matls.com/services/services.asp, 2006. (document), 2.2

B. McBride and S. Gordon. Computer program for calculation of complex chemical equilibrium compositions and applications, ii. Users Manual and Program Description, NASA Reference Pub. 1311, 1996. 5.2

B. McBride, M. Zehe, and S. Gordon. Nasa glenn coefficients for calculating thermodynamic properties of individual species. Technical Report TP-2002-211556, NASA, 2002. *a*, 5.2

M. Metghalchi and J.C. Keck. Burning velocities of mixtures of air with methanol isoctane and indolene at high pressures and temperatures. *Combustion and Flame*, 48:191–210, 1982. (document), 4.3.2, 4.3, A, A.1

A. Meyer, C. Schroll, and R. Lesieur. Development and evaluation of mult-fuel cell power plant for transportation applications. In *Fuel Cell Technology for Vehicles*, volume PT-84 of *SAE International Progress in Technology Series*, pages 111–119, 2000. 1.1

R. A. Meyers. *Handbook of Petroleum Refining Processes*. McGraw-Hill, Toronto, 2nd edition, 1997. 1.1, 1.3.11

Inc. Mindrum Precision. *Ceramic Properties*, 2003. http://www.mindrum.com/tech.html. 4.2

R. Mital, J.P. Gore, and R. Viskanta. A study of the structure of submerged

reaction zone in porous ceramic radiant burners. *Combustion and Flame*, 111: 175–184, 1997. 1.4.4

N. Muradov. Hydrogen via methane decomposition: an application for decarbonization of fossil fuels. *International Journal of Hydrogen Energy*, 26:1165–1175, 2001. 1.3.5

N. Muradov and T. Veziroglu. From hydrocarbon to hydrogen-carbon to hydrogen economy. *Internation Journal of Hydrogen Energy*, 30:225–237, 2005. 1.3.5, 1.3.7

N. Z. Muradov. Carbon dioxide-free production of hydrogen by catalytic pyrolysis of hydrocarbon fuel. *Energy and Fuels*, 12:41–48, 1998. 1.3.5

R. Murray. Flame temperature measurement experiment. Technical report, California Institute of Technology, 1994. 4.4.1

A. Naidja, C.R. Krishna, T. Butcher, and D. Mahajan. Cool flame partial oxidation and its role in combustion and reforming of fuels for fuel cell systems. *Progress in Energy and Combustion Science*, 29:155–191, 2003. 5.3.1

D. Nield and A. Bejan. *Convection in Porous Media*. Springer, New York, 1992. 1.4.1

Omega. *Non-Contact Temperature Measurement*, 2nd edition, 1998. 2.4.1

R. Orenstein and D. Green. Thermal shock behavior of open-cell ceramic foams. *Journal of the American Ceramic Society*, 75:1899–1905, 1992. 4.7

M. Ozisik. *Heat Transfer A Basic Approach*. McGraw-Hill, 1985. C

H. Pedersen-Mjaanes. Hydrogen production from rich combustion. Master's thesis, Eng. Dept. University of Cambridge, 2003. 5.3.4

H. Pedersen-Mjaanes, L. Chan, and E. Mastorakos. Hydrogen production from rich combustion in porous meida. *International journal of Hydrogen Energy*, 30:579–592, 2005. 1.4.1

J. Piskorz, D. Scott, and D. Radlein. Pyrolysis oils from biomass: Producing, analyzing and upgrading. *ACS Symposium Series 376; American Chemical Society*, pages 167–178, 1988. 1.3.5

B. Poling, J. Prausnitz, and J. O'Connell. *The Properties of Gases and Liquids*. McGraw-Hill, Toronto, 5th edition, 2001. 3.2

A. Polo, M. Itokazu, and N. Iha. Metal complex seisitizers in dye-sensitized solar cells. *Coordination Chemistry Reviews*, 248:1343–1461, 2004. 1.3.10

M. Radler. Crude oil production climbs as reserves post modest rise. *Oil & Gas Journal*, 102(47):18, 2004. 1.1

Sandvik. Kanthal® apmt tube. Technical Report 10-04-3000, Sandvik Materials Technology, 2006. (document), 2.2

S. Sathe, R. Peck, and T. Tong. Flame stabilization and multimode heat transfer in inert porous media: A numerical study. *Combustion Science and Technology*, 70:93–109, 1990. 4.3.2

Sembach. http://www.sembach.de/uk/werkstoffe/cordierit/index.htm. Internet, 2003. 2.3

D. Simbeck and E. Chang. Hydrogen supply: Cost estimate for hydrogen pathways - scoping analysis. Technical Report NREL/SR-540-32525, National Renewable Energy Laboratory, 2002. 1.3.1, 1.3.6

Rachid B. Slimane, Francis S. Lau, Remon J. Dihu, Mark Khinkis, Jacques Bingue, Alexei Saveliev, Alexander Fridman, and Lawrence Kennedy. Production of hydrogen by superadiabatic decomposition of hydrogen sulfide. Proceeding of the 2002 U.S. DOE Hydrogen Program review, 2002. 1.4.3

R.B. Slimane, F.S. Lau, M. Khinkis, J.P. Bingue, A.V. Saveliev, and L.A. Kennedy. Conversion of hydrogen sulfide to hydrogen by superadiabatic partial oxidation: Thermodynamic consideration. *International Journal of Hydrogen Energy*, 29:1471–1477, 2004. 1.4.3

M.T. Smucker and J.L. Ellzey. Computational and experimental study of a two-section porous burner. *Combustion Science and Technology*, 176:1171–1189, 2004. 1.4.4

A. Steinfeld. From solar to chemical energy. *Fuel Cell World Proceedings*, pages 356–366, 2002. 1.3.8

R. Svehla and B. McBride. Fortran iv computer program for calculation of thermodynamic and transport properties of complex chemical systems. Technical Report TND-7056, NASA, 1973. 5.2

T. Takeno and K. Sato. An excess enthalpy flame theory. *Combustion Science and Technology*, 20:73–84, 1979. 1.4.1

ThermaCAM. *ThermaCAM Researcher User's mamual*. FLIR Systems, 2003. (document), 2.7, 2.4.1

B. Todd and J. Young. Thermodynamic and transport properties of gases for use in solid oxide fuel cell modelling. *Journal of Power Sources*, 110:186–200, 2002. 3.2, 3.2

D. Trimis, F. Durst, O. Pickencker, and K. Pickencker. Porous medium combustor versus combustion systems with free flames. In *2nd International Symposium on Heat Transfer Enhancement and Energy Conservation*, pages 339–345, 1997. 1.4.1, 1.4.4

D. Trimis and K. Wawrzinek. Flame stabilization of highly diffusive gas mixtures in porous inert media. In *The 12th International Conference on Fluid Flow Technologies Budapest, Hungary (CMFF'03)*, pages 61–68, 2003. 1.4.4

Dimosthenis Trimis and Franz Durst. Combustion in a porous medium-advances and applications. *Combustion Science and Technology*, 121:153–168, 1996. 1.4.4

H. Tuovinen. Co formation from soot and CO_2 in the hot gas layer. Report 2002:08, SP Sweedish National Testing and Research Institute, 2002. 4.5

S. R. Turns. *An Introduction to Combustion.* McGraw-Hill, New York, 2nd edition, 2000. (document), 1.4.1, 1.5, 4.2, 4.2, *a*

K. Vasudeva, N. Mitra, P. Umasankar, and S. Dhingra. Steam reforming of ethanol for hydrogen production: Thermodynamic analysis. *International Journal of Hydrogen Production*, 21(1):13–18, 1996. 5.3.3

J. Vernes. *L'ile Mystrieuse.* 3 vol. London, 1875. 1.1

A. Virtanen, J. Ristimaki, M. Marjamaki, K. Vaaraslahti, K. Keskinen, and M. Lappi. Effective density of diesel exhaust particles as a function of size. 2002-01-0056, SAE Technical Paper, 2002. 4.5

A. Virtanen, J. Ristimaki, K. Vaaraslahti, and J. Keskinen. Effect of engine load on diesel soot particles. *Environmental Science and Technology*, 38:2551–2556, 2004. 4.5

M. Vollmer, S. Henke, D. Karstadt, K. Mollmann, and F. Pinno. Challenges in infrared imaging: Low emissivities of hot gases, metals and metallic cavities. In *InfraMation*, volume 104, 2004. C, C

A. Vosloo. Fischer-tropsch: a futuristic view. *Fuel Processing Technology*, 71: 149–155, 2001. 1.1

J. P. Wagner and H. Takeda. Co purification for fuel cells using selective methanation catalysts. American Institute of Chemical Engineers Conference, 2001. 1.3.11

F. Weinberg. Combustion temperatures: The future? *Nature*, 233:239–241, 1971. 1.4.1

F.J. Weinberg, T.G. Bartleet, F.B. Carleton, and P. Rimbotti. Partial oxidation of fuel-rich mixtures in a spouted bed combustor. *Combustion and Flame*, 72: 235–239, 1988. 1.4.2

E. Weisstein. Sphere packing. http://mathworld.wolfram.com/spherepacking.html, 1999. 1.4.1

B. Yildiz and M. Kazimi. Efficiency of hydrogen production systems using alternative nuclear energy technologies. *International Journal of Hydrogen Energy*, NA, 2005. 1.3.8

Y. Yoshizawa, K. Sasaki, and R. Echigo. Analytical study of the structure of radiation controlled flame. *International Journal of Heat and Mass Transfer*, 31(2):311–319, 1988. 5.3.1

F. Zeleznik and S. Gordon. Calculation of complex equilibria. *Industrial and Engineering Chemistry Research*, 60(6):27–57, 1968. 5.2

K. Zepter and J. E. Hustad. Combustion and emission studies in a porous inert media burner. *Meeting of the Scandinavian-Nordic Section of the Combustion Institute*, 2001. 1.4.4, 4.3.2

S.A. Zhdanok. Porous media combustion based hydrogen production. In *European Combustion Meeting*, 2003. 1.4.1, 1.4.3, 2.6, 4.4, 5.4